Crystallographically Consistent Percolation Theory for Grain Boundary Networks

by

Megan E. Frary

B. S., Materials Science and Engineering
Northwestern University, 1999

M. S., Materials Science and Engineering
Northwestern University, 2001

SUBMITTED TO THE DEPARTMENT OF MATERIALS SCIENCE AND ENGINEERING
IN PARTIAL FULFILLMENT OF THE REQUIREMENTS FOR THE DEGREE OF

DOCTOR OF PHILOSOPHY IN MATERIALS SCIENCE AND ENGINEERING
AT THE
MASSACHUSETTS INSTITUTE OF TECHNOLOGY

JUNE 2005

Signature of Author: _____
Department of Materials Science and Engineering
May 16, 2005

Certified by: _____
Christopher A. Schuh
Danae and Vasilios Salapatas Assistant Professor of Metallurgy
Thesis Supervisor

Accepted by: _____
Gerbrand Ceder
Chair, Departmental Committee for Graduate Students

Crystallographically Consistent Percolation Theory for Grain Boundary Networks

by

Megan E. Frary

Submitted to the Department of Materials Science and Engineering
on May 16, 2005 in Partial Fulfillment of the Requirements for the Degree of
Doctor of Philosophy in Materials Science and Engineering

ABSTRACT

Grain boundaries are known to play a role in many important material properties including creep resistance, ductility and cracking resistance. Although the structure and properties of individual boundaries are important, the overall behavior of the material is determined largely by the connectivity of grain boundaries in the microstructure. Grain boundary networks may be studied in the framework of percolation theory by classifying boundaries as special or general to the property of interest. In standard percolation theory, boundaries are randomly assigned as special or general; however, this approach is invalid in realistic grain boundary networks due to the requirement for crystallographic consistency around any closed circuit in the microstructure. The goal of this work is to understand the effects of these local constraints on the connectivity and percolation behavior of crystallographically consistent grain boundary networks. Using computer simulations and analytical models, the behavior of crystallographically consistent networks is compared to that of randomly-assembled networks at several different length scales. At the most local level, triple junctions and quadruple nodes are found to be preferentially coordinated by special and general boundaries, leading to nonrandom network topologies that are quantified using topological parameters. Although the properties of the simulated microstructures, including connectivity length and average cluster radius of gyration, are described by the same scaling exponents as in standard percolation theory, the amplitude prefactors in the scaling relationships are changed as a result of the crystallographic constraint. The percolation threshold, an important parameter in microstructural design, is also found to differ from that of standard percolation theory by as much as ±0.05. Although all of the simulated grain boundary networks studied here are distinctly nonrandom, no two cases have the same behavior, the details of which depend strongly on the specific microstructural model. Therefore, a unified approach for locally correlated percolation problems is developed that allows the effects of the requirement for crystallographic consistency to be compared directly from system to system. This new approach can be extended beyond the study of grain boundary networks to include other locally-correlated percolation problems.

Thesis Supervisor: Christopher A. Schuh

Title: Danae and Vasilios Salapatas Assistant Professor of Metallurgy

Acknowledgements

I would like to acknowledge the members of my thesis committee, Professor Bernhardt Wuensch and Professor Linn Hobbs, for their time and insightful comments. Their suggestions lead me to consider some interesting problems that I would not have otherwise addressed. I also greatly appreciate the patience they had with the seemingly endless math that I presented.

I would also like to thank the other students in our group, Yuttanant (Vee) Boonyongmaneerat, Andy Detor, Corinne Packard, Ying Chen, Jason Trelewicz, and Jeff Zelinski, who made being at work as much as I was as enjoyable as possible.

Finally, I would like to thank my advisor Chris Schuh. When I was assigned as an undergraduate to work with Chris almost seven years ago, I could not possibly have imagined what would have happened since then. I owe much of who I am as a scientist to the enthusiastic and patient guidance of Chris. I am fortunate to have had an advisor who led by example, and who pushed me to work harder and tackle more challenging problems than I had thought possible. As I move on in my own career, I can only hope to make as much of a difference to one of my students as Chris has made to me.

Table of Contents

List of Figures

sharpness of the texture is increased (moving left to right) by decreasing the maximum rotation angle for any grain from 95° to 7°.

Figure 2.7: (001) pole figure illustrating the grain orientations that result from rotating a grain with an initial cube texture (open circles) through one of the four unique Σ3 rotations. The resulting orientation after each possible rotation is given by a different symbol (squares, circles, diamonds and triangles).

Figure 2.8: (001) pole figures for simulated twinned polycrystals with $L = 100$ (10,000 total grains). The number of twin rotations per grain, t, is indicated above each pole figure. Although the number of grain orientations mapped in each pole figure is constant, more of the grains assume unique orientations as t increases, resulting in more unique points appearing in the pole figure.

Figure 2.9: The disorientation angle distribution for fiber textured (a – c) and general textured (d – f) microstructures with either tetragonal (a, d), hexagonal (b, e) or cubic (c, f) symmetry. The different distributions correspond to different maximum rotation angles, ϕ_{max}, as labeled on the graphs. For the general textured microstructures, the distribution of disorientation angles for a random assemblage of polycrystals with the given symmetry is also shown.

Figure 2.10: The frequency of twin variant boundaries ($\Sigma 3^n$), other CSL boundaries (with $\Sigma \leq 29$), and general boundaries is plotted for simulated microstructures with $t = 0.5$, 2.0, 5.0 or 10.0 twin rotations per grain.

Figure 2.11: Fraction of low-angle boundaries, p, as a function of the sharpness of texture, given by the rotational tolerance, ϕ_{max}, for polycrystals with cubic, hexagonal, and tetragonal symmetry where the low-angle threshold is 15°. For the fiber textured microstructures, the curves are truncated at the minimum value of p achievable as explained in the text.

Figure 2.12: Fraction of low-angle boundaries, p, as a function of the rotational tolerance, ϕ_{max}, normalized by the low-angle boundary threshold, θ_t for fiber textured or general textured polycrystals.

Figure 2.13: Fraction of special (CSL) boundaries, p, as a function of t, the number of twin rotations per grain for simulated cubic polycrystals.

Figure 2.14: The probability of a simulated fiber textured microstructure containing a percolating cluster of general boundaries as a function of p, the fraction of special boundaries in the microstructure. The width of the transition region, from percolating to non-percolating, decreases as L, the number of grains per side in the simulated structures, increases. The dotted lines indicate the error bar on the percolation threshold for simulations with $L = 1000$.

Figure 3.1: Complementary spatial distribution of general (left column) and special boundaries (right column) for $p = 0.5$ on small, two-dimensional honeycomb (a – h) or irregular lattices (i, j). The polycrystals were assembled either randomly (a and b) or with crystallographic consistency (c, d: general textured; e, f: twinned, g – j: fiber textured).

Figure 3.2: Triple junction distribution for simulated microstructures with crystallographic consistency (fiber texture: solid lines, general texture: dashed lines). Also shown are the TJD for a random network (dotted lines, Eq. (1.5)), and experimental triple junction distributions, where the symbols are the same as in Figure 1.4.

Figure 3.3: Local transition probabilities, Π_x^y, for (a) $y = 0$, (b) $y = 1$, and (c) $y = 2$, which give the local probability of assigning the next boundary as a special boundary. The expectation value for a random lattice is given by the dashed line, $\Pi_x^y = p$. Deviations above this line indicate that a special boundary is more likely to coordinate the junction, while deviations below indicate that a general boundary is more likely.

Figure 3.4: Analytical triple junction distribution for fiber textured microstructure given by Eqs. (3.1) and (3.3) (solid line). Also shown are the simulated fiber textured microstructures (points) and the distribution for a random lattice as given by Eq. (1.5) (dashed lines).

Figure 4.1: (a) The four tetrakaidecahedral grains that comprise a quadruple node. The grains are labeled G_i ($i = 0$ to 3), and boundaries are labeled with lower-case letters. (b) The shared faces of the tetrakaidecahedra are the grain boundaries in the quadruple node. The lightly shaded boundaries have general character, while the darker boundaries are special. The six boundaries are labeled *a* through *f*. (c) Two-dimensional topological map of the same quadruple node as in part (b) where thinner lines indicate general boundaries and thicker lines are special boundaries. The four grains, which have the same shading as in part (a), are the enclosed areas between the lines and grain G_3 is the entire area outside the triangle. The circuit in (c) represents a second-order constraint involving four grains and four boundaries.

Figure 4.2: The quadruple node distributions for simulated three-dimensional fiber textured (circles), general textured (squares), and twinned (diamonds) microstructures. The lines represent the QND for the case where boundaries are randomly assigned character (Eq. (4.1)). The 2-D topological map is also shown for one configuration of each type of quadruple node, where thinner lines are general boundaries and thicker lines are special boundaries.

Figure 4.3: The topological map for a Q_{21} quadruple node, where the boundaries are labeled *a* through *f*, with special boundaries indicated by the thick lines and general boundaries by thinner lines. Three of the triple junctions are labeled as *i*, *ii* and *iii*, and are assigned a character in order to form this specific Q_{21} quadruple node. The possible assignments at each triple junction are shown in columns *i*, *ii* and *iii* on the right, where the correct assignment that leads to this specific quadruple node is indicated by the dashed box.

Figure 4.4: The error between Q_{ij} as predicted by Eq. (4.6) and as found from the simulations for (a) fiber textured, (b) general textured and (c) twinned microstructures. Positive ΔQ_{ij} values indicate that Eq. (4.6) overpredicts Q_{ij}, while negative ΔQ_{ij} values indicate underprediction of Q_{ij}. The maximum error for each microstructure is shown by the dashed lines and is ~0.05 for each. However, the

majority of the Q_{ij} are predicted quite accurately, and 75% of these errors lie within the dotted lines at $\Delta Q_{ij} \sim 0.015$.

Figure 4.5: The decrease in configurational entropy (Eq. (4.8)) from the maximum entropy configuration, S_o, for fiber textured (circles), general textured (squares) and twinned (diamonds) microstructures due to crystallographic constraints. For nearly every value of p in all three systems, the decrease in entropy is greater when both first- and second-order constraints are imposed (filled points) than with first-order constraints only (open points).

Figure 5.1: The complementary relationship between a percolating 1-D chain of special boundaries (darker shading) and a 2-D surface of general boundaries (lighter shading). The presence of the percolating chain of special boundaries removes the possibility of a sample-spanning surface of general boundaries, as at least one boundary on the surface of general boundaries must be part of the percolating cluster of special boundaries.

Figure 5.2: The average radius of gyration, R_s, as a function of cluster mass for simulated honeycomb lattices at the percolation threshold; for random networks $p = 0.653$ (diamonds), for general boundary networks $p = 0.601$ (squares, offset in R_s by a factor of 10), and for special boundary networks $p = 0.689$ (circles, offset in R_s by a factor of 100). The lines represent the best fit of Eq. (5.1).

Figure 5.3: The cluster mass distribution at the percolation threshold for random networks at $p = 0.653$ (diamonds), general boundary networks at $p = 0.601$ (squares, offset in n_s by a factor of 10), and special boundary networks at $p = 0.689$ (circles, offset in n_s by a factor of 100). The results were obtained from simulations on 2-D honeycomb lattices. The lines represent the best fit of Eq. (5.2).

Figure 5.4: The connectivity length ξ as a function of $|p - p_c|$ both below (a) and above (b) the critical point (given in Table 5.1) for random networks (diamonds), general boundary networks (squares, offset in ξ by a factor of 10), and special boundary networks (circles, offset in ξ by a factor of 100). Above the percolation threshold, the contribution of the lattice-spanning cluster is not included in the determination of ξ. These simulations used 2-D honeycomb lattices, and the lines represent the best fit of Eq. (5.3).

Figure 5.5: The dependence of the strength of the "infinite" or lattice-spanning cluster, P, as a function of $|p - p_c|$. The values of p_c are given in Table 5.1. The diamonds represent random networks, the squares general boundary networks (offset in P by a factor of 3), and the circles special boundary networks (offset in P by a factor of 9). The results were obtained from simulations on 2-D honeycomb lattices. The lines represent the best fit of Eq. (5.4).

Figure 5.6: For 2-D honeycomb networks, the cluster mass distribution at the percolation threshold is plotted for small values of s in random networks at $p = 0.653$ (open diamonds) and special boundary networks at $p = 0.689$ (filled circles).

Figure 5.7: Taxonomy of grain boundary clusters. The left column illustrates clusters with different masses. In the middle column, some topologically unique animals with $s = 9$ are shown. The animals are labeled a-b-c, where a is the number of J_1, b the

crystallographically consistent networks (green curves). In (a), the data points are the same data as presented in Figure 1.4, while the light green and dark green curves are for fiber textured and general textured microstructures, respectively. In (b), the data points were gathered by Schuh *et al.* for microstructures where the boundaries were classified as CSL vs. non-CSL and the green curve is for the twinned microstructural family.

Figure 6.3: Schematic network structures corresponding to the segregated state (left, with $\eta_{SO} > 0$) along the $J_0 - J_3$ edge or ordered state (right, with $\eta_{SO} < 0$) along the $J_1 - J_2$ edge. The surface plotted in the coordination tetrahedron is for points with $\eta_{SO} = 0$ (Eq. (6.3)) and contains the trajectory for a randomly assembled network (black curve).

Figure 6.4: Schematic network structures corresponding to the elongated state (left, with $\eta_{CE} < 0$) along the $J_0 - J_2 - J_3$ face or clumpy state (right, with $\eta_{CE} > 0$) along the $J_0 - J_1 - J_3$ face. The surface plotted in the coordination tetrahedron is for points with $\eta_{CE} = 0$ (Eq. (6.4)) and contains the trajectory for a randomly assembled network (black curve).

Figure 6.5: Schematic representation of the four unique topological states defined by (i) $\eta_{SO} > 0$ and $\eta_{CE} > 0$ (segregated and clumpy), (ii) $\eta_{SO} > 0$ and $\eta_{CE} < 0$ (segregated and elongated), (iii) $\eta_{SO} < 0$ and $\eta_{CE} > 0$ (ordered and clumpy), and (iv) $\eta_{SO} < 0$ and $\eta_{CE} < 0$ (ordered and elongated). At the J_0 and J_3 vertices, all four states converge.

Figure 6.6: For the three microstructural models studied here, the evolution of the grain boundary networks is plotted as a function of the topological parameters (η_{CE} and η_{SO}) and p, the fraction of relevant boundaries (special boundaries for the green curves and general boundaries for the red curves). The black curve is for randomly assembled networks. (a) The black points represent the percolation thresholds determined in Chapter 5. (b) The relative position of the trajectories can be more easily observed in projection along the p-axis where each of the four quadrants represents one of the four topological states. In (b), the intial location of the trajectory in the $p = 0$ plane is indicated by a circle.

Figure 6.7: In the coordination tetrahedron, the points where (a) less than 50% of the simulated networks contained a percolating cluster, (b) greater than 50% contained a percolating cluster, and (c) between 25 and 75% contained a percolating cluster. The data points in (c) are used to determine the polynomial fit for the percolation surface (Eq. (6.7)), also shown in (c).

Figure 6.8: In terms of the topological parameters, the points where (a) less than 50% of the simulated networks contained a percolating cluster, (b) greater than 50% contained a percolating cluster, and (c) between 25 and 75% contained a percolating cluster. The data points in (c) are used to determine the polynomial fit for the percolation surface (Eq. (6.8)), also shown in (c).

Figure 6.9: For (a) randomly assembled, (b) fiber textured, (c) general textured and (d) twinned microstructures, the known trajectories are plotted for special boundary clusters (green curve changing to blue) and general boundary clusters (red curve

changing to blue). The non-percolating part of the random network trajectory is shown in black as it applies to either special or general boundaries. The color change corresponds to the real percolation threshold (Table 5.1) and should occur when the trajectory intersects the surface defined by Eq. (6.7). The errors between the real and predicted values are summarized in Table 6.1.

Figure 6.10: For (a) randomly assembled, (b) fiber textured, (c) general textured and (d) twinned microstructures, the known trajectories are plotted for special boundary clusters (green curve changing to blue) and general boundary clusters (red curve changing to blue). The non-percolating part of the random network trajectory is shown in black as it applies to either special or general boundaries. The color change corresponds to the real percolation threshold and should occur when the trajectory intersects the surface as defined by Eq. (6.8).

Figure 6.11: Logarithmic contour map of the connectivity length for sections through the $\eta_{CE} - \eta_{SO} - p$ space where (a) $\eta_{CE} = 0$ or (b) $\eta_{SO} = 0$. The points with the highest values of connectivity length lie on or near the percolation surface. In addition to illustrating how ξ changes with the topoplogical parameters and p, this figure also shows how the percolation threshold changes with these variables.

Figure 6.12: The variation in the amplitude prefactor in the connectivity length scaling law, C_ξ, as defined in Eq. (6.9) for values of p (a) below the percolation threshold and (b) above the percolation threshold. The surfaces plotted here are polynomial fits to the binned data as explained in the text and are given by Eq. (6.10).

Figure B.1: Labeling scheme for angles at a triple junction; ϕ_X are grain orientations which occupy the range $(-\phi_{max}, \phi_{max})$, while θ_x are grain boundary disorientations and exist on the range $(-2\phi_{max}, 2\phi_{max})$.

Figure B.2: Fraction of low-angle boundaries, p, as a function of the ratio of the allowed grain rotation, ϕ_{max}, to the low-angle threshold, θ_t. The points are from simulated fiber textured microstructures and the solid line is given by Eq. (B.8).

Figure B.3: The distribution of disorientation angles of grain boundary b, $f(\theta_b)$, for different values of θ_a as given by Eq. (B.14). The different line styles correspond to evenly spaced increments of θ_a from 0 to $-2\phi_{max}$ (left) or 0 to $2\phi_{max}$ (right).

Figure B.4: Disorientation of boundary a, θ_a, as a function of disorientation of boundary b, θ_b. The distribution F_x^1 can be found by integration of Eq. (B.14) over the regions shown in this map according to Eq. (B.10). The shaded regions are differentiated by whether boundary b has previously been assigned as special (labeled F_1^1) or as general (labeled F_0^1). The white regions are physically impossible combinations as given by Eq. (B.15). It is important to note that the shaded areas do not give the function explicitly, they give only the limits of integration on the disorientation angles.

Figure B.5: These maps are used in determining the functions F_x^2. When the disorientation of boundary c, θ_c, is plotted as a function of θ_a, the disorientation of boundary b is also known explicitly at every point due to the requirement of crystallographic

consistency (Eq. (B.2)). The different shadings correspond to how many of boundaries *a* and *b* are classified as special boundaries based on their disorientation angles. The different regions give the limits of integration on Eq. (B.10) to find F_x^2.

Figure B.6: To determine the local transition probability, Π_x^y, the distribution F_x^y is integrated according to Eq. (B.28). For $\phi_{max} > \theta_t$ (a and c) or $\phi_{max} < \theta_t$ (b and d), these maps show the limits of integration on the function F_x^y. The regions with solid shading are points where the next boundary assigned will be classified as a special boundary. These maps should be compared to those in Figures B.4 and B.5 which showed the regions of integration to find F_x^y. It is important to note that the shaded areas do not give the function explicitly; they give only the limits of integration on the disorientation angles.

Figure C.1: The variation of the Lagrange multiplier μ with the fraction of special boundaries for the both the TJD (dashed line) and the QND (solid line). The open points represent the fit of μ for the QND as given by Eq. (C.8).

Figure E.1: The first three orders of constraint in 2-D honeycomb lattices are shown schematically. The order of the constraint, *B*, is given by the number of triple junctions encircled by a Frank-Nabarro circuit. The number of unique species, ω, of each order is identified as well. For $B = 1$ and $B = 3$, a representative structure is shown for each of the unique species in which the thicker lines indicate special boundaries and the thinner lines general boundaries.

Figure E.2: The magnitude of the total entropy change between a randomly assembled network and one in which full crystallographic constraints are imposed, plotted as a function of *p*. ΔS_3^0 is calculated from Eq. (E.2) using the population of $B = 3$ boundary structures.

Figure E.3: The contribution of each constraint level (*B*) to the change in configurational entropy, ΔS_3^B, evaluated at $p = 0.35$ for the $B = 3$ boundary structure.

Figure E.4: The percolation thresholds for (a) special boundaries and (b) general boundaries in fiber textured (circles), general textured (squares), or twinned (triangles) microstructures as a function of the constraints imposed on the system. The percolation thresholds are summarized in Table 6.1, and left to right, these data correspond to either random boundary assignment (no constraints imposed), triple junction assignment (only first-order constraints imposed), or grain orientation assignment (resulting in full crystallographic constraint).

Figure E.5: Frank-Nabarro circuits of fourth (a, b) and fifth (c) order.

List of Tables

Nomenclature

The following list defines the variables and acronyms used in this work and, where appropriate, the equation in which the variable is first defined or introduced:

b_{ij}	Components of the grain boundary misorientation matrix (Eq. (A.9))
c_{ij}	Components of the grain boundary misorientation matrix (Eq. (A.9))
c	Fitting parameter to describe the variation of the Lagrange multiplier with p (Eq. (C.8))
d	Common denominator between Σ_a and Σ_b in the sigma combination rule (Eq. (1.3))
f	Density distribution of disorientation angles when another angle is fixed (Eq. (B.10))
$\mathbf{g_i}$	Grain orientation matrix (Eq. (2.1))
j_{CE}	Term which determines the form of η_{CE} (Eq. (6.2b))
j_{SO}	Term which determines the form of η_{SO} (Eq. (6.2a))
m	Number of topologically unique isomers for a given junction composition (Eq. (C.3))
n_s	Cluster size distribution (Eq. (5.2))
p	Fraction of boundaries classified as either special or general
p_c	Percolation threshold
q	Fraction of general boundaries
r_i	Center of mass of an individual grain boundary (Eq. (2.3))
r_o	Center of mass of a grain boundary cluster (Eq. (2.4))
s	Grain boundary cluster mass
t	Number of $\Sigma 3$ rotations per grain
w	Exponent used in determining a threshold angle for classification of coincidence site lattice boundaries (Eq. (1.1))
z	Number of boundaries that coordinate a junction (Eq. (C.2b))
A_i	Grain boundary area (Eq. (2.3))
B	Order of constraint
CSL	Coincidence site lattice
C_x	Amplitude prefactors in scaling laws
D	Scaling exponent that describes the variation in average radius of gyration (Eq. (5.1))
E	Function to minimize in Monte Carlo algorithm (Eq. (6.6))
F	Global density distribution of an orientation or disorientation angle (Eq. (B.3))
F_y^x	Global density distribution of a disorientation angle given that x boundaries were assigned and y were assigned as special (Eq. (B.16))
GBE	Grain boundary engineering
GBCD	Grain boundary character distribution
H	Inner-product of rotation axes for boundaries b and c (Eq. (A.14))
I	Identity matrix
J_i	Fraction of triple junctions coordinated by i special boundaries (Eq. (1.5))
L	Number of grains per side in simulated microstructures

$\mathbf{M_x}$ Grain boundary misorientation matrix (Eq. (1.2))

N Number of different species of a given type of junction (Eq. (C.1))

P Strength of the infinite or lattice-spanning cluster ((Eq. (5.4))

Q_{ij} Fraction of quadruple nodes coordinated by *i* special boundaries and *j* triple junction comprised of two or more special boundaries (Eq. (4.1))

QND Quadruple node distribution

R_s Average radius of gyration for clusters with mass *s* (Eq. (5.1))

R_g Radius of gyration of an individual grain boundary cluster (Eq. (2.3))

S Configurational entropy (Eq. (4.8))

T Number of distinct texture components in a microstructure

TJD Triple junction distribution

U_i Population of second-order boundary species

V_i Population of third-order boundary species

X_i Fraction of unspecified junctions of the i^{th} type (Eq. (C.9))

Y Function that yields the Lagrange multiplier μ for the maximum entropy triple junction distribution (Eq. (C.7))

Z Function whose roots give the Lagrange multiplier μ (Eq. (C.5))

α Possible triple junction assignments given one boundary has been assigned as general (Eq. (4.7a))

β Scaling exponent that describes the variation in the strength of the infinite cluster (Eq. (5.4))

γ Possible triple junction assignments given one boundary has been assigned as special (Eq. (4.7b))

δ Simplifying functions in the definition of the triple junction distribution in terms of the topological parameters (Eqs. (D.1-4))

η Topological parameter (Eq. (6.1))

θ_t Threshold angle for classification as a low-angle boundary (Eq. (1.1))

θ_x Deviation angle from an ideal coincidence site lattice misorientation relationship

λ Probability of correctly assigning one of the triple junctions that makes up a quadruple node (Eq. (4.2))

μ Lagrange multiplier used to determine the maximum entropy distribution (Eq. (C.4))

ν Scaling exponent that describes the variation in the connectivity length (Eq. (5.3))

σ Ratio of configurational entropy with first- to first-plus-second-order constraints (Eq. (4.9))

τ Scaling exponent that describes the variation in the cluster mass distribution (Eq. (5.3))

ϕ_{max} Grain rotation limit

ϕ_x Grain orientation angle

ξ Connectivity length (Eq. (2.5))

Γ Fraction of animals with a given topology

Δ Grain boundary deviation matrix (Eq. (A.4))

Θ_M Maximum disorientation between grains in fiber textured microstructures

Θ_x Maximum deviation angle of a coincidence site lattice boundary (Eq. (1.1))

Λ Probability of assembling a specific quadruple node from three triple junction assignments (Eq. (4.2))

Π_y^x Local transition probability (Eq. (B.28))

Σ Reciprocal coincidence site density of a grain boundary

Ω Number of conformations for a quadruple node (Eq. (4.1))

Chapter 1: Introduction

1.1. The Role of Grain Boundaries in Material Properties

Grain boundaries have long been known to affect nearly all material properties; these may be divided into two general classes depending on the role the grain boundaries play:

- *Intergranular* phenomena are those in which chemical species or defects (i.e., cracks) are transported along the grain boundaries. Some common intergranular phenomena where the character of the grain boundaries is known to be critical are cracking [1], corrosion [2], diffusion [3], creep [4], electromigration [5], and dynamic embrittlement [6].
- *Transgranular* phenomena are those in which the transport occurs across the grain boundaries. The importance of grain boundary character in transgranular phenomena is well known in cleavage cracking [7], plasticity [8], electrical conductivity [9], and superconductivity [10].

While individual grain boundaries have five macroscopic degrees of freedom [11-13], it would be difficult to explicitly consider each when modeling a material property as a function of grain boundary character. For most phenomena, both intergranular and transgranular, the five degrees of freedom may be consolidated and the grain boundary given a binary classification based on its overall structure. The binary classification identifies a boundary as either *special* or *general* to the property of interest based on *a priori* knowledge of how the grain boundary structure affects the property. For example, if a material is to undergo plastic deformation, dislocations should be able to pass from one grain to the next through the grain boundaries. Therefore, a boundary will be labeled "special" if the grains on either side are misoriented in such a way that their activated slip systems are aligned, while a "general" boundary would not allow for the passage of dislocations [14-17]. The detailed atomic structure of the boundary is therefore important in determining the classification of the boundary, but for purposes of studying plasticity, it is often sufficient to classify the boundary as one that will or will not impede dislocation motion.

Another commonly used binary classification method classifies each boundary in the framework of the coincidence site lattice (CSL) model. In the CSL model, each boundary is classified by a Σ value, which gives the reciprocal density of sites coincident to the two grains. It is unusual for a grain boundary to have an exact CSL misorientation; therefore, grain boundaries are commonly classified with both a Σ value and an angle θ by which the boundary deviates from

that ideal CSL relationship [11, 18]. The maximum deviation allowable for a boundary to be classified as special is Θ_x, given by:

$$\Theta_x = \theta_t \Sigma^{-w} \tag{1.1}$$

where $\theta_t \approx 15°$ is the low-angle boundary limit (for $\Sigma = 1$), and the exponent w lies between ½ and 1 [19-22]. In face-centered cubic metals, it has been shown that only low Σ values ($\Sigma \leq 29$) exhibit special behavior [23]. Special boundaries classified using this binary method are known to be resistant to corrosion [2, 24-27], intergranular cracking [7, 28-32], and creep [4, 33].

A final and perhaps the most frequently used binary classification method separates boundaries on the basis of their disorientation angles alone. Those boundaries with disorientations below a property-specific threshold value, θ_t, are classified as special, while boundaries with higher disorientation angles are deemed general. This classification method is particularly relevant to high temperature superconductors, where boundaries with disorientations greater than $\theta_t \approx 8°$ are known to have low critical current densities and to impede the current flow across the microstructure [10, 34-36]. The approach of classifying low-angle boundaries as "special" and high-angle boundaries as "general" is also applicable to grain boundary sliding [37-39], corrosion resistance [24], and electromigration [40-42].

For many materials properties, either CSL or low-angle boundaries are known to have special properties; therefore, bulk materials properties may be improved by increasing the fraction of special boundaries in the microstructure. Recently, a class of processing techniques has been developed which tailors microstructures in this way [1, 43-48], referred to broadly as "grain boundary engineering" (GBE). Most GBE processing methods involve straining and annealing, often in a cyclic manner [43, 49-53], and have been shown to lead to orders of magnitude enhancements in properties such as intergranular corrosion [2, 54], stress corrosion cracking [30, 31, 55], electromigration resistance [40, 41], creep resistance [33], and superconductivity [56, 57]. Through the practice of GBE, the grain boundary character distribution (GBCD) has become an adjustable parameter in materials design. To appreciate how such dramatic property enhancements can be achieved with GBE, it is necessary to consider the connectivity of general and special grain boundaries at both the local and global length scales.

1.2. Local Connectivity of Grain Boundaries

It is now appreciated that not only the properties of individual boundaries are important to the behavior of a material, but that the connectivity of special and general boundaries can largely determine the material properties [4, 47, 55, 58-61]. For example, on the local level, if an intergranular crack propagates along a path of general boundaries as shown schematically by the thick lines in Figure 1.1, each vertex in the diagram represents a "decision point". For the progress of the crack to be arrested at its current position, the boundaries labeled *a* and *b* must both be special boundaries which are resistant to cracking. The importance of the boundary composition of triple junctions in intergranular phenomena has been incorporated into models for several material properties. Lim and Watanabe [58] were perhaps the first to develop a model for intergranular fracture which involved the probability of finding a boundary susceptible to fracture at a triple junction. In their model, all triple junctions with two special boundaries act as crack-arrest sites (c.f., Figure 1.1). Palumbo *et al.* [55] developed a similar model for intergranular stress corrosion cracking, in which both the inherent structure of the boundary and its alignment with respect to the applied stress determined whether the boundary was susceptible to cracking. The authors have used their model to predict average crack length as function of the fraction of special boundaries in the microstructure. A similar approach was taken by Alexandreanu *et al.* [4] to predict the effect of special boundaries on the creep behavior of nickel-based alloys. Gertsman *et al.* further developed the model in Ref. [55] to account for the possibility of correlations among boundaries at a triple junction. Their modified approach finds

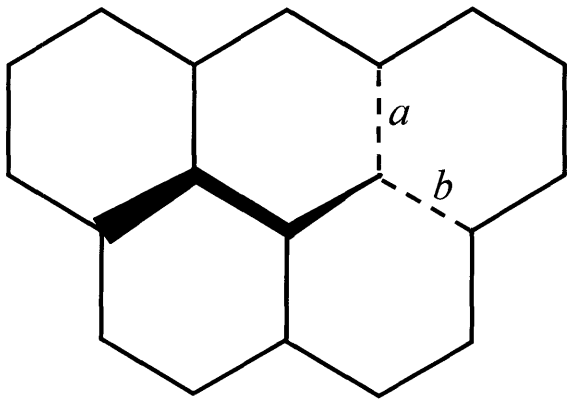

Figure 1.1: Schematic representation of the propagation of an intergranular crack. Thin, solid lines are general boundaries, dashed lines are special boundaries, and the thick line is the crack. At the triple junction with two special boundaries (labeled *a* and *b*), crack propagation is arrested.

the probability of intergranular crack arrest as a function of different triple junction populations. Other authors including Pan *et al.* [59] and Gertsman and Tangri [60] have developed models for cracking based on a Markov chain process for crack growth in which the only boundaries with the potential for cracking are those with at least one neighbor that has cracked. More recently, Thomson and Randle [47] have introduced the term "secure triple junctions" to describe those triple junctions coordinated by at least two special boundaries. Finally, Kumar *et al.* [53] have suggested that models such as Ref. [61] underpredict the probability of crack arrest since the probability should exclude triple junctions with three special boundaries which are never sampled by an advancing crack. Using a modified criterion, these authors can more accurately model the maximum size of grain boundary clusters, a predictor of many materials properties [50, 62]. With regard to grain boundary engineering, the improved materials properties which arise due to an increase in the fraction of special boundaries may also be a result of changing the local boundary connectivity at triple junctions.

1.3. Percolation-Based Models of Grain Boundary Networks

Grain boundary engineering can also result in a change in global connectivity of grain boundaries (i.e., the topology of the grain boundary network). To illustrate how the grain boundary network may evolve during GBE, Figure 1.2 shows a simulated 2-D microstructure whose global fraction of special boundaries, p, is increasing. In Figure 1.2, the special boundaries are the thinner lines and the general boundaries the thicker lines. When the special fraction is low (Figure 1.2a, $p = 0.15$), the microstructure is composed of almost all general boundaries, which are highly interconnected and would readily allow for a crack to "percolate" across the sample. As the special fraction increases (Figure 1.2b, $p = 0.35$), a percolating path of general boundaries across the microstructure still exists, but the special boundaries are beginning to disrupt the network of general boundaries. At higher values of p (Figure 1.2c, $p = 0.55$), there is no longer a connected path of general boundaries that spans the microstructure due to the large population of special boundaries. As the special fraction increases further (Figure 1.2d, $p = 0.75$), remaining paths of general boundaries continue to decrease in both number and length. In Figure 1.2, the network undergoes a topological phase transition from a phase with a percolating cluster to a phase without one. In an infinitely large network, this second-order phase transition occurs exactly at a critical value of p known as the percolation threshold, p_c [63-65]. The

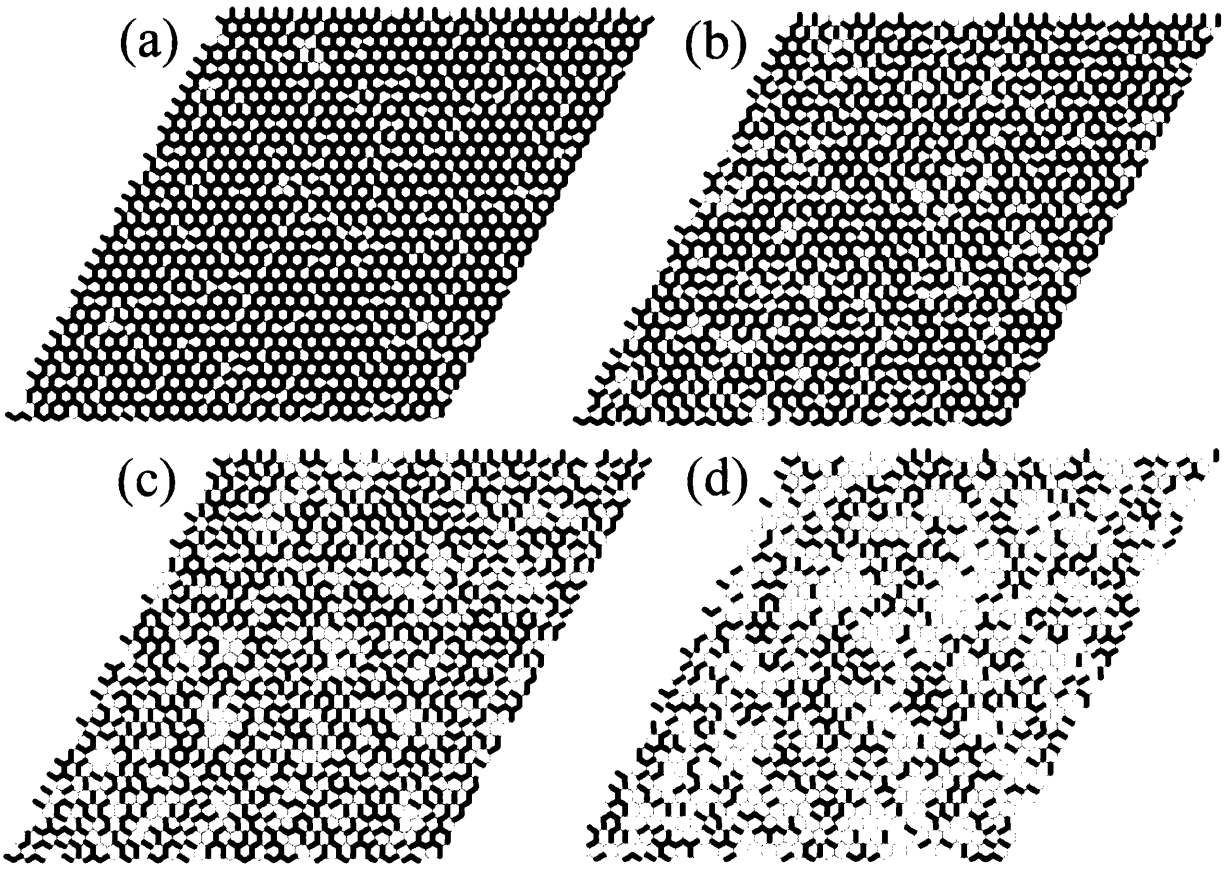

Figure 1.2: Simulated 2-D microstructures using a honeycomb grid on which grain boundaries (the edges of the hexagons) are randomly assigned as special (thin lines) or general (thicker lines) with probability p. The fraction of special boundaries is (a) $p = 0.15$, (b) $p = 0.35$, (c) $p = 0.55$ and (d) $p = 0.75$.

dramatic increases in materials properties due to GBE may thus be realized by engineering the microstructure to have a large enough value of p to break up any long paths of general boundaries. Using electron backscattered diffraction (EBSD) and grain orientation mapping software to follow the evolution of networks of special and general boundaries during grain boundary engineering, many authors have shown that networks of general boundaries are broken up during GBE, while the networks of special boundaries become more interconnected with further processing [50, 53, 54].

The spatial extent of clusters, or connected paths, of grain boundaries has also been studied [50, 60, 66-68] through either an average cluster size or the "connectivity length", a length scale above which clusters are exponentially rare [64, 69]. Gertsman and Tangri [60]

used simulated microstructures to study the average crack length from a nucleation site on the surface as a function of the fraction of crack resistant boundaries. More recently, Wang and Zuo [67] used computer simulations to measure a correlated crack length as a function of applied stress. In their model, the fraction of boundaries susceptible to cracking is a dynamic property; although initially resistant to cracking, each CSL boundary will crack when the stress component normal to the boundary plane reaches a critical fracture stress, σ_f, which is a function of the Σ value of the boundary. The cluster properties described above have also been investigated through experimental work by Volovitch *et al.* [66] who measured the cluster density for grain boundaries in zinc that had been wetted by gallium, and by Henrie *et al.* [68] who determined the mean cluster diameter for clusters of sensitized boundaries in stainless steel. Most recently, Schuh *et al.* [50] have developed algorithms which can extract a wide variety of cluster properties from EBSD data sets, including the mean and maximum cluster mass, connectivity length and maximum linear dimension of a cluster. The authors evaluate each of these properties in their grain boundary engineered microstructures as a function of the number of processing cycles (i.e., with the evolution of the special boundary fraction).

The concepts presented above, specifically the statistical behavior of grain boundary clusters and the existence of a percolation threshold, suggest that grain boundary networks can be studied in the context of percolation theory. Standard percolation theory is a very well understood field that has been used to study the connectivity of a wide variety of systems [69], where each site or bond on a lattice is randomly assigned as occupied or unoccupied. The percolation threshold depends on both the shape and dimensionality of the underlying lattice; for 2-D honeycomb "bond" problems, as in Figure 1.2, p_c is known analytically to be $1-2\,\mathrm{Sin}(\pi/18)$ (≈ 0.653) [70]. When standard percolation-based models are applied to grain boundary networks, each grain boundary in the microstructure is randomly assigned as special (occupied) with a probability p or general (unoccupied) with probability $1-p$. Many materials properties, including superconductivity [71-75], stress corrosion cracking [59, 60, 76], magnetotransport [77, 78], electromigration [41, 79, 80], and grain boundary wetting [66, 81] have been studied in the context of percolation theory. Nearly all of these works followed the model of standard percolation theory in which the grain boundaries are randomly assigned character from a known global distribution. As will be explained in the subsequent section, this

approach is unphysical for the case of grain boundary networks and results in networks whose topologies differ qualitatively and quantitatively from those of real grain boundary networks.

1.4. Correlations among Grain Boundaries at a Triple Junction

Standard percolation theory is based on the assumption that each boundary can be assigned as special or general at random, independent of the character of the neighboring boundaries. However, this assumption is known to not hold in grain boundary networks, as crystallographic consistency at triple junctions requires that grain boundary misorientation be conserved. Around a triple junction such as that in Figure 1.3, a circuit originating in grain *A* will cross each boundary exactly once where there will be a discontinuous change in orientation (the grain boundary misorientations). However, the circuit ends in the same grain where it began, which requires the misorientations to be conserved and self-consistent. This consistency requirement may be expressed in terms of the grain boundary misorientation matrices as [82]:

$$\mathbf{M}_a\mathbf{M}_b\mathbf{M}_c = \mathbf{I} \tag{1.2}$$

where $\mathbf{M}_x$ is the 9-component misorientation matrix for boundary x and $\mathbf{I}$ is the identity matrix. Eq. (1.2) implies that if the misorientations of two of the boundaries are chosen at random, the misorientation of the third boundary is fixed by the requirement for crystallographic consistency.

Although Eq. (1.2) exactly specifies which boundaries may coordinate a triple junction, grain boundaries are rarely classified by their full misorientation matrices and more often labeled by either a Σ value or simply by their disorientation angle. In either case, Eq. (1.2) may be simplified so as to result in a useful "rule" which specifies either the Σ-values or disorientation

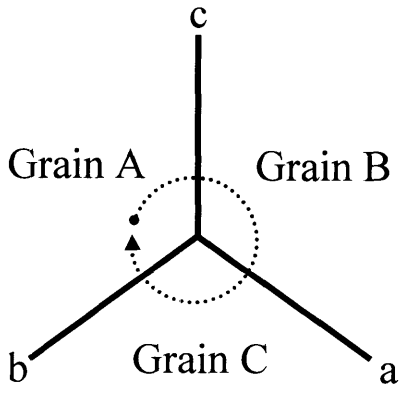

Figure 1.3: An idealized triple junction between three grains, *A*, *B*, and *C*. For a complete circuit around the junction (dashed line), three grain boundaries, *a*, *b*, and *c*, are crossed, giving three step-changes in Euler orientation space. Since the beginning and end of the circuit lie in the same grain, these changes must sum to zero; misorientation is conserved.

angles of boundaries that can coordinate a triple junction. When three CSL boundaries meet at a triple junction, their Σ values must obey the well-known "sigma combination rule":

$$\Sigma a \cdot \Sigma b = d^2 \Sigma c \tag{1.3}$$

where Σx is the CSL-type of boundary *x* and *d* is a common divisor of Σa and Σb. This relationship was substantially proven by Miyazawa *et al.* [83] for the special case where boundaries *a* and *b* involve 180° degree rotations. More recently, Gertsman has rigorously proven that Eq. (1.3) is valid generally, given that all three boundaries have ideal CSL misorientations [84].

The sigma combination rule has proven valuable in many experimental and theoretical analyses of individual triple junctions. For example, Furley and Randle [85], as well as Kumar et al. [86], have examined many individual triple junctions composed of CSL boundaries with a common axis, and demonstrated conformity with Eq. (1.3). Palumbo et al. used Eq. (1.3) to establish the so-called "twin-limited" microstructure [87]; according to the sigma combination rule, no more than two twin boundaries, with Σ = 3, may meet at any triple junction, so that no more than two-thirds of the boundaries may be twin boundaries in any microstructure.

In the derivation of the sigma combination rule, all of the boundaries were assumed to have ideal CSL misorientations, and the rule is strictly applicable only in this situation. However, in reality, most boundaries will deviate from their ideal CSL misorientation. In the case where three non-ideal CSL boundaries meet at a triple junction, each will be described by its Σ value and its deviation angle θ. It has recently been shown that crystallographic consistency requires that not only must the Σ values obey Eq. (1.3), but the angular deviations must obey the so-called "deviation limit rule" [88]:

$$\theta_{max} \leq \theta_1 + \theta_2 \tag{1.4}$$

where θ_{max} is the greatest of the three angular deviations and θ_1 and θ_2 are the deviations of the other two boundaries in no particular order. The details of the derivation of the deviation limit rule are presented in Appendix A. Equations (1.3) and (1.4) should be viewed as complementary rules which must be simultaneously satisfied at any triple junction where the boundaries are classified in the CSL framework.

The deviation limit rule may also be applied to the case where boundaries are classified by their misorientation angle only. Strictly speaking, this represents the special case where the misorientation of each boundary is the deviation angle with respect to the ideal Σ1 misorientation. If all three boundaries are classified as Σ1 boundaries, Eq. (1.3) is automatically satisfied and the misorientation angles must then obey the deviation limit rule. It is easily seen that if boundaries were randomly assigned misorientation angles as in standard percolation models, physically unrealistic combinations would likely result which violate Eq. (1.4).

1.5. Influence of Crystallographic Constraint on Grain Boundary Connectivity

As materials properties depend largely on the local connectivity among special and general boundaries, the influence of crystallographic constraint on the distribution of triple junction types is of much importance. The triple junction distribution (TJD) is used to measure correlations among neighboring boundaries and gives J_i, the fraction of triple junctions coordinated by i (= 0 to 3) special boundaries [53, 60, 62, 89-92]. In the absence of crystallographic constraint, each boundary is randomly assigned as special with the probability p and the TJD is obtained from a straightforward probabilistic argument:

$$J_i = \binom{3}{i} p^i (1-p)^{3-i} \tag{1.5}$$

where the combinations $\binom{3}{i}$ are equal to 1, 3, 3 and 1 for i = 0, 1, 2 and 3, respectively. This distribution is shown by the lines in Figure 1.4. Prior to this thesis research, the TJD had been measured mainly in microstructures where the boundaries were classified as CSL (special) or non-CSL (general) [50, 53, 62, 89, 91, 93]. The results of these experimental studies of grain boundary network topology have shown asymmetry in the connectivity and clustering characteristics of special vs. general boundaries. In these experimental works and in earlier simulations of grain boundary networks [89], J_2 triple junctions (i.e., two special boundaries and one general boundary) were less abundant than predicted by Eq. (1.5). Recent theoretical work has also emphasized the role of crystallographic consistency on grain boundary connectivity. For example, when Σ = 3, 9, and 27 special boundaries are assembled along with general boundaries in a manner consistent with Eq. (1.3), Minich *et al.* have analytically derived a highly non-random distribution of triple junction types that is consistent with experimental results [92].

Symbol	Material	Space Group	θ_t (deg)	Ref.	Symbol	Material	Space Group	θ_t (deg)	Ref.
○	Nickel	$Fm\bar{3}m$	15	[94]	◇	8090 Al-Li alloy	$Fm\bar{3}m$	15	[95]
▲	Nickel	$Fm\bar{3}m$	15	[85]	◘	Aluminum 5052	$Fm\bar{3}m$	15	[96]
△	Nickel	$Fm\bar{3}m$	15	[97]	□	Cu-1Al	$Fm\bar{3}m$	15	[98]
●	Nickel	$Fm\bar{3}m$	4	[99]	▧	Platinum	$Fm\bar{3}m$		[100]
⊠	Nickel	$Fm\bar{3}m$	10	[101]	▽	Fe-35Al-4.3Cr-0.1Zr-0.05B	$Pm\bar{3}m$	15	[102]
⊞	Nickel	$Fm\bar{3}m$	7	[99]	■	$(Bi,Pb)_2Sr_2Ca_2Cu_3O_x$	I4/mmm	15	[103]
◣	Nickel	$Fm\bar{3}m$	5	[57]	◢	$(Bi,Pb)_2Sr_2Ca_2Cu_3O_x$	I4/mmm	15	[104]
◆	Nickel	$Fm\bar{3}m$	10	[57]	▼	$YBa_2Cu_3O_7$	Pmmm	10	[105]

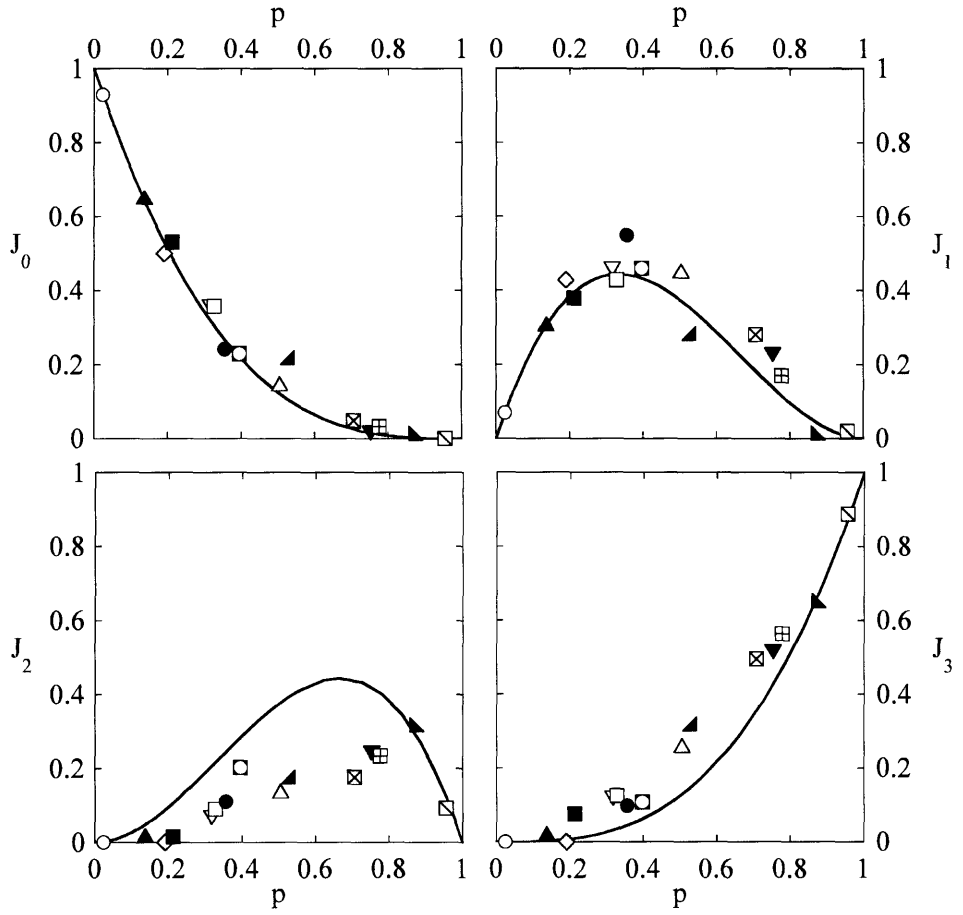

Figure 1.4: Triple junction distributions from existing experimental data (points), covering a range of materials and crystal systems, including pure metals, intermetallic alloys and superconducting oxides, with low-angle thresholds θ_t between 4 and 15°. These data are compared to the triple junction distribution for a random assemblage of boundaries as given by Eq. (1.5) (solid lines).

Until recently, only one study had investigated the effects of crystallographic constraint on the percolation threshold in simulated grain boundary networks [62]. Schuh *et al.* found that the threshold for percolation of general boundaries shifted from $p_c = 0.35$ for standard percolation theory to $p_c \approx 0.5$ in crystallographically consistent grain boundary networks. If the percolation threshold is to be used as a parameter in materials design, it is critical to know the appropriate value for p_c, which as these preliminary results indicate, can depend strongly on the requirement for crystallographic consistency.

Although a similar trend is expected in networks where boundaries are classified as low-angle (special) or high-angle (general), no systematic studies have investigated the triple junction distributions in these networks, either experimentally, analytically or through computer simulations. To establish whether experimental microstructures follow the distribution predicted by Eq. (1.5), the triple junction distribution was obtained from several experimental microstructures presented by other researchers studying grain boundary networks in which boundaries are classified on the basis of their disorientation angle [57, 85, 94-105]. The experimental data in Figure 1.4 were taken from a wide variety of materials and crystal systems, including pure metals, intermetallics alloys and superconducting oxides. Additionally, the definition of what constitutes a low-angle boundary differs among these data sets, with the special boundary threshold θ_t ranging from 4° to 15°, as noted in the legend. Despite these differences, these independent data sets all lie on reasonably common trend lines in Figure 1.4. Furthermore, the collected data clearly do not follow the expected random distribution, showing a significant reduction of J_2 junctions and a concurrent increase in J_3 junctions, similar to the triple junction distributions for CSL and non-CSL boundaries [53, 62, 91, 92]. These deviations are indicative of the underlying crystallographic constraint which affects the local grain boundary connectivity. These data underscore the fact that standard percolation models cannot be applied to grain boundary networks; instead, new crystallographically consistent models are required.

1.6. Problem Statement

The goal of this work is to understand the effects of crystallographic constraint in grain boundary networks on several different length scales. Specifically:

- The triple junction distribution is determined for grain boundary networks assembled in a crystallographically consistent manner where grain boundaries are classified on the basis of their disorientation angles. An analytical model is developed to describe the statistical distribution of triple junctions that are subject to crystallographic constraint. This model illustrates how crystallographic constraints result in nonrandom triple junction distributions for grain boundary networks.
- As material microstructures are inherently three dimensional (3-D), the role of local crystallographic constraint is considered at quadruple nodes in 3-D systems which may contain a higher degree of constraint than is present at triple junctions. The relative strength of the constraints around triple junctions and quadruple nodes is also determined.
- With a thorough understanding of the preferential coordination of triple junctions, the percolation thresholds are determined for several common microstructural textures (e.g., fiber texture, cube texture) in both two and three dimensions. The scaling behavior of grain boundary networks is compared to the universal scaling exponents for standard percolation theory to determine whether grain boundary networks are in the same universality class. The scaling behavior is also studied in two dimensions with grains that are irregularly shaped.
- As grain boundary networks represent only one variety of infinitely many correlated systems, a "coordination tetrahedron," or map of the correlation space, is developed for percolation in locally-correlated systems that may be used to guide materials design. Although the development of the coordination tetrahedron is presented in the context of grain boundary networks, the concept can easily be extended to other locally correlated percolation problems.

Chapter 2: Simulation Procedures

In the present work, both two- and three-dimensional microstructures are simulated, where orientations are assigned to each grain and grain boundary misorientations are determined from the orientations of the neighboring grains, similar to the procedure used in Ref. [106]. Assignment of grain orientations rather than grain boundary misorientations ensures that crystallographic consistency is maintained throughout the microstructure. In this chapter, the procedure for assembling and analyzing a crystallographically consistent grain boundary network is described in detail following the flowchart presented in Figure 2.1.

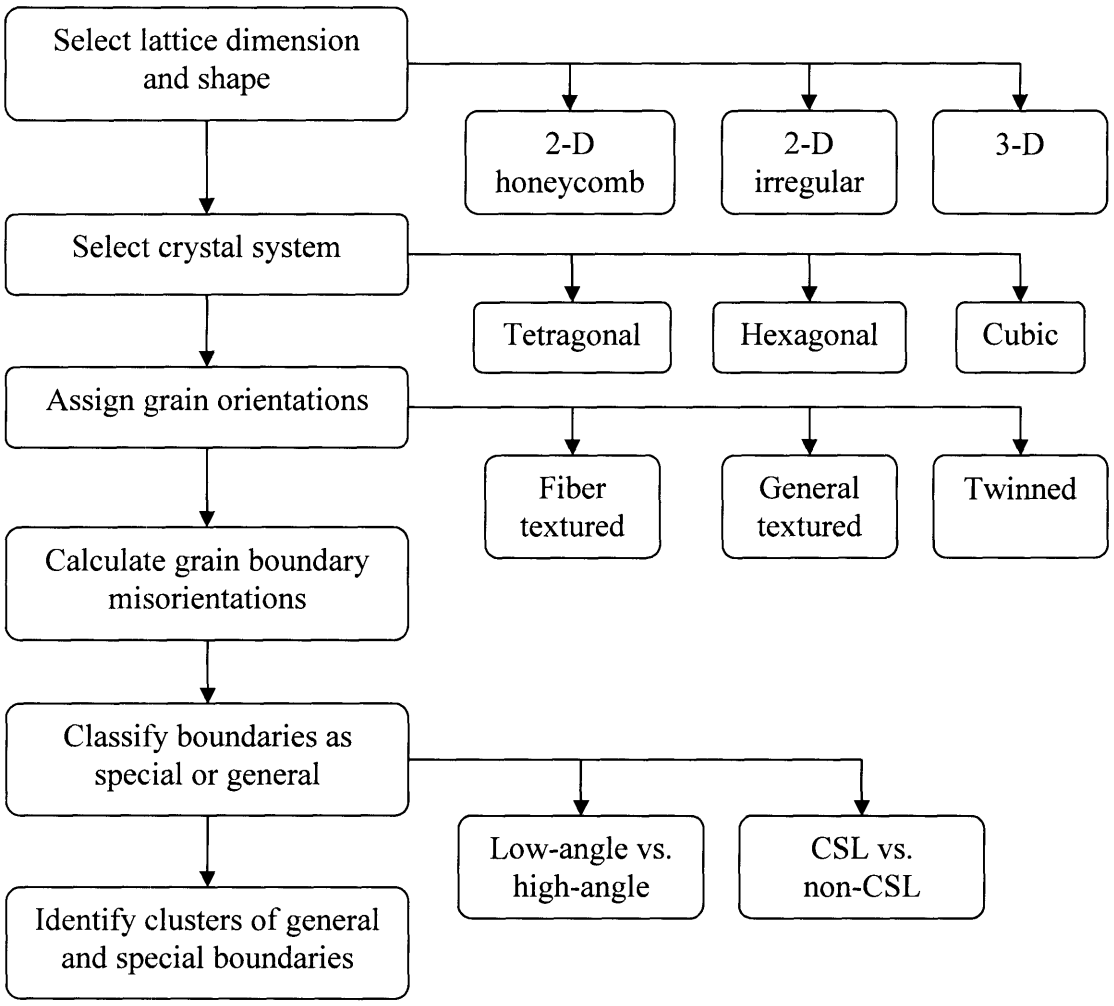

Figure 2.1: Procedure for assembling a crystallographically consistent grain boundary network

2.1. Assignment of Grain Structure

In 2-D, most of the simulations are performed on microstructures where all grain boundaries have the same length and all grains have six sides (i.e., a honeycomb lattice). A representative honeycomb lattice is shown in Figure 2.2a, with L, the number of grains per side, equal to 30. Simulations in 2-D are also performed on irregular lattices like those in Figure 2.2b, where the number of sides per grain is allowed to vary (although the average number of sides is still equal to six). A Monte Carlo algorithm is used to create these structures by randomly inducing grain neighbor switches via the procedure illustrated in Figure 2.3. Beginning with a perfect honeycomb lattice and sequentially applying these topological changes to randomly chosen boundaries, the distribution of grain shapes (i.e., the number of sides per grain) can be controlled. Unless otherwise noted, the 2-D networks have 1500 grains per side (2,250,000 total grains). Finally, to simulate 3-D microstructures, grains are modeled as fourteen-sided tetrakaidecahedra in a space-filling configuration [25, 58, 76, 106], as illustrated in Figure 2.4. In this configuration of 3-D grains, no more than three grains meet along a line (the triple junctions) and no more than four grains meet at a point (the quadruple nodes). All of the simulated 3-D networks have 100 grains per side (1,000,000 total grains).

Once the grain shape is chosen, the next step is to select the crystal system of the grains from three different crystal systems: tetragonal, hexagonal or cubic. These three crystal systems are considered here to determine whether the effects of crystallographic constraint vary as a function of crystal system. However, the vast majority of the simulations use

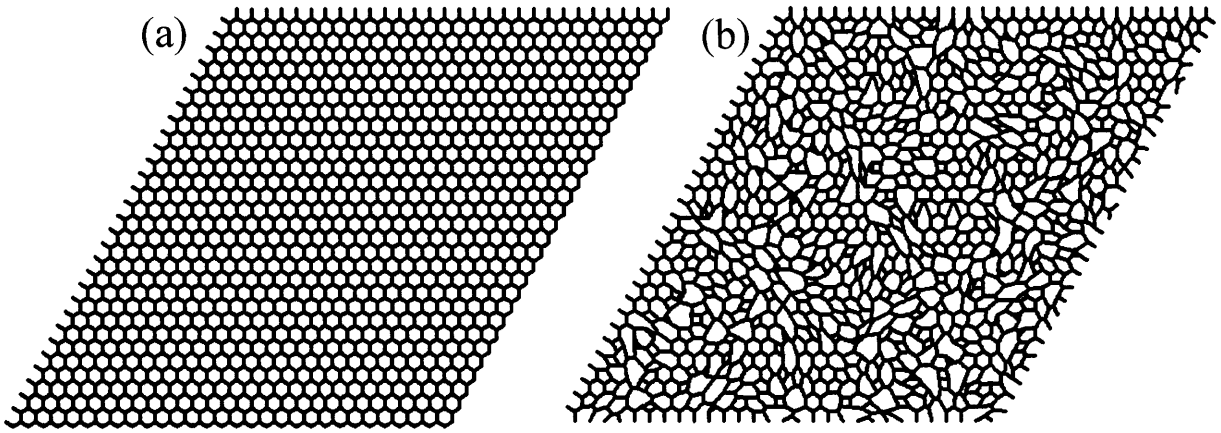

Figure 2.2: Examples of two-dimensional networks with 30 grains per side that have either (a) a honeycomb structure or (b) an irregular structure.

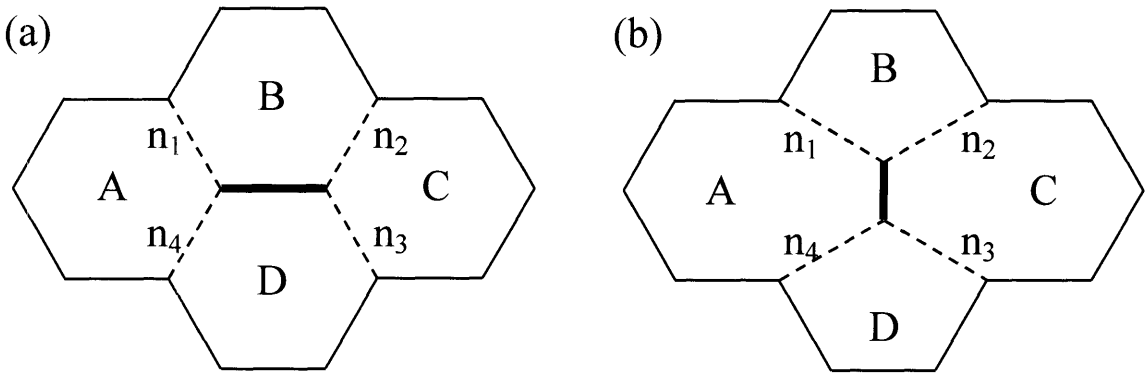

Figure 2.3: Schematic illustration of the procedure used to create irregular lattices. The four grains that are affected by the reorientation of the bold boundary are labeled *A*, *B*, *C*, and *D*. The boundary to be reoriented (the bold line) has neighboring boundaries labeled n_1, n_2, n_3, and n_4. When the boundary is reoriented (b), the number of sides in grains *B* and *D* decreases by one, while the number of sides in grains *A* and *C* increases by one.

microstructures with cubic symmetry, and the crystal system will only be noted when it is either tetragonal or hexagonal. It is important to note the distinction between the labels honeycomb and hexagonal. Honeycomb applies to the *shape* of the grains in an idealized 2-D microstructure, while hexagonal refers to the *crystal system* of the grains.

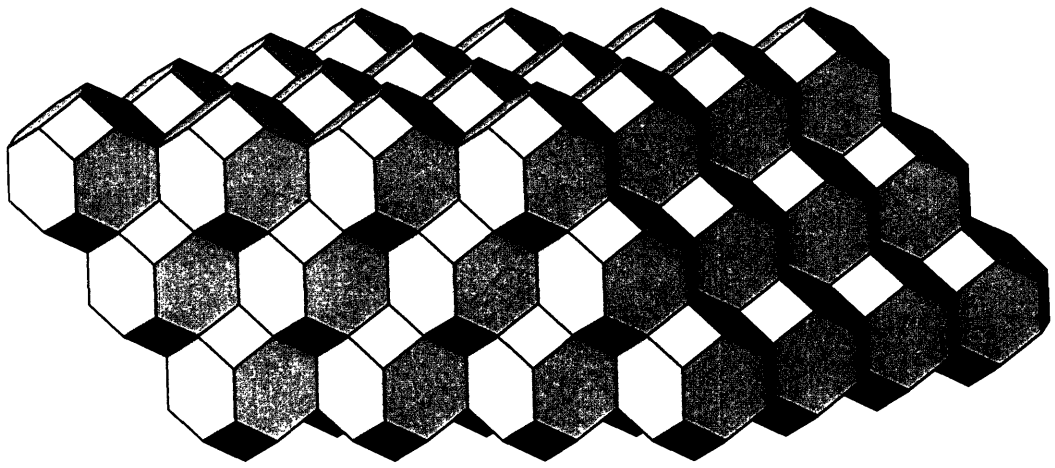

Figure 2.4: Schematic illustration of the three-dimensional grain structure used in the simulations where grains are modeled as 14-sided tetrakaidecahedra.

2.2. Assignment of Grain Orientations

To begin, all grains are initially assigned a common orientation and then one of three different methods is applied to rotate the grains and give a distribution of grain orientations. In the first method, all grains are individually rotated randomly within a prescribed tolerance, ϕ_{max}, about a common, high symmetry axis. The resulting microstructures can be compared with, e.g., epitaxial films or extruded materials. The control parameter ϕ_{max} directly dictates the sharpness of the texture as shown in Figure 2.5, where typical discrete pole figures are given for

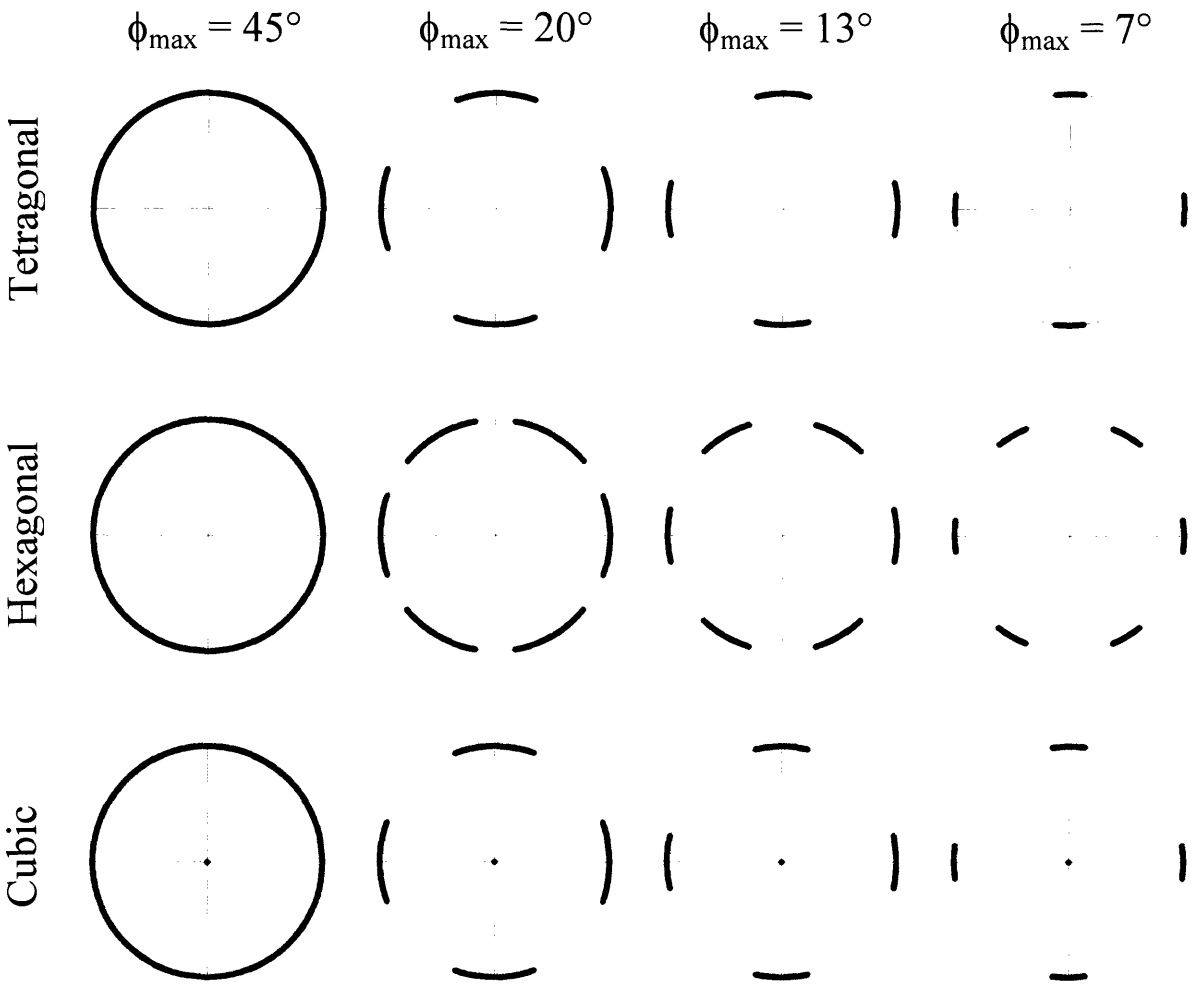

Figure 2.5: Pole figures for fiber textured polycrystals. Top row: (100) pole figures for tetragonal polycrystals, middle row: $(10\bar{1}0)$ pole figures for hexagonal polycrystals, and bottom row: (100) pole figures for cubic polycrystals. The sharpness of the texture is increased (moving left to right) by decreasing the maximum rotation angle for any grain, ϕ_{max}, as indicated above the different columns.

microstructures with tetragonal, hexagonal and cubic symmetry where the maximum rotation angle, ϕ_{max}, is 45°, 20°, 13° and 7°. At the largest value of ϕ_{max}, the microstructures resemble ideal fiber textures and as ϕ_{max} decreases, the texture evolves toward an ideal single crystal texture. As will be seen later, this simplified microstructure admits an analytical solution for the triple junction distribution.

In the second method, each grain is rotated about a randomly selected axis within a prescribed tolerance, ϕ_{max}. This procedure creates a single, unspecified texture component in the structure (e.g., a "cube texture" in cubic lattices). Since many textures can be described as superpositions of just a few select components, this case allows ready extension to many practical situations, and is also expected to compare with many experimental data sets. Figure 2.6 shows pole figures for these simulated microstructures in tetragonal, hexagonal and cubic polycrystals with ϕ_{max} equal to 95°, 28°, 16.5° and 7°. When ϕ_{max} is large, the microstructures approach a perfectly random texture, while as ϕ_{max} decreases, the microstructures approach a perfect single-component texture.

In the third method, individual grains are randomly selected and rotated through one of four $\Sigma 3$ transformation variants at random [107]. The four possible grain orientations that result are illustrated by different symbols in the (001) pole figure in Figure 2.7. The resulting microstructures resemble those of highly twinned materials, such as low stacking fault energy face-centered cubic materials after annealing. In this procedure, the randomization of the microstructure is controlled through the parameter t, the number of "twinning" events that are executed per grain. As before, the randomization of the simulated microstructures can be ovserved in the pole figures shown in Figure 2.8 after t = 0.5, 2.0, 5.0 or 10.0 twin rotations per grain. It is important to note that the same number of grain orientations is represented in each pole figure. However, when t is small, many of the grains have common orientations, leading to fewer distinct points in the pole figure.

The microstructures that result from these three different methods will hereafter be referred to as (1) fiber textured, (2) general textured, and (3) twinned.

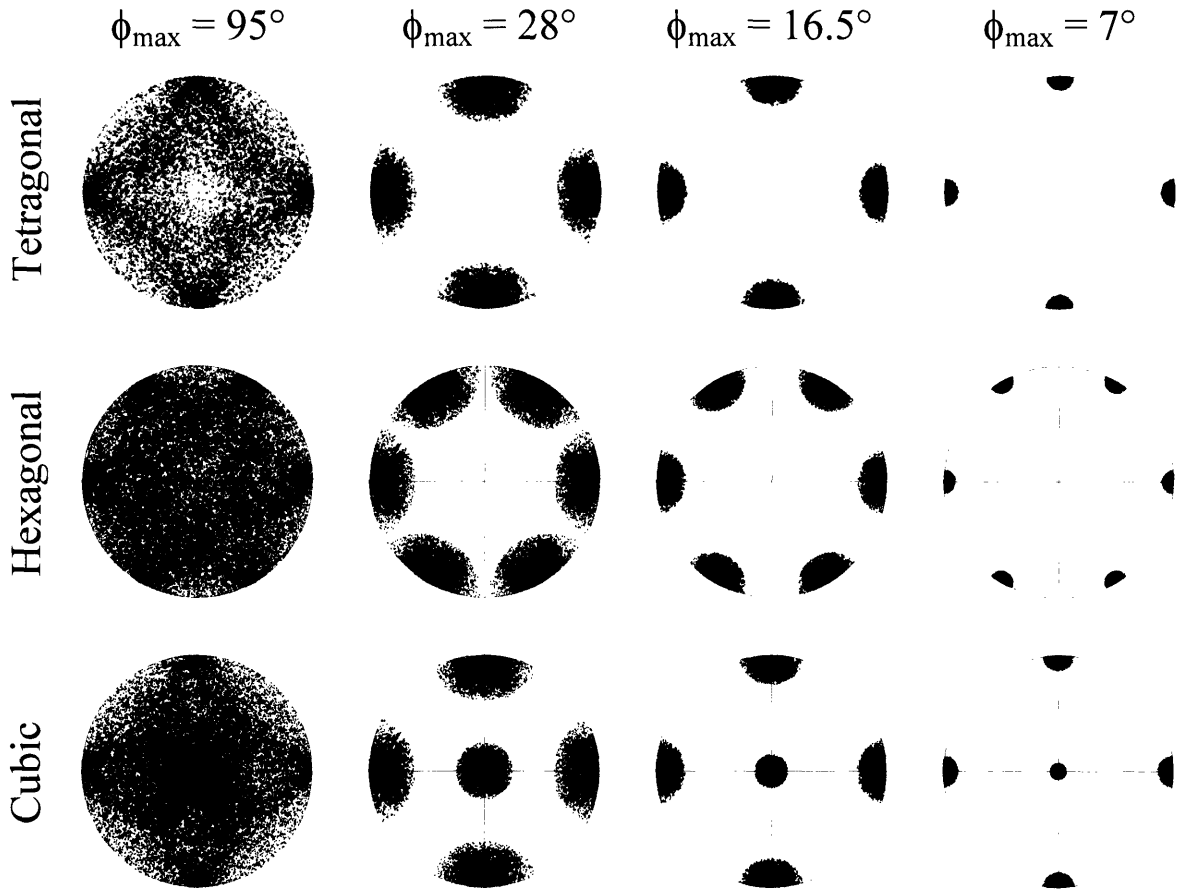

Figure 2.6: Pole figures for general textured polycrystals. Top row: (100) pole figures for tetragonal polycrystals, middle row: $(10\bar{1}\,0)$ pole figures for hexagonal polycrystals, and bottom row: (100) pole figures for cubic polycrystals. The sharpness of the texture is increased (moving left to right) by decreasing the maximum rotation angle for any grain from 95° to 7°.

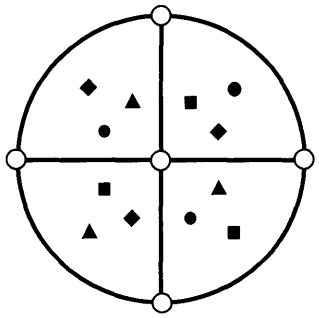

Figure 2.7: (001) pole figure illustrating the grain orientations that result from rotating a grain with an initial cube texture (open circles) through one of the four unique Σ3 rotations. The resulting orientation after each possible rotation is given by a different symbol (squares, circles, diamonds and triangles).

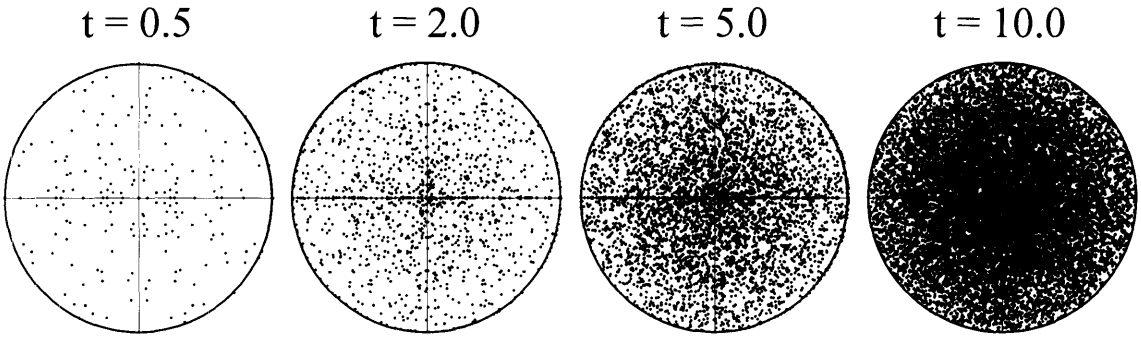

Figure 2.8: (001) pole figures for simulated twinned polycrystals with L = 100 (10,000) total grains. The number of twin rotations per grain, t, is indicated above each pole figure. Although the number of grain orientations mapped in each pole figure is constant, more of the grains assume unique orientations as t increases, resulting in more unique points appearing in the pole figure.

2.3. Determination of Grain Boundary Character

Once the orientation of each grain, $\mathbf{g_X}$, is known in terms of its Euler angles (using the Bunge notation) [108], the misorientation of the grain boundary between grains A and B, $\mathbf{M_c}$, can be calculated from the orientation of the two grains as (refer to Figure 1.3 for naming conventions):

$$\mathbf{M_c} = \mathbf{g_B}\mathbf{g_A}^{-1} \tag{2.1}$$

Here $\mathbf{M_c}$ and $\mathbf{g_X}$ are 3 x 3 matrices, and $\mathbf{g_X}$ specifies the orientation of grain X [82]. The grain boundary misorientation can be equivalently expressed as an axis/angle pair, where a rotation by the angle θ about the crystallographic axis [*hkl*] will bring the two grains into alignment. The angle θ can be found from the matrix representation through the relationship:

$$2\cos(\theta)+1 = \mathrm{tr}(\mathbf{M_c}) \tag{2.2}$$

where tr denotes the trace operator ($\mathrm{tr}(\mathbf{M_c}) \equiv M_{c,11} + M_{c,22} + M_{c,33}$). As described in Chapter 1, several different binary classifications are possible and depend on the detailed crystallographic structure of the boundary. Therefore, from the full crystallographic description of the boundary character, one of two different binary classification methods is applied to differentiate between special and general boundaries on the basis of the misorientation as given by Eq. (2.1). In the

first method, only the disorientation of the grain boundary is considered. If this angle is lower than a threshold value, θ_t (taken here as 15°), the boundary is classified as a special boundary. A statistical description of the grain boundary disorientations is possible through the disorientation distribution, as shown in Figure 2.9 for microstructures where grains shared a common rotation

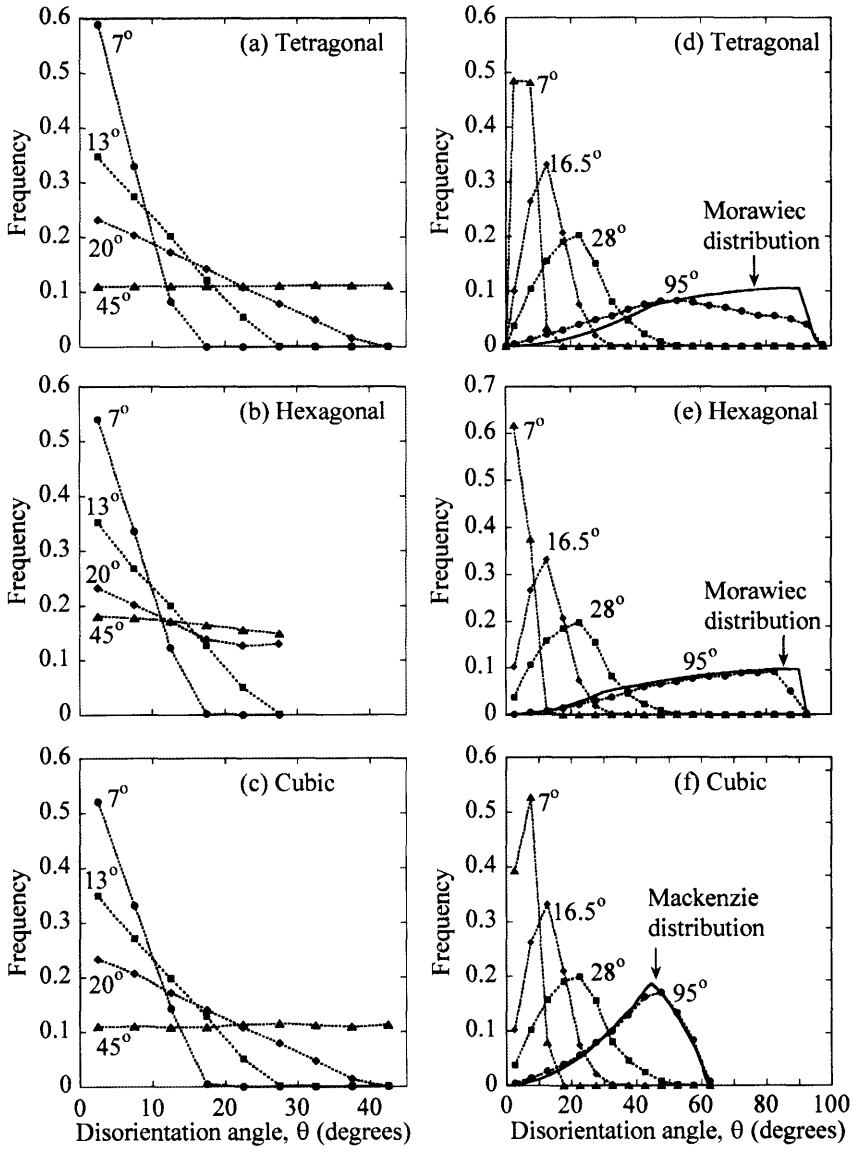

Figure 2.9: The disorientation angle distribution for fiber textured (a – c) and general textured (d – f) microstructures with either tetragonal (a, d), hexagonal (b, e) or cubic (c, f) symmetry. The different distributions correspond to different maximum rotation angles, ϕ_{max}, as labeled on the graphs. For the general textured microstructures, the distribution of disorientation angles for a random assemblage of polycrystals with the given symmetry is also shown [109, 110].

axis (fiber textured, Figure 2.9 a-c), or could rotate about any axis (general textured, Figure 2.9 d-f). In the fiber textured microstructures (Figure 2.9 a-c), when ϕ_{max} is small (7°), nearly all of the boundaries have disorientations less than θ_t = 15°. As ϕ_{max} increases, the fraction of boundaries with low disorientation angles decreases, corresponding to a weakening of the texture (c.f., Figure 2.5). In these microstructures where grain rotation occurs around a common axis, the maximum disorientation between grains, Θ_M, is given by the symmetry of that axis; e.g., there are ±30° of unique orientation for rotation about the c-axis in hexagonal polycrystals and ±45° in cubic or tetragonal polycrystals. If the rotational tolerance ϕ_{max} is less than half of Θ_M, the disorientation distribution is essentially a sloped line that intersects the horizontal axis at $2\phi_{max}$. When $2\phi_{max}$ exceeds Θ_M, the disorientation distribution begins to level off, such that for very high ϕ_{max}, the distribution is uniform. The grain boundary disorientations in the simulated microstructures with general textures are also characterized by the disorientation distribution. Unlike the case for fiber textured microstructures, where high values of ϕ_{max} resulted in a uniform distribution of disorientation angles, here an increase in ϕ_{max} shifts the distribution toward that of randomly oriented polycrystals, as derived by Mackenzie [110] for cubic polycrystals and more generally by Moraweic [109] for other crystal systems.

In the second approach, each boundary is classified as a CSL boundary with $\Sigma \leq 29$. To determine the appropriate Σ value, the deviation of the boundary is calculated with respect to each $\Sigma \leq 29$, and is labeled with the Σ value that resulted in the smallest angular deviation. Boundaries whose deviation angles are smaller than that allowed by a selection criterion (Eq. (1.1) where w = ½) are classified as special, while boundaries with larger deviations are labeled general. In this case, the grain boundary character distribution (GBCD) is used to describe the statistical evolution of grain boundary types. The GBCD gives the fraction of boundaries classified as Σ1 (low-angle boundaries), Σ3, Σ9, Σ27, other CSL boundaries with $\Sigma \leq 29$, or as general boundaries. Figure 2.10 shows the GBCD for twinned microstructures with t = 0.5, 2.0, 5.0 and 10.0. For t = 0.5, the fraction of general boundaries is almost zero, while over 80% of the boundaries are either Σ1 or Σ3 boundaries. As t increases, the fraction of Σ1 and Σ3 boundaries decreases, while the populations of other twin variant boundaries ($\Sigma 3^n$) and general boundaries increase. As Figure 2.10 illustrates, when t = 10.0, more than 80% of the boundaries are classified as general boundaries.

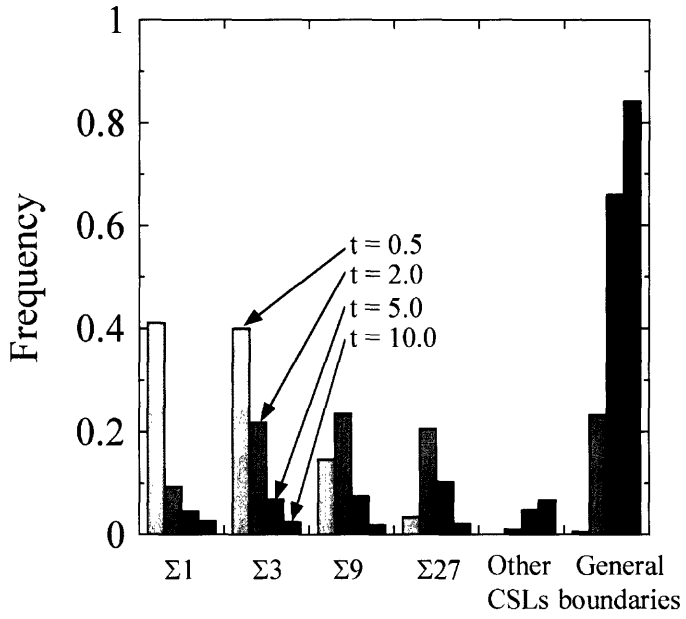

Figure 2.10: The frequency of twin variant boundaries ($\Sigma 3^n$), other CSL boundaries (with $\Sigma \leq 29$), and general boundaries is plotted for simulated microstructures with t = 0.5, 2.0, 5.0 or 10.0 twin rotations per grain.

The relationship between the texture and grain boundary character in fiber textured and general textured microstructures is summarized in Figure 2.11. Here the sharpness of the texture is given by the rotational tolerance, ϕ_{max}. Similarly, the disorientation distribution has also been collapsed into a single parameter p, the fraction of low-angle (special) boundaries. As shown in Figure 2.11 for tetragonal, hexagonal, and cubic polycrystals with low-angle threshold $\theta_t = 15°$, all of the crystal systems show similar behavior, with a minimum grain rotation of 7.5° required before there are any high-angle boundaries in the microstructure. Although the form of the curves in Figure 2.11 changes with the definition of a low-angle boundary (i.e., the choice of θ_t), normalization of the rotational tolerance by the low-angle threshold results in a single curve for each of the fiber textured and general textured microstructural families. The master curves in Figure 2.12 illustrate that there is a well-defined and monotonic relationship between the texture of the simulated polycrystals and the low-angle boundary fraction, as noted previously by other authors [111-113]. From Figure 2.12, it is clear that the choice of a smaller low-angle threshold requires a sharper texture in order to achieve the same fraction of special boundaries.

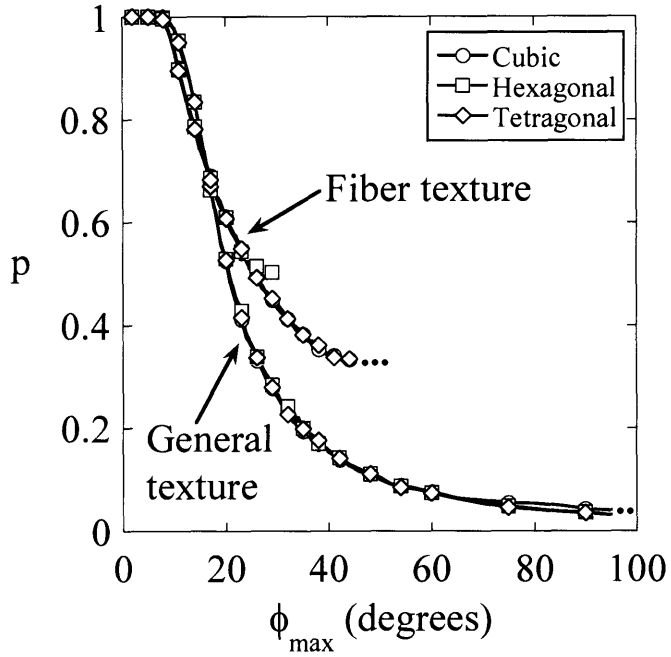

Figure 2.11: Fraction of low-angle boundaries, p, as a function of the sharpness of texture, given by the rotational tolerance, ϕ_{max}, for polycrystals with cubic, hexagonal, and tetragonal symmetry where the low-angle threshold is 15°. For the fiber textured microstructures, the curves are truncated at the minimum value of p achievable as explained in the text.

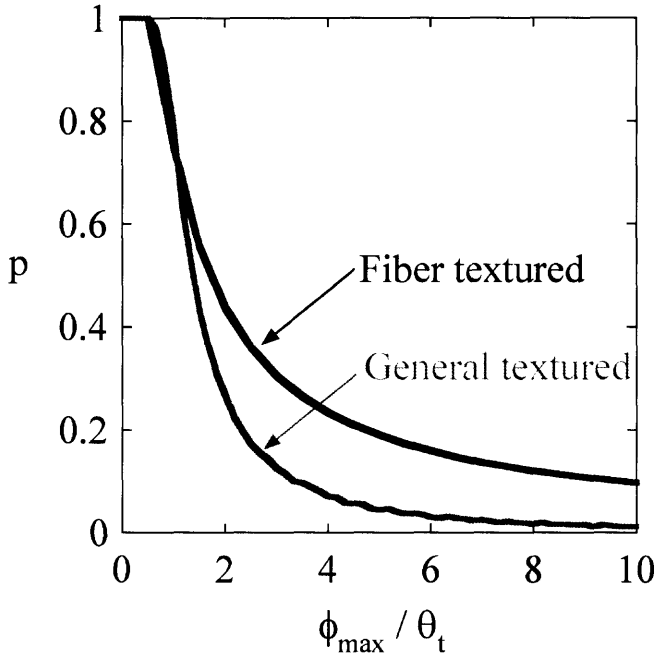

Figure 2.12: Fraction of low-angle boundaries, p, as a function of the rotational tolerance, ϕ_{max}, normalized by the low-angle boundary threshold, θ_t for fiber textured or general textured polycrystals.

A similar approach can be taken for the twinned microstructures as well. In Figure 2.13, the GBCD has been consolidated to the single parameter p, which is plotted as a function of t, the number of twin rotations per grain. Similar to ϕ_{max} which controlled the texture in the fiber textured and general textured polycrystals, t is found to be an effective parameter in controlling the fraction of special boundaries in the twinned polycrystals.

It is important to note that in the twinned microstructures, the CSL vs. non-CSL approach is used to classify boundaries, while in the fiber textured and general textured microstructures, boundaries are classified based on low vs. high-angle disorientations; in what follows we use the terms "special" and "general" boundaries for all of these cases.

2.4. Identification of Grain Boundary Clusters

Once every grain boundary in the network has been classified as special or general, clusters of special (or general) boundaries are tracked and labeled using the Hoshen-Kopelman algorithm [114]. After unique clusters of boundaries are identified, the lattice is scanned for a cluster which percolates in every direction (i.e., top to bottom and left to right in 2-D, also front to back in 3-D). To accurately determine the percolation threshold, thousands of lattices are

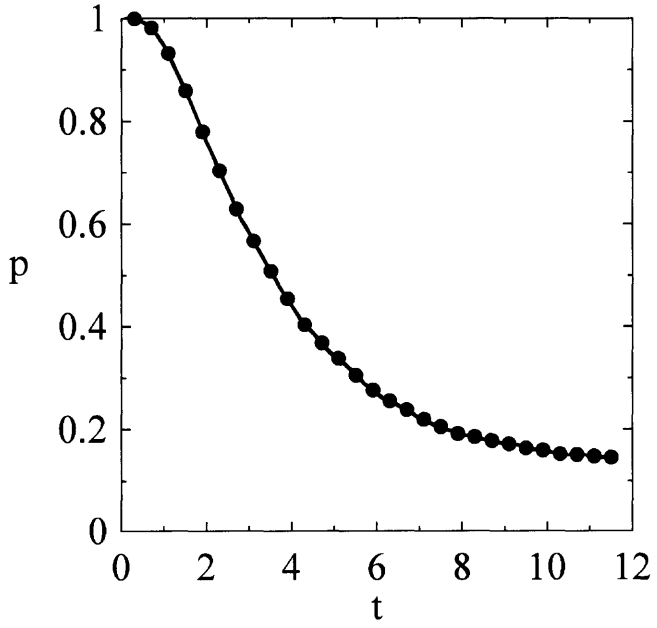

Figure 2.13: Fraction of special (CSL) boundaries, p, as a function of t, the number of twin rotations per grain for simulated cubic polycrystals.

simulated near the expected percolation threshold. Over small increments of p, the fraction of lattices that have a percolating cluster is determined and the percolation threshold is taken to be the value of p where 50% of the lattices percolated. In order to determine the percolation threshold more exactly for fiber textured honeycomb networks, we also simulate lattices with 5000 grains per side, where the Enhanced Hoshen-Kopelman technique [115], which is less memory-intensive, is used to identify and label grain boundary clusters. Our approach to determining the percolation threshold is illustrated in Figure 2.14, where the fraction of simulated networks containing a percolating cluster, or percolation probability, is plotted as a function of p for general boundary networks in a fiber textured microstructure. As the different curves in Figure 2.14 illustrate, the width of the transition from percolating to non-percolating states decreases as L, the size of the simulated network, increases. The size of the error bar we report corresponds to the range of p over which the percolation probability lies between 0 and 1, as illustrated in Figure 2.14 by the dashed lines for the $L = 1000$ curve.

In addition to checking the lattice for a percolating cluster, the properties of individual clusters in the network, including their mass and radius of gyration, are also determined. The mass of a grain boundary cluster, s, is simply the total number of grain boundaries comprising the cluster. For $s < 1000$, the number of clusters with mass s was tracked explicitly during the simulation to find n_s, the number of clusters of a given mass per lattice site[1]. The radius of gyration of an individual cluster, R_g, is given by [69]:

$$R_g^2 = \frac{\sum_{i=1}^{s} A_i \left|\mathbf{r}_i - \mathbf{r}_o\right|^2}{\sum_{i=1}^{s} A_i} \tag{2.3}$$

Here $\boldsymbol{r}_i$ is a vector pointing to the center of the i^{th} boundary in the cluster, and $\boldsymbol{r}_o$ points to the center of mass of the cluster, defined as [69]:

$$\mathbf{r}_o = \frac{\sum_{i=1}^{s} A_i \mathbf{r}_i}{\sum_{i=1}^{s} A_i} \tag{2.4}$$

[1] It is important to note that n_s is counted and not binned; when a binning procedure is used to find the cluster size distribution, the scaling exponent changes, owing to the integration over s that is implicit in binning.

In these equations, A_i is the area of the i^{th} grain boundary. For the 2-D networks, which represent the largest focus of this work, all boundaries have an area (length) of 2 units. The average radius of gyration for clusters with mass s, R_s, is found by averaging the radius of gyration of individual clusters, R_g, over all clusters with mass s. Using the distributions n_s and R_s, the connectivity length, ξ, is defined as [69]:

$$\xi^2 = \frac{2\sum_s R_s^2 s^2 n_s}{\sum_s s^2 n_s} \tag{2.5}$$

As noted in the introduction, the connectivity length represents a characteristic linear dimension for the clusters. Finally, the strength of the largest, or "infinite", cluster, P, is found for percolating systems by dividing the mass of the lattice-spanning cluster by the total mass of all clusters. The procedures outlined here are used in the chapters that follow to study the effects of crystallographic constraints in grain boundary networks from the local to the global length scales.

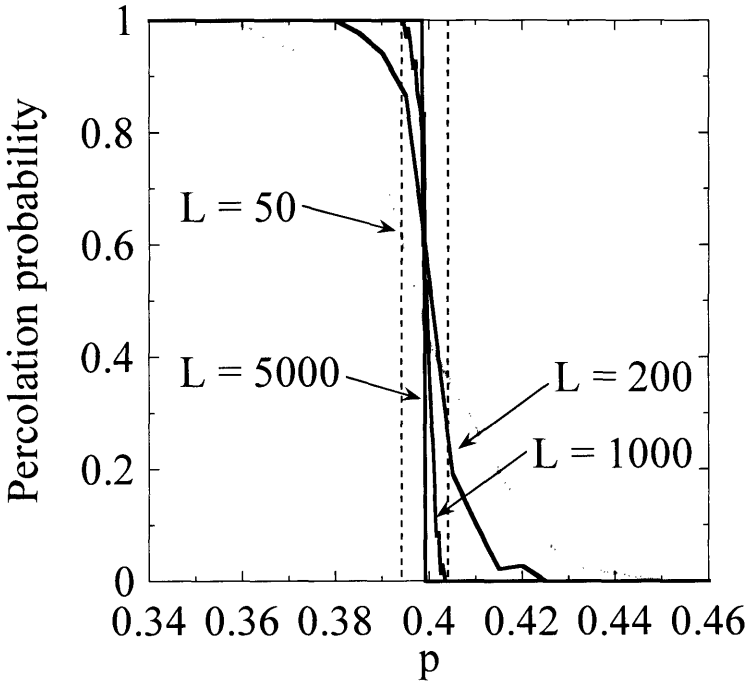

Figure 2.14: The probability of a simulated fiber textured microstructure containing a percolating cluster of general boundaries as a function of p, the fraction of special boundaries in the microstructure. The width of the transition region, from percolating to non-percolating, decreases as L, the number of grains per side in the simulated structures, increases. The dotted lines indicate the error bar on the percolation threshold for simulations with L = 1000.

Chapter 3: Crystallographic Constraint at Triple Junctions

In this chapter, we use the techniques previously described to simulate crystallographically consistent grain boundary networks. The topologies of these networks are found to be nonrandom, both qualitatively and quantitatively. By developing a closed-form analytical solution for the triple junction distribution in a crystallographically constrained fiber textured polycrystal, we can better understand how the constraint leads to nonrandom nearest-neighbor correlations. Both simulations and the analytical model provide physical insight as to how local constraints influence global network topology.

3.1. Topology of Simulated Interfacial Networks

As described in Chapter 1, the topology of a realistic interfacial network can differ greatly from that of a random network. To illustrate this point, we have constructed grain boundary networks using the typical approach of percolation theory, whereby each boundary is assigned as special or general with probability p or $1 - p$, respectively, without regard for crystallography. The constraining effects of crystallography can then be appreciated qualitatively by direct observation of the spatial distribution of both general and special boundaries on two-dimensional lattices. In Figure 3.1, the complementary populations of general and special boundaries are highlighted on small lattices with $p = 0.5$, for grain boundary networks that were assembled both randomly and using the crystallographically consistent methods described in Chapter 2. In the randomly assembled lattices (Figure 3.1a and b), the spatial distribution of both types of boundaries is expectedly uniform, with no obvious tendency to cluster beyond that which occurs by chance. In contrast, in the crystallographically consistent networks, the spatial distributions of both types of boundaries are decidedly nonrandom. The general boundaries (Figure 3.1c, e, g, i) tend to cluster together, especially in the form of small, complete rings (Figure 3.1c and e), or long strings (Figure 3.1g and i). Unlike the general boundaries, the special boundaries in crystallographically consistent networks (Figure 3.1d, f, h, j) have a tendency to form more compact structures with many branches and "dangling bonds". By comparing the fourth and fifth rows of Figure 3.1 which illustrate fiber textured polycrystals on a honeycomb or an irregular lattice, it can be seen that the nonrandom topology which results from the crystallographic constraints is independent of lattice shape; Figures 3.1g and i are qualitatively equivalent (as are Figures 3.1h and j). Overall, the crystallographically

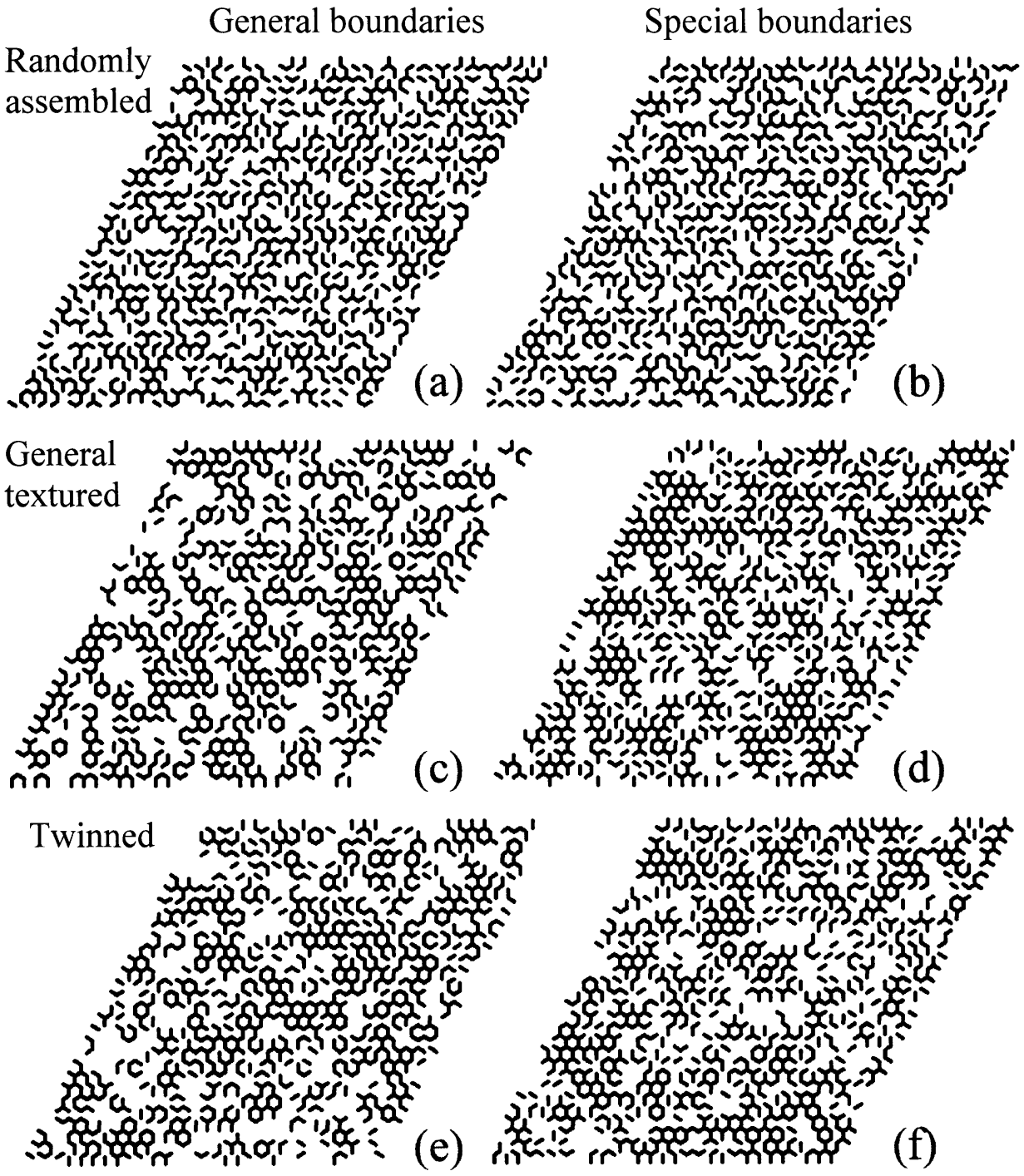

Figure 3.1: Complementary spatial distribution of general (left column) and special boundaries (right column) for $p = 0.5$ on small, two-dimensional honeycomb (a – h) or irregular lattices (i, j). The polycrystals were assembled either randomly (a and b) or with crystallographic consistency (c, d: general textured; e, f: twinned, g – j: fiber textured).

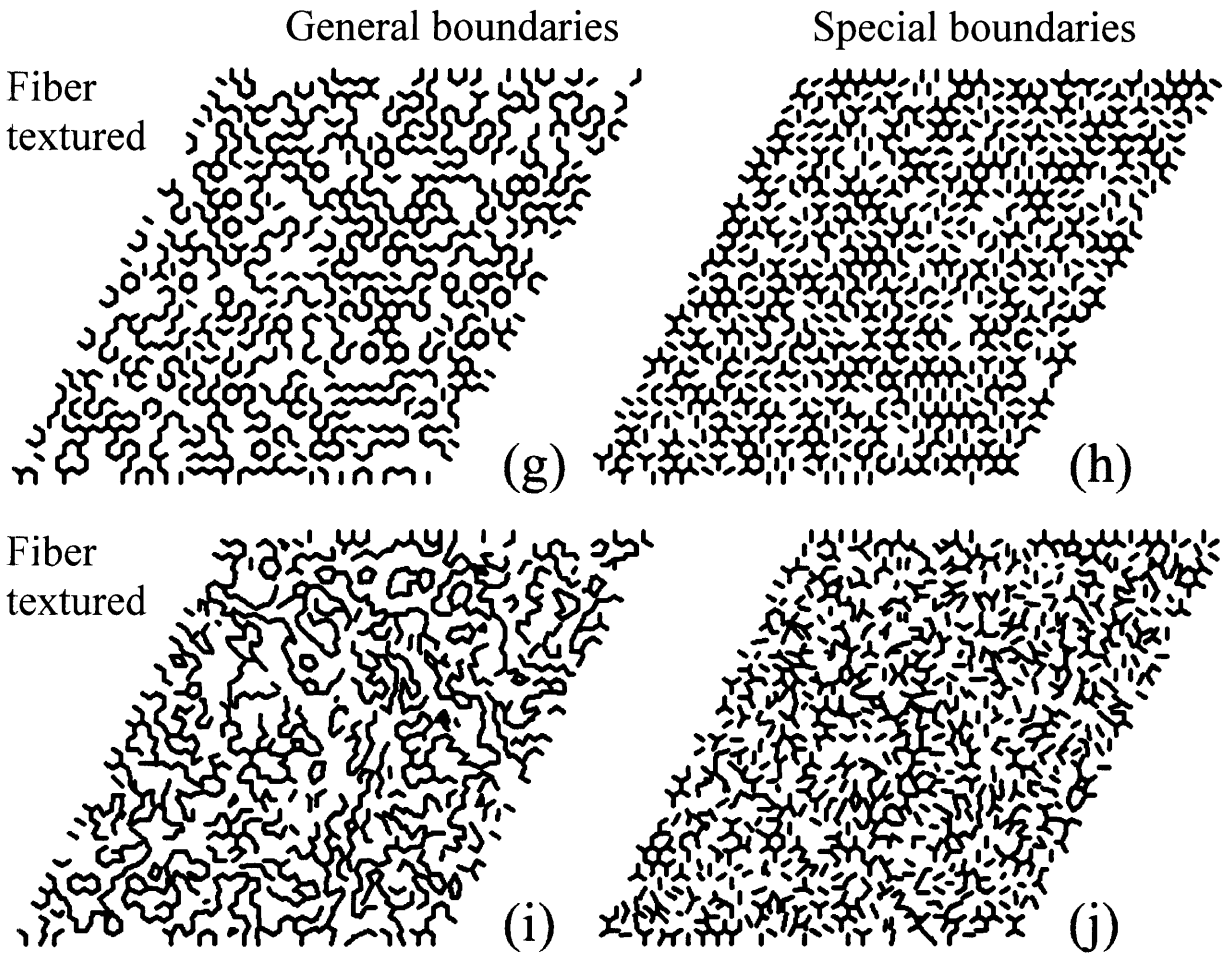

Figure 3.1 continued.

consistent lattices, whether they are for the fiber textured, general textured, or twinned polycrystals, exhibit large regions in which only special (or general) boundaries exist; enforcing consistent crystallography results in a patchier grain boundary network. Although the focus of the present chapter is the local correlations among grain boundaries, it is evident in Figure 3.1 that longer-range implications of this preferential clustering are likely; this will be discussed in detail in a subsequent chapter.

The clustering tendency observed qualitatively in Figure 3.1 may be quantified by considering the triple junction distributions, which are given in Figure 3.2 for the crystallographically consistent lattices with both fiber and general textures (the solid and dashed curves, respectively). These curves should be compared with those for the random case (dotted

lines, Eq. (1.5)). The populations of J_2 junctions (i.e., two special boundaries and one general boundary) in both types of constrained lattices are considerably diminished with respect to the random lattices, while there is a relative increase in the population of J_3 junctions. In the fiber textured microstructures, there is a significant increase in the fraction of J_1 junctions as well. These results quantitatively capture the clustering observed in Figure 3.1d, h, and j, where there are few junctions coordinated by only one general boundary (i.e., J_2 junctions, which would lead to elongated clusters in Figure 3.1d, h, and j).

An important point that is not explicitly observed in Figure 3.2 is that the triple junction distributions have been determined for lattices with cubic, hexagonal and tetragonal crystal systems, and we find that crystal symmetry has *no measurable effect* on this distribution among the centro-symmetric crystal systems. Furthermore, the triple junction distributions in Figure 3.2 are also found to be independent of the low-angle boundary threshold, θ_t. Changes in θ_t affect the sharpness of texture required to produce a given special fraction, p, but do not change the network topology in a fundamental way. Another variable which does not affect the resulting TJD is the shape of the lattice; fiber textured polycrystals with both regular and irregular grain shapes result in identical distributions. The invariance of the triple junction distribution with changes in θ_t, crystal symmetry, or grain shape suggests that the curves in Figure 3.2 can be regarded essentially as universal expectation curves for any polycrystal. This explains why many independent experiments lie on common curves in Figure 3.2, and in fact the simulation results match quite closely with the collected data. Although these simulations have modeled a single-component texture, very similar triple junction distributions can also be expected for multi-component textures which, in the present context, would be superpositions of these single texture-component results. However, in a homogeneous microstructure with T distinct texture components, the maximum achievable special fraction is $\sim 1/T$, since texture components are usually separated by more than $\theta_t = 15°$ of rotation.

The deviation of the triple junction distribution in Figure 3.2 from the random population is due to the crystallographic consistency required around a triple junction. In these simulations, all of the boundaries are classified based on their disorientation angles and these angles must obey Eq. (1.4): $\theta_{max} \leq \theta_1 + \theta_2$. Accordingly, if two of the boundaries (e.g., θ_1 and θ_2) have low disorientation angles, it is unlikely that their sum will exceed the low-angle boundary threshold,

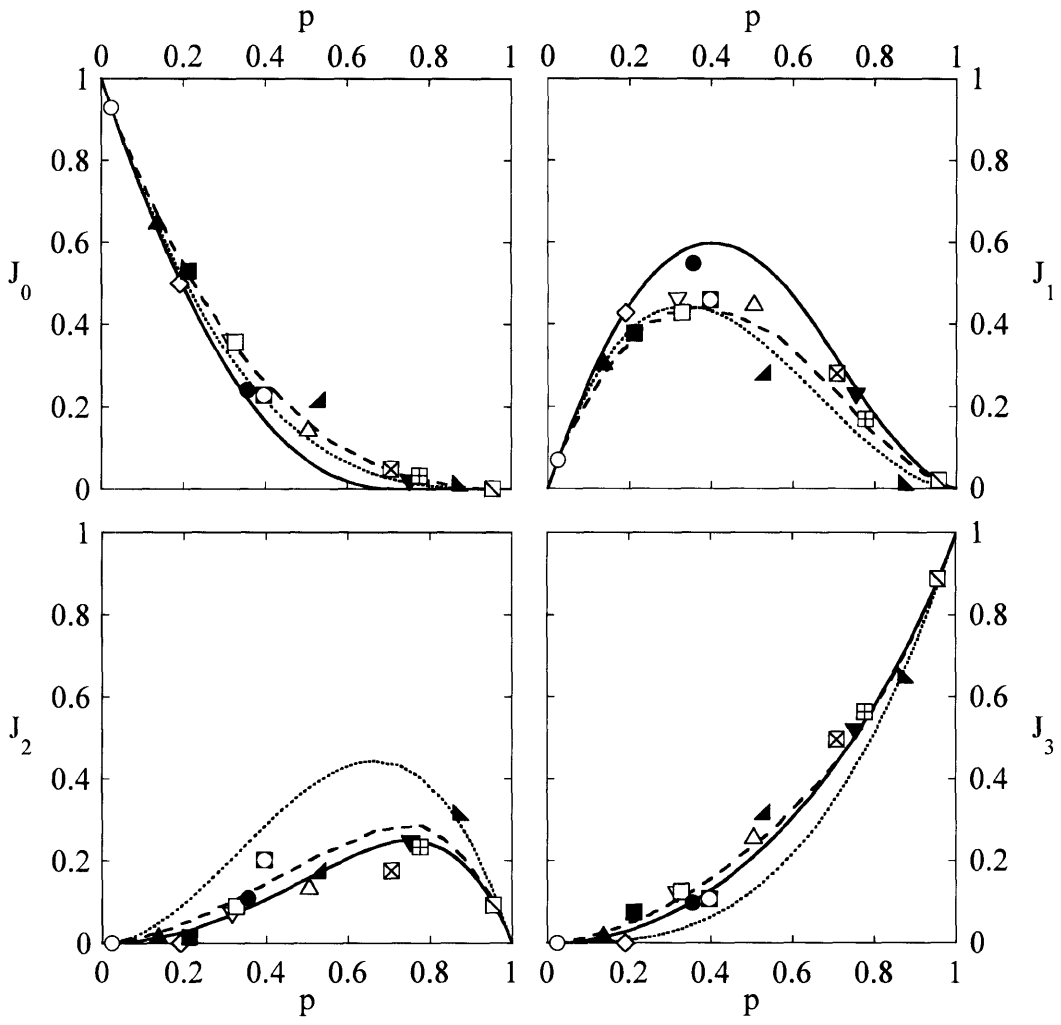

Figure 3.2: Triple junction distribution for simulated microstructures with crystallographic consistency (fiber texture: solid lines, general texture: dashed lines). Also shown are the TJD for a random network (dotted lines, Eq. (1.5)), and experimental triple junction distributions, where the symbols are the same as in Figure 1.4.

resulting in relatively few junctions coordinated by only two special boundaries (J_2 junctions). In addition, since the presence of two boundaries with low disorientation angles often requires the third boundary also to have a low disorientation angle, there will be a relative increase in the number of triple junctions coordinated by three low-angle boundaries (J_3 junctions). It is for this reason that the measured populations of J_2 junctions from both experiment and crystallographically consistent simulations lie below the prediction for a randomly assembled network, while the measured populations of J_3 junctions are higher than expected.

3.2. Analytical Model for the Triple Junction Distribution

In the previous section, we have shown both qualitatively and quantitatively that the topology of polycrystals is nonrandom and that the TJDs of these simulated polycrystals agree well with those of experimental microstructures. However, there currently exist no closed-form analytical solutions for these nonrandom distributions. In what follows, we present such a solution in the case of fiber textured microstructures where the grain boundary disorientations have a rigid constraint [116]. Our analytical results also offer physical insight on the role of crystallographic constraint on the topology of interfacial networks.

3.2.1. Analytical Approach

The triple junction distribution, as described in Chapter 1, gives J_i, the fraction of junctions coordinated by i special boundaries. If all boundaries have the probability p of being assigned as special boundaries, then the triple junction distribution is given by Eq. (1.5). However, as we will show explicitly in what follows, at triple junctions that obey the constraint of Eq. (1.2), the probabilities for each boundary assignment are not independent, and the local assignment probabilities depend not only on how many of the three boundaries have been assigned, but on their character as well. For example, the first grain boundary at any triple junction can be assigned a disorientation on a truly random basis with the probability p of being assigned as a special boundary. However, once the first boundary at the triple junction has been assigned, there exists a limited range of disorientations that the second boundary may take on, such that its being assigned as a special boundary is dependent on the disorientation of the first boundary. Furthermore, once the first two boundaries have been assigned, the disorientation of the third boundary is fixed by the crystallographic constraint (Eq. (1.2)). In order to find the triple junction distribution in a crystallographically consistent lattice, we seek expressions for these local transition probabilities, defined as Π_x^y, the density distribution of special boundaries at a triple junction where y (= 0, 1 or 2) boundaries have been assigned, x ($\leq y$) of which have been classified as low-angle boundaries. In terms of the local transition probabilities which are order-dependent, the triple junction distribution is given as:

$$J_0 = \left(1-\Pi_0^0\right)\cdot\left(1-\Pi_0^1\right)\cdot\left(1-\Pi_0^2\right), \tag{3.1a}$$

$$J_1 = \Pi_0^0\cdot\left(1-\Pi_1^1\right)\cdot\left(1-\Pi_1^2\right)+\left(1-\Pi_0^0\right)\cdot\Pi_0^1\cdot\left(1-\Pi_1^2\right)+\left(1-\Pi_0^0\right)\cdot\left(1-\Pi_0^1\right)\cdot\Pi_0^2, \tag{3.1b}$$

$$J_2 = \Pi_0^0 \cdot \Pi_1^1 \cdot \left(1 - \Pi_2^2\right) + \Pi_0^0 \cdot \left(1 - \Pi_1^1\right) \cdot \Pi_1^2 + \left(1 - \Pi_0^0\right) \cdot \Pi_0^1 \cdot \Pi_1^2, \tag{3.1c}$$

$$J_3 = \Pi_0^0 \cdot \Pi_1^1 \cdot \Pi_2^2. \tag{3.1d}$$

The expressions for J_1 and J_2 each have three terms, as there are three possible configurations for each junction type (e.g., the single special boundary in a J_1 junction could be associated with either the first, second or third boundary). In the unconstrained system where all boundaries are assigned randomly, there is no order dependence as to whether any given boundary will be assigned as special, i.e., all $\Pi_x^y = p$, and Eq. (3.1) reduces to the form of the random triple junction distribution of Eq. (1.5). We note that Eq. (3.1) represents a generalization of the method used by Minich et al. in their study of triple junctions in CSL networks [92]. Those authors assumed that the first two boundaries at a triple junction could be assigned a character at random, and introduced local transition probabilities for the assignment of the third boundary $\left(\Pi_x^2\right)$. However, for the present case of low- and high-angle boundaries, all six terms $\left(\Pi_x^y\right)$ are required and can be obtained in closed-form for the special case where grains share a common rotation axis. In this case, the disorientation angles of the three grain boundaries must obey the relationship:

$$\theta_a + \theta_b + \theta_c = 0. \tag{3.2}$$

Eq. (3.2) represents a simplification of the deviation limit rule (Eq. (1.4)) for the fiber textured case. The derivation of the local transition probabilities Π_x^y is presented in much detail in Appendix B; here we discuss only the effects of crystallographic constraint on the resulting probability distributions.

3.2.2. Local Transition Probabilities

At triple junctions in grain boundary networks, the requirement for crystallographic consistency results in nonrandom coordination of special boundaries at triple junctions. If all of the boundaries could be assigned at random, each of the six local transition probabilities would equal p, which is shown as a dashed line in Figure 3.3. Instead, we find the following analytical expressions for Π_x^y in terms of $q = 1 - p$:

$$\Pi_0^0 = 1 - q, \tag{3.3a}$$

$$\Pi_0^1 = \begin{cases} \dfrac{1-6q^{1/2}+15q-10q^{3/2}}{3q}, & p \le 0.75, \\ \dfrac{3-2q^{1/2}}{3}, & p > 0.75, \end{cases} \tag{3.3b}$$

$$\Pi_1^1 = \begin{cases} \dfrac{2+8q^{1/2}-10q}{3+3q^{1/2}}, & p \le 0.75, \\ \dfrac{3-6q+2q^{3/2}}{3-3q}, & p > 0.75, \end{cases} \tag{3.3c}$$

$$\Pi_0^2 = \begin{cases} \dfrac{2-12q^{1/2}+24q-14q^{3/2}}{-1+6q^{1/2}-12q+10q^{3/2}}, & p \le 0.75, \\ 1, & p > 0.75, \end{cases} \tag{3.3d}$$

$$\Pi_1^2 = \begin{cases} \dfrac{1-5q^{1/2}+4q}{-1+5q^{1/2}-10q}, & p \le 0.75, \\ \dfrac{3-4q^{1/2}}{3-2q^{1/2}}, & p > 0.75, \end{cases} \tag{3.3e}$$

$$\Pi_2^2 = \begin{cases} \dfrac{3+6q^{1/2}}{2+10q^{1/2}}, & p \le 0.75, \\ \dfrac{3-9q+6q^{3/2}}{3-6q+2q^{3/2}}, & p > 0.75, \end{cases} \tag{3.3f}$$

These functions are plotted in Figure 3.3 for all values of the special fraction. In these graphs, it is clear that only the first boundary may be assigned randomly; Π_0^0 is exactly equal to p. Deviations of Π_x^y from p indicate that crystallographic constraint creates triple junctions with special boundaries more (or less) frequently than expected. Where any of the curves Π_x^y lies above the dashed line, it is more likely for a special boundary to coordinate the junction, while if it falls below this line a general boundary is more likely.

As the number of previously assigned boundaries increases from zero to two, the constraint on the system increases, as the three disorientations must sum to zero (Eq. (3.2)).

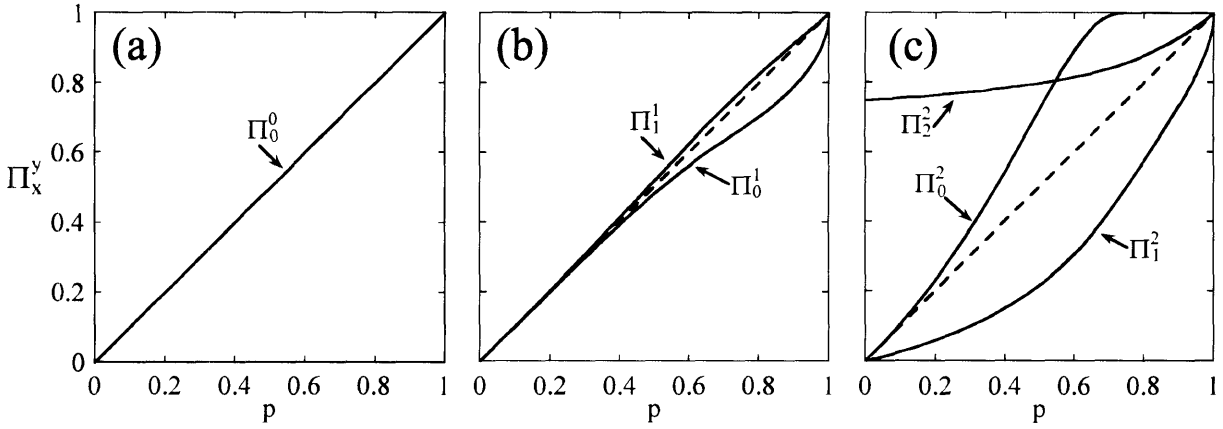

Figure 3.3: Local transition probabilities, Π_x^y, for (a) $y = 0$, (b) $y = 1$, and (c) $y = 2$, which give the local probability of assigning the next boundary as a special boundary. The expectation value for a random lattice is given by the dashed line, $\Pi_x^y = p$. Deviations above this line indicate that a special boundary is more likely to coordinate the junction, while deviations below indicate that a general boundary is more likely.

When the first boundary is assigned, there is only a weak constraint on the second disorientation; in Figure 3.3b, Π_0^1 and Π_1^1 deviate only slightly from p. If the first boundary (*a*) is a general boundary, the density distribution of the second boundary (*b*) is weighted such that boundaries with high disorientation angles are more probable (i.e., $\Pi_0^1 < p$ in Figure 3.3b). Similarly, if the first boundary is a special boundary, there is a slight tendency for another special boundary to coordinate the junction (i.e., $\Pi_1^1 > p$ in Figure 3.3b). In both cases the density distribution of the second boundary is *not* random, but its deviation from $\Pi_x^1 = p$ is rather small.

The most dominant effects of the crystallographic constraint appear after two boundaries have been previously assigned. Unlike when only θ_a had been assigned and θ_b was still relatively free, the assignment of θ_a and θ_b necessarily fixes θ_c (Eq. (3.2)). Therefore, for a given θ_a and θ_b, there will be only one θ_c allowed, representing a much stricter constraint on possible triple junction combinations. This is seen as the distribution density functions, Π_x^2 (Figure 3.3c), deviate significantly from the random case.

With the expressions for Π_x^y in hand, a full closed-form solution for the triple junction distribution is obtained by introducing them into Eq. (3.1). In Figure 3.4, the solution for J_i is

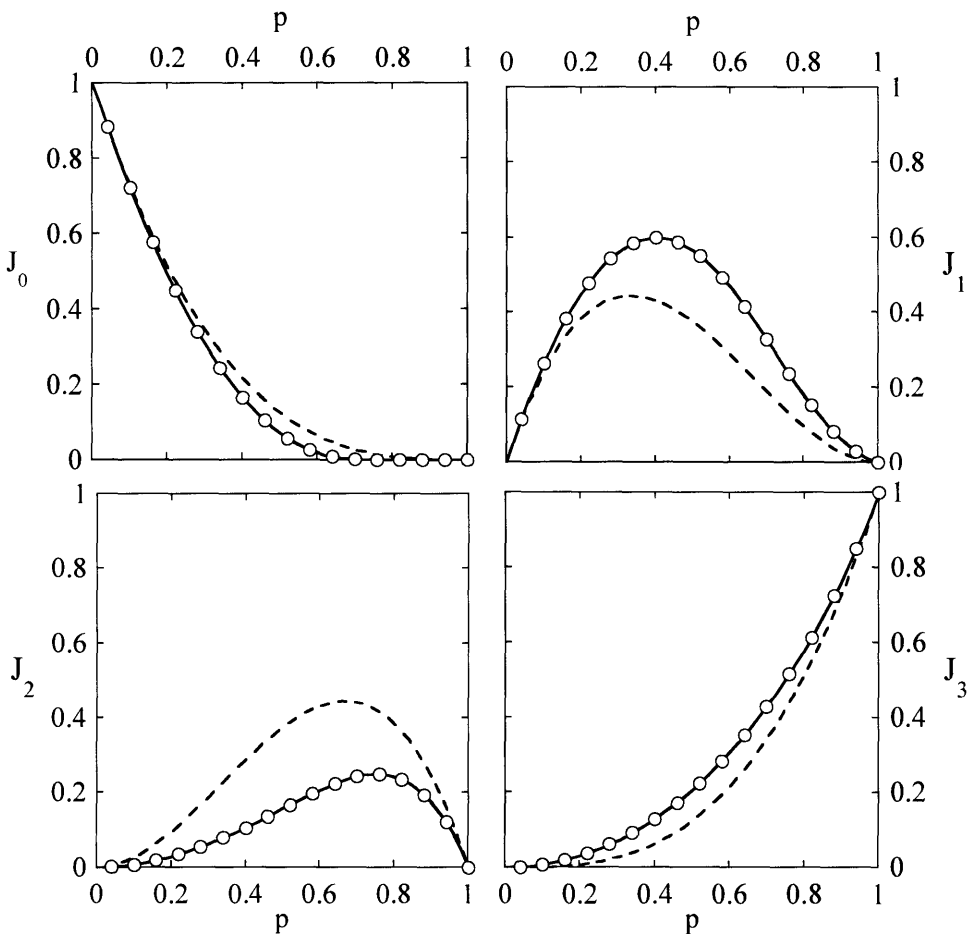

Figure 3.4: Analytical triple junction distribution for fiber textured microstructure given by Eqs. (3.1) and (3.3) (solid line). Also shown are the simulated fiber textured microstructures (points) and the distribution for a random lattice as given by Eq. (1.5) (dashed lines).

shown by the solid lines, while the points are the results of computer simulations for fiber textured polycrystals. Shown for comparison in dashed lines are the random distributions of Eq. (1.5). Clearly, the analytical model and computer simulations give identical results, distinctly different from the purely probabilistic approach. To our knowledge, this is the first closed-form analytical solution for the triple junction distribution of a polycrystal.

The analytical derivation of Π_x^y also gives significant insight into the crystallographic constraints in polycrystals, especially with regard to the assignment of the third boundary, Π_x^2.

1. In Figure 3.3c, for all values of the special fraction, Π_0^2 is greater than p, such that if two general boundaries coordinate a junction, it is likely that the third boundary will be a special

boundary. This is manifested in the triple junction distribution (Figure 3.4) by an increase in J_1 junctions and a reduction in J_0 junctions. When $p \geq 0.75$ ($\theta_t \geq \phi_{max}$), $\Pi_0^2 = 1$ and there cannot be any J_0 junctions (i.e., two general boundaries will always result in a special boundary). Since boundaries *a* and *b* have been assigned as general boundaries, θ_c must be less than ϕ_{max} (and therefore θ_t) according to Eq. (3.2).

2. For all values of *p*, Π_1^2 is lower than the expected random value, meaning that at junctions coordinated by one special and one general boundary, the third boundary will frequently be general. This constraint increases the population of J_1 junctions further, while decreasing the population of J_2 junctions.

3. The deviation of Π_2^2 above the line $\Pi_x^y = p$ contributes more strongly to the decreased population of J_2 junctions in the networks. The presence of two special boundaries strongly promotes the presence of a third, so that J_2 junctions are produced infrequently while J_3 junctions are profuse.

3.3. Concluding Remarks

In the present chapter, the random assignment of boundaries as special or general was found to be insufficient for modeling networks of grain boundaries classified based on their disorientation angles. Instead, the distribution of triple junction types in grain boundary networks was nonrandom as a result of the requirement for crystallographic consistency. A closed-form analytical expression for the triple junction distribution in fiber textured microstructures was derived with the use of local transition probabilities. The nonrandom local coordination of special and general boundaries is expected to persist in three dimensions as well; this will be explored in the following chapter.

Chapter 4: Crystallographic Constraint at Quadruple Nodes

In the previous chapter, the triple junction distributions for crystallographically consistent grain boundary networks were shown to differ from those in randomly assembled networks due to the requirement of crystallographic consistency around a triple junction. However, realistic microstructures are rarely two-dimensional, and it is not clear whether the current understanding of crystallographic constraint from a triple junction perspective can be applied to understand or predict the grain boundary connectivity and network topology in three dimensions.

In this chapter, the concept of the triple junction distribution is extended to the characterization of quadruple nodes, and expectation curves are developed for the statistical distribution of quadruple node types (i.e., the quadruple node distribution (QND)) for several different types of microstructures. Because quadruple nodes exhibit conformational isomerism, whereas triple junctions do not, the complexity of such a statistical analysis becomes significant in 3-D. However, as 3-D microstructural analysis techniques such as serial sectioning and three-dimensional x-ray diffraction microscopy become more widely used, we expect that the QND will be the first 3-D point of contact between experiments and the developing theory of grain boundary networks [117-120]. In addition, we quantitatively examine the relationship between the nonrandom TJDs that were found in Chapter 3 and QNDs determined here. Finally, although it is known that there are additional crystallographic constraints around quadruple nodes as compared to those around triple junctions [107, 121], it remains unclear what the relative influence of each constraint is. We use the concept of configurational entropy to assess the relative strength of the crystallographic constraints around triple junctions and quadruple nodes.

4.1. Quadruple Node Distributions

In three-dimensional grain boundary networks, the zero-dimensional points of grain boundary connectivity are called quadruple nodes. A quadruple node is a complex microstructural feature that involves four grains, six grain boundaries, and four triple junctions that meet at a point. Figure 4.1a is a schematic representation of a quadruple node where the grains have the shape of tetrakaidecahedra and are labeled G_i, where i (= 0, 1, 2 or 3) indicates the grain number. The six shared faces (grain boundaries) that are part of the quadruple node are shown again in Figure 4.1b and are labeled *a* through *f*. The four triple junctions are shown in Figure 4.1b as thick lines.

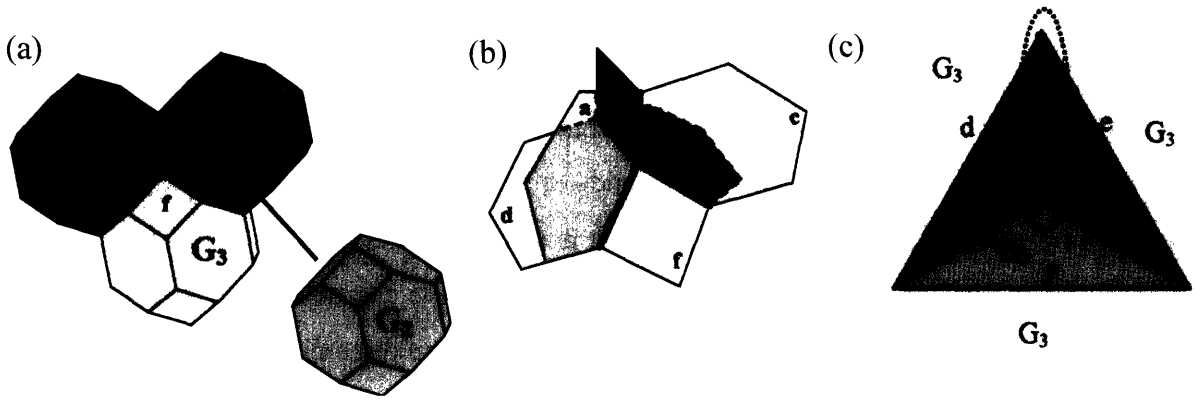

Figure 4.1: (a) The four tetrakaidecahedral grains that comprise a quadruple node. The grains are labeled G_i (i = 0 to 3), and boundaries are labeled with lower-case letters. (b) The shared faces of the tetrakaidecahedra are the grain boundaries in the quadruple node. The lightly shaded boundaries have general character, while the darker boundaries are special. The six boundaries are labeled *a* through *f*. (c) Two-dimensional topological map of the same quadruple node as in part (b) where thinner lines indicate general boundaries and thicker lines are special boundaries. The four grains, which have the same shading as in part (a), are the enclosed areas between the lines and grain G_3 is the entire area outside the triangle. The circuit in (c) represents a second-order constraint involving four grains and four boundaries.

The character of the grain boundaries around a given quadruple node can be quite variable, and Figure 4.1b is an example of one possible configuration: several boundaries have been lightly shaded to denote them as general boundaries, while those shaded more darkly are special boundaries. As seen in Figure 4.1b, the coordination among the grain boundaries and triple junctions at the quadruple node is quite difficult to visualize in projection from 3-D. Alternatively, we choose to represent a quadruple node using a topological map represented in 2-D. Such a map is illustrated in Figure 4.1c for the same quadruple node as in Figure 4.1b, where the lines represent grain boundaries and the triple junctions lie at the vertices. In this example, the thick lines denote special boundaries and thinner lines general boundaries. The grains, again labeled as G_i, are now the enclosed areas between the lines; grain G_3 occupies the entire area outside of the triangle. Although in the 2-D topological map the triple junctions do not appear to meet at a single point as in Figure 4.1a, it is important to remember that in three dimensions they do; the topological map in Figure 4.1c extends over a finite area, but it represents only a single point in space.

In analogy to the triple junction distribution, each quadruple node may be classified based on the number of special boundaries that coordinate the junction, i.e., the boundary *composition* of the node. However, unlike the case of triple junctions, quadruple nodes exhibit isomerism; two quadruple nodes with the same boundary composition can exhibit topologically unique conformations. For example, the quadruple node in Figure 4.1c is coordinated by two special boundaries *b* and *e*, which meet at a triple junction. Redistributing the same boundaries such that *b* and *f* are classified as special instead of *b* and *e* results in a topologically distinct node where there are still exactly two special boundaries, but they no longer meet at a triple junction. The most general definition of the quadruple node distribution must therefore account for both node composition and isomerism. We propose to label quadruple nodes as Q_{ij}, where i (= 0 to 6) is the number of special boundaries that coordinate the quadruple node and j (= 0 to 4) is the number of triple junctions coordinated by at least two special boundaries. In this scheme, there are eleven different quadruple node types, as shown pictorially in Figure 4.2. As in Eq. (1.5), the quadruple node distribution may be found analytically for the (unphysical) case where boundaries are randomly assigned as special with probability p:

$$Q_{ij} = \Omega_{i+j} \cdot p^{i} (1-p)^{6-i} \tag{4.1}$$

where Ω_{i+j} is the number of possible configurations for each node and is equal to 1, 6, 3, 12, 4, 12, 4, 12, 3, 6 and 1 for $i + j = 0, 1, 2, 3, 4, 5, 6, 7, 8, 9$ and 10, respectively.

In order to determine the expectation curves for the QND in realistic microstructures, 3-D polycrystals, including fiber textured, general textured and twinned polycrystals, are simulated following the procedure described in Chapter 2. The quadruple node distributions are obtained for each of the three types of simulated microstructures and the results are shown by the points in Figure 4.2 for comparison with the random distributions of Eq. (4.1). As with the TJD, the populations for all types of quadruple nodes are seen to deviate from those predicted for a randomly assembled network. In some cases, these deviations are quite pronounced, being a factor of two more or less likely to occur than one would normally expect. As with the TJD, the deviation of the QND from Eq. (4.1) is due to the requirement of crystallographic consistency. To some extent, the deviations from the random distributions seen in Figure 4.2 can be

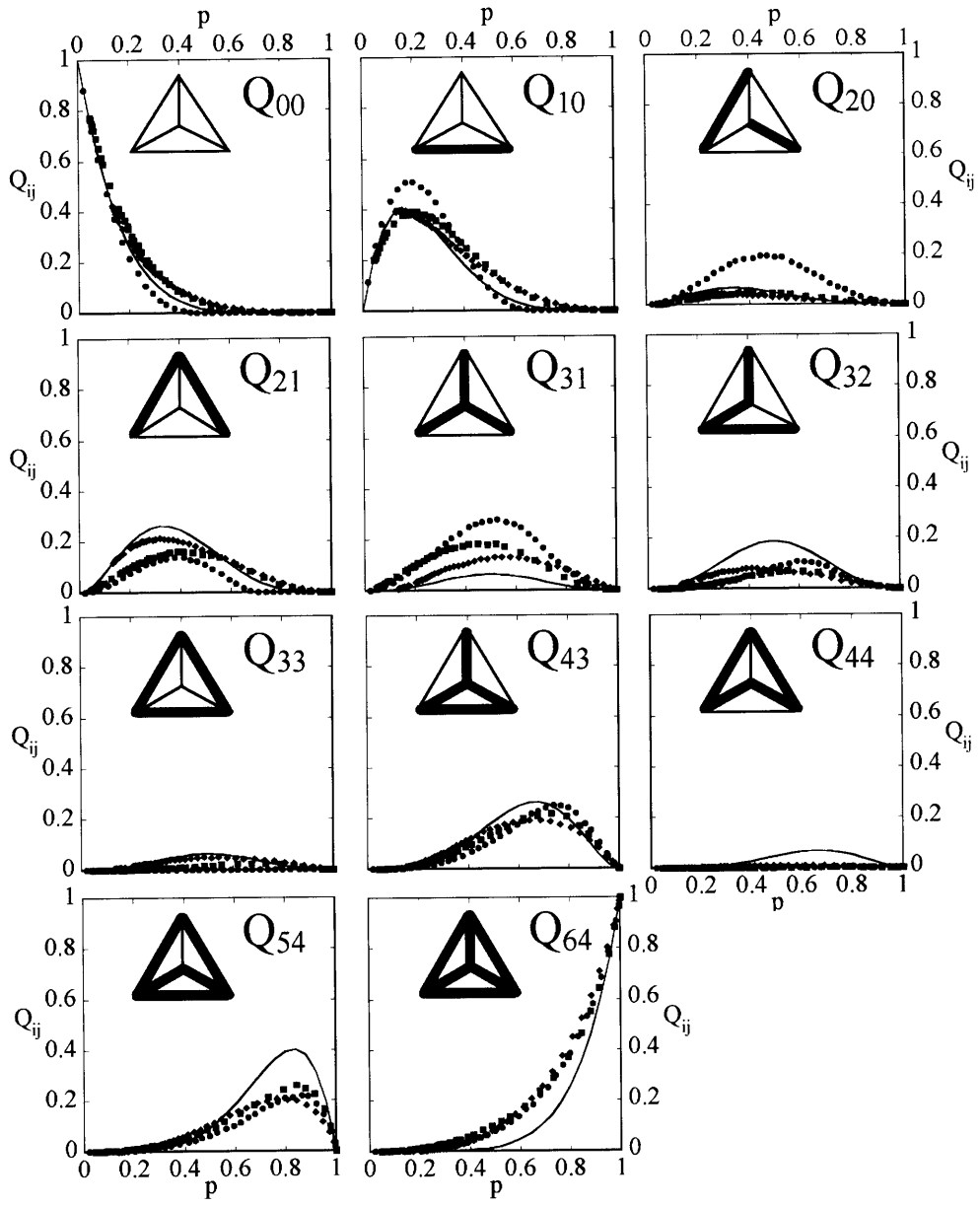

Figure 4.2: The quadruple node distributions for simulated three-dimensional fiber textured (circles), general textured (squares), and twinned (diamonds) microstructures. The lines represent the QND for the case where boundaries are randomly assigned character (Eq. (4.1)). The 2-D topological map is also shown for one configuration of each type of quadruple node, where thinner lines are general boundaries and thicker lines are special boundaries.

anticipated by considering the types of triple junctions that comprise the quadruple node. For example, fiber textured microstructures do not have any Q_{44} nodes, while general textured and twinned microstructures never have greater than 1% of these nodes. All four triple junctions

comprising a Q_{44} node are J_2 junctions, which were shown in Figure 3.2 to be unfavorable; therefore, it is expected that the population of Q_{44} nodes in the distribution would be greatly decreased. The converse is true for Q_{64} nodes, which are more abundant than predicted by Eq. (4.1) for all simulated microstructures. In Q_{64} nodes, all four triple junctions are J_3 junctions which showed an increased population in Figure 3.2.

4.2. Crystallographic Constraints around Quadruple Nodes

In analyzing the TJD, the QND, or even longer-range structures in the grain boundary network, it is important to keep in mind that crystallographic constraints are present at every length scale in the microstructure. These constraints arise due to the need for consistency around closed circuits through the microstructure. For example, in Chapter 1, it was established that misorientation must be conserved for a closed circuit around a triple junction (Figure 1.3). This circuit around an individual triple junction is the smallest nontrivial circuit possible in a microstructure, and therefore represents a constraint of the *first order*.

Beyond the first-order triple junction circuit described above, the next smallest non-redundant circuit is one that passes through four grains and intersects four of the six boundaries associated with a quadruple node. Such a circuit is indicated by the dotted oval in Figure 4.1c and is more restrictive than those only around the triple junctions, as it requires crystallographic compatibility among all four grains. This longer range constraint represents a constraint of *second order*. In the previous section, we examined the QND of our simulated polycrystals, and we saw that in many cases, the quadruple node coordination could be qualitatively anticipated by examining the TJD, which incorporates only first-order constraints. However, the situation is actually more complicated because of second-order constraints. For example, Gertsman has illustrated how a set of four individually consistent triple junctions fail to produce a valid quadruple node [121]. However, it is unclear what the relative importance of the first- and second-order constraints is, and to what extent the exact form of the nonrandom QND is a result of the nonrandom TJD alone. In what follows, we formulate the probabilistic expressions required to predict the QND based only on first-order constraints (i.e., from a known TJD) and compare these predictions with the results of the 3-D simulations. As we will see, this analysis allows us to assess the relative importance of first- and second-order (i.e., triple junction and quadruple node) constraints on the grain boundary connectivity.

4.2.1. Relationship between Triple Junction and Quadruple Node Distributions

To examine the quantitative relationship between the TJD and QND, we assemble triple junctions into every self-consistent quadruple node possible; the probability of a given quadruple node appearing in the microstructure may then be determined based on the types of triple junctions that make up the quadruple node. The development of this probabilistic argument is complicated by the fact that many triple junction combinations are impossible at a quadruple node; for example, J_0 and J_3 junctions may not coexist at a quadruple node as they would be required to share at least one boundary that cannot simultaneously be special and general. The most straightforward approach to this problem is to build each quadruple node by assigning one triple junction at a time around it. The first junction may be assigned independently, specifying the character of three of the six boundaries. At the second triple junction, one boundary's character is already known, and the junction assignment must be consistent; the character of five of the six boundaries is then fixed. Finally, assignment of a third triple junction consistent with all the prior assignments fixes the character of the final boundary. Therefore, the probability of a specific quadruple node configuration appearing in the microstructure can be defined as the product of three assignment probabilities:

$$\Lambda = \lambda_{i}\lambda_{ii}\lambda_{iii} \tag{4.2}$$

where the subscript Roman numerals denote the three triple junction "decision points"; these points are circled on the quadruple node shown in Figure 4.3. In what follows, we work out in detail the values of λ_x required to build the specific quadruple node shown in Figure 4.3; the procedure is then easily generalized to develop probabilistic expressions for the full QND.

For the specific conformation of the Q_{21} quadruple node in Figure 4.3, we begin by determining the probability of assigning the triple junction *i* with the appropriate J_1 type in the correct orientation, i.e., such that the special boundary lies on *b*. For this first assignment there are no constraints on the system, so junction *i* could be assigned with any of the eight configurations shown in column *i* of Figure 4.3. The correct assignment requires that we choose one of three J_1 junctions ($(1/3)J_1$), from among these possibilities. The probability of this assignment is therefore:

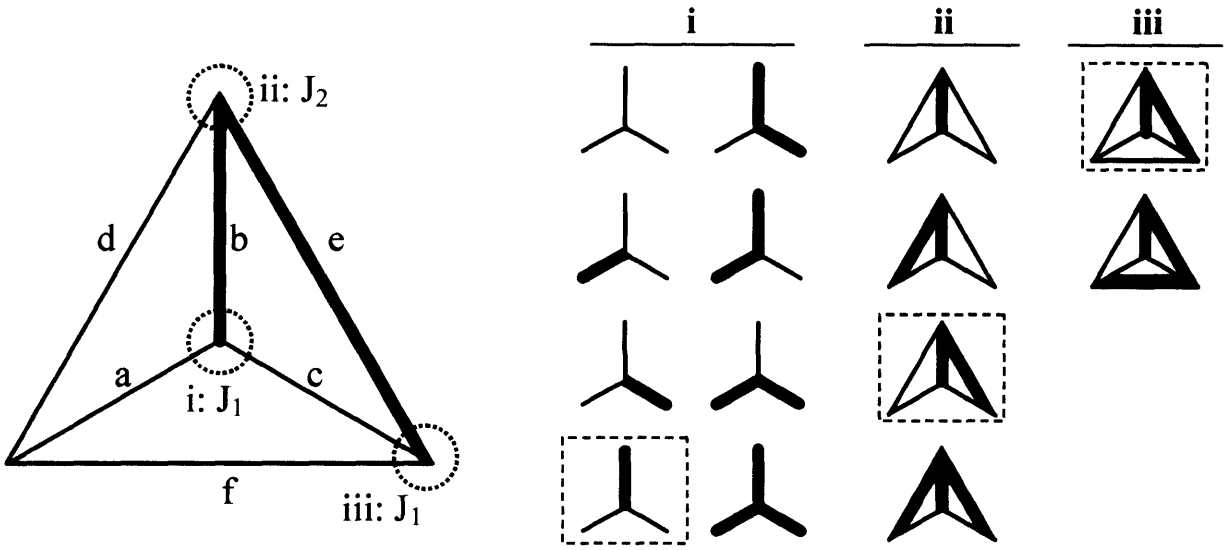

Figure 4.3: The topological map for a Q_{21} quadruple node, where the boundaries are labeled *a* through *f*, with special boundaries indicated by the thick lines and general boundaries by thinner lines. Three of the triple junctions are labeled as *i*, *ii* and *iii*, and are assigned a character in order to form this specific Q_{21} quadruple node. The possible assignments at each triple junction are shown in columns *i*, *ii* and *iii* on the right, where the correct assignment that leads to this specific quadruple node is indicated by the dashed box.

$$\lambda_i = \frac{\frac{1}{3}J_1}{J_0 + J_1 + J_2 + J_3} = \frac{1}{3}J_1 \tag{4.3}$$

The next assignment can occur at any of the three corner junctions in Figure 4.3; we select junction *bde*. The assignment of this triple junction is constrained by the fact that boundary *b* has already been assigned as special. Given this constraint, junction *ii* can assume one of three J_1 configurations (with only *b* special), two of three J_2 configurations (with *b* and *d* or *b* and *e* special), or the J_3 configuration (with all special boundaries), as shown in column *ii* of Figure 4.3. The correct assignment is one of the three J_2 configurations, giving:

$$\lambda_{ii} = \frac{\frac{1}{3}J_2}{\frac{1}{3}J_1 + \frac{2}{3}J_2 + J_3} = \frac{J_2}{J_1 + 2J_2 + 3J_3} \tag{4.4}$$

The final assignment at junction *iii* must conform to the prior assignments of boundaries *c* and *e*, giving only two possibilities: one of three J_1 configurations (with only *e* special) or one of three

J_2 configurations (with both *e* and *f* special), as shown in column *iii* of Figure 4.3. The probability of selecting the correct arrangement is:

$$\lambda_{iii} = \frac{\frac{1}{3}J_1}{\frac{1}{3}J_1 + \frac{1}{3}J_2} = \frac{J_1}{J_1 + J_2} \tag{4.5}$$

According to Eq. (4.2), the total probability of having the specific configuration of the Q_{21} quadruple node shown in Figure 4.3 is thus the product of Eqs. (4.3), (4.4) and (4.5). The same procedure as outlined above has been used to determine the probability of each configuration for all quadruple nodes, and summation over all configurations for each Q_{ij} results in the following expressions for the QND in terms of the TJD:

$$Q_{00} = \frac{9J_0^3}{\alpha_1\gamma_1} \tag{4.6a}$$

$$Q_{10} = \frac{9J_0^2J_1}{\alpha_1\gamma_1} + J_0J_1^2\left(\frac{2}{\alpha_1\gamma_2} + \frac{1}{\alpha_2\gamma_1}\right) \tag{4.6b}$$

$$Q_{20} = \frac{J_1^3}{3}\left(\frac{2}{\alpha_1\gamma_2} + \frac{1}{\alpha_2\gamma_1}\right) \tag{4.6c}$$

$$Q_{21} = \frac{3J_0J_1^2}{\alpha_1\gamma_1} + J_0J_1J_2\left(\frac{4}{\alpha_1\gamma_2} + \frac{2}{\alpha_2\gamma_1}\right) + \frac{J_1^2J_2}{3}\left(\frac{2}{\alpha_2\gamma_2} + \frac{1}{\alpha_1\gamma_3}\right) \tag{4.6d}$$

$$Q_{31} = J_1^2J_3\left(\frac{2}{\alpha_2\gamma_2} + \frac{1}{\alpha_1\gamma_3}\right) + \frac{J_1^3}{3\alpha_1\gamma_1} \tag{4.6e}$$

$$Q_{32} = \frac{J_1^2J_2}{3}\left(\frac{4}{\alpha_1\gamma_2} + \frac{2}{\alpha_2\gamma_1}\right) + \frac{J_1J_2^2}{3}\left(\frac{4}{\alpha_2\gamma_2} + \frac{2}{\alpha_1\gamma_3}\right) \tag{4.6f}$$

$$Q_{33} = J_0J_2^2\left(\frac{2}{\alpha_1\gamma_2} + \frac{1}{\alpha_2\gamma_1}\right) + \frac{J_2^3}{3\alpha_2\gamma_3} \tag{4.6g}$$

$$Q_{43} = \frac{J_1J_2^2}{3}\left(\frac{2}{\alpha_1\gamma_2} + \frac{1}{\alpha_2\gamma_1}\right) + J_1J_2J_3\left(\frac{4}{\alpha_2\gamma_2} + \frac{2}{\alpha_1\gamma_3}\right) + \frac{3J_2^2J_3}{\alpha_2\gamma_3} \tag{4.6h}$$

$$Q_{44} = \frac{J_2^3}{3}\left(\frac{2}{\alpha_2\gamma_2} + \frac{1}{\alpha_1\gamma_3}\right) \tag{4.6i}$$

$$Q_{54} = J_2^2 J_3\left(\frac{2}{\alpha_2\gamma_2} + \frac{1}{\alpha_1\gamma_3}\right) + \frac{9J_2J_3^2}{\alpha_2\gamma_3} \tag{4.6j}$$

$$Q_{64} = \frac{9J_3^3}{\alpha_2\gamma_3} \tag{4.6k}$$

where the denominator terms α and γ correlate with decisions at nodes *ii* and *iii*, respectively:

$$\alpha_1 = 3J_0 + 2J_1 + J_2 \tag{4.7a}$$

$$\alpha_2 = J_1 + 2J_2 + 3J_3 \tag{4.7b}$$

$$\gamma_1 = 3J_0 + J_1 \tag{4.7c}$$

$$\gamma_2 = J_1 + J_2 \tag{4.7d}$$

$$\gamma_3 = J_2 + 3J_3 \tag{4.7e}$$

In the case of random boundary assignment, the TJD is given by Eq. (1.5), which, when introduced into Eq. (4.6), gives exactly Eq. (4.1). In the general case, Eq. (4.6) gives the form of the QND when *only* triple junction correlations (i.e., first-order constraints) are taken into account, and there is no additional, higher-order constraint imposed on the system. In this case, any deviation between the predictions of Eq. (4.6) and the true QND is indicative of such higher-order constraints. This is in fact the case for each of the three simulated microstructures studied here. In Figure 4.4, ΔQ_{ij}, the difference between the true value of Q_{ij} from the 3-D simulations and Q_{ij} from Eq. (4.6), is plotted for all of the populations in each of the three microstructures as a function of the special fraction.

From a mathematical point of view, the deviations between Eq. (4.6) and the true QND in our simulated microstructures are an indication that the full crystallographic constraints around quadruple nodes are not completely captured by simply superposing the constraints around triple junctions. This is in line with the literature on quadruple node crystallography [107, 121] and, as already discussed, arises due to the presence of second-order constraints around the quadruple node. However, from a more practical point of view, we note that the predictions of Eq. (4.6)

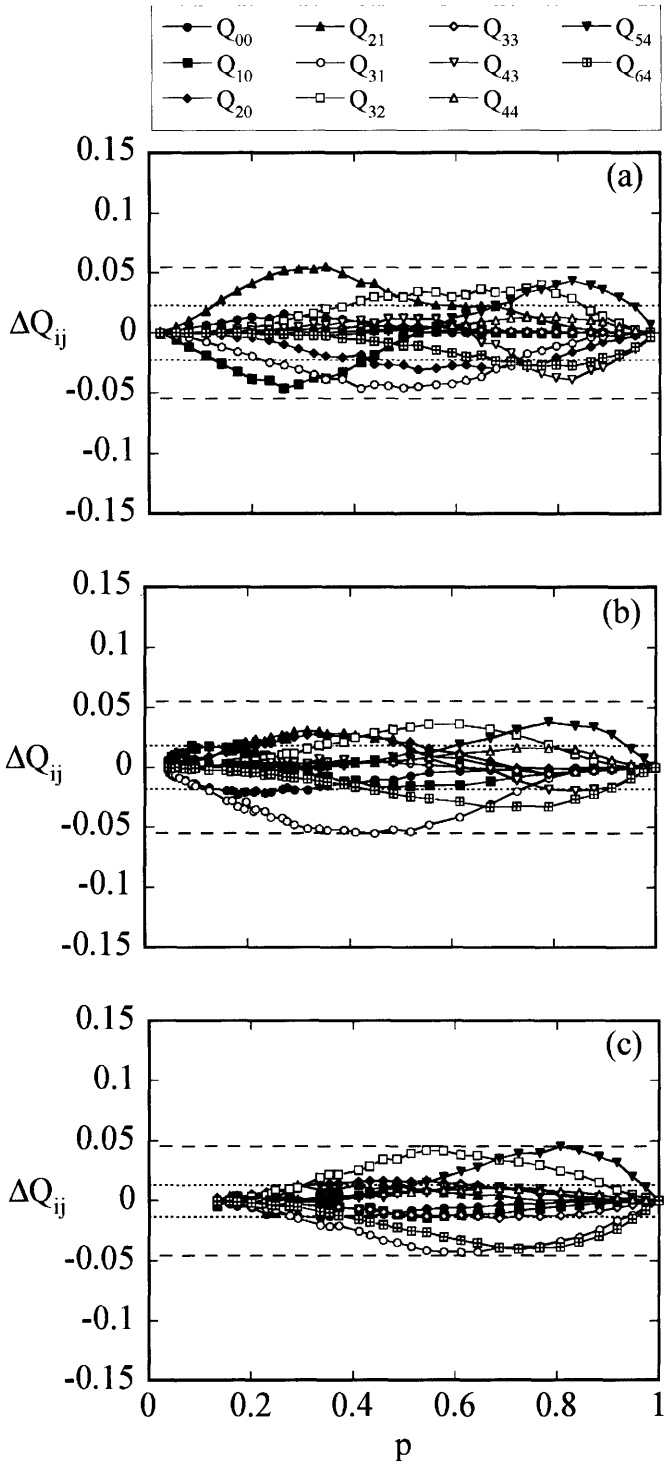

Figure 4.4: The error between Q_{ij} as predicted by Eq. (4.6) and as found from the simulations for (a) fiber textured, (b) general textured and (c) twinned microstructures. Positive ΔQ_{ij} values indicate that Eq. (4.6) overpredicts Q_{ij}, while negative ΔQ_{ij} values indicate underprediction of Q_{ij}. The maximum error for each microstructure is shown by the dashed lines and is ~0.05 for each. However, the majority of the Q_{ij} are predicted quite accurately, and 75% of these errors lie within the dotted lines at $\Delta Q_{ij} \sim 0.015$.

generally do capture the subtle deviations of the QND from the random distribution, and the error between the real and predicted distributions is less than 0.015 for 75% of the populations. Even in the worst cases shown in Figure 4.4, the error between Eq. (4.6) and the true QND is not more than ±0.055. Realistically, this is about the range of error bars for measurements of this kind, which are subject to statistical uncertainty and sampling biases. This means that, to within a good approximation, the first-order constraints in a microstructure dominate the nonrandom connectivity of the grain boundary network, and that higher-order constraints produce only small corrections to the very dominant first-order constraint. We propose, therefore, that in many cases it may be sufficient to measure only a TJD on an unbiased 2-D section in order to make general statements about the network connectivity in 3-D.

4.2.2. Configurational Entropy of Grain Boundary Networks

Although the above analysis illustrates directly the relative importance of first- and second-order constraints around quadruple nodes, it would be valuable to have a simple approach to quantify these effects without resorting to inspection of all 11 curves of the QND. In fact, there is an even more general need for a simple means of classifying just how nonrandom any grain boundary network is using, e.g., a single scalar value or a single function of p. In this section, we develop such a method by considering the configurational entropy of grain boundary networks. Since we are at present interested in 3-D networks, the following developments will be concerned with the entropy among quadruple node types, although it should be recognized that these developments are easily generalized to 2-D networks. For a quadruple node distribution, the configurational entropy S is defined as:

$$S = -\sum_{i+j=0}^{10} Q_{ij} \ln\left(Q_{ij}\right) \tag{4.8}$$

For purposes of comparing one microstructure to another, it is convenient to calculate the entropy difference ΔS with respect to a common reference point, S_o. We propose that the appropriate ground state for this purpose is the microstructure of maximum possible entropy. Any crystallographic constraints in the microstructure will then reduce its entropy (or increase its information content). The maximum entropy distribution can be found using the method of Lagrange multipliers; this procedure is described in Appendix C and S_o is given by Eqs. (C.1, C.3, and C.9).

The values of ΔS for all three microstructures modeled here are shown in Figure 4.5 as a function of p. Two curves are shown for each microstructure, the solid points being for the full 3-D simulations with crystallographic consistency at both first and second order, and the open points having been calculated from Eq. (4.6) for a microstructure with only first-order constraints. Of the three microstructures considered, fiber textured microstructures show the greatest change in configurational entropy, indicating that the effects of crystallographic constraint are strongest in this system. Both general textured and twinned microstructures also show a significant decrease in entropy with respect to the reference configuration. Put another way, crystallographic constraints increase the information content of the QND.

Figure 4.5 also directly shows the relative importance of first- and second-order constraints. For example, in the case of a fiber textured microstructure with p in the vicinity of ~0.5, we see that the first-order constraints are responsible for ~0.33/0.45 = 73% of the entropy decrease in a fully constrained system. This result agrees with intuition that high-order

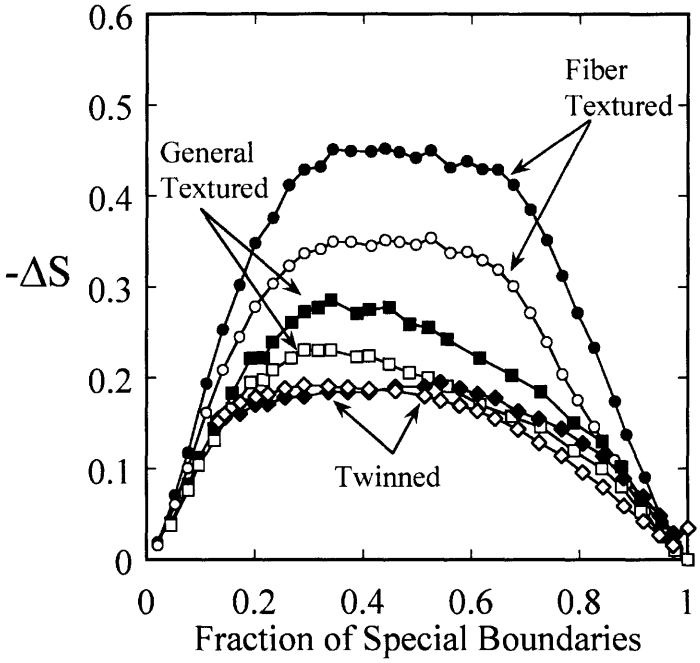

Figure 4.5: The decrease in configurational entropy (Eq. (4.8)) from the maximum entropy configuration, S_o, for fiber textured (circles), general textured (squares) and twinned (diamonds) microstructures due to crystallographic constraints. For nearly every value of p in all three systems, the decrease in entropy is greater when both first- and second-order constraints are imposed (filled points) than with first-order constraints only (open points).

constraints should be of lower relative importance in dictating network connectivity. In the case of twinned microstructures, we see that, to a good approximation, first-order constraints are responsible for all of the entropy in the network. In order to simply quantify the relative importance of first- and second-order constraint around quadruple nodes, we have calculated the ratio of integrated entropy changes:

$$\sigma = \frac{\int_0^1 \Delta S_f \, dp}{\int_0^1 \Delta S_t \, dp} \tag{4.9}$$

where the subscript *f* refers to first-order and the subscript *t* to first-plus-second-order constraints (i.e., the curves with open and solid points in Figure 4.5, respectively). The value of σ then gives the relative importance of first-order constraints in terms of its fractional contribution to the system entropy.

In the case of fiber textured microstructures, first-order constraints account for more than σ = 75% of the total constraint (i.e., the second-order constraints are responsible for only 25% of the entropy in the QND). In general textured and twinned microstructures, the triple junction constraint captures an even more significant fraction of the total with σ = 0.82 and 0.93, respectively. Therefore, although a fully accurate description of the microstructure requires information beyond just triple junction coordinations, we find that in many cases first-order considerations will likely be sufficient; a satisfactory statistical description of the grain boundary network can quite probably be obtained using information from a single, unbiased 2-D section.

4.3. Concluding Remarks

We have used computer simulations to study the effects of crystallographic constraint on grain boundary networks in three-dimensional microstructures and have found that, in analogy to the triple junction distribution, the distribution of quadruple node types was distinctly nonrandom. An analytical model was developed that allowed the TJD acquired from a two-dimensional section to be used to reasonably predict the QND in a three-dimensional microstructure. However, the exact form of the QND could not be predicted by considering only first-order constraints, as small second-order constraints further influenced the boundary coordination at quadruple nodes; these effects were quantified using the configurational entropy.

In this and the previous chapter, we have looked only at the local effects of the requirement for crystallographic consistency. In the following chapter, we consider the long-range implications of preferential coordination of triple junctions and quadruple nodes. We have already seen that the global network topology can change qualitatively, with special and general boundary clusters taking on nonrandom configurations. These results can be further quantified through a study of the percolation and scaling behavior in 2- and 3-D grain boundary networks.

Chapter 5: Percolation and Scaling Behavior of Grain Boundary Networks

In the two previous chapters, two- and three-dimensional grain boundary networks were investigated at the nearest-neighbor level and found to have nonrandom local coordination. The preferential clustering of special and general boundaries, a result of the requirement for crystallographic consistency around any closed circuit in the microstructure, led to network topologies that differed from those of randomly assembled networks. The general boundaries in crystallographically consistent networks tended to form elongated structures in 2-D, while the special boundaries had more compact structures. The crystallographic constraints present in grain boundary networks are also expected to have longer-range implications. For example, since special boundaries cluster together, a larger fraction may be required to form a sample-spanning path, thus increasing the percolation threshold. As explained in Chapter 1, the percolation threshold represents a topological phase transition and is a property of an infinite or quasi-infinite lattice. Since the percolation threshold is an important parameter in materials design, it is essential to determine how crystallographic constraints shift p_c in common microstructural models (i.e., fiber textured, general textured and twinned polycrystals). Other properties of the network, such as how grain boundaries cluster at medium- and long-range below the percolation threshold, will also be determinant in the structure-property relationships for problems such as intergranular cracking or corrosion. For example, the connectivity length ξ, a characteristic size of grain boundary clusters, may be considered a "mean free path" for potential intergranular damage [50].

This chapter explores the effects of crystallographic constraint on the structure of grain boundary networks at medium- and long-range length scales by simulating very large networks, which approximate infinite lattices in the thermodynamic limit. To begin, the percolation thresholds, as well as other lattice properties near the threshold, are determined. In particular, network scaling relationships are assessed, offering a statistical description of any large microstructure given that the fraction of special boundaries is known. Next, the lattice properties are investigated at decreasing length scales down to the nearest neighbor level, where correlations are known to exist at triple junctions. This analysis is relevant for many materials problems where sample sizes are small enough that they may no longer be approximated as

infinite lattices (e.g., in integrated circuits or micro-devices). Finally, a critical length scale is identified, below which local correlations dominate the lattice statistics; i.e., above which a statistical description of the grain boundary network becomes feasible.

5.1. Percolation Thresholds for Grain Boundary Networks

The percolation thresholds are identified using the procedures explained in Chapter 2 for both 2- and 3-D polycrystals with various textures, crystal symmetries and low-angle thresholds. The results are summarized in Tables 5.1 and 5.2 where we tabulate the percolation thresholds for a continuous path of special boundaries, called $p_{c,special}$, as well as the complementary threshold for a continuous path of general boundaries, $p_{c,general}$. Here, the percolation threshold refers to the population of the particular type of boundary at which a percolation event occurs (i.e., $p_{c,special}$ is the fraction of special boundaries, while $p_{c,general}$ is the fraction of general boundaries). When the fraction of relevant boundaries is below the percolation threshold, there is no continuous path of boundaries across the lattice; above the percolation threshold, such a path exists.

5.1.1. Percolation Thresholds in Two-Dimensional Grain Boundary Networks

The percolation thresholds that are found for 2-D fiber textured, general textured and twinned microstructures are summarized in Table 5.1. The effects of crystal system and low-angle threshold are investigated in the 2-D lattices only, and as we found in Chapter 3 for the triple junction distributions, there is no effect of crystal system or θ_t on either percolation threshold within the accuracy of this study (Table 5.1). Furthermore, all of the values of p_c identified here for polycrystals are distinctly different from those observed in random lattices. For example, values of $p_{c,special} \approx 0.689$ and $p_{c,general} \approx 0.601$ were found for fiber textured microstructures, which are different from the value 0.653 in the random case. It is also interesting to note that the enforcement of crystallographic constraint breaks the symmetry normally seen in percolation problems; whereas $p_{c,special} = p_{c,general}$ for a random lattice, this is not generally true in polycrystals.

The deviations of p_c in Table 5.1 from the random cases are consistent with the triple junction distribution in Figure 3.2, and also can be rationalized qualitatively by examination of the networks in Figure 3.1. For example, for polycrystals with a fiber texture, we find $p_{c,general} = 0.601 \pm 0.005$, lower than that of a random lattice at 0.653. At the same time, the network of

Table 5.1: Percolation thresholds for a continuous path of special ($p_{c,special}$) or general ($p_{c,general}$) boundaries for various textures on 2-D honeycomb lattices. Here, $p_{c,special}$ refers to the fraction of special boundaries, and $p_{c,general}$ to the fraction of general boundaries, above which the lattice contains a percolating cluster. Although the thresholds differ among microstructural models, variations in crystal symmetry (cubic, hexagonal or tetragonal) and low-angle threshold (θ_t = 2 to 15 degrees) have no effect on the percolation threshold.

	θ_t (degrees)	$p_{c,special}$ (± 0.005)	$p_{c,general}$ (± 0.005)
Random lattice		0.653	0.653
General texture			
Cubic	15	0.664	0.676
Hexagonal	15	0.664	0. 676
Tetragonal	15	0.663	0. 676
Fiber texture			
Cubic	15	0.689 [1]	0.601 [1]
Hexagonal	15	0.687	[2]
Tetragonal	15	0.687	0. 601
Tetragonal	10	0.687	0. 601
Tetragonal	8	0.686	0. 601
Tetragonal	6	0.687	0.600
Tetragonal	4	0.687	0.600
Tetragonal	2	0.687	0. 601
Twinned		0.666	0.659

1 These values were determined on lattices with 5000 grains per side. The error bar has a value of ±0.001.
2 The maximum fraction of general boundaries that can be achieved is 0.5, given by the symmetry of the structure and the low-angle threshold, such that there will never be a continuous path of general boundaries.

general grain boundaries in Figure 3.1g has a considerably more elongated structure than does the random network in Figure 3.1a, with longer chains of general boundaries and fewer grains surrounded by general boundaries. This change in topology corresponds to a significant increase in J_1 junctions above the random value (Figure 3.2), and the tendency of general boundaries to assemble into long chains slightly reduces the population needed for a spanning cluster. In the case of general texture, $p_{c,general} \approx 0.676$ is somewhat *higher* than the random value of 0.653, which is a result of a tendency to form large clusters rather than strings (c.f., Figure 3.1c, where it is clear that both the special and general boundaries tend to cluster with like boundaries).

With regard to the percolation thresholds for special boundaries, all of the simulated microstructures exhibit a threshold $p_{c,special} \approx 0.66$ to 0.69, higher than the expected value of

$p_{c,special}$ = 0.653 for a randomly assembled lattice. This result implies that a relative excess of special boundaries is needed for a continuous path to develop, and results from the scarcity of J_2 junctions seen in these structures (Figure 3.1d, f, h). Since the J_2 junctions most facilitate the connectivity of special boundaries across the lattice, crystallographic suppression of these junctions requires $p_{c,special}$ to increase.

5.1.2. Percolation Thresholds in Three-Dimensional Grain Boundary Networks

The 3-D percolation thresholds are summarized in Table 5.2 for fiber textured, general textured and twinned microstructures. For comparison, the value for a randomly assembled tetrakaidecahedral lattice is also determined in this work; this value is similar to the one reported by Wells et al. [76] for the same geometry. For crystallographically consistent lattices, these threshold values are seen to differ by as much as 0.07 from the value for standard percolation theory. For example, $p_{c,special}$ shifts from 0.225 to 0.287 (both ± 0.005) in fiber textured microstructures. Of greater interest in materials design is $p_{c,general}$ (Table 5.2), the threshold above which there exists a connected path of general boundaries, but below which no such paths remain. In a randomly assembled lattice, $p_{c,general}$ is also 0.225 ± 0.005, which decreases to 0.158 ± 0.005 for fiber textured lattices. In fact, in all three microstructures, $p_{c,general}$ is lower than expected from standard percolation theory, implying that a relative excess of special boundaries is necessary to break up potential damage paths.

Table 5.2: Percolation thresholds in randomly-assembled and crystallographically consistent three-dimensional grain boundary networks. The percolation thresholds are given for both 1-D chains and 2-D surfaces in a 3-D lattice. The values of p_c for a 2-D surface through a 3-D lattice represent lower bounds for the existence of a percolating surface as explained in the text.

	1-D chain in a 3-D lattice		2-D surface in a 3-D lattice	
	$p_{c,special}$ (± 0.005)	$p_{c,general}$ (± 0.005)	$p_{c,special}$ (± 0.005)	$p_{c,general}$ (± 0.005)
Randomly assembled	0.225	0.225	0.775	0.775
Fiber textured	0.289	0.158	0.842	0.712
General textured	0.182	0.165	0.835	0.818
Twinned	0.211	0.199	0.801	0.789

The percolation thresholds discussed above are for a connected path (1-D chain) of boundaries to develop across the lattice. However, for many material properties, a more important feature may be a 2-D *surface* of general boundaries that spans the 3-D microstructure, being more closely related to, e.g., crack propagation [122]. In the case of grain boundary networks, the percolation threshold for 2-D surfaces is complementarily related to the threshold for percolation along 1-D chains. When there is a 1-D percolating cluster of special boundaries (in all three principal directions), there cannot be any sample-spanning surfaces of general boundaries. This concept is illustrated in Figure 5.1, where a percolating path of special boundaries is seen to disrupt a surface on which all other boundaries are general. The existence of a 1-D percolating chain necessarily rules out the existence of a 2-D percolating surface in any lattice, provided that all grain boundary junctions are three-fold coordinated. This is because the propagation of a 1-D chain past a triple junction requires two of three boundaries to be special. At the point where the chain intersects the surface, at least one of these two special boundaries will be part of the surface cluster, which must necessarily be punctured by the chain. Therefore,

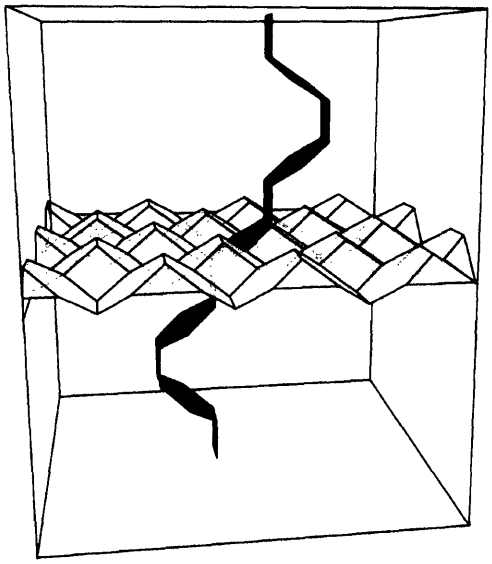

Figure 5.1: The complementary relationship between a percolating 1-D chain of special boundaries (darker shading) and a 2-D surface of general boundaries (lighter shading). The presence of the percolating chain of special boundaries removes the possibility of a sample-spanning surface of general boundaries, as at least one boundary on the surface of general boundaries must be part of the percolating cluster of special boundaries.

$p_{c,special}$ can also be viewed as the upper-bound threshold above which no such surfaces can exist. Table 5.2 contains both the percolation thresholds for 1-D chains and 2-D surfaces for each type of boundary. Of course, in practice, the presence of one small "hole" in an otherwise contiguous 2-D cluster may not physically impact properties like cracking resistance. Nonetheless, the approximate thresholds given in Table 5.2 are good as general guidelines, and illustrate the importance of crystallography in shifting the percolation threshold.

5.2. Scaling Laws for Grain Boundary Networks in the Thermodynamic Limit

In order to predict the structure of the network at or near p_c, the scaling behavior of the system must be determined. Here, we consider the scaling behavior of four network properties, each of which is a function of either the mass of a grain boundary cluster or the system's proximity to the percolation threshold $(|p - p_c|)$. The four properties explored are the average radius of gyration of grain boundary clusters, R_s, the number of clusters of a given mass per lattice site, n_s, the connectivity length, ξ, and the strength of the "infinite" or lattice-spanning cluster, P. These properties are relevant to the structure-property linkage in grain boundary engineered materials, and experimental tools to extract these properties from electron backscattered diffraction data are already available [50]. At or near the percolation threshold, each of these properties exhibits a characteristic power-law dependence on s or $|p - p_c|$:

$$R_s = C_R s^{1/D} \qquad (\text{at } p = p_c) \tag{5.1}$$

$$n_s = C_n s^{-\tau} \qquad (\text{at } p = p_c) \tag{5.2}$$

$$\xi = C_\xi |p - p_c|^{-\nu} \tag{5.3}$$

$$P = C_P |p - p_c|^{\beta} \tag{5.4}$$

Here, the coefficients C_x are amplitude prefactors that can vary with, e.g., texture, and may give some physical insight on differences between microstructure types. The scaling exponents D, τ, ν, and β are constants, and for a standard percolation problem depend only on the dimensionality of the lattice, regardless of the lattice shape; the scaling exponents for 2-D and 3-D lattices are given in Table 5.3 from Ref. [69]. In some correlated percolation problems with long-range correlations, the scaling exponents are changed [123-125], and such systems are said to be in a

Table 5.3: Scaling exponents for standard percolation theory in 2-D and 3-D lattices from Ref. [69]. The values given as fractions of integers are assumed exact, while the others are numerical estimates.

Exponent	2-D	3-D
$D\ (p = p_c)$	91/48	2.53
$\tau\ (p = p_c)$	187/91	2.18
ν	4/3	0.88
β	5/36	0.41

different *universality class* than standard percolation problems. However, provided the correlations act only over a short range, the scaling exponents remain unchanged, even though the percolation thresholds may differ from those of standard percolation theory [65, 126-129]. As described in Chapters 3 and 4, grain boundary networks are known to exhibit correlations at the local level, and their percolation thresholds are in fact shifted from those of a random network. However, it is not expected that the correlations exist over a particularly long range [130], so in principle, we expect that the scaling exponents for grain boundary networks should be the same as those given in Table 5.3 for standard percolation problems. In this section, we confirm this expectation and identify the numerical values of the amplitude prefactors for these scaling laws. To begin, we verify that grain boundary networks are in the same universality class as random percolation problems in the thermodynamic limit through a study of the scaling laws, Eqs. (5.1) to (5.4). Although subsequent sections will consider the properties of 3-D as well as irregular 2-D grain boundary networks, for the purposes of this section we will consider only two-dimensional honeycomb networks.

In standard percolation theory, where boundaries are randomly assigned character, the networks of special and general boundaries have identical behavior around their percolation thresholds. However, in crystallographically consistent grain boundary networks, this symmetry is broken as special and general boundaries are not interchangeable (Tables 5.1 and 5.2). Therefore, the behavior of special and general boundary clusters in crystallographically consistent networks must be considered separately. Accordingly, we discuss three different cases in what follows: (i) special boundary clusters in randomly assembled networks, (ii) special boundary clusters in fiber textured polycrystals, and (iii) general boundary clusters in fiber

textured polycrystals. These three cases will hereafter be referred to as random networks, special boundary networks, and general boundary networks, respectively. In the remainder of this chapter, we choose to study the scaling behavior of fiber textured polycrystals only; this system has been shown to have the most nonrandom TJD and percolation thresholds which deviate the most from the random value. Therefore, we expect that this represents a limiting case in determining whether grain boundary networks are in the same universality class as standard percolation theory. Following the convention established for Table 5.1, p_c refers to the population of the relevant type of boundary (i.e., special boundaries in random and special boundary networks, and general boundaries in general boundary networks). Similarly, the fraction of boundaries p simply refers to the global fraction of the relevant type of boundaries.

In Figure 5.2, the average radius of gyration is plotted as a function of s at p_c for all three types of networks. The different data sets are offset from one another by a factor of ten in R_s for clarity of presentation, and the solid lines represent the best fit according to Eq. (5.1). In Figure 5.2, we see that the crystallographically consistent networks are well described by the same scaling exponent as in standard percolation theory, although closer inspection reveals that each type of network has a different amplitude; from the best fit, the values of C_R were determined and are presented in Table 5.4. For general boundary networks, C_R = 1.0, while in random networks, C_R is found to be 0.94; this indicates that clusters of the same mass will have a larger spatial extent in general boundary networks than in random networks. This can be observed qualitatively in Figure 3.1g, where general boundary clusters are more elongated than random boundary clusters (Figure 3.1a). In contrast, C_R = 0.87 for special boundary networks; these clusters have more compact structures in Figure 3.1h as compared to random boundary clusters (Figure 3.1b).

The cluster mass distribution at p_c is also a function of cluster mass, as shown in Figure 5.3, where n_s is plotted as a function of s for random networks, general boundary networks and special boundary networks. The different data sets are again offset from one another by a factor of ten, and the lines represent the best fit according to Eq. (5.2). In this case, the scaling exponents are again the same, and the fitted amplitude prefactors for all three types of networks are also almost identical (Table 5.4).

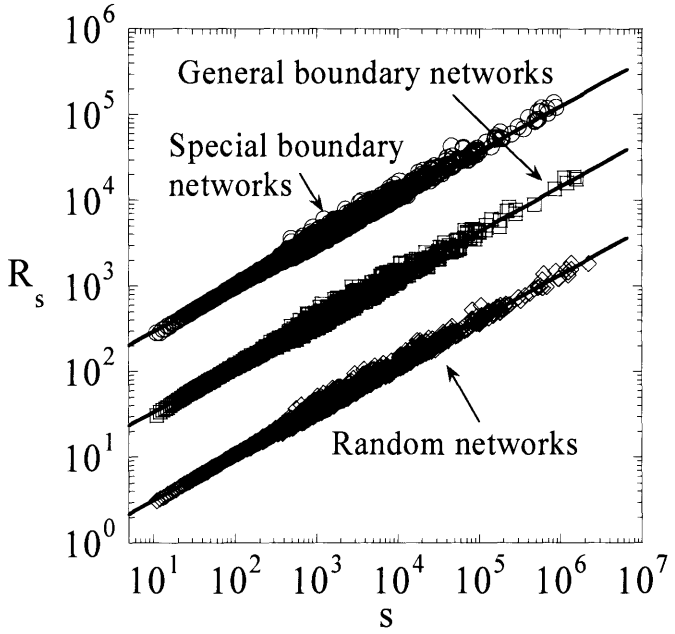

Figure 5.2: The average radius of gyration, R_s, as a function of cluster mass for simulated honeycomb lattices at the percolation threshold; for random networks $p = 0.653$ (diamonds), for general boundary networks $p = 0.601$ (squares, offset in R_s by a factor of 10), and for special boundary networks $p = 0.689$ (circles, offset in R_s by a factor of 100). The lines represent the best fit of Eq. (5.1).

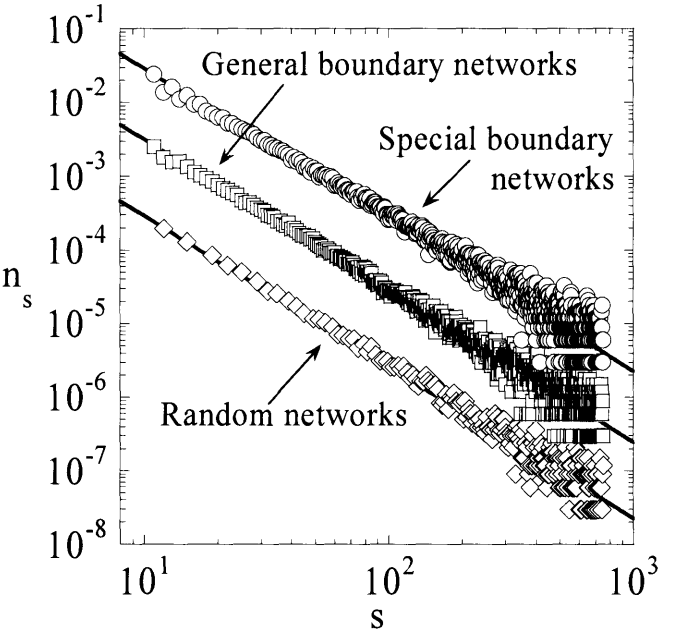

Figure 5.3: The cluster mass distribution at the percolation threshold for random networks at $p = 0.653$ (diamonds), general boundary networks at $p = 0.601$ (squares, offset in n_s by a factor of 10), and special boundary networks at $p = 0.689$ (circles, offset in n_s by a factor of 100). The results were obtained from simulations on 2-D honeycomb lattices. The lines represent the best fit of Eq. (5.2).

The connectivity length (Eq. (5.3)) depends on both n_s and R_s and is defined both above and below the percolation threshold, as long as the lattice-spanning cluster is not included in the summation above p_c. In Figures 5.4a and 5.4b, the connectivity length on both sides of the percolation threshold is shown as a function of $|p - p_c|$ for all three networks, where the different data sets are offset by a factor of ten in ξ. As before, the amplitudes, C_ξ^- below the percolation threshold and C_ξ^+ above it, are found by fitting Eq. (5.3) to the data in Figure 5.4, and the results are compiled in Table 5.4. On either side of the percolation threshold, C_ξ for special boundary networks is higher than it is for random networks. Physically, this means any network of special boundaries will have a larger size in crystallographically constrained networks than standard percolation theory would have predicted.

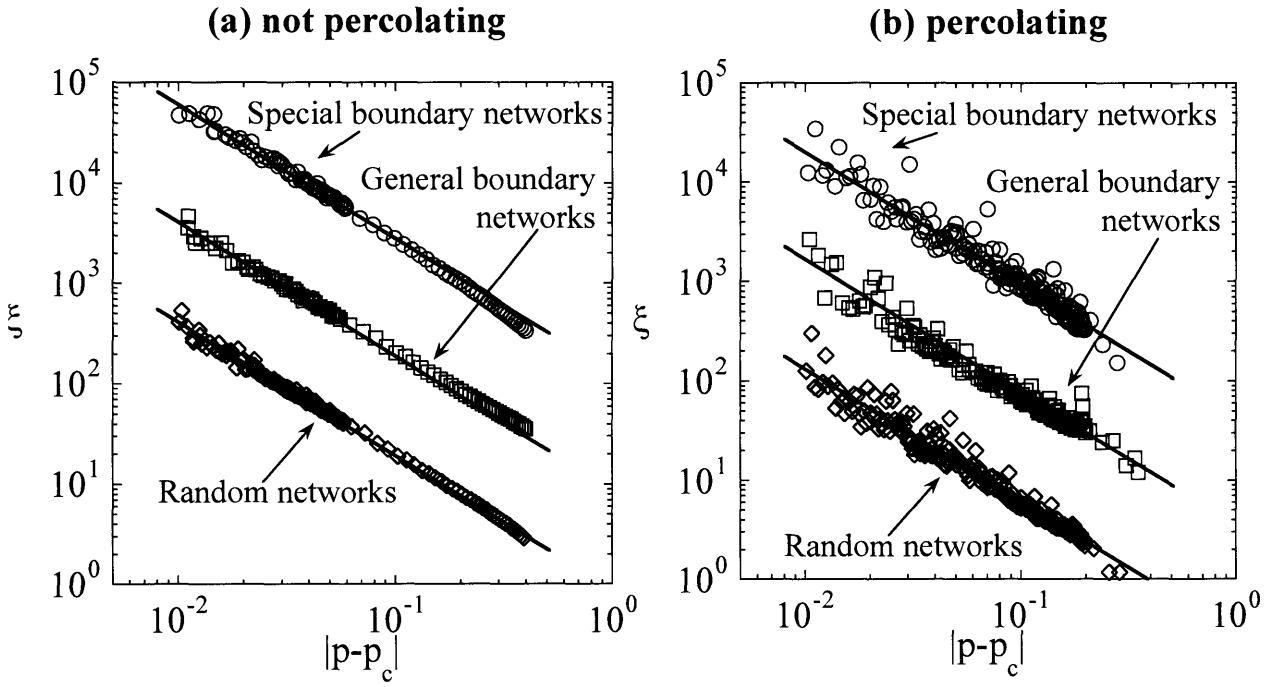

Figure 5.4: The connectivity length ξ as a function of $|p - p_c|$ both below (a) and above (b) the critical point (given in Table 5.1) for random networks (diamonds), general boundary networks (squares, offset in ξ by a factor of 10), and special boundary networks (circles, offset in ξ by a factor of 100). Above the percolation threshold, the contribution of the lattice-spanning cluster is not included in the determination of ξ. These simulations used 2-D honeycomb lattices, and the lines represent the best fit of Eq. (5.3).

Finally, the strength of the lattice-spanning cluster is plotted as a function of $|p - p_c|$ in Figure 5.5, where the data sets are offset from one another by a factor of three in P. The lines represent the best fit according to Eq. (5.4), and in this case, the values of C_P tabulated in Table 5.4 are very close, regardless of network type. In the case of crystallographically consistent networks, there is more scatter of the simulation data at low values of $|p - p_c|$; this is primarily due to uncertainty in the value of p_c for these cases, as compared to the case of a random network for which p_c is known exactly analytically.

Through the consideration of four main lattice properties (Eqs. (5.1) to (5.4)), we have verified that crystallographically consistent 2-D grain boundary networks obey the same scaling laws as standard percolation theory. By extension, we conclude that the correlations in grain boundary networks act only over finite length scales, since these systems are in the same universality class as standard percolation theory. This implies that for reasonably large microstructures, only p must be known and the relationships of standard percolation theory may be applied to determine lattice properties using Eqs. (5.1) to (5.4) as well as the other derivative

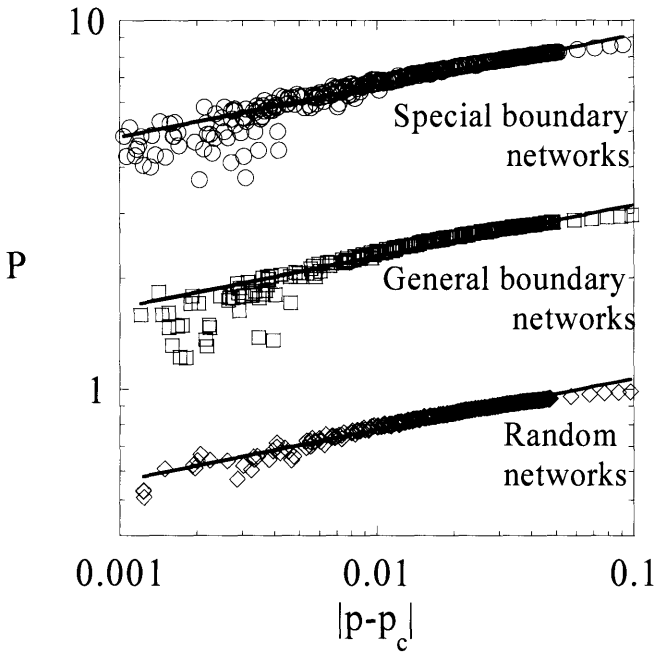

Figure 5.5: The dependence of the strength of the "infinite" or lattice-spanning cluster, P, as a function of $|p - p_c|$. The values of p_c are given in Table 5.1. The diamonds represent random networks, the squares general boundary networks (offset in P by a factor of 3), and the circles special boundary networks (offset in P by a factor of 9). The results were obtained from simulations on 2-D honeycomb lattices. The lines represent the best fit of Eq. (5.4).

Table 5.4: The amplitude prefactors, C_x, for the scaling laws which describe the average radius of gyration (C_R, Eq. (5.1)), cluster mass distribution (C_n, Eq. (5.2)), connectivity length (C_ξ, Eq. (5.3)), and strength of the lattice-spanning cluster (C_P, Eq. (5.4)) for 2-D fiber textured microstructures. The values of C_x were found by fitting the data in Figures 5.2 – 5.5 to the scaling laws described in Eqs. (5.1) to (5.4).

Property	Random networks	General boundary networks	Special boundary networks
C_R (at p_c)	0.94	1.0	0.87
C_n (at p_c)	3.3×10^{-2}	3.6×10^{-2}	3.3×10^{-2}
C_ξ^-	0.89	0.88	1.29
C_ξ^+	0.28	0.36	0.43
C_P	1.47	1.45	1.40

scaling relationships for percolation problems [69]; it is possible to infer the entire structure of a grain boundary network, including the cluster mass distribution and connectivity length, without recourse to a complex experimental analysis. However, a note of caution is required in this regard. Although the scaling exponents in grain boundary networks are the same as those in random networks, the amplitude prefactors may be expected to shift from system to system. In general, a shift in the percolation threshold is expected to herald a shift in the amplitudes C_x, and p_c is known to be dependent on the lattice geometry [69], definition of special boundaries [62, 116, 130], and the type of texture in the microstructure [116, 130].

We have looked at a very specific example, i.e., an ideal, 2-D honeycomb lattice with idealized textures ranging from fiber to cube, and where special vs. general boundary character is based on disorientation angle alone. Because this family of microstructures is the most correlated system at the first nearest-neighbor level studied to date, we expect that it represents a limiting case for studies of physically realistic grain boundary networks. However, the main result here, namely that grain boundary networks are in the same universality class as standard percolation problems, allows an even broader conclusion to be drawn: *the scaling behavior of any grain boundary network will follow Eqs. (5.1) to (5.4), as well as other standard scaling laws of percolation theory [69], with the power-law exponents in Table 5.3.* Due to the principle of universality, this assertion holds for irregular lattices (for any distribution of grain sizes and shapes), for any possible crystallographic texture, and even for any arbitrary crystallographic definition of what constitutes a special boundary. Future developments with regard to the grain

boundary structure-property relationship in the full five-parameter space [12, 13] may refine the definition of boundary "specialness", but the scaling behaviors of the grain boundary networks are invariant to such refinements. Furthermore, although our results in this section are for 2-D lattices, the scaling exponents for 3-D percolation problems are also tabulated [69], and will apply to any grain boundary network in 3-D. Although percolation thresholds may vary from one type of microstructure to the next, the scaling laws are indeed universal.

5.3. Medium-Range Effects of Crystallography

In the previous section, we showed that large (infinite) grain boundary networks obey the scaling laws of standard percolation theory. However, we expect that these laws must fail at the nearest-neighbor level, where the nonrandom correlations of crystallography alter the character of the TJD and QND (c.f., Figure 3.2 and 4.2). For example, the cluster mass distribution (Figure 5.3) is a function of s, and it must be affected by local correlations as s decreases to the nearest-neighbor level. This is explored in Figure 5.6, where the cluster mass distribution is plotted for random and special boundary networks; these are the same data from Figure 5.3, but we now focus on small values of s approaching the nearest-neighbor level. We see in Figure 5.6 that in this limit, the number of clusters with a given mass no longer decreases monotonically in

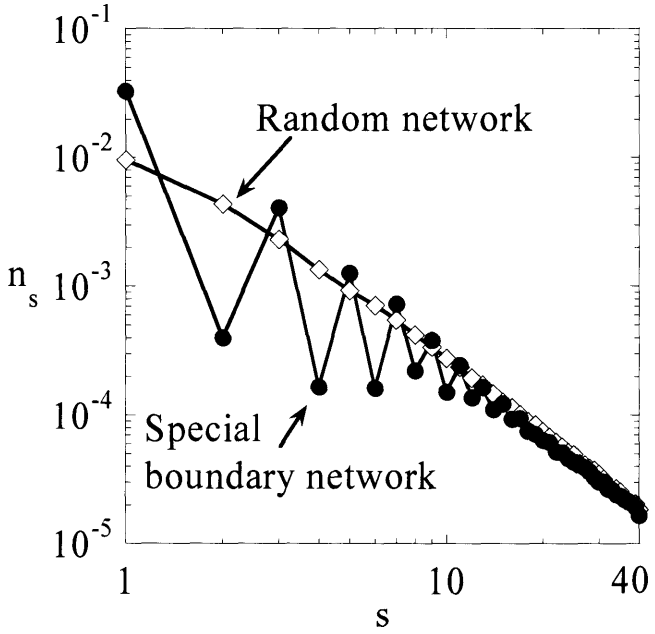

Figure 5.6: For 2-D honeycomb networks, the cluster mass distribution at the percolation threshold is plotted for small values of s in random networks at $p = 0.653$ (open diamonds) and special boundary networks at $p = 0.689$ (filled circles).

special boundary networks as predicted by Eq. (5.2). Instead, small clusters with even values of s are up to 10 times less prevalent than expected, leading to an oscillatory cluster mass distribution. This breakdown of scaling behavior at small cluster masses is significant because real microstructural systems cannot always be approximated as infinite; as the system size is reduced, the local-level crystallographic correlations will have a larger relative influence on the structure-property relationships. Obvious scenarios where such local effects may dominate include microscale systems, or the process zone around an advancing crack tip. For these reasons, it is of interest to consider how grain boundary networks behave on a smaller scale (e.g., below fifty grain diameters); it is the purpose of this section to explore correlations in grain boundary networks at medium-range through a study of grain boundary cluster structure.

In order to appreciate how local correlations influence the frequency and geometry of clusters with low mass, it will be useful to develop a taxonomy for grain boundary clusters (Figure 5.7). To begin, a cluster is first identified by its mass; the left column of Figure 5.7 shows sample clusters with s = 8, 9, 10 and 11 that are formed on honeycomb lattices. Clusters with a given mass may assume different topological configurations which are called *animals*. Animals are labeled here *a-b-c*, where a is the number of J_1 triple junctions, b the number of J_2 triple junctions, and c the number of J_3 triple junctions that comprise the animal. To clarify this labeling scheme, several different example animals with s = 9 are shown in the middle column of Figure 5.7. These animals have different topologies and are labeled as 5-2-3, 4-4-2, and 1-7-1, based on the triple junctions in the animal. Finally, for any given animal, several different *conformations*, i.e., animals of the same topology but with different spatial configurations, are possible. An example of a few of the conformations with decreasing radius of gyration of the 2-8-0 (s = 9) animal are shown in the right column of Figure 5.7; 645 more conformations of this animal are also possible on a honeycomb lattice and are not shown.

The most noticeable effects of crystallographic constraint on grain boundary clusters are evident when considering the distribution of animals of the same mass. Such a distribution is given by the fraction of animals, Γ, with each possible topology *a-b-c* for a given mass. For example, in a regular honeycomb lattice, there are eight topologically unique animals with s = 9, and Figures 5.8a and 5.8b show the animal distributions for special boundary networks (Γ_{SB}) and for random networks (Γ_R), respectively, at p = 0.55. In the random network case, the animal

distribution is dominated by configurational entropy considerations; those animals with more possible configurations are present more often in the microstructure. In the case of special boundary networks, the crystallographic constraints compete with entropy and significantly shift the animal distribution. In Figure 5.8c, the value Γ_{SB} is normalized by Γ_R to illustrate the relative abundance of each animal directly induced by crystallographic constraint. As the figure shows,

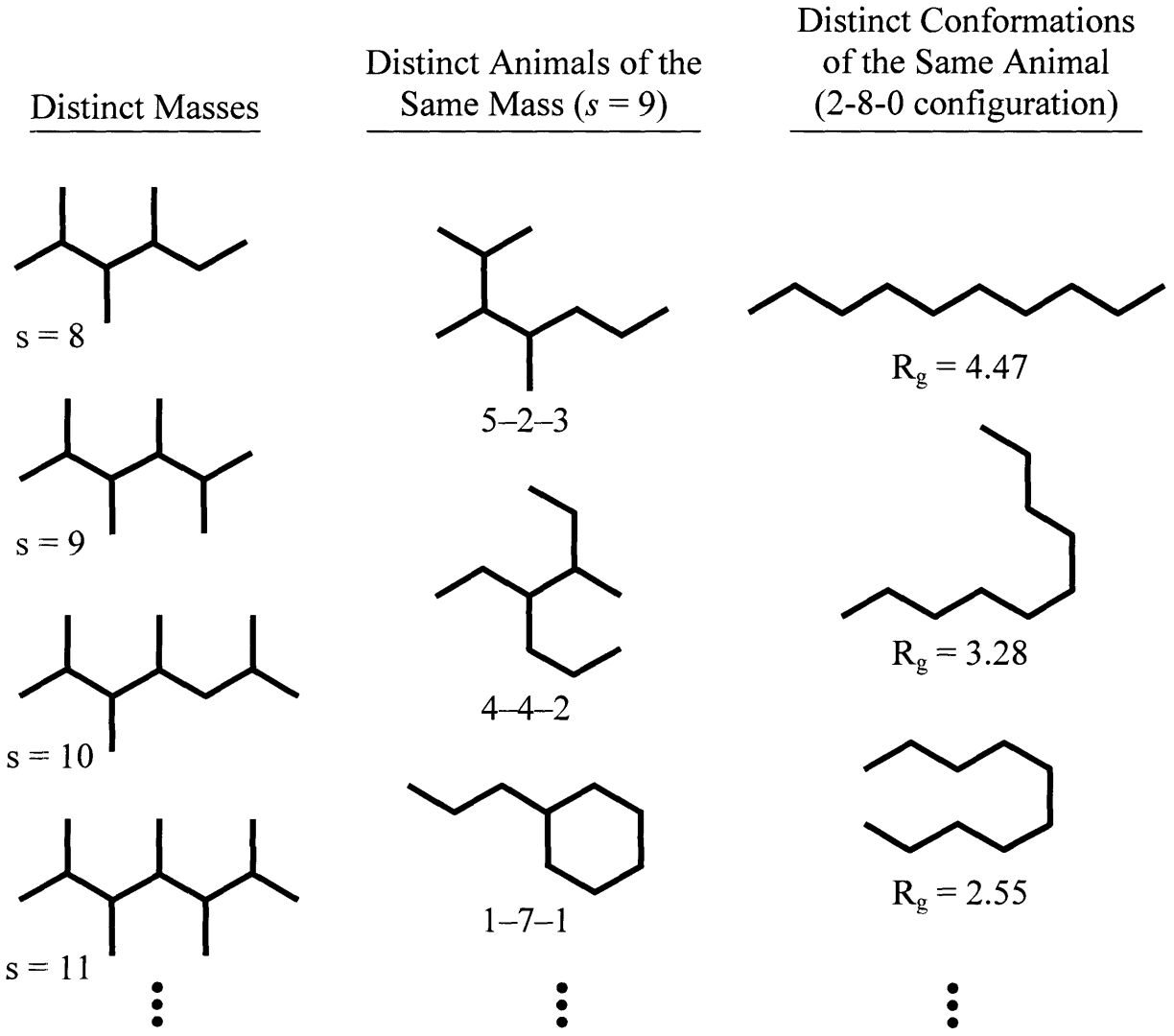

Figure 5.7: Taxonomy of grain boundary clusters. The left column illustrates clusters with different masses. In the middle column, some topologically unique animals with $s = 9$ are shown. The animals are labeled *a-b-c*, where *a* is the number of J_1, *b* the number of J_2 and *c* the number of J_3 junctions in the animal. The right column shows some of the conformations available to the $s = 9$, 2-8-0 animal, each of which has a different radius of gyration.

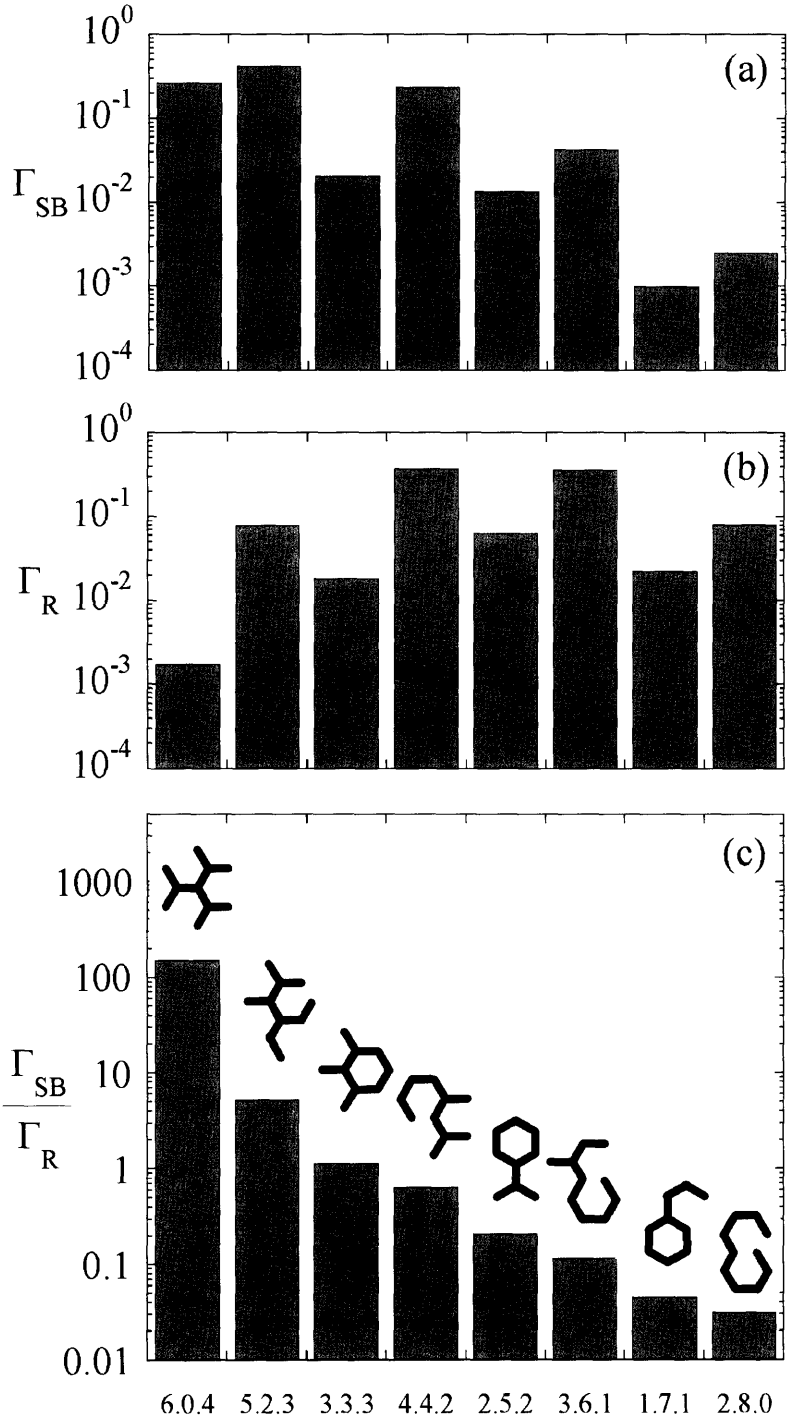

Figure 5.8: The fraction of animals of mass $s = 9$ with each possible topology in (a) special boundary networks (Γ_{SB}) and (b) random networks (Γ_R). In (c), Γ_{SB} is normalized by Γ_R for the 8 topologically unique animals with $s = 9$ on a honeycomb lattice. A representative conformation is also shown for each animal in (c). These simulations were performed at $p = 0.55$.

6-0-4 animals are more than 100 times more likely to occur in special boundary networks, while 2-8-0 animals are nearly 100 times less prevalent. In other words, we see that compact, branched animals are preferred by four orders of magnitude as compared to elongated structures. This result can be understood on the basis of crystallographic constraints at the triple-junction level. As seen earlier in the triple junction distribution (Figure 3.4), the population of J_2 junctions is suppressed in fiber textured polycrystals, while J_1 and J_3 junctions are more abundant. Therefore, animals with fewer J_2 triple junctions should be preferred to those with many J_2 triple junctions, and close inspection of Figure 5.8c show that this is indeed the case; in the figure, the data are sorted according to the number of J_2 junctions required to construct the animal.

The above example for $s = 9$ clusters illustrates how short-range correlations lead to preferred cluster structure at medium-range in grain boundary networks. However, we expect that this trend, i.e., the predominance of animals with fewer J_2 junctions, will persist for all values of s, even to very large structures. Figure 5.9 shows the animal distribution for random and special boundary networks for several different cluster masses less than 200 at $p = 0.55$. In this plot, the animals are distinguished from one another solely on the basis of the number of J_2 junctions required to construct them. As expected, at each mass, special boundary networks favor animals with fewer J_2 junctions than do random networks. In fact, when the cluster mass exceeds ~100, the animal distributions of the two different networks do not even overlap; crystallographic constraints alter the character of grain boundary cluster structures to the point that no large grain boundary cluster will resemble any of those observed in random networks. This preference for cluster structures with fewer J_2 junctions can be observed in Figures 3.1h and j, where the special boundary clusters avoid forming elongated shapes. Although the scaling laws are obeyed at large s, this important topological difference persists at all length scales; this is the reason that the amplitudes, C_x, and the percolation threshold, p_c, shift in crystallographically consistent networks.

Just as the nonrandom triple junction correlations can explain why one cluster topology is preferred to another, the same explanation may be applied to understand the nonlinear behavior of n_s at small s as shown in Figure 5.6. In special boundary networks, clusters with even masses occur up to 10 times less frequently than in randomly assembled lattices (Figure 5.6), leading to a fluctuating mass distribution that violates the expected scaling law. These fluctuations may be understood by considering possible configurations of clusters with even and odd masses. On a

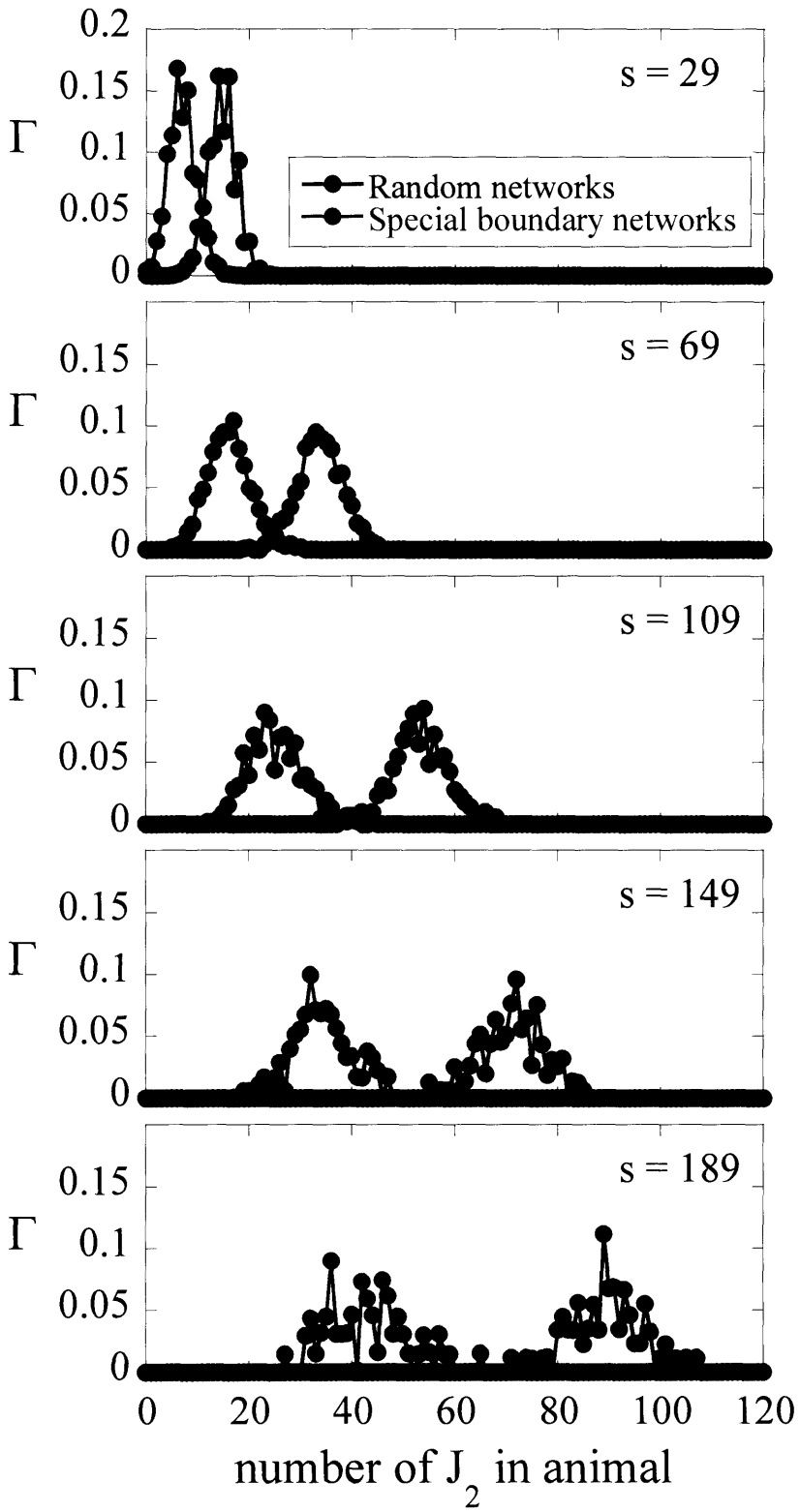

Figure 5.9: The animal distribution, Γ, as a function of the number of J_2 junctions needed to construct the animal in random networks (black points) and special boundary networks (gray points) for clusters with s = 29, 69, 109, 149, and 189. These simulations were performed at p = 0.55.

honeycomb lattice, small clusters with even values of s necessarily include at least one J_2 triple junction, while those with odd mass may be composed entirely of J_1 and J_3 triple junctions. As was the case with the lattice animals, cluster masses which minimize the overall number of J_2 junctions are preferred. For example, in the case of $s = 9$, we saw in Figure 5.9c that a compact animal composed entirely of J_1 and J_3 junctions was preferred. To construct a cluster of mass s = 8 or 10, one boundary from this animal would be removed or added, respectively, necessarily creating a J_2 junction. Therefore, this behavior is not an artifact of the honeycomb lattice, but results from the crystallographic correlations at triple junctions. Similar energetic considerations lead to clusters with "magic numbers" in a variety of other physical problems as well [131, 132]. For example, in "annealed percolation" problems, the population of small clusters is reduced and compact islands with even s are found to be more stable than those with odd s [133].

Because local correlations lead to substantial fluctuations around the expected scaling behavior in n_s, other properties that depend on s may also be expected to exhibit such behavior. For example, the average radius of gyration, R_s also exhibits oscillatory step-like behavior for clusters with mass less than 20 as shown in Figure 5.10. This behavior is an indirect

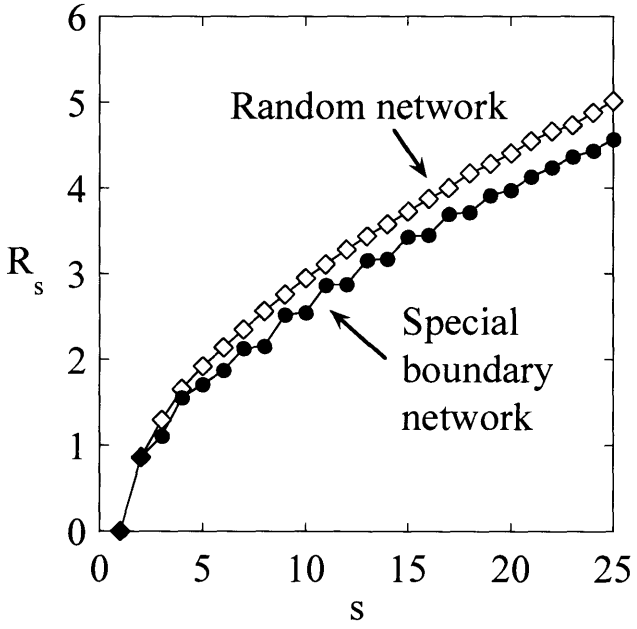

Figure 5.10: For 2-D honeycomb networks, average radius of gyration, R_s, is plotted for small values of s in random networks at $p = 0.653$ (open diamonds) and special boundary networks at $p = 0.689$ (filled circles).

consequence of the preferred animal topology described above: animals with more J_2 junctions have larger radii of gyration when averaged over all conformations because J_2 junctions promote elongated cluster shapes.

The above discussion has focused on special grain boundary networks, but the local correlations in crystallographically-consistent systems also influence the clustering of general grain boundaries. In Figure 5.11, the general boundary cluster mass distribution is plotted for small values of s for 2-D honeycomb networks assembled both randomly and with crystallographic consistency, in either case at the critical point. In the crystallographically constrained case, we again see a failure of the expected scaling law for small values of s. In this case, we see that clusters with mass of 6 are more prolific than clusters with masses of 3, 4 or 5. Detailed examination of general grain boundary networks as in Figure 3.1g reveals an abundance of hexagonal structures as illustrated in Figure 5.11. Physically, this represents a single grain whose orientation differs drastically from those of its neighbors. There are similar local maxima in n_s for general boundary networks at s = 10 and 14, for complete loops around two or three adjacent grains, respectively, as illustrated in Figure 5.11. As was the case for special boundary

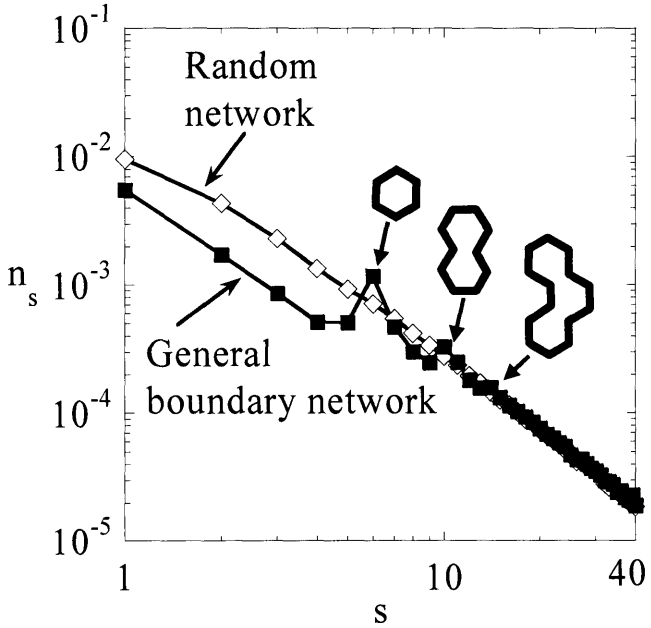

Figure 5.11: For 2-D honeycomb networks, the cluster mass distribution is plotted for small values of s in random networks at p = 0.653 (open diamonds) and general boundary networks at p = 0.601 (filled squares).

clusters (Figure 5.6), the magic cluster structures seen in Figure 5.11 become less statistically relevant at large s. Although ring structures certainly continue to be preferred at larger s, the number of animals increases greatly with increasing cluster mass, and local maxima associated with complete grain loops become less noticeable. However, unlike the case of special boundary networks, the magic numbers in Figure 5.11 are very dependent on the shape of the lattice. This will be explored in more detail in the next section.

5.4. Effects of Lattice Topology and Dimensionality

In the foregoing sections, we have focused our discussion on the properties of 2-D honeycomb networks. As described earlier, the scaling behavior of larger networks is not a function of lattice topology, so there is no need to evaluate the scaling exponents for other lattices. Furthermore, our observations about magic cluster numbers and preferred animal types have been shown to result from crystallographic constraint, which is also present independently of lattice shape. However, the details of preferred cluster structure can certainly vary with lattice shape and/or dimensionality, and we briefly explore this issue in what follows.

To begin, we will return to the example studied earlier, the distribution of animals with $s = 9$, and explore microstructures in which grains have an arbitrary number of sides (c.f., Figures 3.1i and j). In Figure 5.12, we plot the animal distribution using the number of J_2 junctions to differentiate animals at $p = 0.55$. In this plot, we follow the form of Figure 5.8c, in which the animal frequency for special boundary clusters, Γ_{SB}, is normalized by that seen in a random network, Γ_R. The solid points in Figure 5.12 are the same results presented earlier for the ideal honeycomb lattice, while the open points are data for an irregular lattice in which only 25% of the grains had six sides. Once the lattice geometry is relaxed, the number of topologically unique animals with $s = 9$ increases from 8 to over 250. Accordingly, the number of J_2 junctions in the animal does not uniquely distinguish it from many other distinct animals, and there are many data points in each column of Figure 5.12. It is clear from Figure 5.12 that even though the irregular lattice geometry severely complicates the study of lattice animals, there is still a clear preference for animals with fewer J_2 junctions. This result can be compared to the special boundary network in Figure 3.1j, which, like Figure 3.1h, lacks elongated clusters.

This preferred cluster structure also carries over to the cluster mass distribution which, as in the regular lattices, deviates from the expected scaling behavior for small values of s (Figure

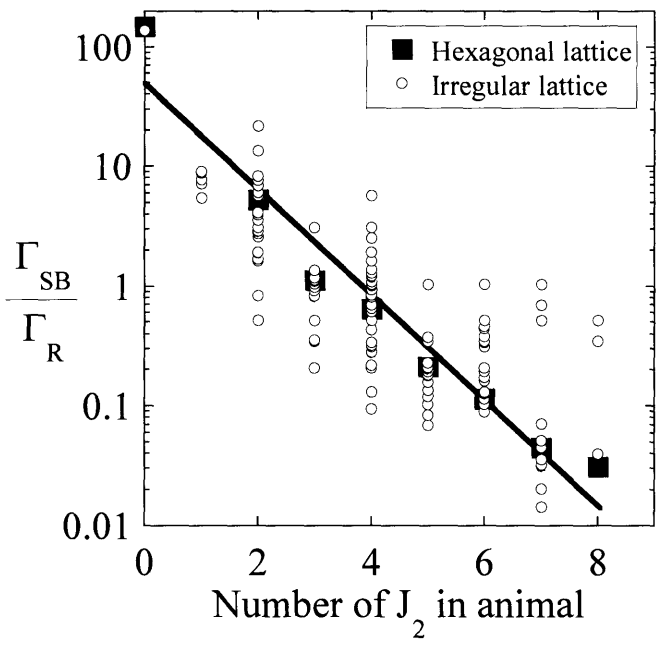

Figure 5.12: The fraction of animals, Γ_{SB}, with each possible topology in special boundary networks, normalized by the respective animal frequency in random networks, Γ_R. These simulations were done at $p = 0.55$. The filled squares are for 2-D honeycomb lattices (where only eight animals are possible), and the solid line is an exponential fit to those data. The unfilled circles are for 2-D irregular lattices in which 25% of the grains had six sides. In this case, more than 250 animals are possible.

5.13a). The oscillating trend for magic cluster masses persists in the irregular 2-D networks, even as the irregularity of the lattice increases (i.e., the distribution of the number of sides per grain broadens). However, two factors act to reduce the magnitude of the oscillatory trend in the irregular lattices. First, on an irregular lattice, the number of distinct animals for any value of s is much greater than for a honeycomb lattice, as seen in Figure 5.12 for animals with $s = 9$. Second, as the lattice geometry becomes more irregular, it is increasingly possible to create animals with even mass using only J_1 and J_3 triple junctions. For these reasons, magic cluster masses become irrelevant at a somewhat smaller value of s than in a regular honeycomb network.

In the case of general boundary clusters, while the magic cluster masses still depend on local correlations, they also depend strongly on the shape of the lattice. This can be seen in Figure 5.13b where the magic cluster mass $s = 6$ becomes less prominent as the fraction of grains with exactly six sides decreases. The preference for closed-ring clusters around individual grains

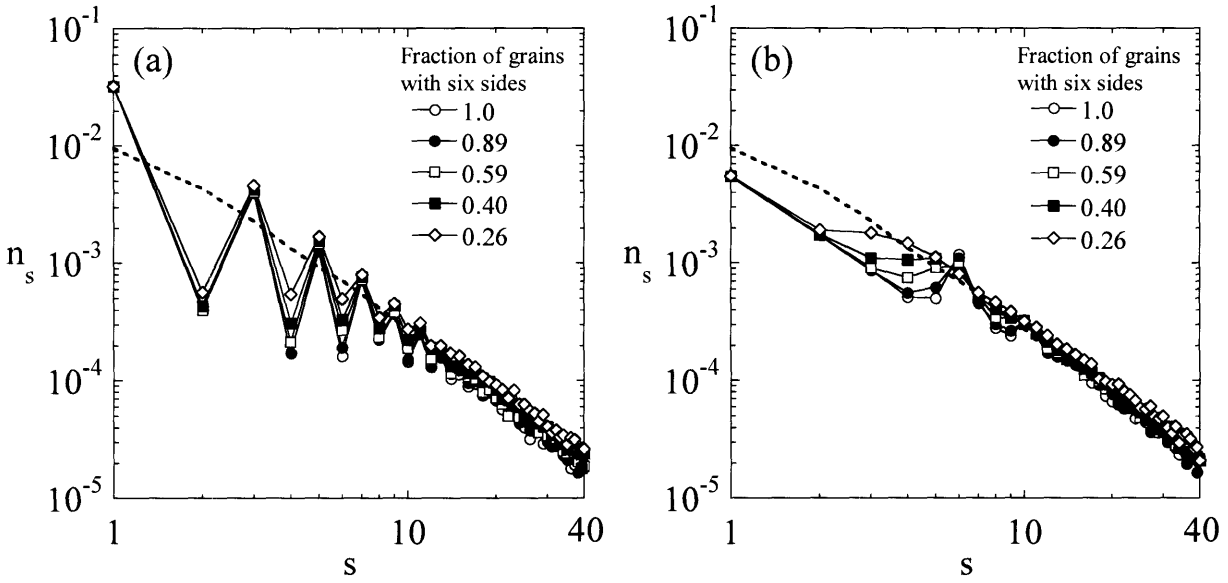

Figure 5.13: For 2-D irregular networks, the cluster mass distribution is plotted for small values of s in: (a) special boundary networks at $p = 0.689$ and (b) general boundary networks at $p = 0.601$. The different points correspond to different fractions of grains with six sides.

still exists (c.f., Figure 3.1i), but with fewer six-sided grains in the system, the peak in Figure 5.13b is spread over $s = 4, 5, 7$, etc. In this case, the medium-range preferred cluster masses are diluted, but it is important to note that at the nearest neighbor level ($s = 1, 2, 3$), crystallographic constraints always lead to deviation from the scaling law.

Finally, the analysis of low-mass clusters in crystallographically consistent networks may be extended to 3-D. In an analogous method to that used in 2-D, we define the mass of a grain boundary cluster to be equal to the number of boundaries that comprise the cluster. An alternative definition would be based on the total grain boundary area of the cluster. Although the latter definition may be more useful in calculating, e.g., the conductivity of the network [134], the definition based solely on the number of boundaries will more clearly illustrate the effects of local crystallographic constraint on cluster mass. In 3-D, we again find that preferential cluster masses exist in both special and general boundary networks (Figure 5.14). Special boundary clusters with even masses are less abundant than those with odd masses (Figure 5.14a), and all general boundary clusters with $s < 8$ are less abundant than expected in a random network (Figure 5.14b). As compared to the 2-D networks, the magic cluster trends are weaker in 3-D because even on a regular tetrakaidecahedral lattice, small values of s have a large

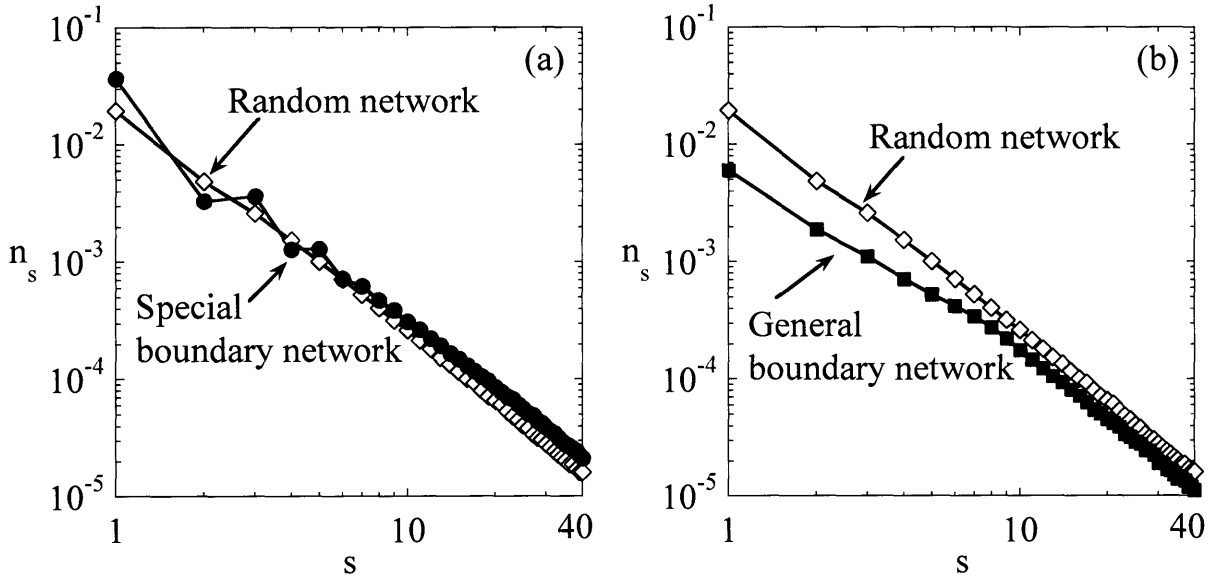

Figure 5.14: For 3-D tetrakaidecahedral networks, the cluster mass distribution is plotted for small values of s in random networks with $p = 0.220$ (unfilled diamonds in (a) and (b)), special boundary networks at $p = 0.280$ (filled circles in (a)), and general boundary networks at $p = 0.152$ (filled squares in (b)).

number of possible animals; the extra degree of freedom in 3-D relaxes the need for medium-range order in the network.

5.5. A Critical Length Scale for Grain Boundary Networks

The present analysis has shown that although grain boundary networks can be described by the same scaling exponents used in standard percolation theory at large length scales, the networks deviate significantly from the expected scaling behavior at small length scales. Separating these two regimes of behavior is a new, critical length scale below which local correlations dominate the lattice statistics, and above which a statistical description of the grain boundary network is possible in terms of the classical scaling laws. Although we believe this work to be the first to identify this new, critical microstructural length scale for polycrystals, similar situations have been observed for other percolative physical phenomena. For example, Voss *et al.* identified a cutoff length for scaling properties in gold films that exhibited preferential clustering below this cutoff length [65], and Meinke *et al.* studied the scaling behavior of fracture surfaces and found a critical length scale below which cleavage occurs [122]. Here, we will identify the critical cluster size as the value at which the cluster mass distribution begins to convincingly obey Eq. (5.2); Figure 5.13 indicates that the critical cluster

size is around $s \sim 20$, which corresponds to a critical length scale of $R_{s,cutoff} \approx 4$ units (c.f., Figures 5.2 and 5.10). This length scale corresponds to an average dimension on the order of ~3 grain diameters.

The cutoff length scale found here is in line with prior work on the length scale of correlations among grain boundary character. First, Beran *et al.* found that the misorientation distribution function (MDF) between points separated by three grain diameters differed from that expected among randomly oriented grains, but that the MDF was random when sampled across a separation of seven grain diameters [135]. Second, as discussed in the previous chapter, crystallographic constraints around triple junctions are responsible for the vast majority of the information content in 3-D grain boundary networks, and higher-order correlations are of decreasing significance [130]. These two examples further indicate that the extent of local crystallographic correlations is on the order of a few grains. It is important to note that although the critical length scale may seem inconsequential, it will be significant when the system size is small (e.g., in integrated circuit components) or for local phenomena (e.g., at the tip of a "short" crack). Only when the microstructure to be modeled is significantly larger than ~3 grains in all dimensions can the scaling exponents that describe the behavior of random networks be applied to grain boundary networks.

5.6. Concluding Remarks

We have studied the scaling behavior of crystallographically consistent grain boundary networks near their percolation thresholds by simulating both two- and three-dimensional microstructures. Although the percolation thresholds for all of the crystallographically consistent grain boundary networks were found to differ from those of standard percolation theory, in the limit of infinite length-scales, grain boundary networks were found to be in the same universality class as standard percolation theory. However, the amplitude prefactors differed from those expected for a random network. These differences arose due to local correlations in grain boundary networks. At finite length-scales, grain boundary networks exhibited preferential cluster structures, which were explained on the basis of local correlations among neighboring boundary types. The existence of preferential cluster masses was particularly evident at small cluster masses below the cutoff length of about 3 grain diameters where the scaling laws were seen to fail.

In this chapter, we have explored the size and shape of grain boundary clusters through properties such as the average radius of gyration as a function of cluster mass. However, this measure alone does not define the topological state of the network. In addition, we found that the clustering behavior of the boundaries can lead to changes in the percolation threshold. This implies that if the details of the constraint change from system to system (i.e., their TJDs are different), the percolation threshold should also shift. Therefore, the next chapter will develop a unified approach for looking at percolation problems in locally constrained systems.

Chapter 6: A Unified Approach for Locally-Correlated Percolation Problems

In the preceding chapters, we have explored grain boundary connectivity in many different families of microstructures with varying textures and using different binary classifications for the grain boundaries. In each case, the triple junction distribution deviated from that of a random assemblage of boundaries and the percolation thresholds also shifted from those of standard percolation theory. However, no two cases had identical behavior and other families of microstructures are expected to exhibit their own unique behavior. As discussed in Chapter 1, percolation is a second-order phase transition between a non-percolating phase and a percolating phase. Since the percolation threshold is a critical parameter in materials design, it would be useful to identify whether or not a microstructure is expected to have a percolating cluster of boundaries on the basis of an easily measured property such as the triple junction distribution. This approach corresponds to labeling every topologically distinct point as being in either the percolating or non-percolating phase based on its local correlations as captured by the TJD. Therefore, it is necessary to develop a unifying concept that relates the details of the correlation to the expected shift in the percolation threshold. Although the developments that follow will be discussed mainly in the context of grain boundary networks, they could be readily extended to include other correlated percolation problems.

6.1. Topological Descriptions of Locally-Correlated Systems

To begin, we present two different, but interchangeable schemes for representing the correlations in a network. The first approach uses the TJD directly to measure nearest-neighbor correlations. In contrast, the scond approach relies on the development of two topological parameters to describe the state of the network. In the direct method, we propose that the state of any 2-D microstructure is uniquely specified by its triple junction distribution, an assumption that holds as long as triple junction correlations are dominant. The four triple junction populations may then be viewed as compositional variables which occupy the vertices of what will hereafter be referred to as the "coordination tetrahedron", as illustrated in Figure 6.1a. In this space, each point represents a unique combination of J_0, J_1, J_2 and J_3. Therefore, for any family of microstructures, the evolution of the network from $p = 0$ (J_0 vertex) to $p = 1$ (J_3 vertex) can be mapped as a trajectory in this space. This is illustrated in Figure 6.1a for the families of

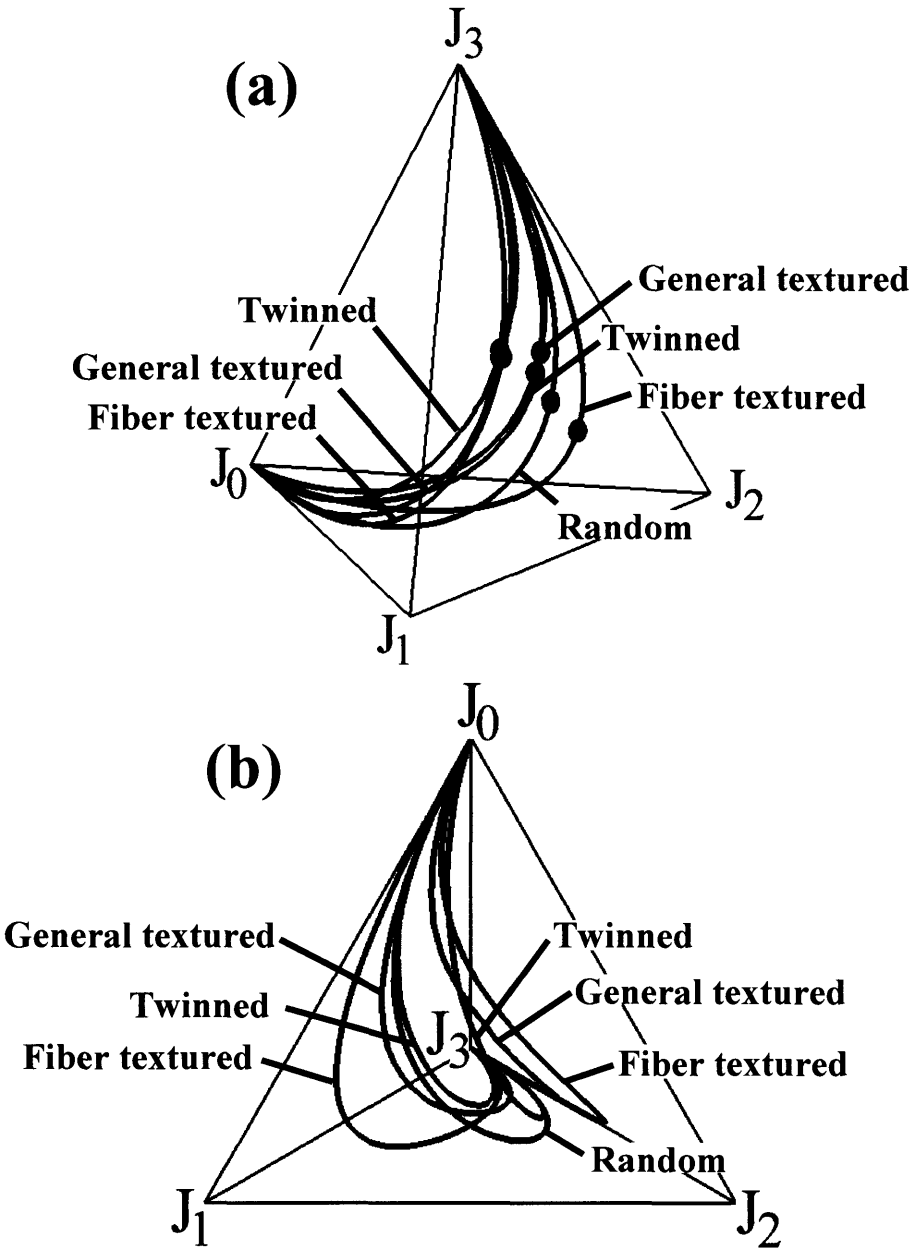

Figure 6.1: Coordination tetrahedron whose vertices are the triple junction populations (i.e., J_0, J_1, J_2 and J_3). The trajectories show the evolution of the TJD through this space for random networks (black curve), special boundary networks (green curves) or general boundary networks (red curves) from $p = 0$ (J_0 vertex) to $p = 1$ (J_3 vertex). (a) The black points represent the percolation thresholds determined in Chapter 5. (b) The relative position of the trajectories can be more easily observed in projection along the J_3 axis.

microstructures studied in this work and for a random assemblage of grain boundaries. In this figure, the trajectories for special boundary networks are shown by the green curves and the trajectories for the general boundary networks by the red curves. The evolution of the microstructures through this space can be more easily appreciated in a projection along the J_3 axis (Figure 6.1b). As compared to the random trajectory (black curve), the trajectory for special boundary networks in fiber textured microstructures more closely approaches the J_1 vertex, a direct consequence of J_1 junctions being more prolific in these microstructures (c.f., Figure 3.2). In the special boundary networks for all three microstructures, the trajectories avoid the J_2 vertex; these junctions are rarer in all special boundary networks. Qualitative differences in the trajectories for general boundary networks can be observed as well. These trajectories should also be compared to the curve labeled random since that trajectory is independent of boundary type. All of the general boundary network trajectories lie closer to the $J_0 - J_2 - J_3$ face, indicating an abundance of J_2 junctions. This was also seen in Figure 3.1 where the general boundary networks had many elongated clusters, facilitated by a large fraction of J_2 junctions (here two general boundaries and one special boundary). It is interesting to note that, although the special and general boundary networks have complementary structures, there is no obvious relationship between their trajectories in Figure 6.1. When the second description of the correlations is developed, this relationship will be more obvious. Finally, we point out that this coordination tetrahedron is not restricted to the description of grain boundary networks; any system with three-fold coordination can be defined by a point in the volume. However, it is important to note that this approach assumes that there are only nearest-neighbor correlations.

The triple junction distributions for experimentally determined microstructures can also be plotted as points in the coordination tetrahedron for comparison with the trajectories for the simulated microstructural families. In Figure 6.2a, the blue points correspond to the data for experimental microstructures in which boundaries were classified based on their disorientation angles; these are the same data as in Figures 1.4 and 3.2. The trajectories for special boundary networks in randomly assembled, fiber textured and general textured networks are shown by the black, light green and dark green curves, respectively, for comparison. It is clear from this figure that the experimental data lie far from the trajectory for a randomly assembled network and much closer to those of the crystallographically consistent simulations. In the case where boundaries are classified in the CSL framework, special boundary networks in randomly

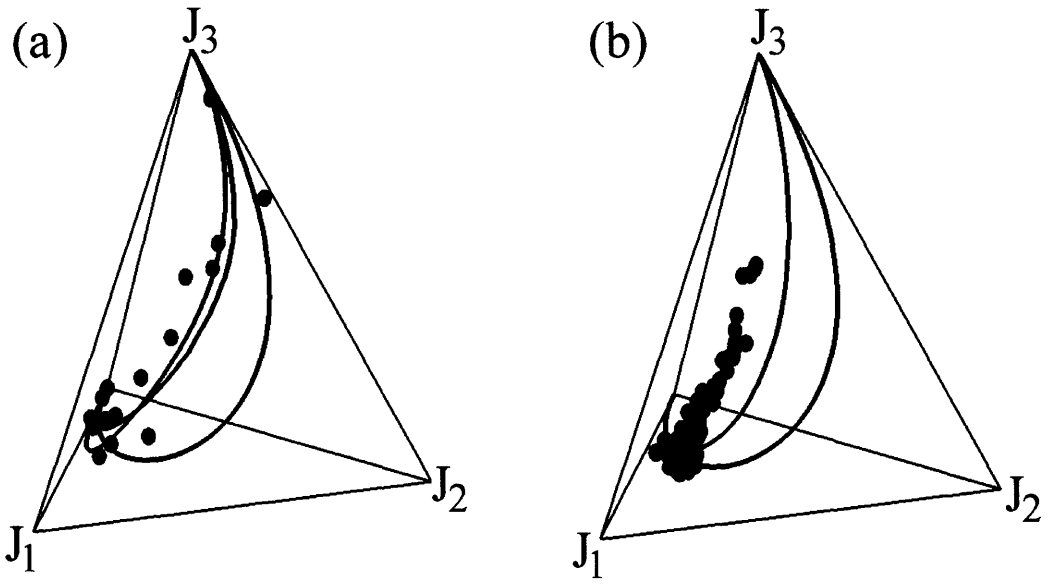

Figure 6.2: The triple junction distributions for experimental microstructures (blue points) are compared to the trajectory for a randomly assembled network (black curve) or crystallographically consistent networks (green curves). In (a), the data points are the same data as presented in Figure 1.4, while the light green and dark green curves are for fiber textured and general textured microstructures, respectively. In (b), the data points were gathered by Schuh *et al.* [91] for microstructures where the boundaries were classified as CSL vs. non-CSL and the green curve is for the twinned microstructural family.

assembled (black curve) and twinned (green curve) microstructures are compared to experimental data gathered by Schuh *et al.* [91] in Figure 6.2b. Here, the experimental data are even further from the trajectory for a randomly assembled network and agree more closely with the simulation results for the twinned microstructural family.

The coordination tetrahedron in Figure 6.1 is a useful construct as it allows the state of a network to be represented by a single point in the space when described by its triple junction distribution. However, the topological state of the network will differ greatly depending on where in the coordination tetrahedron the point lies. Therefore, an alternate approach to quantify the state of a network is through the use of two topological parameters: η_{SO}, which differentiates segregation from ordering, and η_{CE}, which differentiates the tendency for boundaries to form either clumpy or elongated clusters. These are defined as:

$$\eta_{SO} = \begin{cases} 1 - j_{SO} & \text{for} \quad j_{SO} < 1 \\ (j_{SO})^{-1} - 1 & \text{for} \quad j_{SO} > 1 \end{cases} \tag{6.1a}$$

$$\eta_{CE} = \begin{cases} 1 - j_{CE} & \text{for} \quad j_{CE} < 1 \\ (j_{CE})^{-1} - 1 & \text{for} \quad j_{CE} > 1 \end{cases} \tag{6.1b}$$

where

$$j_{SO} = \left(\frac{J_1 + J_2}{J_0 + J_3}\right)\left(\frac{R_0 + R_3}{R_1 + R_2}\right) \tag{6.2a}$$

$$j_{CE} = \frac{J_2}{J_1}\frac{R_1}{R_2} \tag{6.2b}$$

Here R_i corresponds to J_i for randomly assembled triple junctions (Eq. (1.5)). Both η_{SO} and η_{CE} exist on (-1, 1) and are exactly zero for any randomly assembled network. The meaning of each topological parameter and its relationship to the coordination tetrahedron can be appreciated by considering several example networks which illustrate the extrema of the topological parameters, as illustrated in Figures 6.3 and 6.4. For example, when the microstructure is composed entirely of J_0 and J_3 triple junctions (points along the $J_0 - J_3$ edge in Figure 6.3), general and special boundaries will tend to be surrounded by the same type of boundary, leading to a segregated structure as shown in Figure 6.3 for a network with $\eta_{SO} = 1$. In contrast, a network described by a point along the $J_1 - J_2$ edge assumes an ordered structure with $\eta_{SO} = -1$. For all other points in the volume of the coordination tetrahedron, a continuum in η_{SO} exists from -1 to 1. Given the definition for η_{SO} (Eq. (6.1a)), a surface can be determined which separates segregated ($\eta_{SO} > 0$) from ordered ($\eta_{SO} < 0$) states. In terms of the TJD, the interface between these regions is defined by:

$$-\frac{1}{3}(J_1 + 2J_2)^2 + J_2 + J_3(3 - 2J_1 - 4J_2 - 3J_3) = 0 \tag{6.3}$$

The interface between these two regions in the coordination tetrahedron is also shown in Figure 6.3. The black curve is the trajectory for randomly assembled networks and by definition, it lies entirely in the interface ($\eta_{SO} = 0$ for all p). A similar approach can be taken with respect to η_{CE}.

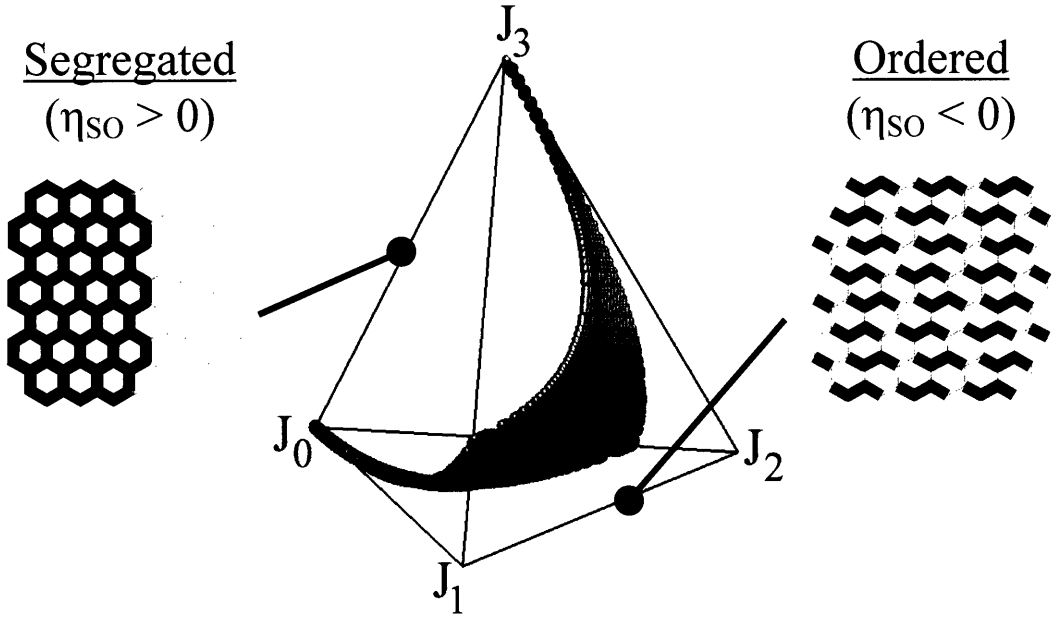

Figure 6.3: Schematic network structures corresponding to the segregated state (left, with $\eta_{SO} > 0$) along the $J_0 - J_3$ edge or ordered state (right, with $\eta_{SO} < 0$) along the $J_1 - J_2$ edge. The surface plotted in the coordination tetrahedron is for points with $\eta_{SO} = 0$ (Eq. (6.3)) and contains the trajectory for a randomly assembled network (black curve).

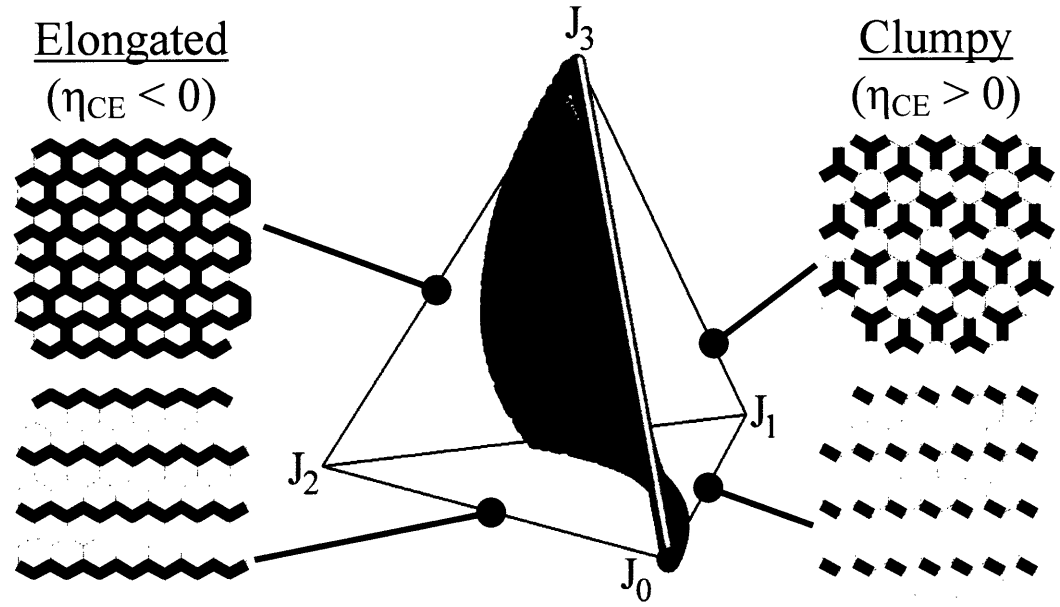

Figure 6.4: Schematic network structures corresponding to the elongated state (left, with $\eta_{CE} < 0$) along the $J_0 - J_2 - J_3$ face or clumpy state (right, with $\eta_{CE} > 0$) along the $J_0 - J_1 - J_3$ face. The surface plotted in the coordination tetrahedron is for points with $\eta_{CE} = 0$ (Eq. (6.4)) and contains the trajectory for a randomly assembled network (black curve).

As discussed in the previous chapter, the prominence of J_1 junctions, especially in points near the $J_0 - J_1 - J_3$ face, tends to promote clumpy network structures ($\eta_{CE} > 0$); two examples with $\eta_{CE} = 1$ are illustrated in Figure 6.4. In contrast, an abundance of J_2 junctions in points on the $J_0 - J_2 - J_3$ face leads to elongated structures; Figure 6.4 also shows two networks with $\eta_{CE} = -1$. As before, there exists a continuum between these two values across the coordination tetrahedron, and the interface between the clumpy and elongated states is defined by $\eta_{CE} = 0$. In terms of the TJD, the interface is defined as:

$$\frac{2J_2^2}{3} + \frac{J_1^2}{3} - J_2 + J_1J_2 + J_1J_3 + J_2J_3 = 0 \qquad (6.4)$$

This surface through the coordination tetrahedron is also shown in Figure 6.4.

As Figures 6.3 and 6.4 illustrate, changes in the signs of the topological parameters correspond to qualitative changes in the network topology. Since the two topological parameters can take on a sign independent of each other, there are four possible combinations for the signs of η_{SO} and η_{CE} which represent topologically unique states:

(i) when $\eta_{SO} > 0$ and $\eta_{CE} > 0$, the network is segregated and clumpy,

(ii) when $\eta_{SO} > 0$ and $\eta_{CE} < 0$, the network is segregated and elongated,

(iii) when $\eta_{SO} < 0$ and $\eta_{CE} > 0$, the network is ordered and clumpy,

(iv) when $\eta_{SO} < 0$ and $\eta_{CE} < 0$, the network is ordered and elongated.

These four regions are illustrated in the coordination tetrahedron in Figure 6.5. At the points where $p = 0$ (J_0 vertex) and $p = 1$ (J_3 vertex), all four states converge. This implies that for each state, there exist trajectories which lie exclusively in that state. In the ordered and clumpy state, the trajectories will necessarily approach the J_1 vertex, while in the ordered and elongated state the trajectories will approach the J_2 vertex (see Figure 6.5).

As every point in the coordination tetrahedron is defined by a value of η_{CE}, η_{SO} and p which are independent variables, all states can be plotted in a Cartesian space defined by these variables as shown in Figure 6.6. In Figure 6.6a, the vertical axis gives the value of p (i.e., the bottom plane corresponds to $p = 0$ and the top plane to $p = 1$), and the other two axes differentiate states of order from segregation and the tendency to form elongated or clumpy clusters. The evolution of the grain boundary networks from $p = 0$ to $p = 1$ can be plotted as a

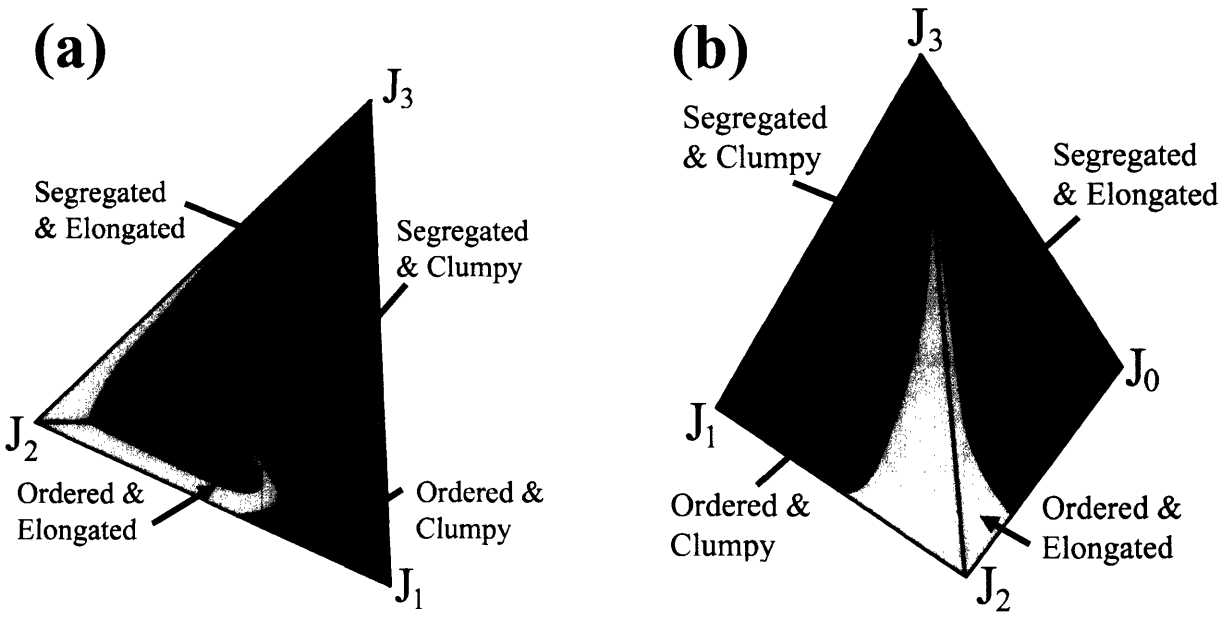

Figure 6.5: Schematic representation of the four unique topological states defined by (i) $\eta_{SO} > 0$ and $\eta_{CE} > 0$ (segregated and clumpy), (ii) $\eta_{SO} > 0$ and $\eta_{CE} < 0$ (segregated and elongated), (iii) $\eta_{SO} < 0$ and $\eta_{CE} > 0$ (ordered and clumpy), and (iv) $\eta_{SO} < 0$ and $\eta_{CE} < 0$ (ordered and elongated). At the J_0 and J_3 vertices, all four states converge.

trajectory in this space as well, as shown in Figure 6.6a. In order to more easily visualize the topological evolution of these microstructural families, we can consider the p-axis projection where each quadrant of the graph corresponds to one of the four topological states. Each trajectory is marked with a circle that indicates the position of the trajectory in the $p = 0$ plane. In Figure 6.6b, we can easily see that for all values of p, the special boundary networks (green curves) are both segregated and clumpy. For comparison, randomly assembled grain boundary networks occupy the origin for all values of p. It is interesting to note that while the special boundary networks in fiber textured microstructures have high values of η_{CE} for all values of p, they are not as segregated as the special boundary networks in general textured or twinned microstructures. The twinned microstructures have the most diverse topologies; they have both the minimum and maximum values of both η_{CE} and η_{SO}. Figure 6.6 also shows the topological parameters for general boundary networks (red curves), where the same topological parameters (Eq. (6.1)) are used to describe these networks. In contrast to Figure 6.1 where there was no obvious relationship between the trajectories for special and general boundaries, Figure 6.6 clearly illustrates the complementary nature of the two types of boundaries. While special boundary networks are always defined by $\eta_{CE} > 0$ (clumpy), general boundary networks have η_{CE}

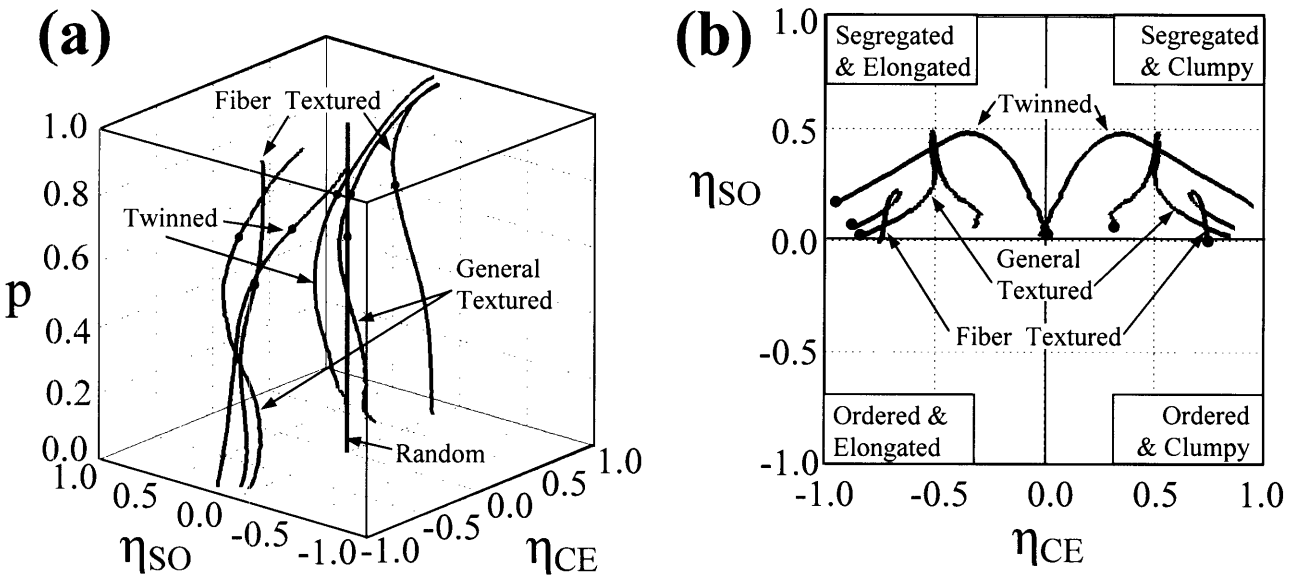

Figure 6.6: For the three microstructural models studied here, the evolution of the grain boundary networks is plotted as a function of the topological parameters (η_{CE} and η_{SO}) and p, the fraction of relevant boundaries (special boundaries for the green curves and general boundaries for the red curves). The black curve is for randomly assembled networks. (a) The black points represent the percolation thresholds determined in Chapter 5. (b) The relative position of the trajectories can be more easily observed in projection along the p-axis where each of the four quadrants represents one of the four topological states. In (b), the intial location of the trajectory in the $p = 0$ plane is indicated by a circle.

< 0 (elongated). However, because of the complementary structure of the special and general boundary networks, both have $\eta_{SO} > 0$ over all values of p.

Through the definition of the topological parameters, we are able to quantify the nonrandom spatial distributions that were observed in Figure 3.1. For example, in the crystallographically consistent networks, there is a clear tendency for like boundaries to cluster together. Earlier, this behavior was said to lead to a patchier grain boundary network; in the context of the topological parameters, this tendency toward *segregation* is now quantified. Furthermore, inspection of the general boundary networks (left column of Figure 3.1) shows that the fiber textured microstructures have the most elongated clusters which correlates with their high values of η_{CE} at $p = 0.5$. In Figures 6.1 and 6.6, we have presented two interchangeable methods for describing the correlated state of a network. Although they may seem unrelated, the axes of Figure 6.1 (i.e., the triple junction populations) were transformed using Eq. (6.1) to those

of Figure 6.6 (i.e., η_{CE}, η_{SO} and p). The reverse transformation, from the topological parameters to the TJD, is also possible and is summarized in Appendix D.

6.2. Determination of the Percolation Phase Boundary

As we discussed at the beginning of this chapter, our goal is to determine how the correlations in the network will affect the percolation threshold. We can begin to address this problem by considering the percolation thresholds along the trajectories in Figures 6.1a and 6.6a. In these figures, the black spheres represent the percolation thresholds for clusters of special boundaries (along the green trajectories) or clusters of general boundaries (along the red trajectories). Along these trajectories, points that lie above the thresholds (i.e., nearer to the J_3 vertex or the $p = 1$ plane) will be in the percolating phase, while points on the trajectories that lie below will occupy the non-percolating phase. Given that all points will be in one of the two phases, there should be a surface through the coordination tetrahedron that separates these two regions and contains the points on the known trajectories. Determination of this surface can be quite complex as there are points in the coordination tetrahedron (i.e., triple junction distributions) that do not correspond directly to a microstructural texture, making them inaccessible with the current approach of assigning grain orientations. However, these inaccessible points may well describe other physical systems of interest with three-fold coordination and nearest-neighbor correlations and therefore are valuable to consider. As this section will explain, we have developed a method to probe the space of triple junction distributions and have found the surface which separates the two phases.

In order to explore the space of $J_0 - J_1 - J_2 - J_3$ points, we return to the assumption that a network is fully specified by its TJD. For example, to build a network which resembles a fiber textured microstructure at $p = 0.5$, we can either assign grain orientations as described in Chapter 2 or assign triple junctions consistent with the known TJD in this microstructure. If the TJD sufficiently captures the correlations in the network, these methods will produce statistically identical networks. To determine the percolation surface, we use the approach of assigning TJDs and begin by defining a grid of points in the coordination tetrahedron of Figure 6.1. For each target TJD (i.e., J_o^T, J_1^T, J_2^T and J_3^T), every boundary in a 2-D honeycomb network with 300 grains per side is initially assigned at random as special (with probability p) or general (with probability $1 - p$), where p is consistent with the target TJD and is given by:

$$p = \sum_{i=0}^{3} \frac{i}{3} J_i^T \tag{6.5}$$

A Monte Carlo algorithm is used to evolve the network toward the target TJD; the quantity which is minimized during the simulations is:

$$E = \sum_{i=0}^{3} \left| J_i - J_i^T \right| \tag{6.6}$$

where J_i is the current triple junction population. A single Monte Carlo step involves randomly selecting two boundaries of opposite character (i.e., one special and one general) from the network, exchanging them, and recalculating the value of E after the switch (Eq. (6.6)). If E decreases, the switch is accepted; if it increases, the boundaries are switched back. The system continues to evolve in this manner toward the target TJD until E is less than 0.02 or until 2×10^6 switches have been attempted. Upon completion of the Monte Carlo algorithm, the same procedure as outlined in Chapter 2 is used to identify clusters of special boundaries and to check the lattice for a percolating cluster. It is important to note that although this procedure allows us to probe a greater volume of the coordination tetrahedron than assignment of grain orientations does, there are still regions which are inaccessible using this technique (e.g., highly segregated structures).

This procedure was repeated in excess of one million times to determine the location of the "percolation surface". To accurately identify the surface, the coordination tetrahedron is divided into increments of 0.01 in J_0, J_1, J_2 and J_3, and every data point assigned to one of these bins based on its final TJD. Within each bin, the fraction of networks which contained a percolating cluster is determined and those with less than 50% are assigned to the non-percolating phase (Figure 6.7a), while those with greater than 50% are assigned to the percolating phase (Figure 6.7b). The boundary between the two phases can be visualized by plotting only the points where between 25% and 75% of the networks contain a percolating cluster, as shown in Figure 6.7c. Although the simulations could not access the points along all of the edges of the coordination tetrahedron, the data suggest that the points $J_2 = 1$ and $J_0 = J_3 = ½$ may lie on the percolation surface.

The percolation surface as defined by the points in Figure 6.7c is not planar and its surface curvature can be captured by fitting the data points with a second-order polynomial.

Only three of the variables J_i are independent; the resulting equation which gives J_3 as a function of J_1 and J_2 is found to be:

$$J_3 \geq 0.4522 + 0.3000\ J_1 - 0.1746\ J_1^2 - 1.1192\ J_2 + 1.0283\ J_1 J_2 + 0.7858\ J_2^2 \qquad (6.7)$$

Eq. (6.7) is given as an inequality and defines the points which occupy the percolating phase.

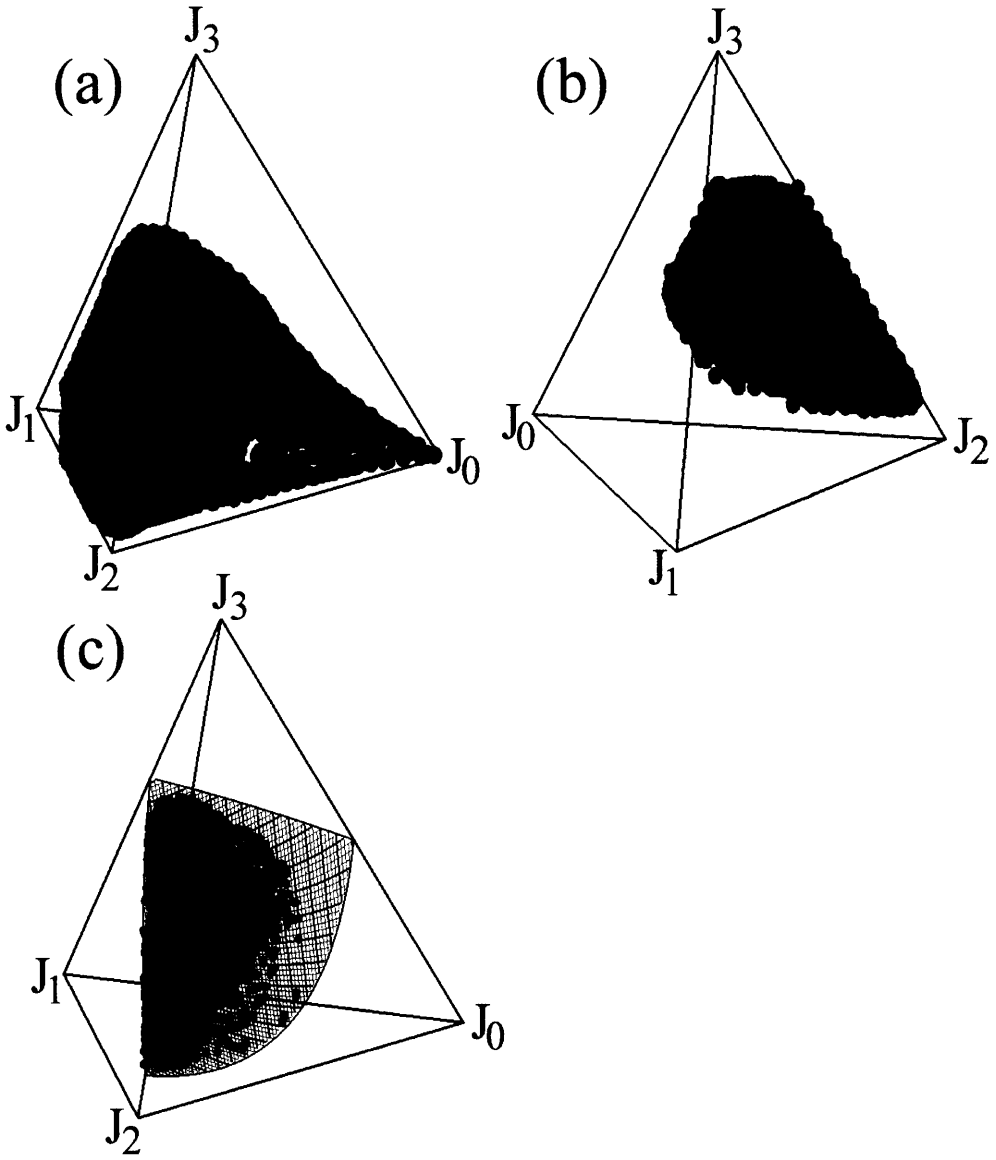

Figure 6.7: In the coordination tetrahedron, the points where (a) less than 50% of the simulated networks contained a percolating cluster, (b) greater than 50% contained a percolating cluster, and (c) between 25 and 75% contained a percolating cluster. The data points in (c) are used to determine the polynomial fit for the percolation surface (Eq. (6.7)), also shown in (c).

The effect of variations in the network topology on the percolation surface can be more easily visualized in terms of the topological parameters, where one of the independent variables is p. As before, the simulation data were divided into bins based on their values of η_{CE}, η_{SO} and p. The non-percolating and percolating points are plotted in Figures 6.8a and b, respectively, and Figure 6.8c shows all of the points where between 25 and 75% of the simulated networks

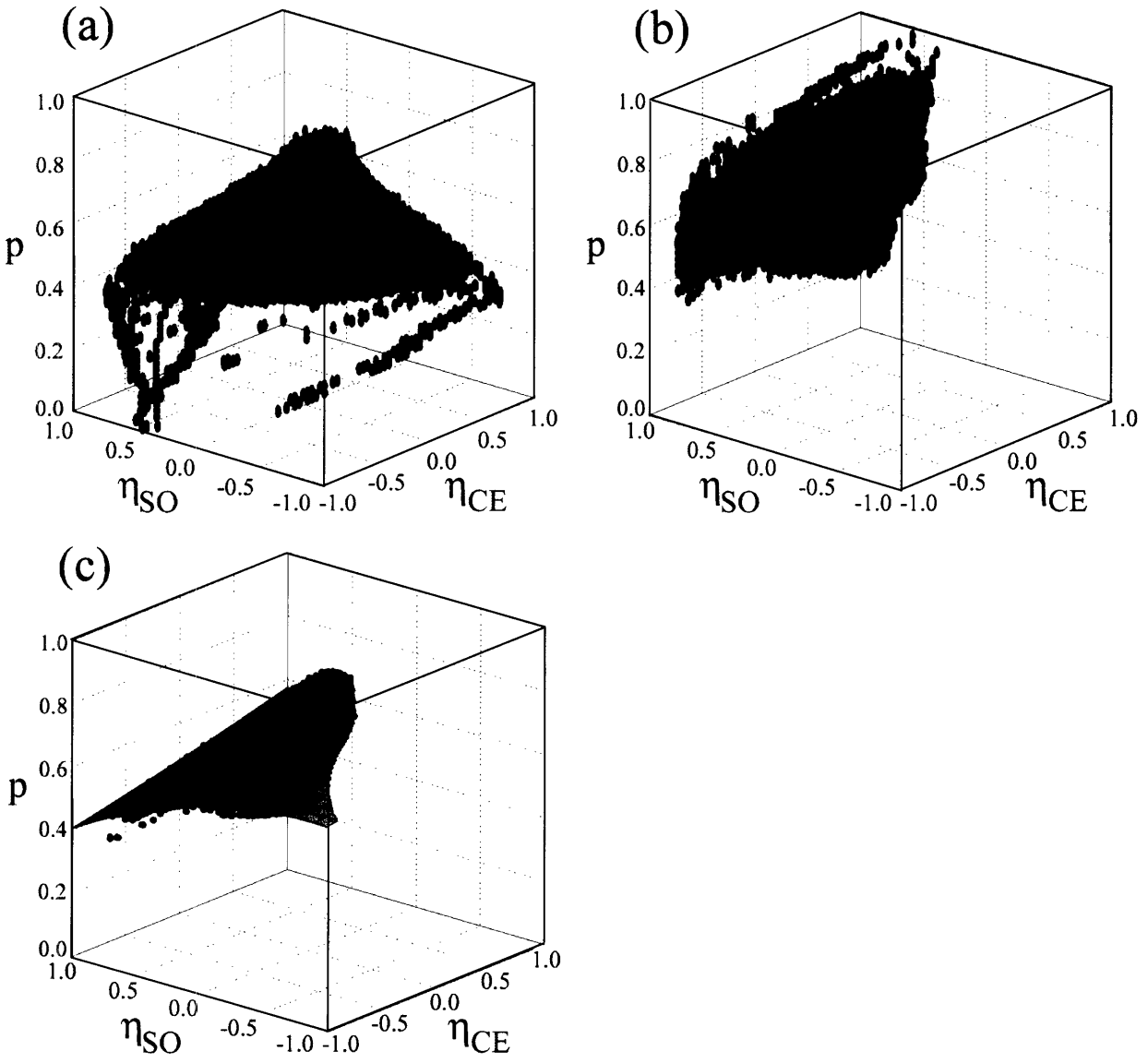

Figure 6.8: In terms of the topological parameters, the points where (a) less than 50% of the simulated networks contained a percolating cluster, (b) greater than 50% contained a percolating cluster, and (c) between 25 and 75% contained a percolating cluster. The data points in (c) are used to determine the polynomial fit for the percolation surface (Eq. (6.8)), also shown in (c).

contained a percolating cluster. Changes in p_c with η_{CE} and η_{SO} can be observed directly from this figure. For example, as η_{CE} approaches -1, the percolation threshold decreases; this follows our earlier discussion that as clusters become more elongated, percolation can occur at lower values of p. In contrast, when $\eta_{CE} > 0$, the clusters are clumpier, requiring a relative increase in p for percolation to occur. In terms of η_{SO}, the percolation threshold is lower for $\eta_{SO} > 0$ where the network is segregated. Segregation of boundary types will also facilitate percolation as like boundaries tend to connect together. The points in Figure 6.8c can also be fitted with a second-order polynomial that can be used to define the points which occupy the percolating phase as a function of the topological parameters. From the points in Figure 6.8c, we find that the percolating phase is defined as:

$$p \geq 0.6605 + 0.0719\ \eta_{CE} + 0.0064\ \eta_{CE}^2 - 0.1066\ \eta_{SO} + 0.0132\ \eta_{CE}\ \eta_{SO} - 0.0697\ \eta_{SO}^2 \quad (6.8)$$

As in Figure 6.7, some of the points in this volume were inaccessible using the current simulation technique. However, there are also points within the volume of Figure 6.8 which do not correspond to a physical TJD (i.e., $0 \leq J_i \leq 1$ for all i). For this reason, the surface fit presented in Figure 6.8c is shown for only physical values of the TJD.

In order to assess the accuracy of the percolation surface determined here, we compare it to the known thresholds along the trajectories for randomly assembled, fiber textured, general textured and twinned microstructures. In each of these four cases, the trajectories shown in Figures 6.1a and 6.6a can be plotted in the coordination tetrahedron of the topological parameter space with the percolation surface. In Figures 6.9 and 6.10, the fitted surface (Eq. (6.7) or (6.8), respectively) is plotted along with each pair of trajectories (special and general boundary clusters). The color change in the trajectory represents the percolation threshold and every trajectory should, in principle, change color exactly as it intersects the surface. This is indeed the case for randomly assembled and fiber textured networks, where all of the thresholds coincide well with the percolation surface. However, in general textured and twinned microstructures, the prediction of the percolation surface does not match the known percolation thresholds presented in Table 5.1 as closely.

Eq. (6.7) or (6.8) can be used to predict the value of p_c along any known trajectory and the magnitude of the error between the real and predicted values assessed. For each of the microstructural models, Eq. (6.7) is evaluated along the TJD (i.e., at values of J_1 and J_2) and the

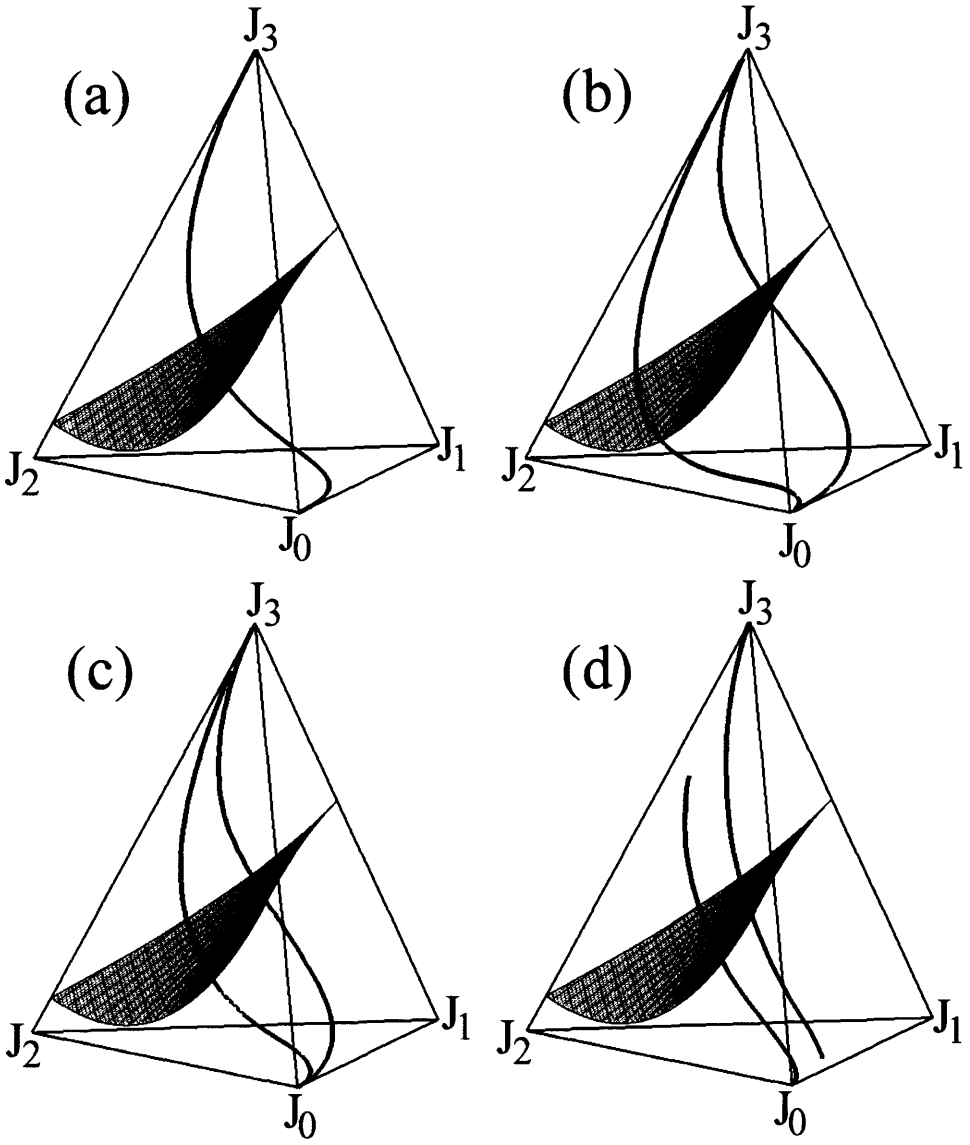

Figure 6.9: For (a) randomly assembled, (b) fiber textured, (c) general textured and (d) twinned microstructures, the known trajectories are plotted for special boundary clusters (green curve changing to blue) and general boundary clusters (red curve changing to blue). The non-percolating part of the random network trajectory is shown in black as it applies to either special or general boundaries. The color change corresponds to the real percolation threshold (Table 5.1) and should occur when the trajectory intersects the surface defined by Eq. (6.7). The errors between the real and predicted values are summarized in Table 6.1.

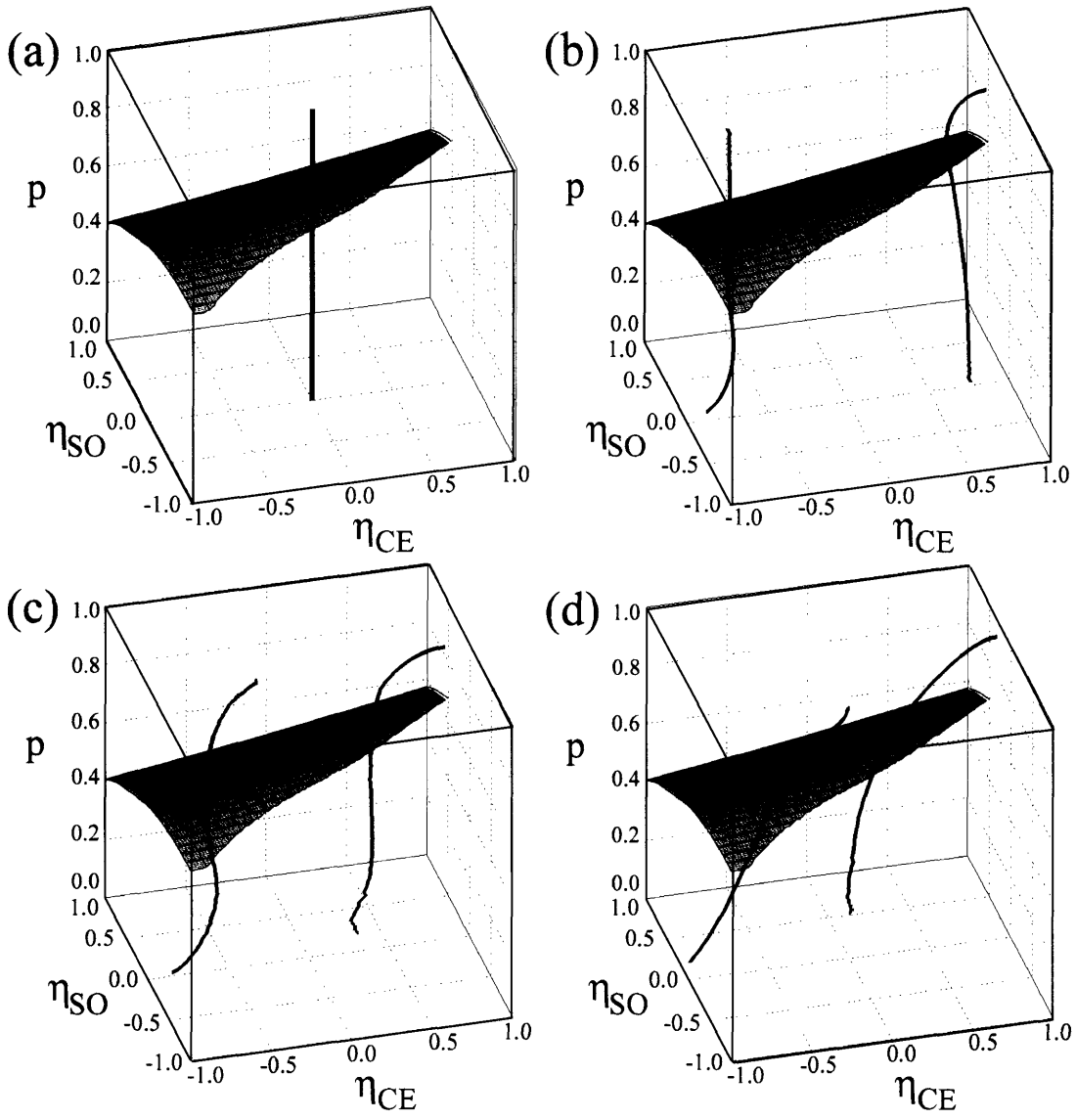

Figure 6.10: For (a) randomly assembled, (b) fiber textured, (c) general textured and (d) twinned microstructures, the known trajectories are plotted for special boundary clusters (green curve changing to blue) and general boundary clusters (red curve changing to blue). The non-percolating part of the random network trajectory is shown in black as it applies to either special or general boundaries. The color change corresponds to the real percolation threshold and should occur when the trajectory intersects the surface as defined by Eq. (6.8).

point at which the fitted value of J_3 matches the actual value of J_3 is used to find the value of p_c. The predicted values of p_c for the seven separate cases are presented in Table 6.1, along with the error as compared to the actual value of the threshold. The data in Table 6.1 confirm that the percolation surface accurately predicts $p_{c,special}$ and $p_{c,general}$ for random and fiber textured networks, but that the error is greater than 0.02 for general textured and twinned networks. In order to offer a possible explanation of the error on the predicted values for general textured and twinned networks, it is necessary to revisit the assumptions used in determining the percolation surface; specifically, that a network is described solely by its triple junction distribution. This implies that the dominant constraints on the system (e.g., crystallography) are captured in the TJD. Therefore, if the percolation threshold is predicted incorrectly, this suggests that correlations exist beyond the triple junctions in general textured and twinned microstructures. In Appendix E, a method for quantifying such longer-range correlations is presented and the results of that analysis confirm that, in general textured and twinned microstructures, longer-range correlations contribute to the total system constraint. However, for networks in which nearest-neighbor correlations dominate, the inequalities in Eqs. (6.7) and (6.8) can be used to determine, on the basis of a TJD alone, whether or not a percolating cluster is expected.

Table 6.1: The predicted percolation thresholds for networks of special or general boundaries in randomly assembled, fiber textured, general textured and twinned microstructures. The actual values of p_c are those found in Chapter 5 and the predicted values were found using Eq. (6.7).

Microstructural Model	Actual p_c	Predicted p_c	Error
Random	0.653	0.653	0.000
Special boundary networks			
Fiber texture	0.689	0.681	0.008
General texture	0.663	0.642	0.021
Twinned	0.666	0.628	0.038
General boundary networks			
Fiber texture	0.601	0.597	0.004
General texture	0.676	0.573	0.103
Twinned	0.659	0.610	0.049

6.3. Effects of Local Correlations on Connectivity Length

Although the percolation threshold is an important parameter in microstructural design, for some materials properties, it may not be the most important in determining the behavior of the material. For example, in the case of stress-corrosion cracking, a component may fail before there is a sample-spanning (percolating) crack, i.e., when the crack reaches a critical length. The connectivity length, which is related to the characteristic cluster size, would thus be more significant in determining the behavior of the component. Therefore, it is useful to consider how changes in the triple junction distribution lead to changes in the connectivity length as a function of the fraction of special boundaries. For each of the simulated microstructures built with a different triple junction distribution, the connectivity length, ξ, was determined following the procedure described in Chapter 2. The same binning procedure that was used to determine the percolation probability was also used to find the average connectivity length within a given bin. The variation in connectivity length as a function of the correlations can be visualized by plotting contour maps for sections through the $\eta_{CE} - \eta_{SO} - p$ space where $\eta_{CE} = 0$ (Figure 6.11a) or $\eta_{SO} = 0$ (Figure 6.11b). In this figure, the different colors correspond to different values of Log(ξ), with a maximum value of ~2.6 indicated by the red regions. Again, the planes are not entirely filled either because the points in the plane do not correspond to a TJD or they are inaccessible using the current simulation technique.

Several observations can be made regarding the behavior of the connectivity length as a function of the local correlations. First, as described in Chapter 5, the connectivity length diverges at the percolation threshold (Eq. (5.3)); therefore, in Figure 6.11, the red band coincides with the percolation surface shown in Figure 6.8. Second, for a constant value of the topological parameter (i.e., moving along a vertical line in Figure 6.11), the range of p over which the color changes from red to blue corresponds to the amplitude C_ξ. Here, C_ξ below p_c is greater than C_ξ above p_c, consistent with the results presented in Table 5.4. Finally, these contour maps offer insight as to how changes in the topological parameter affect the connectivity length at a constant value of p (i.e., moving along a horizontal line in Figure 6.11a). For example, at $p = 0.6$, ordered states have smaller values of ξ than do segregated states. As the connectivity length is the size above which clusters are exponentially rare, those states which allow larger clusters to form at a given value of p (i.e., segregated states) are expected to have higher values of ξ.

The contour maps in Figure 6.11 are useful in that they illustrate how local correlations influence the connectivity length. However, these only represent a small fraction of the $\eta_{CE} - \eta_{SO} - p$ space. More generally, using Eq. (5.3), the value of $C_\xi(\eta_{CE}, \eta_{SO})$ can be found as:

$$C_\xi = \frac{\xi(\eta_{CE}, \eta_{SO}, p)}{|p - p_c(\eta_{CE}, \eta_{SO})|^{-4/3}} \tag{6.9}$$

where $\xi(\eta_{CE}, \eta_{SO}, p)$ is the average value of ξ in each bin and $p_c(\eta_{CE}, \eta_{SO})$ is found from Eq. (6.8). There are two cases which must be considered separately (i.e., $p < p_c$ and $p > p_c$), but in

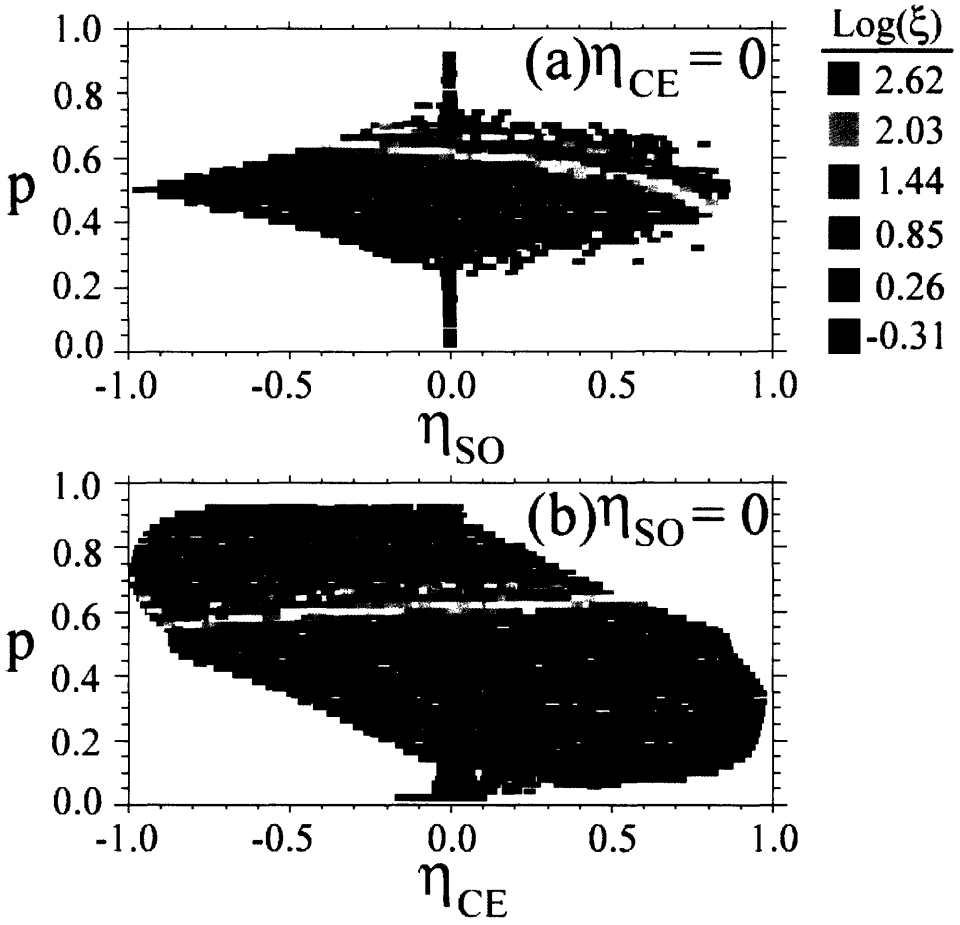

Figure 6.11: Logarithmic contour map of the connectivity length for sections through the $\eta_{CE} - \eta_{SO} - p$ space where (a) $\eta_{CE} = 0$ or (b) $\eta_{SO} = 0$. The points with the highest values of connectivity length lie on or near the percolation surface. In addition to illustrating how ξ changes with the topological parameters and p, this figure also shows how the percolation threshold changes with these variables.

both cases, $C_\xi(\eta_{CE}, \eta_{SO})$ can be described reasonably well by a third-order polynomial. Fitting the data, we find for $p < p_c$:

$$C_\xi^-(\eta_{CE},\eta_{SO}) = 0.847 + 0.843\,\eta_{CE} + 0.105\,\eta_{CE}^2 - 1.10\,\eta_{CE}^3 - 0.505\,\eta_{SO} + 0.347\,\eta_{SO}^2$$
$$+ 1.90\,\eta_{SO}^3 - 0.127\,\eta_{CE}\,\eta_{SO} + 0.998\,\eta_{CE}^2\,\eta_{SO} - 0.988\,\eta_{CE}\,\eta_{SO}^2 \qquad (6.10a)$$

and for $p > p_c$:

$$C_\xi^+(\eta_{CE},\eta_{SO}) = 0.200 - 0.222\,\eta_{CE} + 0.0986\,\eta_{CE}^2 + 0.304\,\eta_{CE}^3 + 0.203\,\eta_{SO} + 0.221\,\eta_{SO}^2$$
$$+ 0.0354\,\eta_{SO}^3 + 0.0848\,\eta_{CE}\,\eta_{SO} - 0.114\,\eta_{CE}^2\,\eta_{SO} - 0.0108\,\eta_{CE}\,\eta_{SO}^2 \qquad (6.10b)$$

The variation in C_ξ as defined by Eq. (6.10) is shown in Figure 6.12 a function of η_{CE} and η_{SO} for values of p both below (C_ξ^-, Figure 6.12a) and above (C_ξ^+, Figure 6.12b) the percolation threshold. For values of $p > p_c$, the surface is defined only for points which correspond to physical triple junction distributions. Over the entire range of the topological parameters, C_ξ^- is

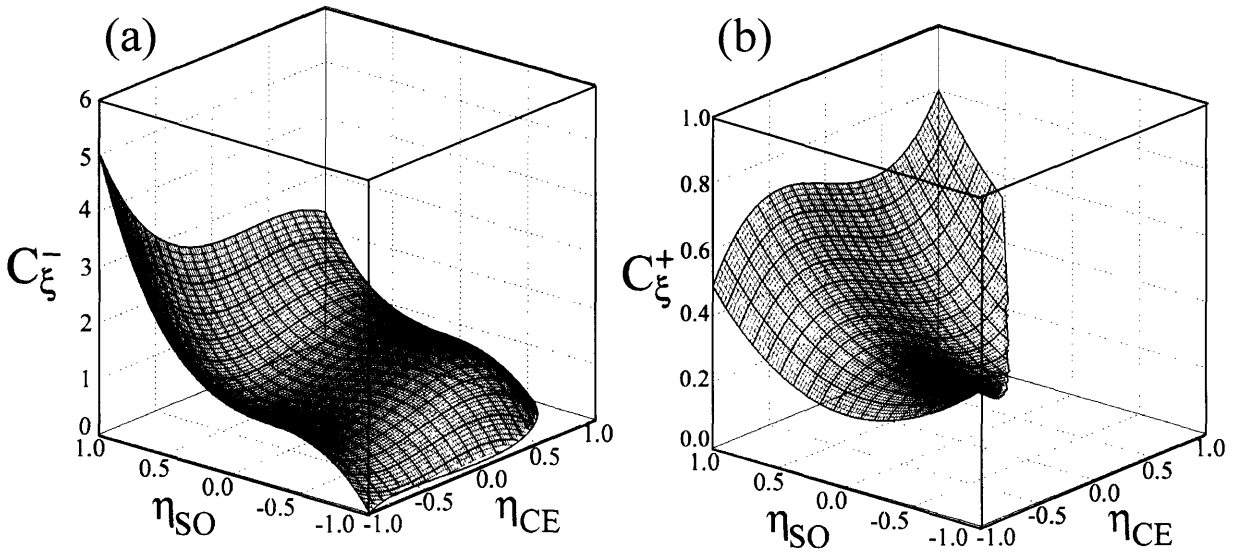

Figure 6.12: The variation in the amplitude prefactor in the connectivity length scaling law, C_ξ, as defined in Eq. (6.9) for values of p (a) below the percolation threshold and (b) above the percolation threshold. The surfaces plotted here are polynomial fits to the binned data as explained in the text and are given by Eq. (6.10).

greater than C_ξ^+, in line with the previous results. Furthermore, segregated states are found to have much larger values of C_ξ than do ordered states both above and below the threshold, another trend that was observed in the $\eta_{CE} = 0$ cross-section. The variation in C_ξ with respect to η_{CE} is more subtle than with respect to η_{SO} and seems to depend on whether the network is segregated or ordered. Although Eq. (6.10) is an estimate of $C_\xi(\eta_{CE}, \eta_{SO})$, it is evident from Figure 6.12 that local correlations can significantly impact the amplitude of the connectivity length.

6.4. Concluding Remarks

In this chapter, we have developed a new framework in which locally-correlated networks can be studied. Two different, but equivalent methods to parameterize the local correlations were presented. First, a coordination tetrahedron was developed whose vertices are the fraction of triple junction types. Second, topological parameters based on the triple junction distribution were used to quantify the state of the network. The effects of local correlations on the percolation threshold were determined by identifying the surface which separates percolating from non-percolating points in the correlation space. The percolation threshold was found to decrease as the network became either more elongated than clumpy, or more segregated than ordered. Local correlations were also found to affect the connectivity length; for all values of p, the connectivity length in segregated networks was larger than in ordered networks by approximately a factor of five.

Although the discussion in this chapter was focused on grain boundary networks, we believe that these developments could be extended in a straightforward manner to consider other locally correlated percolation problems including bootstrap, diffusion, or annealed percolation [126, 127, 133]. In some cases with three-fold coordination and nearest-neighbor correlations, these problems could be mapped directly into the correlation spaces presented here. Other problems, such as percolation on a square lattice could be mapped into their own analogous correlation spaces. Our approach allows for seemingly unrelated problems to be studied in the same framework and for the effects of local correlations on the percolation thresholds or network properties to be understood.

Conclusions

The goal of this work was to understand how the topological properties of grain boundary networks were affected by the requirement for crystallographic consistency. A method was developed to simulate two- and three-dimensional crystallographically consistent grain boundary networks resembling fiber textured, general textured, or highly twinned microstructures, and grain boundaries were separated into two classes (special or general) on the basis of their structure. Although the requirement for crystallographic consistency is often considered to be a local constraint (i.e., around a single triple junction), we have found that this is not necessarily true and that network properties at every length scale are influenced by the constraint.

At the most local level, coordination of special boundaries at triple junctions and quadruple nodes was found to be different from that expected for a random assemblage of special and general boundaries in all three microstructural models. The topological changes in the network associated with the nonrandom TJD were quantified using two topological parameters which distinguished between segregated and ordered states, and between the tendencies to form elongated or clumpy clusters. In the fiber textured case, an analytical, closed-form solution for the nonrandom triple junction distribution was developed using the concept of local transition probabilities. As defined in Chapter 3, the local transition probability is the probability of assigning a boundary as special given that other boundaries at the triple junction have been previously assigned character.

Grain boundary networks were also found to have nonrandom behavior beyond the nearest-neighbor level. For example, fiber textured microstructures exhibited preferential cluster structures; small clusters of boundaries with odd masses were up to 100 times more abundant than those with even masses. Furthermore, at all cluster sizes, special boundary clusters in these networks favored configurations which minimize the number of J_2 junctions that comprise the cluster, leading to compact structures with many branches. In contrast, general boundary networks tended to form elongated clusters that had larger average radii of gyration than clusters of the same mass in randomly assembled networks.

Finally, at quasi-infinite length scales, the scaling behavior and percolation thresholds were studied for grain boundary networks. Although properties such as the average radius of gyration and connectivity length were found to have the same scaling exponents as standard

percolation theory, the amplitude prefactors differed as a result of the crystallographic constraints. With regard to the percolation thresholds, we found that the thresholds shifted from those of standard percolation theory in both two- and three-dimensional microstructures. While none of the percolation thresholds determined in this work were the same as those of standard percolation theory, the direction and magnitude of the shift was different for each microstructure and depended strongly on the details of the crystallographic constraint.

Although we have found that crystallographic constraints exist at all length scales, several results from this work suggest that the correlations among boundaries exist only over a finite, and reasonably small, distance. First, grain boundary networks were found to be in the same universality class as standard percolation theory; this is known to be the case when correlations act only over a finite length. A cutoff length scale of ~3 grain diameters was identified above which the network could be described by the standard scaling exponents and below which these scaling laws fail. Second, an analytical model was developed to predict the nonrandom quadruple node distribution in three-dimensional networks on the basis of a known triple junction distribution. The discrepancies between the real and predicted values for the QND were indicative of the presence of higher-order correlations beyond those around triple junctions alone. While higher-order constraints were determined to contribute to the nonrandom topology of the 3-D network, they were much weaker than the first-order constraints; at least 75% of the correlations were due to the constraint around triple junctions.

In closing, it is important to note that the work presented here was not specific to any crystal system, material or property. Although three microstructural models were selected for closer examination, the conclusions will hold for any network constrained by the requirement for crystallographic consistency. Therefore, this requirement should be included in any physical microstructural model of polycrystalline materials.

Directions for Future Work

This thesis work has taken initial steps in understanding the effects of crystallographically-induced correlations on the topological behavior of grain boundary networks. However, there are several directions in which it can be extended to offer a more complete understanding of these networks:

1. In Chapter 6, the correlations in grain boundary networks were mapped into a coordination tetrahedron whose vertices were the triple junction populations. This correlation space is only sufficient for systems dominated by nearest-neighbor correlations, a description that is inadequate in general textured and twinned microstructures. The concept of determining the percolation threshold as a function of local correlations could be extended beyond the triple junction level to a higher-dimensional space which captures longer-range correlations. However, the complexity of this problem quickly becomes enormous. For example, to consider even second-order correlations in two-dimensional networks requires an 11-dimensional space, as there are 12 topologically unique species whose populations act as the vertices in the coordination space.

2. In the present work, grain boundaries were classified as special or general based only on the misorientation of the boundary as defined by three of the five macroscopic degrees of freedom available to the boundary. However, it is believed that the grain boundary plane can also play an important role in determining the properties of the grain boundary [12, 136, 137]. Therefore, it would be useful to simulate microstructures in such a way as to sample a wide variety of grain boundary planes, as well as to modify the classification scheme to include the crystallography of the grain boundary plane. Furthermore, if the simulated structures contain information regarding the atomic arrangement at the boundary, the microscopic description of the boudnary could also be included in the binary classification criteria.

3. To directly apply the approach of standard percolation theory, a binary special vs. general classification was applied to every boundary based on its structure. However, in practice grain boundaries will exhibit a continuous spectrum of properties. The current models could be modified to include a gray-scale classification of boundaries and network properties such as the connectivity length reanalyzed for these new networks. In a model of this nature, grain

boundaries could be assigned a level of damage tolerance as a function of their misorientation, in contrast to the current assignment of boundaries as simply damage-resistant (special) or damage-susceptible (general). Many physical problems would be more accurately described in this manner, including electromigration, where boundaries may allow for a small amount of electromigration damage before being labeled as fully damaged.

4. The current model also assumes a homogeneous distribution of special boundaries throughout the entire network. Although a homogeneous special fraction may result from some bulk processing techniques, other surface engineering methods may result in either a layered structure or a gradient in the distribution of special boundaries. In fact, one study has found that grain boundary engineering results in such a bimodal microstructure, where a surface layer with a much higher fraction of special boundaries forms than in the bulk [54]. Therefore, the current model could be adapted to study the effects of a gradient in special fraction by assignment of a heterogeneous distribution of grain orientations. In the case of the twinned microstructures, this could be achieved by allowing only perfect $\Sigma 3$ grain rotations near the surface, but allowing the grains in the bulk to rotate by an additional deviation, resulting in more $\Sigma 3^n$ boundaries near the surface than in the interior of the microstructure.

5. Although the present work is applicable to many different materials and properties, the understanding regarding the effects of constraint could be applied to study a specific property. In this case, the grain orientations can be assigned such that the resulting texture matches that in the known microstructure. The binary classification can also be chosen in line with the property of interest and be applied to the model system. Finally, the characteristics of the network most determinant for the material property can be measured. Better analytical models may also be developed that allow not only for non-uniform boundary properties, but which also take into account the spatial correlations among special and general boundaries.

References

1. Watanabe, T., *The Impact of Grain Boundary Character Distribution on Fracture in Polycrystals.* Materials Science and Engineering, 1994. **A176**: p. 39-49.
2. Lehockey, E.M., et al., *Mitigating Intergranular Attack and Growth in Lead-Acid Battery Electrodes for Extended Cycle and Operating Life.* Metallurgical and Materials Transactions, 1998. **29A**: p. 387-396.
3. Peterson, N.L., *Grain-Boundary Diffusion - Structural Effects, Models and Mechanisms*, in *Grain Boundary Structure and Kinetics*. 1979, American Society for Metals: Metals Park, OH. p. 209-238.
4. Alexandreanu, B., et al., *The effect of grain boundary character distribution on the high temperature deformation behavior of Ni-16Cr-9Fe alloys.* Acta Materialia, 2003. **51**(13): p. 3831-48.
5. Riege, S.P., J.A. Prybyla, and A.W. Hunt, *Influence of microstructure on electromigration dynamics in submicron Al interconnects: Real-time imaging.* Applied Physics Letters, 1996. **69**(16): p. 2367-9.
6. Bika, D. and C.J. McMahon, Jr., *A model for dynamic embrittlement.* Acta Metallurgica et Materialia, 1995. **43**(5): p. 1909-16.
7. Argon, A.S. and Y. Qiao, *Cleavage Cracking Resistance of Large-Angle Grain Boundaries in Fe-3wt% Si Alloy.* Philosophical Magazine, 2002. **A82**(17/18): p. 3333-3347.
8. Van Swygenhoven, H., A. Caro, and D. Farkas, *Grain boundary structure and its influence on plastic deformation of polycrystalline fcc metals at the nanoscale: a molecular dynamics study.* Scripta Materialia, 2001. **44**(8-9): p. 1513-16.
9. Xin, G., *Physical origin of the intrinsic grain-boundary resistivity of stabilized-zirconia: role of the space-charge layers.* Solid State Ionics, Diffusion & Reactions, 1995. **81**(3-4): p. 235-42.
10. Hilgenkamp, H. and J. Mannhart, *Grain boundaries in high-T_c superconductors.* Reviews of Modern Physics, 2002. **74**(2): p. 485-549.
11. Sutton, A.P. and R.W. Balluffi, *Interfaces in Crystalline Materials*. 1995: Oxford Science Publication.
12. Saylor, D.M., A. Morawiec, and G.S. Rohrer, *The relative free energies of grain boundaries in magnesia as a function of five macroscopic parameters.* Acta Materialia, 2003. **51**(13): p. 3675-86.
13. Saylor, D.M., A. Morawiec, and G.S. Rohrer, *Distribution of grain boundaries in magnesia as a function of five macroscopic parameters.* Acta Materialia, 2003. **51**(13): p. 3663-74.
14. Lee, T.C., I.M. Robertson, and H.K. Birnbaum, *TEM in situ Deformation Study of the Interaction of Lattice Dislocations with Grain Boundaries in Metals.* Philosophical Magazine, 1990. **A62**(1): p. 131-153.
15. Winther, G., *Slip Patterns and Preferred Dislocation Boundary Planes.* Acta Materialia, 2003. **51**: p. 417-429.
16. Su, J.-Q., M. Demura, and T. Hirano, *Mechanical Behaviour of $\Sigma 3$ Boundaries in Ni_3Al.* Acta Materialia, 2003. **51**: p. 2505-2515.
17. De Koning, M., et al., *Modelling grain-boundary resistance in intergranular dislocation slip transmission.* Philosophical Magazine, 2002. **A82**(13): p. 2511-2527.

18. Grimmer, H., W. Bollman, and D.H. Warrington, *Coincidence Site Lattices and Complete Pattern Shift Lattices in Cubic Crystals.* Acta Crystallographica, 1974. **A30**: p. 197.
19. Brandon, D.G., *The Structure of High-Angle Grain Boundaries.* Acta Metallurgica, 1966. **14**: p. 1479-1484.
20. Ishida, Y. and M. McLean, *Burgers Vectors of Boundary Dislocations in Ordered Grain Boundaries of Cubic Materials.* Philosophical Magazine, 1973. **A27**: p. 1125-1134.
21. Dechamps, M., F. Baribier, and A. Marrouche, *Grain Boundaries: Criteria of Specialness and Deviation from CSL Misorientation.* Acta Metallurgica, 1987. **35**(1): p. 101-107.
22. Palumbo, G. and K.T. Aust, *Structure-Dependence of Intergranular Corrosion in High Purity Nickel.* Acta Metallurgica et Materialia, 1990. **38**: p. 2343-2352.
23. Palumbo, G. and K.T. Aust, *Special Properties of Sigma Grain Boundaries*, in *Materials Interfaces*, D. Wolf and S. Yip, Editors. 1992, Chapman and Hall: London. p. 190-211.
24. Kim, S.H., et al., *Grain Boundary Character Distribution and Intergranular Corrosion Behavior in High Purity Aluminum.* Scripta Materialia, 2001. **44**: p. 835-839.
25. Lehockey, E.M., et al., *On the relationship between grain boundary character distribution and intergranular corrosion.* Scripta Materialia, 1997. **36**(10): p. 1211-1218.
26. Zhou, Y., et al., *Effects of Grain Boundary Structure on Carbide Precipitation in 304L Stainless Steel.* Scripta Materialia, 2001. **45**: p. 49-54.
27. Bedrossian, P.J., et al. *Observation of localized corrosion of Ni based alloys using coupled orientation imaging microscopy and atomic force microscopy.* in *Interfacial Engineering for Optimized Properties II.* 2000. Boston, MA, USA: Mater. Res. Soc.
28. Gourgues, A.-F., *Electron backscatter diffraction and cracking.* Materials Science and Technology, 2002. **18**(2): p. 119-33.
29. Qiao, Y. and A.S. Argon, *Cleavage Cracking Resistance of High Angle Grain Boundaries in Fe-3%Si Alloy.* Mechanics of Materials, 2003. **35**: p. 313-331.
30. Alexandreanu, B., B. Capell, and G.S. Was, *Combined Effect of Special Grain Boundaries and Grain Boundary Carbides on IGSCC of Ni-16Cr-9Fe-xC Alloys.* Materials Science and Engineering, 2001. **A300**: p. 94-104.
31. Pan, Y., et al., *Grain-Boundary Structure Effects on Intergranular Stress Corrosion Cracking of Alloy X-750.* Acta Materialia, 1996. **44**: p. 4685-4695.
32. Gertsman, V.Y. and S.M. Bruemmer, *Study of grain boundary character along intergranular stress corrosion crack paths in austenitic alloys.* Acta Materialia, 2001. **49**: p. 1589-1598.
33. Lehockey, E.M. and G. Palumbo, *On the Creep Behavior of Grain Boundary Engineered Nickel.* Materials Science and Engineering, 1997. **A237**: p. 168-172.
34. Polyanskii, A.A., et al., *Magneto-optical study of flux penetration and critical current densities in [001] tilt $YBa_2Cu_3O_{7-\delta}$ thin-film bicrystals.* Physical Review B, 1996. **53**(13): p. 8687-8697.
35. Heinig, N.F., et al., *Evidence for Channel Conduction in Low Misorientation Angle [001] Tilt $YBa_2Cu_3O_{7-x}$ Bicrystal Films.* Applied Physics Letters, 1996. **69**(4): p. 577-579.
36. Dimos, D. and P. Chaudhari, *Superconducting transport properties of grain boundaries in $YBa_2Cu_3O_7$ bicrystals.* Physical Review B, 1990. **41**(7): p. 4038-4049.
37. Yoshida, H., et al., *High-temperature grain boundary sliding behavior and grain boundary energy in cubic zirconia bicrystals.* Acta Materialia, 2004. **52**(8): p. 2349-2357.

38. Kato, M. and T. Mori, *Internal Friction of Copper Bicrystals with [001] Twist Boundaries.* Philosophical Magazine, 1993. **A68**(5): p. 939-949.
39. Sato, E., et al., *Microstructure Control for Superplasticity of an Ultra-High Carbon Steel.* Materials Science Forum, 1999. **304-306**: p. 133-138.
40. Knorr, D.B. and K.P. Rodbell, *The Role of Texture in the Electromigration Behavior of Pure Aluminum Lines.* Journal of Applied Physics, 1996. **79**(5): p. 2409-2417.
41. Kononenko, O.V., V.N. Matveev, and D.P. Field, *Electromigration Properties of Multigrain Aluminum Thin Film Conductors as Influenced by Grain Boundary Structure.* Journal of Materials Research, 2001. **16**(7): p. 2124-2129.
42. Park, H., S.-J. Hwang, and Y.-C. Joo, *Stress-induced surface damage and grain boundary characteristics of sputtered and electroplated copper thin films.* Acta Materialia, 2004. **52**(8): p. 2435-2440.
43. Lee, S.Y., et al., *Effect of thermomechanical processing on grain boundary characteristics in two-phase brass.* Materials Science & Engineering, 2003. **A363**(1-2): p. 307-15.
44. Gupta, G., B. Alexandreanu, and G.S. Was, *Grain boundary engineering of ferritic-martensitic alloy T91.* Metallurgical and Materials Transactions, 2004. **35A**(2): p. 717-719.
45. Lee, D.S., H.S. Ryoo, and S.K. Hwang, *A grain boundary engineering approach to promote special boundaries in Pb-base alloy.* Materials Science and Engineering, 2003. **354**(1-2): p. 106-111.
46. Palumbo, G., E.M. Lehockey, and P. Lin, *Applications for Grain Boundary Engineered Materials.* JOM, 1998. **50**(2): p. 40-43.
47. Thomson, C.B. and V. Randle, *The Effects of Strain Annealing on Grain Boundaries and Secure Triple Junctions in Nickel 200.* Journal of Materials Science, 1997. **32**: p. 1909-1914.
48. Randle, V., *Mechanism of Twinning Induced Grain Boundary Engineering in Low-Stacking-Fault Energy Materials.* Acta Materialia, 1999. **47**: p. 4187-4196.
49. Randle, V. and H. Davies, *Evolution of microstructure and properties in alpha-brass after iterative processing.* Metallurgical and Materials Transactions A, 2002. **33**(6): p. 1853-1857.
50. Schuh, C.A., M. Kumar, and W.E. King, *Analysis of Grain Boundary Networks and their Evolution During Grain Boundary Engineering.* Acta Materialia, 2003. **51**: p. 687-700.
51. Schwartz, A.J., M. Kumar, and W.E. King, *Influence of Processing Method on the Grain Boundary Character Distribution and Network Connectivity.* Materials Research Society Proceedings, 2000. **586**: p. 3.
52. Randle, V., *Twinning-related grain boundary engineering.* Acta Materialia, 2004. **52**(14): p. 4067-4081.
53. Kumar, M., W.E. King, and A.J. Schwartz, *Modifications to the Microstructural Topology in FCC Materials Through Thermomechanical Processing.* Acta Materialia, 2000. **48**: p. 2081-2091.
54. Shimada, M., et al., *Optimization of grain boundary character distribution for intergranular corrosion resistant 304 stainless steel by twin-induced grain boundary engineering.* Acta Materialia, 2002. **50**(9): p. 2331-2341.
55. Palumbo, G., et al., *Grain Boundary Design and Control for Intergranular Stress-Corrosion Resistance.* Scripta Metallurgica et Materialia, 1991. **25**: p. 1775-1780.

56. Norton, D.P., et al., *Epitaxial $YBa_2Cu_3O_7$ on Biaxially Textured Nickel (001): An Approach to Superconducting Tapes with High Critical Current Density.* Science, 1996. **274**(5288): p. 755-757.
57. Goyal, A., et al., *Conductors with controlled grain boundaries: an approach to the next generation, high temperature superconducting wire.* Journal of Materials Research, 1997. **12**(11): p. 2924-40.
58. Lim, L.C. and T. Watanabe, *Fracture Toughness and Brittle-Ductile Transition Controlled by Grain Boundary Character Distribution (GBCD) in Polycrystals.* Acta Metallurgica et Materialia, 1990. **38**(12): p. 2507-2516.
59. Pan, Y., T. Olson, and B.L. Adams, *Applications of Orientation Imaging Analysis to Microstructural Control of Intergranular Stress Corrosion Cracking.* Canadian Metallurgical Quarterly, 1995. **34**: p. 147-154.
60. Gertsman, V.Y. and K. Tangri, *Modelling of Intergranular Damage Propagation.* Acta Materialia, 1997. **45**: p. 4107-4116.
61. Gertsman, V.Y., M. Janecek, and K. Tangri, *Grain Boundary Ensembles in Polycrystals.* Acta Materialia, 1996. **44**: p. 2869-2882.
62. Schuh, C.A., R.W. Minich, and M. Kumar, *Connectivity and Percolation in Simulated Grain Boundary Networks.* Philosophical Magazine, 2003. **A83**(6): p. 711-726.
63. Gould, H. and J. Tobochnik, *An Introduction to Computer Simulation Methods*. 1996, Reading, MA: Addison-Wesley Publishing Company.
64. Stauffer, D., *Scaling theory of percolation clusters.* Physics Reports, 1979. **54**(1): p. 1-74.
65. Voss, R.F., R.B. Laibowitz, and E.I. Allessandrini, *Fractal (scaling) clusters in thin gold films near the percolation threshold.* Physical Review Letters, 1982. **49**(19): p. 1441-4.
66. Volovitch, P., et al., *Percolation Properties of Internal Wetted Polycrystals: Effect of Stresses and Material Structure.* Materials Science Forum, 2002. **404-407**: p. 373-380.
67. Wang, G., L. Zuo, and C. Esling, *Computer Simulation on the Tendency of Intergranular Fracture in Textured Polycrystalline Materials.* Philosophical Magazine, 2002. **A82**(12): p. 2499-2510.
68. Henrie, A.J., B.L. Adams, and R.J. Larsen, *Creating a Model for Percolation of Grain Boundaries in Polycrystalline Materials.* Materials Science Forum, 2002. **408-412**: p. 419-424.
69. Stauffer, D. and A. Aharony, *Introduction to Percolation Theory*. 1992, London: Taylor & Francis.
70. Grimmett, G., *Percolation*. 1999, Berlin: Springer.
71. Hanisch, J., et al., *Simulation of the critical current density and its dependence on geometrical factors in RABiTS based coated conductors.* Superconductor Science and Technology, 2004. **17**(8): p. 1003-1008.
72. Cai, Z.X. and D.O. Welch, *Simulation study of the critical current density of $YBa_2Cu_3O_7$ ceramics.* Physical Review B, 1992. **45**(5): p. 2385-2390.
73. Evetts, J.E., et al., *Current percolation and the V-I transition in YBa/sub 2/Cu/sub 3/O/sub 7/ bicrystals and granular coated conductors.* Superconductor Science & Technology, 1999. **12**(12): p. 1050-3.
74. Specht, E.D., A. Goyal, and D.M. Kroeger, *Scaling of percolative current flow to long lengths in biaxially textured conductors.* Superconductor Science and Technology, 2000. **13**: p. 592-597.

75. Rutter, N.A., B.A. Glowacki, and J.E. Evetts, *Percolation modelling for highly aligned polycrystalline superconducting tapes.* Superconductor Science and Technology, 2000. **13**: p. L25-L-30.
76. Wells, D.B., et al., *The Use of Percolation Theory to Predict the Probability of Failure of Sensitized, Austenitic Stainless Steels by Intergranular Stress Corrosion Cracking.* Corrosion, 1989. **45**(8): p. 649-660.
77. Strelniker, Y.M., et al., *Percolation transition in a two-dimensional system of Ni granular ferromagnets.* Physical Review E, 2004. **69**(6 2): p. 065105-1.
78. Ju, S., H. Sun, and Z.-Y. Li, *Sudy of Magnetotransport in Polycrystalline Perovskite Manganites.* Journal of Physics: Condensed Matter, 2002. **14**: p. L631-L639.
79. Pennetta, C., et al., *A percolative approach to electromigration in metallic lines.* Journal of Physics D, 2001. **34**(9): p. 1421-9.
80. Wu, K. and R.M. Bradley, *Theory of electromigration failure in polycrystalline metal films.* Physical Review B, 1994. **50**(17): p. 12468-88.
81. Traskine, V., et al., *Grain Boundary Wetting in Polycrystalls: Wettability of Structure Elements and Liquid Phase Connectivity.* Colloids and Surfaces A, 2000. **166**: p. 261-268.
82. Kocks, U.F., C.N. Tome, and H.-R. Wenk, *Texture and Anisotropy.* 1998, Cambridge, UK: Cambridge University Press.
83. Miyazawa, K., et al., *Combination Rule of Sigma Values at Triple Junctions in Cubic Polycrystals.* Acta Crystallographica, 1996. **A52**: p. 787-796.
84. Gertsman, V.Y., *Geometrical Theory of Triple Junctions of CSL Boundaries.* Acta Crystallographica, 2001. **A57**: p. 369-377.
85. Furley, J. and V. Randle, *Mesotexture in Annealed Nickel.* Materials Science and Technology, 1991. **7**: p. 12-19.
86. Kumar, M., A.J. Schwartz, and W.E. King, *Microstructural Evolution During Grain Boundary Engineering of Low to Medium Stacking Fault Energy FCC Materials.* Acta Materialia, 2002. **50**: p. 2599-2612.
87. Palumbo, G., et al., *On Annealing Twin and CSL Distributions in FCC Polycrystals.* Physica Status Solidi, 1992. **131**: p. 425-428.
88. Frary, M. and C.A. Schuh, *Combination Rule for Deviant CSL Grain Boundaries at Triple Junctions.* Acta Materialia, 2003. **51**(13): p. 3731-3743.
89. Fortier, P., W.A. Miller, and K.T. Aust, *Triple Junction and Grain Boundary Character Distribution in Metallic Materials.* Acta Materialia, 1997. **45**(8): p. 3459-3467.
90. Davies, P., et al., *Triple junction distribution profiles as assessed by electron backscatter diffraction.* Journal of Materials Science, 2002. **37**(19): p. 4203-4209.
91. Schuh, C.A. and M. Kumar, *Universal Features of Grain Boundary Networks in FCC Materials.* Journal of Materials Science, 2005. **40**: p. 847-852.
92. Minich, R.W., C.A. Schuh, and M. Kumar, *The Role of Topological Constraints on the Statistical Properties of Grain Boundary Networks.* Physical Review B, 2002. **66**: p. 052101.
93. Randle, V. and P. Davies. *The Influence of Grain Junctions on the Interface Distribution after Recrystallization.* in *The Fourth International Conference on Recrystallization and Related Phenomena.* 1999: The Japan Institute of Metals.
94. Dingley, D.J. and V. Randle, *Microtexture Determination by Electron Backscatter Diffraction.* Journal of Materials Science, 1992. **27**(17): p. 4545-66.

95. Randle, V., *The Influence of Grain Junctions and Boundaries on Superplastic Deformation.* Acta Metallurgica et Materialia, 1995. **43**(5): p. 1741-1749.
96. Liu, J. and J.G. Morris, *Texture and Grain-Boundary Evolutions of Continuous Cast and Direct Chill Cast AA 5052 Aluminum Alloy during Cold Rolling.* Metallurgical and Materials Transactions, 2003. **34A**: p. 951-966.
97. Randle, V., *Grain Assemblage in Polycrystals.* Acta Metallurgica et Materialia, 1994. **42**(6): p. 1769-1784.
98. Weiss, D., O. Kraft, and E. Arzt, *Grain-Boundary Voiding in Self-passivated Cu-1 at.% Al Alloy Films on Si Substrates.* Journal of Materials Research, 2002. **17**(6): p. 1363-1370.
99. Feldmann, D.M., et al., *Influence of nickel substrate grain structure on $YBa_2Cu_3O_{7-\delta}$ supercurrent connectivity in deformation-textured coated conductors.* Applied Physics Letters, 2000. **77**(18): p. 2906-2908.
100. Dingley, D.J., *The Development of Automated Diffraction in Scanning and Transmission Electron Microscopy*, in *Electron Backscatter Diffraction in Materials Science*, A.J. Schwartz, M. Kumar, and B.L. Adams, Editors. 2000, Kluwer Academic: New York. p. 1-18.
101. Fernandez, L., et al., *Influence of the Grain Boundary Network on the Critical Current of $YBa_2Cu_3O_7$ Films Grown on Biaxially Textured Metallic Substrates.* Physical Review B, 2003. **67**: p. 052503.
102. Bystrzycki, J., et al., *Grain Boundary Character Distribution in B2 Intermetallics.* Intermetallics, 2000. **8**: p. 1049-1059.
103. Goyal, A., et al., *Grain boundary misorientations and percolative current paths in high-J_c powder-in-tube $(Bi,Pb)_2Sr_3Ca_3Cu_3O_x$.* Applied Physics Letters, 1995. **66**(21): p. 2903-5.
104. Goyal, A., et al., *Grain boundary studies of high-temperature superconducting materials using electron backscatter Kikuchi diffraction.* Ultramicroscopy, 1997. **67**(1-4): p. 35-57.
105. Iijima, Y., et al., *Structural and Transport Properties of Biaxially Aligned $YBa_2Cu_3O_{7-x}$ Films on Polycrystalline Ni-based Alloy with Ion-Bean-Modified Buffer Layers.* Journal of Applied Physics, 1993. **74**(3): p. 1905-1911.
106. Romero, D., L. Martinez, and L. Fionova, *Computer Simulation of Grain Boundary Spatial Distribution in a Three-Dimensional Polycrystal with Cubic Structure.* Acta Materialia, 1996. **4**(1): p. 391-402.
107. Reed, B.W., et al., *The Structure of the Cubic Coincidence Site Lattice Rotation Group.* Acta Crystallographica, 2004. **A60**: p. 263-277.
108. Bunge, H.-J., *Texture Analysis in Materials Science*. 1993, Gottingen, Germany: Verlag.
109. Morawiec, A., *Misorientation-Angle Distribution of Randomly Oriented Symmetric Objects.* Journal of Applied Crystallography, 1995. **28**: p. 289-293.
110. MacKenzie, J.K., *Second Paper on Statistics Associated with the Random Disorientation of Cubes.* Biometrika, 1958. **45**(1-2): p. 229-240.
111. Randle, V., *Interfacial Geometry in Simulated Rolling and Recrystallization Textures.* Modelling and Simulation in Materials Science and Engineering, 1996. **4**: p. 455-472.
112. Ryoo, H.S., et al., *Grain Boundary Character Distribution of Computer Microstructure Generated in HCP Materials by Gaussian Distribution and the Monte Carlo Method.* Scripta Materialia, 2001. **44**: p. 2583.

113. Garbacz, A. and M.W. Grabski, *The Relationship Between Texture and CSL Boundaries Distribution in Polycrystalline Materials - II. Analysis of the Relationship Between Texture and Coincidence Boundary Distribution.* Acta Metallurgica et Materialia, 1993. **41**(2): p. 475-483.
114. Hoshen, J. and R. Kopelman, *Percolation and Cluster Distribution. I. Cluster Multiple Labeling Technique and Critical Concentration Algorithm.* Physical Review B, 1976. **14**(8): p. 3438-3445.
115. Hoshen, J., M.W. Berry, and K.S. Minser, *Percolation and cluster structure parameters: the enhanced Hoshen-Kopelman algorithm.* Physical Review E, 1997. **56**(2): p. 1455-60.
116. Frary, M. and C.A. Schuh, *Percolation and statistical properties of low and high-angle interface networks in polycrystalline ensembles.* Physical Review B, 2004. **69**: p. 134115.
117. Fu, X., et al., *Non-destructive mapping of grains in three dimensions.* Scripta Materialia, 2003. **49**(11): p. 1093-6.
118. Poulsen, H.F., et al., *Three-dimensional maps of grain boundaries and the stress state of individual grains in polycrystals and powders.* Journal of Applied Crystallography, 2001. **34**(pt.6): p. 751-6.
119. Adams, B.L., et al., *Extracting grain boundary and surface energy from measurement of triple junction geometry.* Interface Science, 1999. **7**(3-4): p. 321-38.
120. Zhang, C., et al., *Characterization of Three-Dimensional Grain Structure of Polycrystalline Iron by Serial Sectioning.* Metallurgical and Materials Transactions, 2004. **35A**(7): p. 1927-1933.
121. Gertsman, V.Y., *Coincidence Site Lattice Theory of Multicrystalline Ensembles.* Acta Crystallographica, 2001. **A57**: p. 649-655.
122. Meinke, J.H., et al., *Scaling laws for critical manifolds in polycrystalline materials.* Physical Review E, 2003. **68**(6): p. 66107-1.
123. Knackstedt, M.A., M. Sahimi, and A.P. Sheppard, *Invasion percolation with long-range correlations: First-order phase transition and nonuniversal scaling properties.* Physical Review E, 2000. **61**(5): p. 4920-34.
124. Knackstedt, M.A., M. Sahimi, and A.P. Sheppard, *Nonuniversality of invasion percolation in two-dimensional systems.* Physical Review E, 2002. **65**(3): p. 035101-1.
125. Bauerschafer, U. and M. Schulz, *Bond percolation on a dilute lattice with short and long range correlations: a numerical simulation.* Physical Review E, 1996. **54**(2): p. 1442-8.
126. Chaves, C.M. and B. Koiller, *Universality, Thresholds and Critical Exponents in Correlated Percolation.* Physica A, 1995. **218**: p. 271-278.
127. Medeiros, M.C. and C.M. Chaves, *Universality in Bootstrap and Diffusion Percolation.* Physica A, 1997. **234**: p. 604-610.
128. Campos, P.R.A., L.F.C. Pessoa, and F.G.B. Moreira, *Cluster-size statistics of site-bond-correlated percolation models.* Physical Review B, 1997. **56**(1): p. 40-2.
129. Prakash, S., et al., *Structural and dynamical properties of long-range correlated percolation.* Physical Review A, 1992. **46**(4): p. R1724-R1727.
130. Frary, M. and C.A. Schuh, *Connectivity and Percolation Behavior of Grain Boundary Networks in Three Dimensions.* Philosophical Magazine, 2005. **85**(11): p. 1123-1143.
131. Lindgard, P.-A. and H. Bohr, *Towards a systematic classification of protein folds.* Physical Review E, 1997. **56**(4): p. 4497-4514.
132. Solov'yov, I.A., et al., *Cluster Growing Process and a Sequence of Magic Numbers.* Physical Review Letters, 2003. **90**(5): p. 053401.

133. Wollman, D.A., M.A. Dubson, and Q. Zhu, *Annealed percolation: determination of exponents in a correlated-percolation problem.* Physical Review B, 1993. **48**(6, pt.2): p. 3713-20.
134. Jerauld, G.R., L.E. Scriven, and H.T. Davis, *Percolation and conduction on the 3D Voronoi and regular networks: a second case study in topological disorder.* Journal of Physics C, 1984. **17**: p. 3429-3439.
135. Beran, M.J., et al., *Bounding elastic constants of an orthotropic polycrystal using measurements of the microstructure.* Journal of the Mechanics and Physics of Solids, 1996. **44**(9): p. 1543-1563.
136. Davies, P. and V. Randle, *Grain Boundary Engineering and the Role of the Interfacial Plane.* Materials Science and Technology, 2001. **17**: p. 615-626.
137. Randle, V., *The Role of the Grain Boundary Plane in Cubic Polycrystals.* Acta Materialia, 1998. **46**: p. 1459-1480.
138. Bollman, W., *Triple Lines in Polycrystalline Aggregates as Disclinations.* Philosophical Magazine, 1984. **A49**(1): p. 73-79.
139. Bollman, W., *Triple-line Disclinations: Representations, Continuity, and Reactions.* Philosophical Magazine, 1988. **A57**(4): p. 637-649.
140. Clarebrough, L.M. and C.T. Forwood, *Secondary Grain-Boundary Dislocation Nodes at the Junction of Three Grains.* Philosophical Magazine, 1987. **A55**(2): p. 217-225.
141. Palumbo, G. and K.T. Aust, *Triple-line Corrosion in High Purity Nickel.* Materials Science and Engineering, 1989. **A113**: p. 139-147.
142. Palumbo, G. and K.T. Aust, *A Coincident Axial Direction (CAD) Approach to the Structure of Triple Junctions in Polycrystalline Materials.* Scripta Metallurgica et Materialia, 1990. **24**: p. 1771-1776.
143. Doni, E.G., G. Palumbo, and K.T. Aust, *Computer Simulation of Triple Line Character Distributions in FCC Materials.* Scripta Metallurgica et Materialia, 1990. **24**: p. 2325-2328.
144. Randle, V., *On the Significance of Grain Junction Topology and Crystallography in Polycrystals.* Scripta Metallurgica et Materialia, 1993. **28**: p. 889-893.
145. Palumbo, G. and K.T. Aust, *Solute Effects in Grain Boundary Engineering.* Canadian Metallurgical Quarterly, 1995. **34**: p. 165-173.
146. Edwards, C.H., Jr. and D.E. Penney, *Elementary Linear Algebra*. 1988, Englewood Cliffs, NJ: Prentice Hall.
147. Grinstead, C.M. and J.L. Snell, *Introduction to Probability*. 1997, Providence, RI: American Mathematical Society.

Appendix A: Derivation of the Deviation Limit Rule

The following derivation yields the relationship for the coordination of three grain boundaries, denoted by *a*, *b*, and *c,* when they meet at a triple junction. Specifically, we focus on cubic crystals where each boundary is described by its Σ value, as well as a single deviation angle θ that describes the minimum rotation away from the ideal Σ orientation; the axis of this deviation is unspecified, and may be different for all three boundaries. The starting point for the derivation to follow is the sigma combination rule (Eq. (1.3)), which specifies the possible relationships among Σa, Σb, and Σc. In what follows, a complementary rule that gives the relationship between the deviation angles θ_a, θ_b, and θ_c is derived.

The misorientation of grain boundary *x* (= *a*, *b*, or *c*) is conveniently expressed as a misorientation matrix, $\mathbf{M_x}$, whose nine elements x_{ij} (*i*, *j* = 1 to 3) are direction cosines that relate the coordinate axes of one grain to those of its neighbor. In the derivation to follow, it will occasionally be more useful to use the equivalent description of misorientation as an axis/angle ([*hkl*], θ) pair. The angle of rotation is found using [82]:

$$2\cos(\theta_x)+1 = \mathrm{tr}(\mathbf{M_x}) \tag{A.1}$$

where *tr* denotes the trace operator ($\mathrm{tr}(\mathbf{M_x}) \equiv x_{11} + x_{22} + x_{33}$). The angle θ_x describes rotation around an axis given by:

$$h_x : k_x : l_x = x_{32} - x_{23} : x_{13} - x_{31} : x_{21} - x_{12} \tag{A.2}$$

where the subscript on *h*, *k*, and *l* is used to distinguish among different values of these indices for different grain boundaries.

At the triple junction of grain boundaries *a*, *b*, and *c*, crystallographic consistency requires that misorientation be conserved; for a Frank-Nabarro circuit around the junction, the orientation at the start and finish of the circuit must be identical, or a disclination defect is present at the junction [95, 138-145]. In terms of the misorientation matrices of the three boundaries, this consistency condition can be expressed as [84]:

$$\mathbf{M_a M_b} = \mathbf{M_c} \tag{A.3}$$

Within the CSL framework, any grain boundary can, in principle, be characterized by an ideal CSL misorientation matrix, $\mathbf{M}_{\Sigma x}$ (available in, e.g., Ref. [18]), as well as a second misorientation matrix Δ_x, which describes the deviation of the boundary from the ideal CSL misorientation. The full misorientation matrix for the boundary may then be written as:

$$\mathbf{M}_x = \mathbf{M}_{\Sigma x}\Delta_x \tag{A.4}$$

The trace of the deviation matrix Δ_x gives, via Eq. (A.1), the angle θ_x by which boundary x deviates from the ideal CSL misorientation. It is this deviation angle that is used with, e.g., the Brandon criterion (Eq. (1.1) with w = ½) to discern if boundary x should be considered a CSL boundary. In the limit where there is no deviation θ_x, the matrix Δ_x equals the identity matrix, $\mathbf{I}$, and $\mathbf{M}_x = \mathbf{M}_{\Sigma x}$.

At a triple junction, generally all three grain boundaries will deviate from ideal CSL misorientations. Then Eq. (A.3) is generalized using Eq. (A.4) to give:

$$\mathbf{M}_{\Sigma a}\Delta_a\mathbf{M}_{\Sigma b}\Delta_b = \mathbf{M}_{\Sigma c}\Delta_c \tag{A.5}$$

In addition to this general consistency condition, we also require that the CSL misorientations, $\mathbf{M}_{\Sigma x}$, are conserved around the junction,

$$\mathbf{M}_{\Sigma a}\mathbf{M}_{\Sigma b} = \mathbf{M}_{\Sigma c} \tag{A.6}$$

This condition is the basis from which the sigma combination rule is derived [83, 84], and is the same as Eq. (A.5) when $\Delta_a = \Delta_b = \Delta_c = \mathbf{I}$ (i.e., when there are no deviations from ideal CSL misorientations). Therefore, for any Σ combinations allowed by Eq. (1.3), there exist matrices $\mathbf{M}_{\Sigma a}$, $\mathbf{M}_{\Sigma b}$, and $\mathbf{M}_{\Sigma c}$ that satisfy Eq. (A.6). We can then combine Eqs. (A.5) and (A.6) and after some manipulation find:

$$\Delta_a = \mathbf{M}_{\Sigma b}\Delta_c\Delta_b^{-1}\mathbf{M}_{\Sigma b}^{-1} \tag{A.7}$$

The form of Eq. (A.7) is such that Δ_a and $\Delta_c\Delta_b^{-1}$ are similar matrices, so their eigenvalues, and therefore their traces, are equal [146]:

$$\mathrm{tr}(\Delta_a) = \mathrm{tr}\left(\Delta_c\Delta_b^{-1}\right) \tag{A.8}$$

By noting that the transpose of an orthogonal matrix is equal to its inverse (i.e., $\Delta_b^{-1} = \Delta_b^{T}$), the right hand side of Eq. (A.8) can be expanded to yield:

$$\mathrm{tr}\left(\Delta_c \Delta_b^{-1}\right) = \sum_{i,j=1}^{3} b_{ij} c_{ij} \tag{A.9}$$

Using Eqs. (A.8) and (A.9) with the definition of the trace operator now gives:

$$\mathrm{tr}(\Delta_a) = \mathrm{tr}(\Delta_b)\mathrm{tr}(\Delta_c) + \sum_{\substack{i,j=1 \\ i \neq j}}^{3} \left[b_{ij} c_{ji} - b_{ii} c_{jj} \right] \tag{A.10}$$

The summation on the right hand side of Eq. (A.10) contains 12 terms which may be individually replaced using the axis/angle expressions for the matrix components [82]:

$$x_{11} = \cos(\theta_x) + h_x^2 [1 - \cos(\theta_x)] \tag{A.11a}$$

$$x_{12} = h_x k_x [1 - \cos(\theta_x)] + l_x \sin(\theta_x) \tag{A.11b}$$

$$x_{13} = h_x l_x [1 - \cos(\theta_x)] - k_x \sin(\theta_x) \tag{A.11c}$$

$$x_{21} = h_x k_x [1 - \cos(\theta_x)] - l_x \sin(\theta_x) \tag{A.11d}$$

$$x_{22} = \cos(\theta_x) + k_x^2 [1 - \cos(\theta_x)] \tag{A.11e}$$

$$x_{23} = k_x l_x [1 - \cos(\theta_x)] + h_x \sin(\theta_x) \tag{A.11f}$$

$$x_{31} = h_x l_x [1 - \cos(\theta_x)] + k_x \sin(\theta_x) \tag{A.11g}$$

$$x_{23} = k_x l_x [1 - \cos(\theta_x)] - h_x \sin(\theta_x) \tag{A.11h}$$

$$x_{33} = \cos(\theta_x) + l_x^2 [1 - \cos(\theta_x)] \tag{A.11i}$$

We note that when expressing these components in terms of the axis/angle pair, the misorientation axis $[h_x k_x l_x]$ must be a unit vector.

For all three of the boundaries *a*, *b*, and *c*, the deviation angles θ_x are small. For example, with either the Brandon or Palumbo-Aust criteria, the largest allowed value of θ occurs for low-

angle boundaries (Σ1), where $\theta \leq 15°$. Thus, for any angle θ that may figure into Eq. (A.10), small angle approximations may be applied:

$$\cos(\theta_x) \approx 1 - \frac{\theta_x^2}{2} \tag{A.12a}$$

$$\sin(\theta_x) \approx \theta_x \tag{A.12b}$$

Substituting Eqs. (A.1), (A.11), and (A.12) into Eq. (A.10) and neglecting highest order terms, we derive the following relationship between the deviations θ_x at a triple junction:

$$\theta_a^2 = \theta_b^2 + \theta_c^2 + 2 \cdot \theta_b \cdot \theta_c \cdot H \tag{A.13}$$

where

$$H = h_b h_c + k_b k_c + l_b l_c \tag{A.14}$$

Here $[h_b k_b l_b]$ and $[h_c k_c l_c]$ are the axes about which boundaries *b* and *c* deviate from their respective ideal CSL misorientations, and the quantity H is recognized as the inner product between these two axes. Accordingly, it is convenient to write $H = \cos(\chi)$, with χ the angle between these axes. Physically, the deviation axes of boundaries *b* and *c* need not be related, so χ may take any value between 0 and π. Over this range, $\cos(\chi)$ is bounded by -1 and 1, so the upper and lower limits on Eq. (A.13) may now be found as:

$$\theta_a = \theta_b + \theta_c \tag{A.15a}$$

when $H = 1$, and

$$\theta_a = \theta_b - \theta_c \tag{A.15b}$$

or

$$\theta_a = \theta_c - \theta_b \tag{A.15c}$$

when $H = -1$.

While Eqs. (A.15) yield the bounding solutions of Eq. (A.13), the value of H can vary, allowing many plausible combinations of θ_a, θ_b, and θ_c between these limits. The general relationship among these θ values is found when the equalities in Eqs. (A.15) are replaced with

inequalities consistent with the allowable range of *H*. We find that the solution may be summarized as:

$$\theta_{max} \leq \theta_1 + \theta_2 \tag{A.16}$$

where θ_{max} is the greatest of θ_a, θ_b, or θ_c, and θ_1 and θ_2 are the deviations of the other two boundaries in no particular order. Thus, for any set of grain boundaries that meet at a triple junction and obey Eq. (A.6), we find that this "deviation limit rule" governs the relationship between their deviation angles. For a detailed explanation of the physical implications of Eq. (A.16), the interested reader is referred to Ref. [88].

Appendix B: Derivation of Local Transition Probabilities for Fiber Textured Microstructures

A closed form analytical solution for the triple junction distribution is possible for the case of the ideal fiber textured material where the state of each grain is fully specified by a single in-plane orientation angle. Although throughout this appendix grain boundaries will be referred to as special and general, it is important to remember that these labels correspond to disorientations below and above the low-angle threshold, θ_t, respectively.

B.1. Relationship among the Global Variables

The geometry and nomenclature of the model system are shown schematically in Figure B.1. The orientations of the three grains, *A*, *B* and *C*, that meet at the triple junction are labeled ϕ_A, ϕ_B, and ϕ_C, and may assume any value on the range $(-\phi_{max}, \phi_{max})$. These angles represent in-plane rotations about a line parallel to the triple junction axis. The grain boundary disorientation angles are θ_a, θ_b, and θ_c, where as a convention, boundary *a* is taken to be opposite grain *A* (Figure B.1). Although disorientation angles are typically unsigned, the derivation to follow is simplified by allowing both positive and negative disorientations. Then, because all grains share

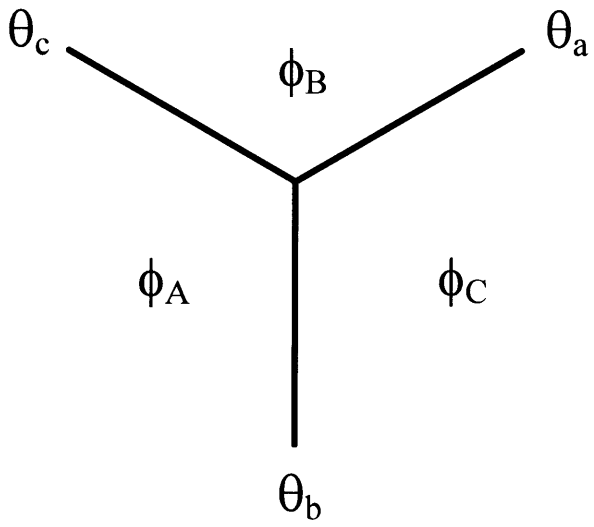

Figure B.1: Labeling scheme for angles at a triple junction; ϕ_X are grain orientations which occupy the range $(-\phi_{max}, \phi_{max})$, while θ_x are grain boundary disorientations and exist on the range $(-2\phi_{max}, 2\phi_{max})$.

a common axis, the grain boundary disorientations may be found as the difference between the orientations of neighboring grains, e.g.:

$$\theta_c = \phi_A - \phi_B, \tag{B.1}$$

and may take any value on the range $(-2\phi_{max}, 2\phi_{max})$. The angle ϕ_{max}, as explained in Chapter 2, controls the sharpness of the texture and also the range of grain boundary disorientation angles in the grain boundary network. The grain boundary disorientations are defined around a clockwise circuit and therefore are constrained by the relationship:

$$\theta_a + \theta_b + \theta_c = 0. \tag{B.2}$$

Since grain orientations are assigned at random, $F(\phi)$ is a uniform distribution:

$$F(\phi) = \begin{cases} \dfrac{1}{2\phi_{max}}, & -\phi_{max} \le \phi \le \phi_{max}, \\ 0, & \text{otherwise}, \end{cases} \tag{B.3}$$

where the subscript on ϕ has been omitted, since Eq. (B.3) applies to all three grains *A*, *B*, and *C*. The distribution of grain boundary disorientations may now be obtained through convolution of the grain orientation distributions as [147]:

$$F(\theta_c) = \int_{-\infty}^{\infty} F(\phi_A) F(\phi_B) d\phi_B, \tag{B.4}$$

where $F(\varepsilon)$ is the global density distribution of either an orientation or disorientation angle ε. If we substitute for ϕ_A according to Eq. (B.1) such that ϕ_B is the only remaining variable, Eq. (B.4) becomes:

$$F(\theta_c) = \int_{-\infty}^{\infty} F(\theta_c + \phi_B) F(\phi_B) d\phi_B. \tag{B.5}$$

Introducing Eq. (B.3) and integrating now yields the global density distribution of boundary disorientations:

$$F(\theta)=\begin{cases}\dfrac{1}{4\phi_{max}^2}(2\phi_{max}+\theta), & -2\phi_n \le \theta \le 0,\\ \dfrac{1}{4\phi_{max}^2}(2\phi_{max}-\theta), & 0 \le \theta \le 2\phi_n,\\ 0, & \text{otherwise.}\end{cases} \tag{B.6}$$

Again, no subscript is given for θ since this result applies to any of the boundaries at the triple junction. If an angular threshold, θ_t, is then applied below which boundaries are classified as low-angle, the global special boundary fraction, *p*, can be found as the fraction of boundaries in the global distribution with absolute disorientations less than θ_t:

$$p=\frac{\int_{-\infty}^{\theta_t} F(\theta)d\theta}{\int_{-\infty}^{\infty} F(\theta)d\theta}. \tag{B.7}$$

If Eq. (B.7) is applied to the density distribution in Eq. (B.6), the resulting global low-angle fraction is obtained in terms of θ_t and ϕ_{max}:

$$p=\frac{\theta_t}{\phi_{max}}-\left(\frac{\theta_t}{2\phi_{max}}\right)^2. \tag{B.8}$$

It is evident from Eq. (B.8) that, for a given low-angle threshold, θ_t, the value of the special fraction may be adjusted by redefining the orientation tolerance, ϕ_{max}. The relationship between the special fraction and the ratio of ϕ_{max} to θ_t is shown in Figure B.2, where the solid line is Eq. (B.8) and the points are for simulated fiber textured polycrystals.

B.2. Local Transition Probabilities

It is important to note that Eqs. (B.6) and (B.8) define the *global* disorientation density distribution and special boundary fraction, properties that are averaged over a large ensemble. Therefore, within the same framework used above, we now develop analytical expressions for the local density distribution functions, Π_x^y, by considering the role of the crystallographic constraint on the distributions $F(\theta)$ at individual triple junctions. Our procedure will be as follows. Starting with the generic triple junction in Figure B.1, we first assign two of the three

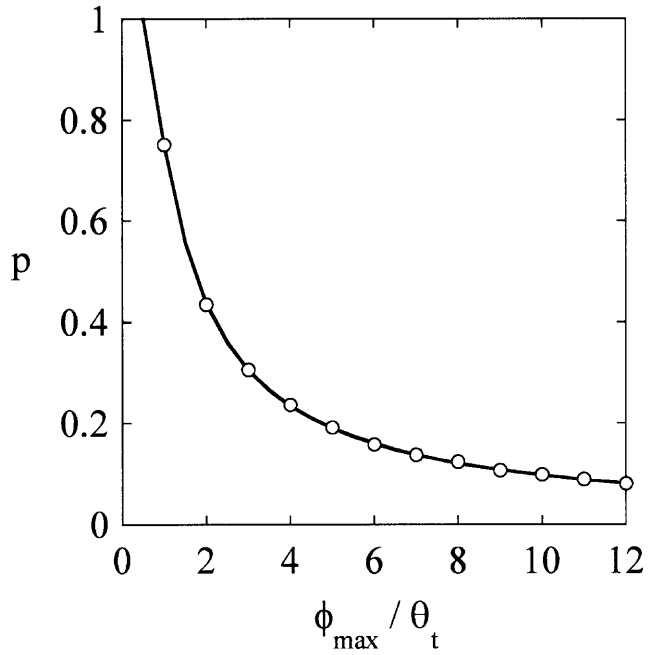

Figure B.2: Fraction of low-angle boundaries, p, as a function of the ratio of the allowed grain rotation, ϕ_{max}, to the low-angle threshold, θ_t. The points are from simulated fiber textured microstructures and the solid line is given by Eq. (B.8).

degrees of freedom of the system by making a choice as to the disorientation of boundary *a*. We then derive the effect that this has on the subsequent choice of a second disorientation, θ_b, by determining the density distribution function $f(\theta_b)$ at a given value of θ_a, from which the global distribution, $F(\theta_b)$ may subsequently be obtained. When these two misorientations are chosen, the third, θ_c, is given explicitly by Eq. (3.2).

To begin, we assume a unique and known value for θ_a, fixing the relationship between ϕ_B and ϕ_C. Then the range of allowed values for ϕ_C (bounded by $\phi_{C,min}$ and $\phi_{C,max}$) may be found from Eq. (B.1) by noting that ϕ_B exists on the range $(-\phi_{max}, \phi_{max})$:

$$\phi_{C,max} = \begin{cases} \phi_{max}, & \theta_a \le 0, \\ \phi_{max} - \theta_a, & \theta_a > 0, \end{cases} \tag{B.9a}$$

$$\phi_{C,min} = \begin{cases} -\phi_{max} - \theta_a, & \theta_a \le 0, \\ -\phi_{max}, & \theta_a > 0. \end{cases} \tag{B.9b}$$

Eq. (B.9) indicates that the random assignment of one disorientation, θ_a, already places a restriction upon the remaining degree of freedom in the system; instead of being randomly distributed on the range ($-\phi_{max}$, ϕ_{max}), ϕ_C distributes only over the ranges given in Eq. (B.9). We now seek the density distribution of θ_b *for a known value of* θ_a, which is denoted as $f(\theta_b)$ to distinguish it from the global density distribution $F(\theta_b)$. The function $f(\theta_b)$ is defined implicitly by the fact that when integrated over all acceptable values of θ_a, it yields $F(\theta_b)$:

$$F(\theta_b) = \int_{-\infty}^{\infty} f(\theta_b) d\theta_a . \tag{B.10}$$

The distribution $f(\theta_b)$ can be found through the convolution of $F(\phi_A)$ with $F(\phi_C)$, which is a uniform random distribution on the range given in Eq. (B.9):

$$f(\theta_b) = \frac{F(\theta_a)}{2\phi_n} \int_{-\phi_{max}}^{\phi_{max}} F(\theta_b + \phi_A) d\phi_A . \tag{B.11}$$

Here, $F(\phi_A)$ has already been replaced by $\frac{1}{2\phi_{max}}$ and the limits of the integral changed to $-\phi_{max}$ to ϕ_{max}, those of ϕ_A. The limits for ϕ_C given in Eq. (B.9) apply to the integrand, whose value is:

$$F(\theta_b + \phi_A) = \begin{cases} \dfrac{1}{(2\phi_{max} - \theta_a)}, & -\phi_{max} \le \theta_b + \phi_A \le \phi_{max} - \theta_a , \\ 0, & \text{otherwise.} \end{cases} \tag{B.12}$$

Eq. (B.12) is for the case where $\theta_a \ge 0$ and the rest of the derivation is for this case; these steps can be easily repeated for $\theta_a \le 0$. The range of allowable values for θ_b depends on the value of ϕ_A which is uniformly distributed on ($-\phi_{max}$, ϕ_{max}) and is:

$$-\phi_{max} - \phi_A \le \theta_b \le \phi_{max} - \theta_a - \phi_A . \tag{B.13}$$

These maximum and minimum values limit the region where the solution to Eq. (B.11) is valid. Specifically, when $\phi_A = \phi_{max}$, $f(\theta_b)$ is defined on the range ($-2\phi_{max}$, $-\theta_a$) as [2]:

---

[2] These equations (Eq. (B.14)) were originally published in Ref. [114] with a typographical error. Each of the equations for $f(\theta_b)$ should contain the term $(2\phi_{max})^{-3}$, as opposed to $(2\phi_{max})^{-1}$ reported in the previous publication.

$$f(\theta_b) = \frac{F(\theta_a)}{2\phi_{max}(2\phi_{max} - \theta_a)} \int_{-\phi_{max}-\theta_b}^{\phi_{max}} d\phi_c = \frac{1}{(2\phi_{max})^3}(2\phi_{max} + \theta_b), \tag{B.14a}$$

and when $\phi_A = -\phi_{max}$, $f(\theta_b)$ is defined on the range $(0, 2\phi_{max} - \theta_a)$ as:

$$f(\theta_b) = \frac{F(\theta_a)}{2\phi_{max}(2\phi_{max} - \theta_a)} \int_{-\phi_{max}}^{\phi_{max}-\theta_a-\theta_b} d\phi_c = \frac{1}{(2\phi_{max})^3}(2\phi_{max} - \theta_a - \theta_b). \tag{B.14b}$$

Evaluation of Eqs.(B.14a) and (B.14b) at $\theta_b = -\theta_a$ and 0, respectively (i.e., the limit of their ranges of applicability), reveals that for θ_b on $(-\theta_a, 0)$:

$$f(\theta_b) = \frac{1}{(2\phi_{max})^3}(2\phi_{max} - \theta_a). \tag{B.14c}$$

For any value of θ_b less than $-2\phi_{max}$ or greater than $2\phi_{max} - \theta_a$, $f(\theta_b)$ will be zero. Following the same procedure for $\theta_a < 0$, we find:

$$f(\theta_b) = \frac{1}{(2\phi_{max})^3} \begin{cases} 0, & -2\phi_{max} < \theta_b < -2\phi_{max} - \theta_a, \quad \text{(B.14d)} \\ 2\phi_{max} + \theta_a + \theta_b, & -2\phi_{max} - \theta_a < \theta_b < 0, \quad \text{(B.14e)} \\ 2\phi_{max} + \theta_a, & 0 < \theta_b < -\theta_a, \quad \text{(B.14f)} \\ 2\phi_{max} - \theta_b, & -\theta_a < \theta_b < 2\phi_{max}. \quad \text{(B.14g)} \end{cases}$$

Eq. (B.14) is plotted in Figure B.3 for all values of θ_a. From both Eq. (B.14) and Figure B.3, we can see how the choice of θ_a limits the values that θ_b may assume; the limits of θ_b as a function of θ_a are:

$$\theta_{b,max} = \begin{cases} 2\phi_{max}, & \theta_a < 0, \\ 2\phi_{max} - \theta_a, & \theta_a > 0, \end{cases} \tag{B.15a}$$

$$\theta_{b,min} = \begin{cases} -2\phi_{max} - \theta_a, & \theta_a < 0, \\ -2\phi_{max}, & \theta_a > 0. \end{cases} \tag{B.15b}$$

In order to validate the distributions in Eq. (B.14), we apply Eq. (B.10) and recover the global density distribution in Eq. (B.6). Eq. (B.14) is critical in determining the final triple junction

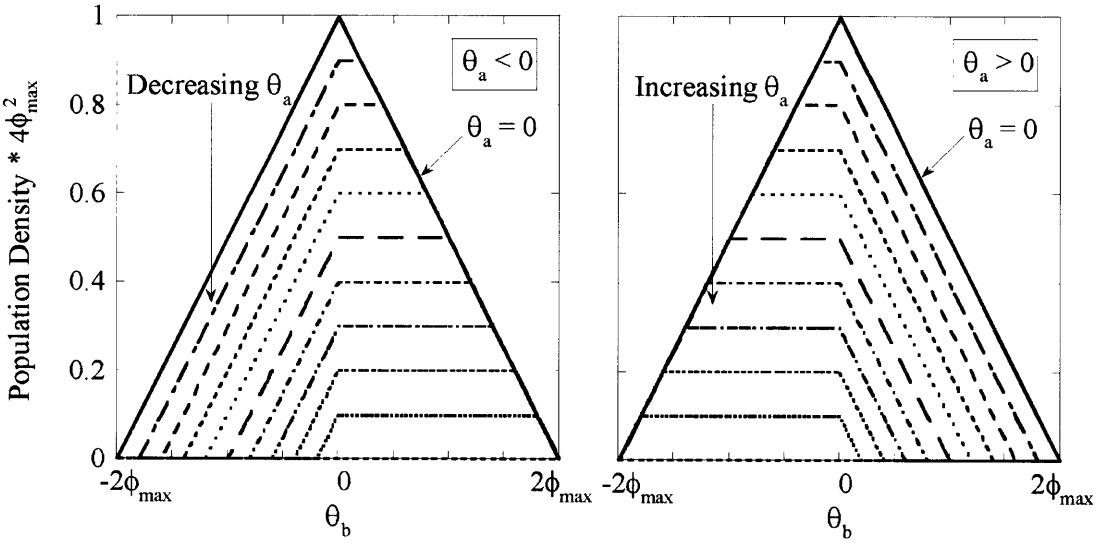

Figure B.3: The distribution of disorientation angles of grain boundary b, $f(\theta_b)$, for different values of θ_a as given by Eq. (B.14). The different line styles correspond to evenly spaced increments of θ_a from 0 to $-2\phi_{max}$ (left) or 0 to $2\phi_{max}$ (right).

distribution, as it gives the distribution of θ_b for a given value of θ_a. Once the first two disorientations are assigned, the third is given explicitly by Eq. (3.2), and its density distribution is $f(\theta_c) = f(-\theta_a - \theta_b)$. The locally constrained distribution of θ_c for a given value of θ_a, $f(\theta_c)$, is described by the same set of equations as given for $f(\theta_b)$ (Eq. (B.14)), and the net distributions $F(\theta)$ obtained from the locally constrained ones, $f(\theta)$, using Eq. (B.10).

With the local density distributions determined at a given triple junction, we now need to identify what fraction of them will be classified as special boundaries, and derive the global coordination among such boundaries. To this end, we now divide the global distributions $F(\theta)$ into several complementary distributions F_x^y for which y boundaries have been previously assigned, x of which were assigned as special boundaries. This is merely a convenient separation of the sub-distributions of different special and general boundary coordinations, and the full distribution can be easily recovered from:

$$\sum_{x=0}^{y} F_x^y(\theta) = F(\theta) \qquad \text{(B.16)}$$

for any given value of y (= 0, 1, or 2). There are six functions F_x^y (where y ranges from 0 to 2, and x ranges from 0 to y), and all are readily derived in closed form through the use of Eqs. (B.10) and (B.14). When zero of the three boundaries have been assigned, the distribution of grain boundary angles for the next boundary to be assigned will simply be given by Eq. (B.6), which exactly defines F_0^0:

$$F_0^0(\theta) = \frac{1}{(2\phi_{max})^2} \begin{cases} (2\phi_{max} + \theta), & -2\phi_{max} \le \theta_c < 0, \\ (2\phi_{max} - \theta), & 0 \le \theta_c \le 2\phi_{max}. \end{cases} \tag{B.17}$$

When one of the boundaries, b, has been assigned, the situation is more complex and is more easily understood with the help of Figure B.4. In Figure B.4, the disorientation of boundary a is plotted as a function of the disorientation of boundary b. The axis out of the page in this figure would correspond to the value of $f(\theta)$. The unshaded areas are those points which are physically impossible combinations of θ_a and θ_b, and the borders of those areas are given by Eq. (B.15). In Figure B.4, the θ_b axis is divided into two regions: one with $|\theta_b| \le \theta_t$ and one with $|\theta_b| \ge \theta_t$. $F_0^1(\theta_a)$ represents the distribution of disorientation angles for boundary a for the case where boundary b has been assigned as a general boundary with an absolute disorientation greater than θ_t; these points lie in the region with the darkest shading. Since the plot is symmetric, $F_0^1(\theta_a)$ can be found by considering only the region with $\theta_a < 0$ and integrating $f(\theta_b)$ over the ranges $(-2\phi_{max}, -\theta_t)$ and $(\theta_t, 2\phi_{max})$. When $\theta_t < \phi_{max}$, the piecewise distribution for $F_0^1(\theta_a)$ is:

$$F_0^1(\theta_a) = \frac{1}{(2\phi_{max})^3} \begin{cases} -(\theta_a + 2\phi_{max})(\theta_a - 2\phi_{max} + 2\theta_t), & -2\phi_{max} \le \theta_a < -2\phi_{max} + \theta_t, \quad \text{(B.18a)} \\ 4\theta_a\phi_{max} + 8\phi_{max}^2 - 4\theta_a\theta_t - 8\phi_{max}\theta_t + \theta_t^2, & -2\phi_{max} + \theta_t \le \theta_a < -\theta_t, \quad \text{(B.18b)} \\ (\theta_a + 2\phi_{max} - \theta_t)^2 + (\theta_t - 2\phi_{max})^2, & -\theta_t \le \theta_a < 0. \quad \text{(B.18c)} \end{cases}$$

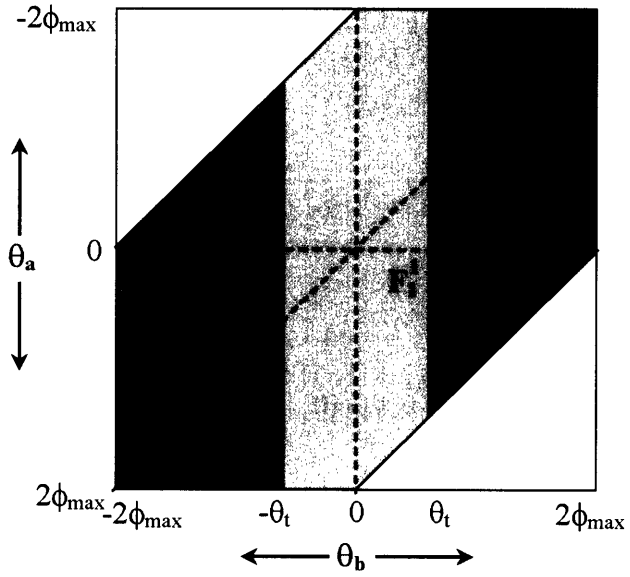

Figure B.4: Disorientation of boundary *a*, θ_a, as a function of disorientation of boundary *b*, θ_b. The distribution F_x^1 can be found by integration of Eq. (B.14) over the regions shown in this map according to Eq. (B.10). The shaded regions are differentiated by whether boundary *b* has previously been assigned as special (labeled F_1^1) or as general (labeled F_0^1). The white regions are physically impossible combinations as given by Eq. (B.15). It is important to note that the shaded areas do not give the function explicitly, they give only the limits of integration on the disorientation angles.

The distribution $F_0^1(\theta_a)$ when $\theta_t > \phi_{max}$ is:

$$F_0^1(\theta_a) = \frac{1}{(2\phi_{max})^3} \begin{cases} -(\theta_a + 2\phi_{max})(\theta_a - 2\phi_{max} + 2\theta_t), & -2\phi_{max} \le \theta_a < -\theta_t, \quad \text{(B.19a)} \\ (\theta_t - 2\phi_{max})^2, & -\theta_t \le \theta_a < -2\phi_{max} + \theta_t, \quad \text{(B.19b)} \\ (\theta_a + 2\phi_{max} - \theta_t)^2 + (\theta_t - 2\phi_{max})^2, & -2\phi_{max} + \theta_t \le \theta_a < 0. \quad \text{(B.19c)} \end{cases}$$

Similarly, $F_1^1(\theta_a)$ represents the distribution of disorientation angles for boundary *a* when boundary *b* has been assigned as a special boundary with a disorientation on $(-\theta_t, \theta_t)$; these points are in the lightly shaded region in Figure B.4. Using the symmetry of the map as before and integrating $f(\theta_b)$ over the range $(-\theta_t, \theta_t)$, $F_1^1(\theta_a)$, for $\theta_t < \phi_{max}$, is found as:

$$F_1^1(\theta_a) = \frac{1}{(2\phi_{max})^3} \begin{cases} (\theta_a + 2\phi_{max})^2 + \theta_t(\theta_a + 2\phi_{max}), & -2\phi_{max} \le \theta_a < -2\phi_{max} + \theta_t, \quad \text{(B.20a)} \\ \theta_t(4\theta_a + 8\phi_{max} - \theta_t), & -2\phi_{max} + \theta_t \le \theta_a < -\theta_t, \quad \text{(B.20b)} \\ -(\theta_a^2 - 2\theta_a\theta_t + 2\theta_t(\theta_t - 4\phi_{max})), & -\theta_t \le \theta_a < 0. \quad \text{(B.20c)} \end{cases}$$

The distribution $F_1^1(\theta_a)$ when $\theta_t > \phi_{max}$ is:

$$F_1^1(\theta_a) = \frac{1}{(2\phi_{max})^3} \begin{cases} (\theta_a + 2\phi_{max})^2 + \theta_t(\theta_a + 2\phi_{max}), & -2\phi_{max} \le \theta_a < -\theta_t, \quad \text{(B.21a)} \\ 4\phi_{max}(\theta_a + \phi_{max} + \theta_t) - \theta_t^2, & -\theta_t \le \theta_a < -2\phi_{max} + \theta_t, \quad \text{(B.21b)} \\ -(\theta_a^2 - 2\theta_a\theta_t + 2\theta_t(\theta_t - 4\phi_{max})), & -2\phi_{max} + \theta_t \le \theta_a < 0. \quad \text{(B.21c)} \end{cases}$$

The situation is still more complex when two of the boundaries, *a* and *b*, have previously been assigned. In Figure B.5, the disorientation of boundary *c* (to be determined) is plotted as a function of θ_a. Due to the strict crystallographic constraint in the problem (Eq. (3.2)), the value of θ_b for each pair of θ_a and θ_c is known explicitly. Therefore, at every point in the map, we can determine the number of boundaries previously assigned as special boundaries. In this case, 0, 1 or 2 of them could have been assigned as special boundaries; these three cases are illustrated by the shaded areas in Figure B.5, where the darkest shading is for zero special boundaries and the lightest shading for two special boundaries. It is important to note that the regions are labeled based only on the character of boundaries *a* and *b*, independent of the value of θ_c. As before, the white regions are physically impossible combinations of disorientation angles. Using the same procedure as described for $F_x^1(\theta_a)$, the functions $F_x^2(\theta_c)$ can be found by integrating over the appropriate ranges of $f(\theta_a)$. The distribution $F_0^2(\theta_c)$ gives the probability of finding a disorientation of θ_c given that neither boundary *a* nor *b* was classified as a special boundary. When $\theta_t < \phi_{max}$, $F_0^2(\theta_c)$ is:

$$F_0^2(\theta_c)=\frac{1}{(2\phi_{max})^3}\begin{cases}-(\theta_c+2\phi_{max})(\theta_c+2\theta_t), & -2\phi_{max}\le\theta_c<-2\phi_{max}+\theta_t, \quad \text{(B.22a)}\\ 2\theta_c\phi_{max}+4\phi_{max}^2-4\theta_c\theta_t-8\phi_{max}\theta_t+\theta_t^2, & -2\phi_{max}+\theta_t\le\theta_c<-2\theta_t, \quad \text{(B.22b)}\\ (\theta_c+2\phi_{max}-\theta_t)^2, & -2\theta_t\le\theta_c<0. \quad \text{(B.22c)}\end{cases}$$

The distribution $F_0^2(\theta_c)$ when $\theta_t > \phi_{max}$ is:

$$F_0^2(\theta_c)=\frac{1}{(2\phi_{max})^3}\begin{cases}0, & -2\phi_{max}\le\theta_c<-2\phi_{max}+\theta_t, \quad \text{(B.23a)}\\ (\theta_c+2\phi_{max}-\theta_t)^2, & -2\phi_{max}+\theta_t\le\theta_c\le 0. \quad \text{(B.23b)}\end{cases}$$

The distribution $F_1^2(\theta_c)$ when $\theta_t < \phi_{max}$ is:

$$F_1^2(\theta_c)=\frac{1}{(2\phi_{max})^3}\begin{cases}(\theta_c+2\phi_{max})(\theta_c+2\phi_{max}+2\theta_t), & -2\phi_{max}\le\theta_c<-2\phi_{max}+\theta_t, \quad \text{(B.24a)}\\ \theta_t(4\theta_c+8\phi_{max}-\theta_t), & -2\phi_{max}+\theta_t\le\theta_c<-2\theta_t, \quad \text{(B.24b)}\\ -(2\theta_c^2+4\theta_c\phi_{max}+\theta_t^2), & -2\theta_t\le\theta_c<-\theta_t, \quad \text{(B.24c)}\\ -\theta_c(\theta_c+4\phi_{max}-2\theta_t), & -\theta_t\le\theta_c\le 0. \quad \text{(B.24d)}\end{cases}$$

The distribution $F_1^2(\theta_c)$ when $\theta_t > \phi_{max}$ is:

$$F_1^2(\theta_c)=\frac{1}{(2\phi_{max})^3}\begin{cases}-(\theta_c+2\phi_{max})(\theta_c-2\phi_{max}+2\theta_t), & -2\phi_{max}\le\theta_c<-\theta_t, \quad \text{(B.25a)}\\ (\theta_t-2\phi_{max})^2, & -\theta_t\le\theta_c<-2\phi_{max}+\theta_t, \quad \text{(B.25b)}\\ -\theta_c(\theta_c+4\phi_{max}-2\theta_t), & -2\phi_{max}+\theta_t\le\theta_c<0. \quad \text{(B.25c)}\end{cases}$$

The distribution $F_2^2(\theta_c)$ when $\theta_t < \phi_{max}$ is:

$$F_2^2(\theta_c) = \frac{1}{(2\phi_{max})^3} \begin{cases} 0, & -2\phi_{max} \le \theta_c < -2\theta_t, \quad \text{(B.26a)} \\ (\theta_c + 2\phi_{max})(\theta_c + 2\theta_t), & -2\theta_t \le \theta_c < -\theta_t, \quad \text{(B.26b)} \\ 2\theta_c\phi_{max} + 4\phi_{max}\theta_t - \theta_t^2, & -\theta_t \le \theta_c \le 0. \quad \text{(B.26c)} \end{cases}$$

The distribution $F_2^2(\theta_c)$ when $\theta_t > \phi_{max}$ is:

$$F_2^2(\theta_c) = \frac{1}{(2\phi_{max})^3} \begin{cases} (\theta_c + 2\phi_{max})(\theta_c + 2\theta_t), & -2\phi_{max} \le \theta_c < -\theta_t, \quad \text{(B.27a)} \\ 2\theta_c\phi_{max} + 4\phi_{max}\theta_t - \theta_t^2, & -\theta_t \le \theta_c \le 0. \quad \text{(B.27b)} \end{cases}$$

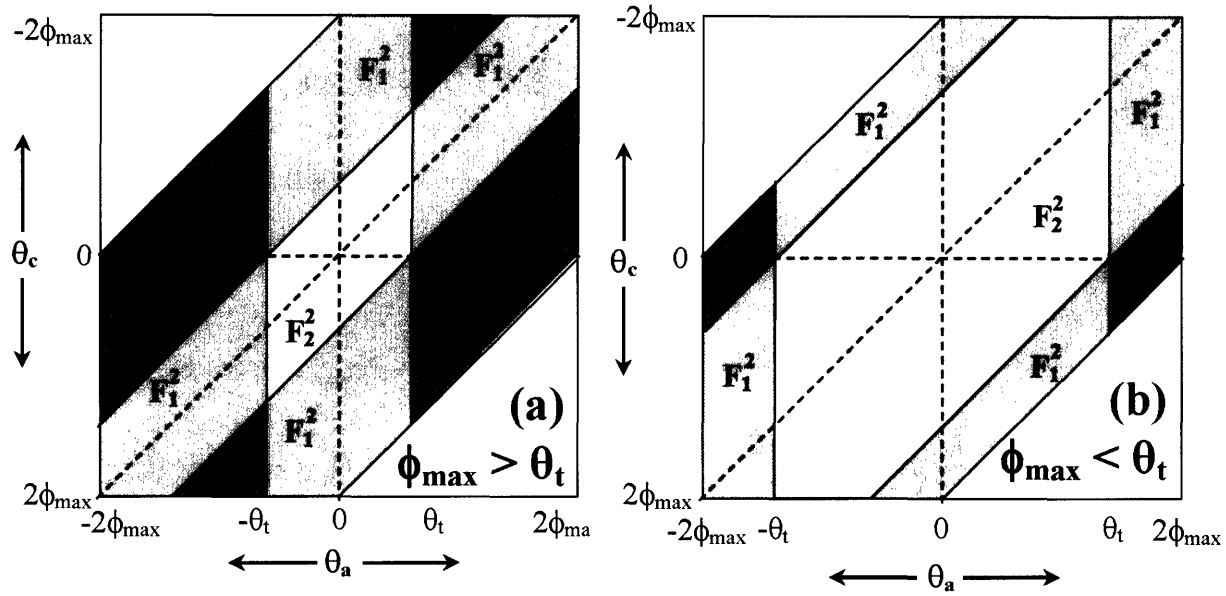

Figure B.5: These maps are used in determining the functions F_x^2. When the disorientation of boundary *c*, θ_c, is plotted as a function of θ_a, the disorientation of boundary *b* is also known explicitly at every point due to the requirement of crystallographic consistency (Eq. (B.2)). The different shadings correspond to how many of boundaries *a* and *b* are classified as special boundaries based on their disorientation angles. The different regions give the limits of integration on Eq. (B.10) to find F_x^2.

Once the functions F_x^y are known, the local transition probabilities, Π_x^y, can be found with the same construction that was used in determining the global special fraction:

$$\Pi_x^y = \frac{\int_{-\theta_t}^{\theta_t} F_x^y(\theta)d\theta}{\int_{-2\phi_{max}}^{2\phi_{max}} F_x^y(\theta)d\theta}. \tag{B.28}$$

To clarify the method, consider first the distribution, $F_0^0(\theta_a)$, the distribution of θ_a given no previously assigned boundaries; this distribution is given exactly by Eq. (B.17). Applying Eq. (B.28) to Eq. (B.17), Π_0^0 is found to equal p. Next, to understand the application of Eq. (B.28) for $y \geq 1$, consider the maps presented in Figure B.6 for $y = 1$ and $y = 2$. For example, to determine Π_0^1, the region of $F_0^1(\theta_a)$ from Figure B.4 is now integrated only over values of $|\theta_a| \leq \theta_t$. The area over which integration occurs is shown by the darker shaded region labeled Π_0^1 in Figure B.6a. Similarly, to determine Π_1^1, the distribution $F_1^1(\theta_a)$ is integrated over the lightly shaded region (i.e., those points with $|\theta_a| \leq \theta_t$). Figures B.6a and b are for ϕ_{max} greater and less than θ_t, respectively, and are provided to illustrate how the limits of integration differ in these two cases. Similar maps are given in Figure B.6c and B.6d for the regions of integration leading to Π_x^2, the probability of boundary c being assigned as special given x of the two boundaries previously assigned are special boundaries. Again, the points with $|\theta_c| \leq \theta_t$ correspond to boundary c being assigned as special. Analytical evaluation of Eq. (B.28) for all possible triple junction coordinations yields the expressions for Π_x^y as given in Chapter 3 (Eq. (3.3)).

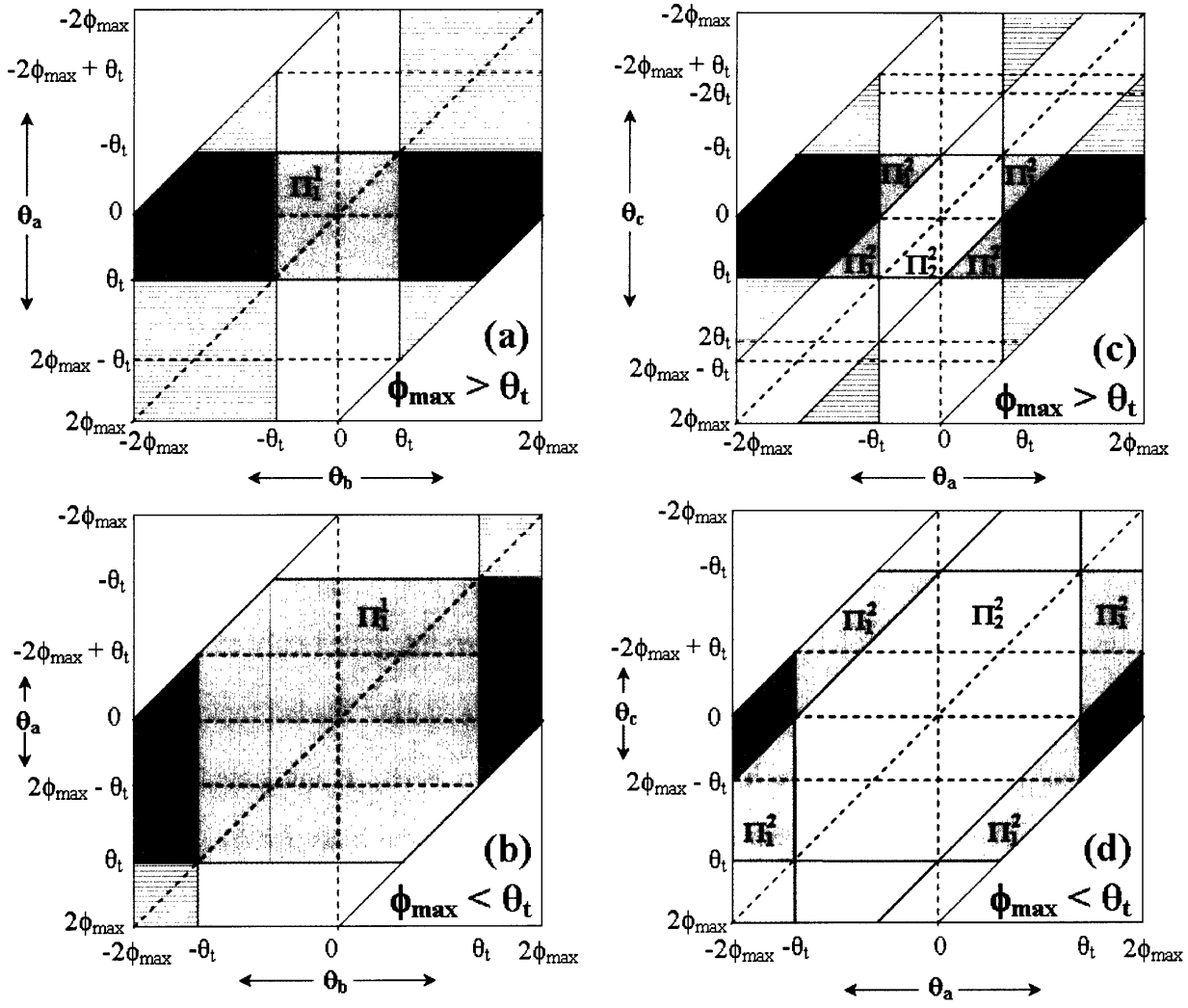

Figure B.6: To determine the local transition probability, Π_x^y, the distribution F_x^y is integrated according to Eq. (B.28). For $\phi_{max} > \theta_t$ (a and c) or $\phi_{max} < \theta_t$ (b and d), these maps show the limits of integration on the function F_x^y. The regions with solid shading are points where the next boundary assigned will be classified as a special boundary. These maps should be compared to those in Figures B.4 and B.5 which showed the regions of integration to find F_x^y. It is important to note that the shaded areas do not give the function explicitly; they give only the limits of integration on the disorientation angles.

APPENDIX C: Maximum Entropy Distribution

The configurational entropy is used to quantify the state of a distribution by comparing the entropy of the given distribution to that of a reference state, such as the maximum entropy state, with ground-state entropy S_o. The procedure to calculate S_o is general and can be applied to any distribution of species (i.e., triple junctions, quadruple nodes, higher-order configurations) in a general population. To determine the maximum entropy reference state, the configurational entropy should be maximized with respect to the distribution of interest (i.e., the triple junction or quadruple node distribution) where the fraction of each species is X_k ($k = 0$ to $N - 1$, where N is the number of species). For triple junctions, $N = 4$ and the X_k are simply J_0, J_1, J_2 and J_3. The expression to be maximized is:

$$S = -\sum_{k=0}^{N-1} X_k \ln(X_k) \tag{C.1}$$

subject to the constraints:

$$\sum_{k=0}^{N-1} X_k = 1 \tag{C.2a}$$

$$\sum_{k=0}^{N-1} iX_k = z \cdot p \tag{C.2b}$$

Here z is the number of total boundaries that coordinate the junction ($z = 3$ for triple junctions and 6 for quadruple nodes) and i is the number of special boundaries that coordinate the junction for species k. The maximization of Eq. (C.1) is accomplished using the method of Lagrange multipliers. Different Lagrange multipliers are applied to both Eqs. (C.2a) and (C.2b); following a standard procedure for maximization problems and substituting for one of the multipliers results in the following expression relating μ, the other Lagrange multiplier, to p:

$$z \cdot p = \frac{\sum_{i=0}^{z} m \cdot i \cdot \mathrm{Exp}(-i\mu)}{\sum_{i=0}^{D} m \cdot \mathrm{Exp}(-i\mu)} \tag{C.3}$$

where m is the number of topologically unique isomers for a given value of i. For all types of triple junctions, $m = 1$; however, isomerism of some quadruple nodes results in values of $m \geq 1$. In principle, μ can be found as a function of p from:

$$\mu = \mathrm{Ln}(\mathrm{Root}(Z(\mu, p))) \tag{C.4}$$

where (Root(Z(μ,p))) is a positive, real root of the polynomial:

$$Z(\mu, p) = \sum_{i=0}^{z} m \cdot \mu^{i} (z \cdot p - z + i) \tag{C.5}$$

In the special case of triple junctions, a closed-form analytical expression for the positive, real root of Eq. (C.5) can be found as:

$$\mu = \mathrm{Ln}\left(\frac{1}{9p} \left(1 - 3p + Y + \frac{1 + 12p - 18p^2}{Y} \right) \right) \tag{C.6}$$

where

$$Y = \left[1 + 18p + 270p^2 (1-p) + 9p\left(6\left(1 + 18p + 144p^2 - 324p^3 + 162p^4\right)\right)^{1/2} \right]^{1/3} \tag{C.7}$$

The dependence of μ on p for the maximum entropy triple junction distribution is shown by the dashed line in Figure C.1. In the case of quadruple nodes, we have not found a closed-form analytical solution for the roots of Eq. (C.5), although the value of μ can easily be found numerically for any value of p, and the functional form of $\mu(p)$ for the maximum entropy quadruple node distribution is given by the solid line in Figure C.1. Although the analytical form of $\mu(p)$ is unknown for the maximum entropy QND, $\mu(p)$ is well approximated by the function:

$$\mu(p) = c \cdot \mathrm{Ln}\left(\frac{1-p}{p} \right) \tag{C.8}$$

where $c = 0.5835$ is a fitting parameter. Once μ is known for the distribution of interest, the population of each species can be found as a function of p from:

$$X_k = \frac{\mathrm{Exp}(-i\mu)}{\sum_{i=0}^{z} m \cdot \mathrm{Exp}(-i\mu)} \tag{C.9}$$

The individual distributions which result in the maximum entropy are given by Eq. (C.9), and when introduced into Eq. (C.1) yield the maximum configurational entropy.

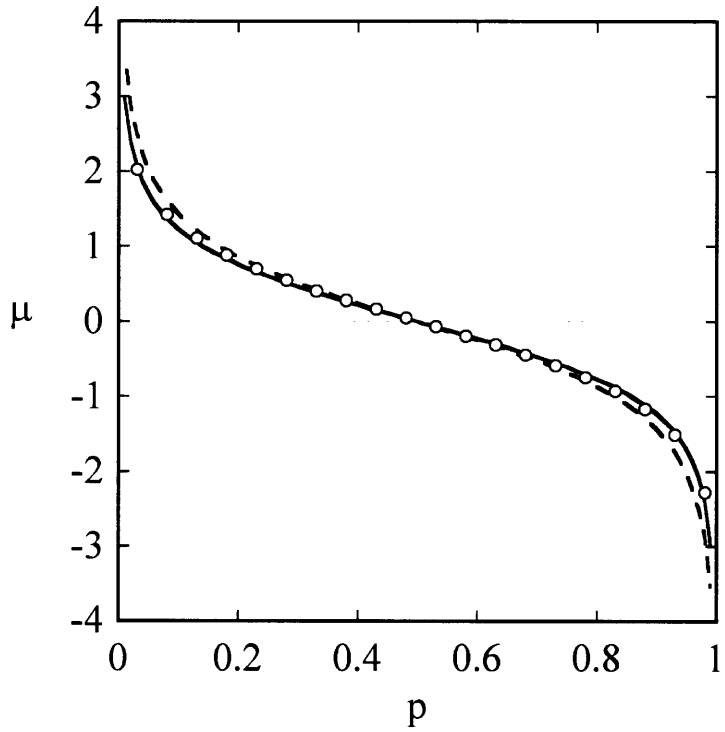

Figure C.1: The variation of the Lagrange multiplier μ with the fraction of special boundaries for the both the TJD (dashed line) and the QND (solid line). The open points represent the fit of μ for the QND as given by Eq. (C.8).

Appendix D: Topological Parameter Expressions for the Triple Junction Distribution

As explained in the text, the nature of the local correlations is fully specified by two topological parameters, η_{SO} and η_{CE}, and the fraction of boundaries, p. The topological parameters were defined in terms of the triple junction distribution (Eq. (6.1)) and since the two definitions of the local correlations are interchangeable, the triple junction distribution can also be derived in terms of the topological parameters. Before presenting the equations for the TJD, it is useful to introduce the following terms:

$$\delta_E = -1 - \eta_{CE}(1-p) \tag{D.1}$$

$$\delta_C = 1 - \eta_{CE} p \tag{D.2}$$

$$\delta_O = 1 + \eta_{SO}(1 - 3p + 3p^2) \tag{D.3}$$

$$\delta_S = -1 + 3\eta_{SO} p(1-p) \tag{D.4}$$

If $\eta_{SO} < 0$ and $\eta_{CE} < 0$ (ordered and elongated), the triple junction distribution is:

$$J_0^{OE} = 1 - p - \frac{p(1-p)(p - 2\eta_{CE}(1-p) - 2)}{\delta_O \delta_E} \tag{D.5}$$

$$J_1^{OE} = \frac{-3p(1-p)^2(1+\eta_{CE})}{\delta_O \delta_E} \tag{D.6}$$

$$J_2^{OE} = \frac{-3p^2(1-p)}{\delta_O \delta_E} \tag{D.7}$$

$$J_3^{OE} = p + \frac{p(1-p)(\eta_{CE}(1-p) + p + 1)}{\delta_O \delta_E} \tag{D.8}$$

If $\eta_{SO} < 0$ and $\eta_{CE} > 0$ (ordered and clumpy), the triple junction distribution is:

$$J_0^{OC} = 1 - p - \frac{p(1-p)(2 - p - \eta_{CE} p)}{\delta_O \delta_C} \tag{D.9}$$

$$J_1^{OC} = \frac{3p(1-p)^2}{\delta_O \delta_C} \tag{D.10}$$

$$J_2^{OC} = \frac{3(1-\eta_{CE})p^2(1-p)}{\delta_O \delta_C} \tag{D.11}$$

$$J_3^{OC} = p - \frac{p(1-p)(1+p-2\eta_{CE}p)}{\delta_O \delta_C} \tag{D.12}$$

If $\eta_{SO} > 0$ and $\eta_{CE} < 0$ (segregated and elongated), the triple junction distribution is:

$$J_0^{SE} = 1 - p - \frac{p(1-p)(2+2\eta_{CE}(1-p)-p)(1-\eta_{SO})}{\delta_S \delta_E} \tag{D.13}$$

$$J_1^{SE} = \frac{3p(1-p)^2(1-\eta_{CE})(1-\eta_{SO})}{\delta_S \delta_E} \tag{D.14}$$

$$J_2^{SE} = \frac{3p^2(1-p)(1-\eta_{SO})}{\delta_S \delta_E} \tag{D.15}$$

$$J_3^{SE} = p - \frac{p(1-p)(1+\eta_{CE}(1-p)+p)(1-\eta_{SO})}{\delta_S \delta_E} \tag{D.16}$$

If $\eta_{SO} > 0$ and $\eta_{CE} > 0$ (segregated and clumpy), the triple junction distribution is:

$$J_0^{SC} = 1 - p - \frac{p(1-p)(p+\eta_{CE}p-2)(1-\eta_{SO})}{\delta_S \delta_C} \tag{D.17}$$

$$J_1^{SC} = \frac{-3p(1-p)^2(1-\eta_{SO})}{\delta_S \delta_C} \tag{D.18}$$

$$J_2^{SC} = \frac{-3p^2(1-p)(1-\eta_{CE})(1-\eta_{SO})}{\delta_S \delta_C} \tag{D.19}$$

$$J_3^{SC} = p + \frac{p(1-p)(1+p-2\eta_{CE}p)(1-\eta_{SO})}{\delta_S \delta_C} \tag{D.20}$$

Appendix E: Correlations beyond the Nearest-Neighbor Level in Grain Boundary Networks

The approach to studying correlations in grain boundary networks is based upon the understanding of crystallographic constraints that are present in any microstructure, and which restrict the way in which grain boundary types may be assembled into a network. These constraints are formally expressed by the need for orientation conservation around a Frank-Nabarro circuit through the microstructure as discussed in Chapter 1. The simplest possible non-trivial circuit of this kind is that which encircles a triple junction (see Figure 1.3); this is referred to as a constraint of first order, and the boundary correlations that arise from this constraint were explained in detail in Chapter 3. In this appendix, we examine higher-order constraints, which represent larger Frank-Nabarro circuits that traverse more grains and grain boundaries (similar to the circuit around the quadruple node in Figure 4.1). In general, we will identify the order of the constraint, B, with the number of triple junctions encircled by the circuit; Figure E.1 illustrates the first three orders of constraint for a 2-D honeycomb network.

Following upon prior work in the field, boundary correlations are quantified through examination of local statistics. At the first-order level there are four topologically unique species of triple junctions as shown in Figure E.1, and their statistics are described by the triple junction distribution. A similar statistical analysis is possible for the higher-order circuits in Figure E.1, although the analysis becomes considerably more complicated due to the rapidly increasing number of topologically unique species (called N, and specified below each unit in Figure E.1). For example, at the third-order level there are $N = 72$ unique species (allowing for mirror-symmetric redundancy), as drawn explicitly in Figure E.1.

E.1. Analysis of Boundary Correlations

To proceed, we would like to quantitatively evaluate the strength of each constraint shown in Figure E.1. For this purpose we will use the configurational entropy, S, of the largest, third-order units:

$$S_3^B = \sum_{i=0}^{71} V_i^B \ln V_i^B \qquad \text{(E.1)}$$

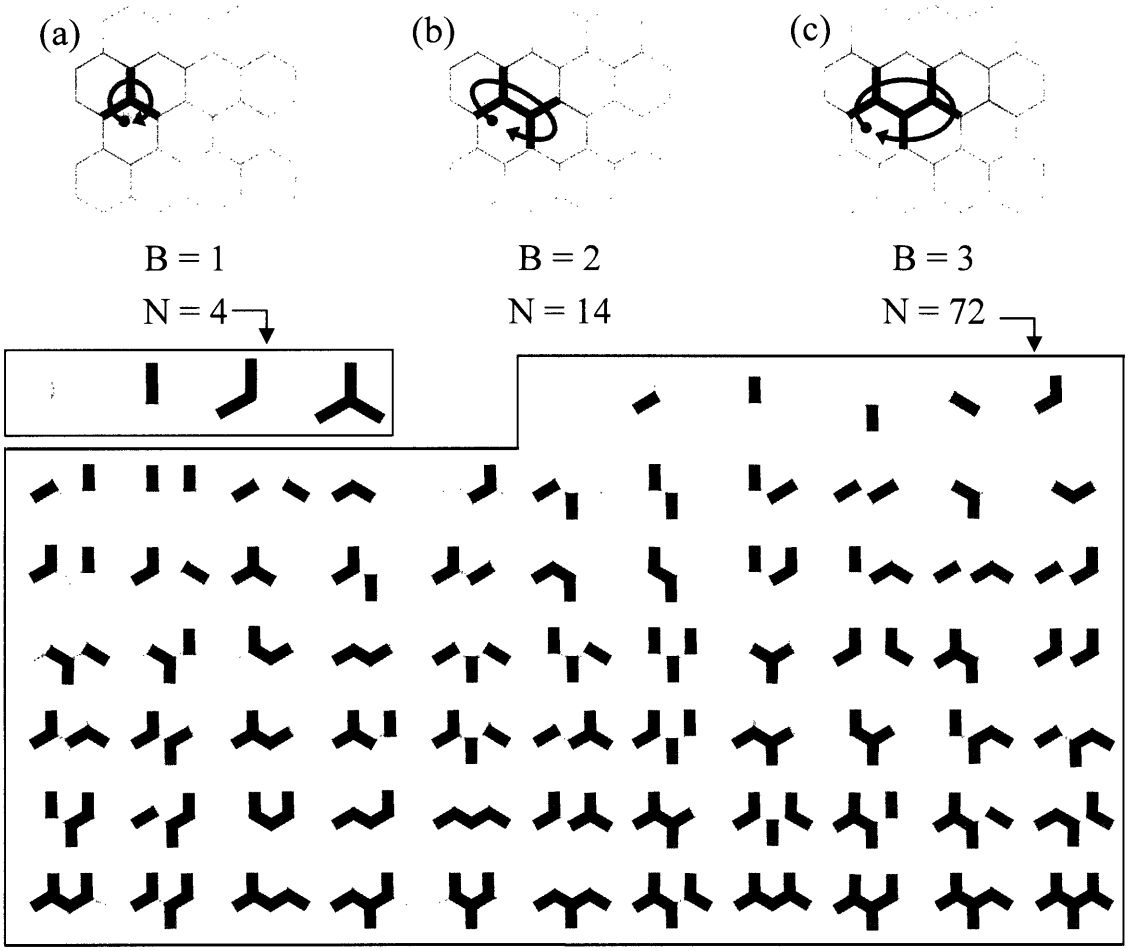

Figure E.1: The first three orders of constraint in 2-D honeycomb lattices are shown schematically. The order of the constraint, B, is given by the number of triple junctions encircled by a Frank-Nabarro circuit. The number of unique species, N, of each order is identified as well. For $B = 1$ and $B = 3$, a representative structure is shown for each of the unique species in which the thicker lines indicate special boundaries and the thin black lines general boundaries.

where V_i^B is the fraction of the i^{th} species from among the $N = 72$ species drawn in Figure E.1. The calculation is performed for the third-order boundary structure simply because this structure contains information about all of the lower-order constraints. In fact, every circuit in Figure E.1 necessarily contains within it smaller loops of lower order, but in general the higher-order circuits involve additional, non-redundant constraints because they encircle some boundaries which they do not cross. In the case of the third-order boundary structure there are three sub-circuits around the triple junctions (first-order constraints), as well as two second-order circuits. None of these is necessarily redundant with one another or with the third-order constraint, and

the important question as we proceed is: how can we deconvolve the individual contributions of each constraint to the configurational entropy?

Our procedure to extract the several entropic contributions follows exactly that described in Chapter 4 for determining the quadruple node distribution from the TJD. Here we use the same general procedure: the probability of finding a structure of third order is calculated using a straightforward probabilistic calculation based on the statistics of the elements of a lower order. Repeating this procedure for B = 1 and 2 gives expectations for the population of third-order species if *only* constraints up to B^{th} order are enforced. In order to compare the strength of the constraint associated with each value of B, we define individual entropy increments in the following way:

$$\Delta S_3^B = \left| S_3^3 - S_3^B \right| \tag{E.2}$$

where S_i^j is the entropy among units of order i, given complete crystallographic constraints up to order j. In the present case where i = 3, S_i^j is given by Eq. (E.1). The populations V_i^B as a function of either J_i (i = 0 to 3, for B = 1) or U_i (i = 0 to 13, for B = 2) are collected at the end of this appendix. In this work we will only examine entropy calculated at the i = 3 level, although the concept is easily extended to higher (or lower) orders. Based on these calculations, we can examine how the entropy of the B = 3 boundary structures (shown in Figure E.1c) evolves as constraints are added in order from least to greatest. Furthermore, we will also compare to the B = 0 case, which is the unconstrained case where boundaries are simply assigned at random.

E.2. Entropy and Constraint

To begin our discussion, we first examine the magnitude of the total entropy change that occurs when all crystallographic constraints up to B = 3 are imposed on an initially random network. This quantity is ΔS_3^0, and is plotted in Figure E.2 for the three microstructural families as a function of the special boundary fraction, p. There are two important points conveyed by this figure. First, the level of constraint in grain boundary networks may vary significantly with the special fraction; grain boundary engineering to increase p may lead to fundamental changes in grain boundary correlations. Second, Figure E.2 also shows that different microstructural families can have distinctly different correlations, with the fiber textured class in this case exhibiting more significant entropy changes due to crystallographic constraint. This result is in

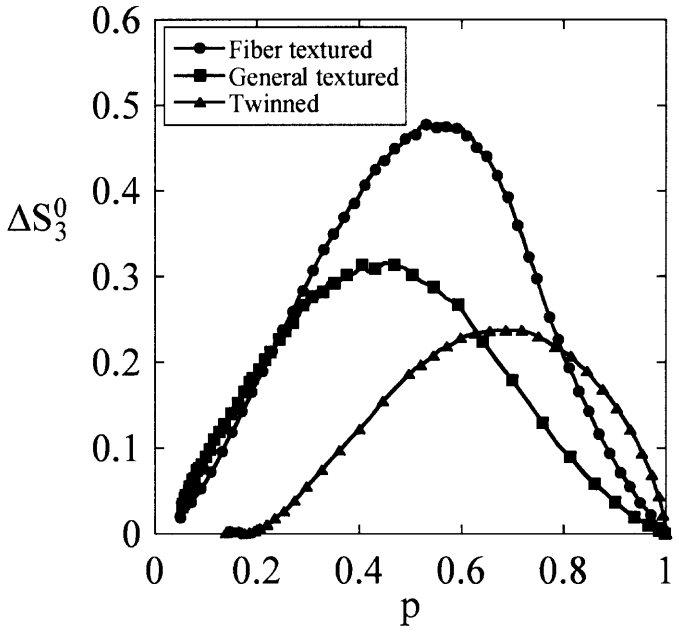

Figure E.2: The magnitude of the total entropy change between a randomly assembled network and one in which full crystallographic constraints are imposed, plotted as a function of p. ΔS_3^0 is calculated from Eq. (E.2) using the population of $B = 3$ boundary structures.

line with our other results on these simulated microstructures (c.f., Chapters 3 and 4), which showed that fiber textured materials have the strongest nearest-neighbor correlations in both 2-D and 3-D.

Although Figure E.2 focused upon the total entropy change given complete crystallographic constraint out to third order, ΔS_3^0, similar plots can be constructed for each of the individual contributions to this total entropy. Rather than examine all of these curves individually, we instead focus upon the behavior in the vicinity of the general boundary percolation threshold ($p \approx 0.35$), because this is the point where correlations have the most impact on network structure and therefore materials properties. Furthermore, this is the threshold which is poorly predicted by considering first-order constraints only (Table 6.1). In Figure E.3, we explicitly plot the contribution of each constraint and examine the entropy change resulting from each. For all of the curves in Figure E.3, we see that the highest entropy is associated with $B = 0$ (i.e., a random network without constraint), and the progressive addition of constraints at $B = 1$, 2 and 3 leads to a decrease in the system entropy. Furthermore, the largest drop in entropy always occurs at the first-order level; this is the triple junction constraint studied

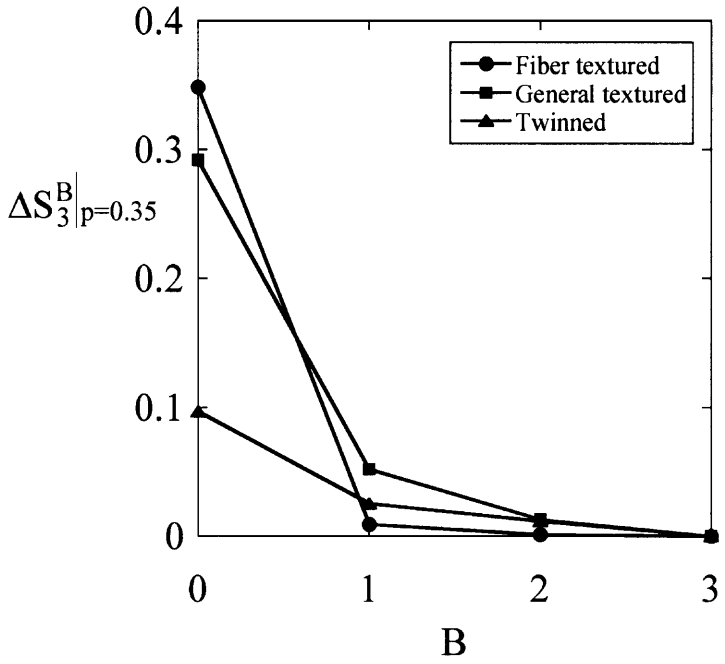

Figure E.3: The contribution of each constraint level (B) to the change in configurational entropy, ΔS_3^B, evaluated at $p = 0.35$ for the $B = 3$ boundary structure.

previously in the literature, which we see here is usually dominant in dictating the system entropy. For example, although the fiber textured microstructures have the largest values of ΔS_3^0 in Figure E.3, ΔS_3^1 in these microstructures approaches zero, suggesting that first-order constraints alone are responsible for virtually all of the information in the system. However, we also clearly see that higher-order constraints are not generally negligible; the entropy drop upon addition of second-order constraints (from $B = 1$ to $B = 2$) in general textured and twinned microstructures, ΔS_3^B is still clearly non-zero. In these microstructural families, it seems that higher-order constraints are relatively more important. To our knowledge, the significance of longer-range correlations has not been appreciated in any prior work on the structure of grain boundary networks. In fact, these effects cannot be observed through studies of, e.g., the triple junction distribution, which samples only first-order effects.

E.3. Percolation Thresholds

One link between grain boundary network structure and properties is through the percolation threshold, which, in a single number, gives information about connectivity over large

length scales. In this thesis work, we have determined the percolation thresholds using either (i) a process of random grain boundary character assignment, (ii) a process of triple junction assignment incorporating first-order constraints (Table 6.1), or (iii) completely crystallographically-consistent assignment of grain orientations (Table 5.1). The thresholds for both special and general boundaries are summarized graphically in Figure E.4 as a function of the constraint on the system. This figure allows us to decouple the effects of first- and higher-order constraints on the resulting shifts of the percolation thresholds.

Looking first at the points for the fiber textured microstructural family, we see that the percolation threshold shifts significantly when first-order constraints are imposed on the system, but that additional higher-order constraints do relatively little to change the picture. This result is consistent with our prior observations from Figure E.3, where we found a dominant first-order constraint in these microstructures. In contrast, the percolation thresholds in both the general textured and twinned microstructures vary with each constraint imposed upon the system. Interestingly, the higher-order constraints seem to have a relatively large impact on the threshold, and in fact, cause a shift *in the opposite direction* as compared to the first-order constraint. This

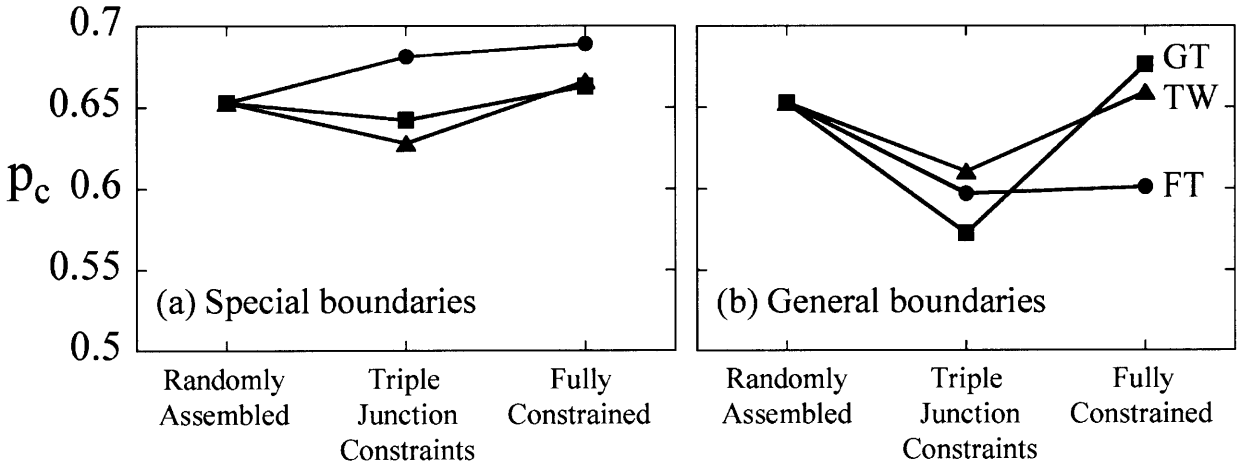

Figure E.4: The percolation thresholds for (a) special boundaries and (b) general boundaries in fiber textured (circles), general textured (squares), or twinned (triangles) microstructures as a function of the constraints imposed on the system. The percolation thresholds are summarized in Table 6.1, and left to right, these data correspond to either random boundary assignment (no constraints imposed), triple junction assignment (only first-order constraints imposed), or grain orientation assignment (resulting in full crystallographic constraint).

result is probably related to the earlier observation from Figure E.3 that these microstructural families have significant higher-order constraints which can compete with the triple junction constraint.

E.4. Discussion of Higher-Order Correlations

One point that emerges from looking at configurational entropy as well as the percolation thresholds is that higher-order constraints cannot, in general, be neglected when studying connectivity of grain boundary networks. The state-of-the-art in experimental network analysis at present is the triple junction distribution; we now suspect that this metric alone is insufficient for a complete understanding of network structure and prediction of properties. Furthermore, we have seen here a great complexity in the way constraints of different order influence the network structure. In particular, constraints of different order may actually *compete with one another* to shift the percolation threshold up or down in p (c.f., Figure E.4).

Another point of particular concern is the significant differences seen from one family of microstructures to the next; whereas polycrystals sharing a common crystallographic axis (fiber textured microstructures) seem to have only very short-range correlations, more complex textures induce longer-range correlations out to at least third order and possibly beyond. We believe this may be related to the details of the crystallographic constraint equations. When the crystals share a crystallographic axis as in our fiber textured materials, it is known that the first-order constraint is rigid (the three signed boundary disorientations sum exactly to zero (Eq. (3.2)). In this case, higher order constraints are, to a large extent, redundant. In contrast, for general textured and twinned microstructures the first-order constraint is much less rigid, so higher-order constraints can provide significantly more information content. The quantitative details as to how crystallographic texture influences grain boundary correlations are certainly not clear at present, and this represents a key issue for the future generalization of percolation theory to any grain boundary network.

Finally, we note that thorough analytical calculations of grain boundary constraints, like those performed here, are rather complex. Already at the third-order level we have to consider the statistics of $N = 72$ structural units. Beyond the third order, additional topological complexities arise because there are non-redundant conformational variations of the Frank-Nabarro circuit. For example, we identify a 'trans' and a 'cis' conformation of the fourth-order

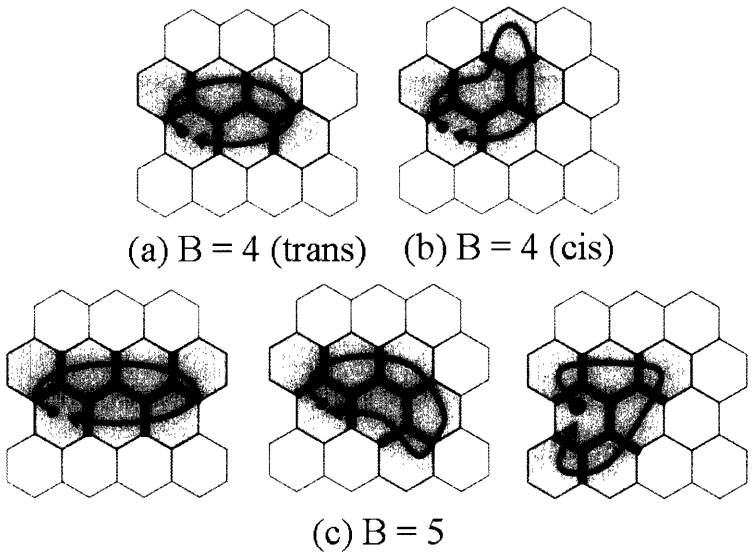

Figure E.5: Frank-Nabarro circuits of fourth (a, b) and fifth (c) order.

circuit (see Figures E.5a and E.5b, respectively), the statistics of which must be considered separately. Figure E.5c shows that there are yet more unique circuits at $B = 5$; it is easy to see how the number of species involved in entropy calculations quickly becomes too large to handle analytically. For this reason, we believe that the study of medium- and long-range structure in grain boundary networks may best be addressed through, e.g., the use of scaling laws, as in Chapter 5.

From this analysis of the length scale of correlations in grain boundary networks, we can understand why the percolation thresholds for fiber textured microstructures are well predicted by the percolation surface in the coordination tetrahedron of Chapter 6 (Figure 6.9), while the thresholds for general textured and twinned microstructures are not. In fiber textured microstructures, first-order constraints are found to dominate higher-order constraints, such that this system is sufficiently described by only its triple junction distribution.

E.5. Expectation Values for Third-Order Boundary Structure Populations

The population of each of the 72 $B = 3$ boundary structures can be predicted from the $B = 1$ or 2 boundary structures following the procedure outlined in Chapter 4 for assembling quadruple nodes from triple junctions. Using the same approach, the $B = 3$ boundary structure populations, V_i^B ($i = 0$ to 71), can be predicted from the triple junction distribution ($B = 1$) as:

$$V_0^1 = \frac{J_0^3}{d_1^2} \tag{E.3}$$

$$V_1^1 = \frac{2 J_0^2 J_1}{3 d_1^2}$$

$$V_2^1 = \frac{2 J_0^2 J_1}{3 d_1^2}$$

$$V_3^1 = \frac{J_0^2 J_1}{3 d_1^2}$$

$$V_4^1 = \frac{2 J_0 J_1^2}{9 d_1 d_2}$$

$$V_5^1 = \frac{2 J_0^2 J_2}{3 d_1^2}$$

$$V_6^1 = \frac{2 J_0 J_1^2}{9 d_1^2}$$

$$V_7^1 = \frac{J_0 J_1^2}{9 d_1^2}$$

$$V_8^1 = \frac{J_0 J_1^2}{9 d_1^2}$$

$$V_9^1 = \frac{2 J_0 J_1 J_2}{9 d_1 d_2}$$

$$V_{10}^1 = \frac{2 J_0 J_1 J_2}{9 d_1 d_2}$$

$$V_{11}^1 = \frac{2 J_0 J_1^2}{9 d_1^2}$$

$$V_{12}^1 = \frac{2 J_0 J_1^2}{9 d_1^2}$$

$$V_{13}^1 = \frac{2 J_1^3}{27 d_1 d_2}$$

$$V_{14}^1 = \frac{2 J_1^3}{27 d_1 d_2}$$

$$V_{15}{}^{1} = \frac{2 J_0 J_1 J_2}{9 d_1 d_2}$$

$$V_{16}{}^{1} = \frac{J_1^2 J_2}{27 d_2^2}$$

$$V_{17}{}^{1} = \frac{2 J_0 J_1 J_2}{9 d_1^2}$$

$$V_{181}{}^{1} = \frac{2 J_0 J_1 J_2}{9 d_1^2}$$

$$V_{19}{}^{1} = \frac{2 J_0 J_1 J_3}{3 d_1 d_2}$$

$$V_{20}{}^{1} = \frac{2 J_0 J_1 J_2}{9 d_1^2}$$

$$V_{21}{}^{1} = \frac{2 J_1^2 J_2}{27 d_1 d_2}$$

$$V_{22}{}^{1} = \frac{2 J_0 J_2^2}{9 d_1 d_2}$$

$$V_{23}{}^{1} = \frac{2 J_0 J_2^2}{9 d_1 d_2}$$

$$V_{24}{}^{1} = \frac{2 J_1^2 J_2}{27 d_1 d_2}$$

$$V_{25}{}^{1} = \frac{2 J_1^2 J_2}{27 d_1 d_2}$$

$$V_{26}{}^{1} = \frac{2 J_1^2 J_2}{27 d_1 d_2}$$

$$V_{27}{}^{1} = \frac{2 J_1^2 J_2}{27 d_1 d_2}$$

$$V_{28}{}^{1} = \frac{2 J_1^2 J_2}{27 d_1 d_2}$$

$$V_{29}{}^{1} = \frac{2 J_1^2 J_2}{27 d_1 d_2}$$

$$V_{30}{}^{1} = \frac{2 J_1 J_2^2}{27 d_2^2}$$

$$V_{31}{}^{1} = \frac{2 J_1 J_2^2}{27 d_2^2}$$

$$V_{32}{}^{1} = \frac{J_1^3}{27 d_1^2}$$

$$V_{33}{}^{1} = \frac{J_1^3}{27 d_1^2}$$

$$V_{34}{}^{1} = \frac{2 J_1^3}{27 d_1^2}$$

$$V_{35}{}^{1} = \frac{J_1^2 J_3}{9 d_2^2}$$

$$V_{36}{}^{1} = \frac{J_0 J_2^2}{9 d_1^2}$$

$$V_{37}{}^{1} = \frac{2 J_0 J_2 J_3}{3 d_1 d_2}$$

$$V_{38}{}^{1} = \frac{2 J_1 J_2^2}{27 d_1 d_2}$$

$$V_{39}{}^{1} = \frac{2 J_1 J_2^2}{27 d_1 d_2}$$

$$V_{40}{}^{1} = \frac{2 J_1 J_2^2}{27 d_1 d_2}$$

$$V_{41}{}^{1} = \frac{2 J_1 J_2 J_3}{9 d_2^2}$$

$$V_{42}{}^{1} = \frac{2 J_1^2 J_3}{9 d_1 d_2}$$

$$V_{43}{}^{1} = \frac{2 J_1^2 J_2}{27 d_1^2}$$

$$V_{44}{}^{1} = \frac{2 J_1^2 J_3}{9 d_1 d_2}$$

$$V_{45}{}^{1} = \frac{2 J_1^2 J_2}{27 d_1^2}$$

$$V_{46}{}^{1} = \frac{2 J_1 J_2 J_3}{9 d_2^2}$$

$$V_{47}{}^{1} = \frac{2 J_1 J_2 J_3}{9 d_2^2}$$

$$V_{48}{}^{1} = \frac{2 J_1 J_2^2}{27 d_1 d_2}$$

$$V_{49}{}^{1} = \frac{2 J_1 J_2^2}{27 d_1 d_2}$$

$$V_{50}{}^{1} = \frac{2 J_1 J_2^2}{27 d_1 d_2}$$

$$V_{51}{}^{1} = \frac{2 J_1 J_2^2}{27 d_1 d_2}$$

$$V_{52}{}^{1} = \frac{J_2^3}{27 d_2^2}$$

$$V_{53}{}^{1} = \frac{2 J_2^3}{27 d_2^2}$$

$$V_{54}{}^{1} = \frac{J_2^3}{27 d_2^2}$$

$$V_{55}{}^{1} = \frac{2 J_1 J_2 J_3}{9 d_1 d_2}$$

$$V_{56}{}^{1} = \frac{2 J_1 J_3^2}{3 d_2^2}$$

$$V_{57}{}^{1} = \frac{J_1 J_2^2}{27 d_1^2}$$

$$V_{58}{}^{1} = \frac{2 J_1 J_2 J_3}{9 d_1 d_2}$$

$$V_{59}{}^{1} = \frac{2 J_1 J_2 J_3}{9 d_1 d_2}$$

$$V_{60}{}^{1} = \frac{2J_2^3}{27 d_1 d_2}$$

$$V_{61}{}^{1} = \frac{2J_2^2 J_3}{9 d_2^2}$$

$$V_{62}{}^{1} = \frac{2J_2^3}{27 d_1 d_2}$$

$$V_{63}{}^{1} = \frac{2J_2^2 J_3}{9 d_2^2}$$

$$V_{64}{}^{1} = \frac{2J_2^2 J_3}{9 d_2^2}$$

$$V_{65}{}^{1} = \frac{J_2^2 J_3}{9 d_2^2}$$

$$V_{66}{}^{1} = \frac{J_2^2 J_3}{9 d_2^2}$$

$$V_{67}{}^{1} = \frac{2J_2^2 J_3}{9 d_1 d_2}$$

$$V_{68}{}^{1} = \frac{J_2 J_3^2}{3 d_2^2}$$

$$V_{69}{}^{1} = \frac{2J_2 J_3^2}{3 d_2^2}$$

$$V_{70}{}^{1} = \frac{2J_2 J_3^2}{3 d_2^2}$$

$$V_{71}{}^{1} = \frac{J_3^3}{d_2^2}$$

where the denominator terms are:

$$d_1 = J_0 + \frac{2J_1}{3} + \frac{J_2}{3} \qquad \text{(E.4)}$$

$$d_2 = \frac{J_1}{3} + \frac{2J_2}{3} + J_3$$

Taking into account all correlations up to second order, the populations V_i^B can be predicted based on the distribution of $B = 2$ boundary structures, U_i ($i = 0$ to 13), as:

$$V_0^2 = \frac{U_0^2}{d_3} \tag{E.5}$$

$$V_1^2 = \frac{U_0 U_1}{2 d_3}$$

$$V_2^2 = \frac{U_0 U_1}{2 d_3}$$

$$V_3^2 = \frac{U_1^2}{16 d_5}$$

$$V_4^2 = \frac{U_1 U_2}{2 d_5}$$

$$V_5^2 = \frac{U_0 U_3}{d_3}$$

$$V_6^2 = \frac{U_1^2}{8 d_3}$$

$$V_7^2 = \frac{U_1^2}{16 d_3}$$

$$V_8^2 = \frac{U_1^2}{16 d_3}$$

$$V_9^2 = \frac{U_1 U_4}{8 d_4}$$

$$V_{10}^2 = \frac{U_1 U_4}{8 d_5}$$

$$V_{11}^2 = \frac{U_1 U_5}{4 d_5}$$

$$V_{12}^2 = \frac{U_1 U_6}{4 d_5}$$

$$V_{13}^2 = \frac{U_2 U_5}{d_4}$$

$$V_{14}^2 = \frac{U_2 U_6}{d_4}$$

$$V_{15}^2 = \frac{U_3 U_4}{4 d_7}$$

$$V_{16}^2 = \frac{U_4^2}{16 d_6}$$

$$V_{17}^2 = \frac{U_1 U_3}{4 d_3}$$

$$V_{18}^2 = \frac{U_1 U_3}{4 d_3}$$

$$V_{19}^2 = \frac{U_1 U_7}{4 d_5}$$

$$V_{20}^2 = \frac{U_1 U_8}{8 d_5}$$

$$V_{21}^2 = \frac{U_2 U_8}{2 d_4}$$

$$V_{22}^2 = \frac{U_3 U_9}{2 d_7}$$

$$V_{23}^2 = \frac{U_3 U_{10}}{2 d_7}$$

$$V_{24}^2 = \frac{U_4 U_5}{4 d_5}$$

$$V_{25}^2 = \frac{U_4 U_5}{4 d_5}$$

$$V_{26}^2 = \frac{U_4 U_6}{4 d_5}$$

$$V_{27}^2 = \frac{U_4 U_6}{4 d_5}$$

$$V_{28}^2 = \frac{U_4 U_8}{8 d_6}$$

$$V_{29}^2 = \frac{U_4 U_8}{8 d_6}$$

$$V_{30}^2 = \frac{U_4 U_9}{4 d_6}$$

$$V_{31}^2 = \frac{U_4 U_{10}}{4 d_6}$$

$$V_{32}^2 = \frac{U_5^2}{4 d_5}$$

$$V_{33}^2 = \frac{U_5 U_6}{4 d_5}$$

$$V_{34}^2 = \frac{U_6^2}{2 d_5}$$

$$V_{35}^2 = \frac{U_7^2}{4 d_8}$$

$$V_{36}^2 = \frac{U_3^2}{4 d_3}$$

$$V_{37}^2 = \frac{U_3 U_{12}}{4 d_7}$$

$$V_{38}^2 = \frac{U_4 U_8}{8 d_4}$$

$$V_{39}^2 = \frac{U_4 U_8}{8 d_4}$$

$$V_{40}^2 = \frac{U_4 U_{11}}{2 d_6}$$

$$V_{41}^2 = \frac{U_4 U_{12}}{8 d_6}$$

$$V_{42}^2 = \frac{U_5 U_7}{2 d_5}$$

$$V_{43}^2 = \frac{U_5 U_8}{4 d_5}$$

$$V_{44}^2 = \frac{U_6 U_7}{2 d_5}$$

$$V_{45}^2 = \frac{U_6 U_8}{4 d_5}$$

$$V_{46}^2 = \frac{U_7 U_{12}}{4 d_8}$$

$$V_{47}^2 = \frac{U_7 U_{12}}{4 d_8}$$

$$V_{48}^2 = \frac{U_8 U_9}{4 d_7}$$

$$V_{49}^2 = \frac{U_8 U_9}{4 d_7}$$

$$V_{50}^2 = \frac{U_8 U_{10}}{4 d_6}$$

$$V_{51}^2 = \frac{U_8 U_{10}}{4 d_6}$$

$$V_{52}^2 = \frac{U_9^2}{4 d_6}$$

$$V_{53}^2 = \frac{U_9 U_{10}}{2 d_6}$$

$$V_{54}^2 = \frac{U_{10}^2}{4 d_6}$$

$$V_{55}^2 = \frac{U_7 U_8}{4 d_5}$$

$$V_{56}^2 = \frac{U_7 U_{13}}{d_8}$$

$$V_{57}^2 = \frac{U_8^2}{16 d_5}$$

$$V_{58}^2 = \frac{U_8 U_{12}}{8 d_6}$$

$$V_{59}^2 = \frac{U_8 U_{12}}{8 d_7}$$

$$V_{60}^2 = \frac{U_9 U_{11}}{d_6}$$

$$V_{61}^2 = \frac{U_9 U_{12}}{4 d_6}$$

$$V_{62}^2 = \frac{U_{10}U_{11}}{d_6}$$

$$V_{63}^2 = \frac{U_{10}U_{12}}{4d_6}$$

$$V_{64}^2 = \frac{U_{12}^2}{8d_8}$$

$$V_{65}^2 = \frac{U_{12}^2}{16d_8}$$

$$V_{66}^2 = \frac{U_{12}^2}{16d_8}$$

$$V_{67}^2 = \frac{U_{11}U_{12}}{2d_7}$$

$$V_{68}^2 = \frac{U_{12}^2}{16d_6}$$

$$V_{69}^2 = \frac{U_{12}U_{13}}{2d_8}$$

$$V_{70}^2 = \frac{U_{12}U_{13}}{2d_8}$$

$$V_{71}^2 = \frac{U_{13}^2}{d_8}$$

where the denominator terms are:

$$d_3 = U_0 + \frac{U_1}{2} + \frac{U_3}{2} \qquad \text{(E.6)}$$

$$d_4 = U_2 + \frac{U_4}{2} + \frac{U_7}{2}$$

$$d_5 = \frac{U_1}{4} + \frac{U_5}{2} + \frac{U_6}{2} + \frac{U_8}{4}$$

$$d_6 = \frac{U_4}{4} + \frac{U_9}{2} + \frac{U_{10}}{2} + \frac{U_{12}}{4}$$

$$d_7 = \frac{U_3}{2} + \frac{U_8}{2} + U_{11}$$

$$d_8 = \frac{U_7}{2} + \frac{U_{12}}{2} + U_{13}$$